

Low Oxidation State Heavy p-Block Metal Compounds Supported by Di(amido) Chelating Ligands

by

Ryan James Schwamm



A thesis

submitted to the Victoria University of Wellington in fulfilment of the
requirements for the degree of
Doctor of Philosophy

Victoria University of Wellington

2018

Acknowledgements

First and foremost, I would like to thank my supervisor Assoc. Prof. Martyn Coles for his support, guidance and leadership. Since joining his group six years ago, the research that we have performed together has been one of the most rewarding experiences of my life. His work ethic and enthusiasm for chemistry are contagious and made the roller coaster of a PhD significantly more enjoyable.

A number of collaborators have been instrumental to the work in this thesis. To my ANSTO co-supervisor, Dr Alison Edwards, thank you for your guidance and support in the neutron diffraction experiments. Our discussions involving the fundamental aspects of crystallography were invaluable to my understanding of X-ray and neutron diffraction. I would also like to thank Dr Matthias Lein for his invaluable insight into my molecules through theoretical studies, Dr Alexander Kilpatrick for collecting cyclic voltammetry data reported in chapter 2, and Dr Chris Fitchett for his help in collecting and solving some of the X-ray crystal structures discussed in this thesis. I would also like to thank the technical staff at Victoria University of Wellington (VUW) for their assistance over my time here. In particular, I would like to thank Ian Vorster for seemingly moving heaven and earth to help me whenever asked. I would also like to thank Prof. Richard Hartshorn (University of Canterbury, New Zealand) for his insight on the systematic IUPAC naming of the (NON^R)-ligand.

Thank you to the various members of the Coles and Fulton groups, past and present, for keeping me somewhat sane over the years. A special thanks goes to Dr J. Robin Fulton for her insight into useful experiments for understanding the mechanisms of complicated processes. Also, thanks to all the people from other groups at VUW that I have had the opportunity to get to know.

Thank you to the various funding sources over the courses of this PhD. In particular, I would like to thank VUW for the VUW Doctoral Scholarship and the Australian Institute of Nuclear

Science and Engineering (AINSE) for the AINSE Postgraduate Research Award (PGRA). Without this financial support, the work presented in this thesis would not have been possible.

I would like to thank my parents and family for their constant and unwavering support and encouragement over the years, despite thinking that I make bombs for a living. Each one of them have impacted my life and made me who I am. Finally, I would like to thank my wife and best friend, Karen. Thank you for waking me up every morning and always being there for me.

Abstract

The work presented in this thesis describes the synthesis and stabilisation of heavy p-block elements (defined herein as being those with 5s/p and 6s/p valence electrons) in low oxidation states using sterically demanding ligands based on a di(amido)siloxane framework ($[(\text{O}\{\text{SiMe}_2\text{N}(\text{R})\}_2)^{2-}]$, abbrev. $[(\text{NON}^{\text{R}})]^{2-}$).

Chapter 1 gives a general introduction to the heavy p-block elements and discusses a number of concepts that define the molecular chemistry of these elements. A brief introduction into low oxidation state main group chemistry is provided and the importance of sterically demanding ligands in this field of research is introduced. The di(amido)siloxane ligand framework utilised in this work is introduced, with common coordination modes and characteristic properties discussed.

Chapter 2 discusses the chemistry of low oxidation state bismuth complexes and follows a recent report by our group on the first structurally authenticated bismuth(II) radical $\bullet\text{Bi}(\text{NON}^{\text{Ar}})$. The synthesis of a series of bismuth(III) monochloride species $\text{Bi}(\text{NON}^{\text{R}})\text{Cl}$ ($\text{R} = t\text{Bu}$, Ph , $2,6\text{-Me}_2\text{C}_6\text{H}_3$ (Ar'), $2,6\text{-}i\text{Pr}_2\text{C}_6\text{H}_3$ (Ar) and $2,6\text{-(CHPh}_2)_2\text{-4-}t\text{Bu-C}_6\text{H}_2$ (Ar^\ddagger)) is discussed, and the steric properties of the ligand systems evaluated. In the case of the $\text{R} = t\text{Bu}$ and Ar^\ddagger derivatives, reduction of the bismuth(III) monochloride gave the dibismuthane $[\text{Bi}(\text{NON}^{t\text{Bu}})]_2$ and bismuth(II) radical $\bullet\text{Bi}(\text{NON}^{\text{Ar}^\ddagger})$, respectively. Further reduction of the bismuth centres resulted in the formation of rare and unprecedented multimetallic bismuth compounds containing $[\text{Bi}_n]^{n+}$ cores. These include the Bi_4 cluster compound $\text{Bi}_4(\text{NON}^{\text{Ar}})_2$, in which the bismuth atoms exist in an unprecedented mixed valent arrangement and may be assigned oxidation states of 0, +1 or +2, and the tribismuthane cluster $[\text{Bi}_3(\text{NON}^{t\text{Bu}})_2]^-$, which features the first structurally characterised Bi_3 chain. The utility of the di(amido) ligand plays a key role in the formation of many of these compounds, with Bi-N bond cleavage suggested to be a key step in many of the reaction pathways.

Chapter 3 discusses the reactivity of the bismuth(II) complexes $[\text{Bi}(\text{NON}^{\text{tBu}})]_2$, $\bullet\text{Bi}(\text{NON}^{\text{Ar}})$ and $\bullet\text{Bi}(\text{NON}^{\text{Ar}\ddagger})$ which feature either a Bi-Bi bond or a bismuth-centred radical. Initial experiments parallel reported reactivity with halogen radical sources (*N*-bromosuccinimide or iodine), chalcogens (S, Se, Te) and the stable nitroxyl radical (2,2,6,6-tetramethylpiperidin-1-yl)oxyl (TEMPO), resulting in oxidative addition to generate bismuth(III) complexes. In the latter case, the isolated reaction products, $\text{Bi}(\text{NON}^{\text{R}})(\text{OTEMP})$, were used to access the catalytic coupling of TEMPO and phenylsilane. Subsequent investigations into the reactivity of the bismuth(II) species revealed the selective activation of white phosphorus (P_4) and terminal aromatic alkynes by $\bullet\text{Bi}(\text{NON}^{\text{Ar}})$, generating the bismuth(III) complexes $[\text{Bi}(\text{NON}^{\text{Ar}})]_2(\text{P}_4)$ and $[\text{Bi}(\text{NON}^{\text{R}})]_2(\text{HC}=\text{C}(\text{C}_6\text{H}_4\text{-4-X}))$, respectively. In both cases, a temperature dependent equilibrium is observed. In contrast, the dibismuthane $[\text{Bi}(\text{NON}^{\text{tBu}})]_2$ and more encumbered bismuth radical $\bullet\text{Bi}(\text{NON}^{\text{Ar}\ddagger})$ do not react with these substrates, demonstrating the importance of the nature of the bismuth centre (i.e. dibismuthane vs. bismuth radical) and ligand bulk on the reactivity of these systems.

Chapter 4 describes the synthesis and characterisation of a series of low oxidation state antimony compounds. A series of distibanes supported by the (NON^{R}) -framework were prepared from the reaction of antimony(III) chloride species $\text{Sb}(\text{NON}^{\text{R}})\text{Cl}$ with magnesium(I) reducing agents $[(\text{BDI}^{\text{Ar}\ddagger})\text{Mg}]_2$ ($\text{Ar}^{\ddagger} = 2,4,6\text{-Me}_3\text{C}_6\text{H}_3$ or Ar). When $\text{R} = \text{tBu}$, Ph or $2,6\text{-Me}_2\text{C}_6\text{H}_3$ (Ar'), a distibane $[\text{Sb}(\text{NON}^{\text{R}})]_2$ is obtained, featuring a Sb-Sb single bond. While the *t*Bu and Ph derivatives contained typical Sb-Sb single bonds, the bonding in the Ar' derivative is elongated, significantly longer than in all other reported distibanes. The weakness of this bond is highlighted in a reaction with P_4 , which shows activation of the P_4 tetrahedron and P-P bond cleavage. In contrast, reduction of the bulkier Ar derivative ($\text{Ar} = 2,6\text{-iPr}_2\text{C}_6\text{H}_3$) with the magnesium(I) reagents results in formation of the distibene $[\text{Sb}(\text{NON}^{\text{R}})\text{Mg}(\text{BDI}^{\text{Ar}\ddagger})]_2$, featuring a Sb=Sb bond.

Chapter 5 describes the synthesis and characterisation of low oxidation state indium compounds supported by the (NON^{Ar}) -ligand. A number of indium(III) chloride species

supported by either the (NON^{Ar})-ligand or the retro-Brook rearranged (NNO^{Ar})-ligand ($\text{NNO}^{\text{Ar}} = [\text{RN}\{\text{Me}_2\text{SiO}\}\{\text{Me}_2\text{SiN(R)}\}]$) were synthesised. In all cases, an equivalent of lithium chloride was retained in the molecular structure, allowing isolation of the indate complexes $\text{In}(\text{NON}^{\text{Ar}})(\mu\text{-Cl})_2\text{Li}(\text{Et}_2\text{O})_2$, $[\text{Li}(\text{THF})_4][\text{In}(\text{NON}^{\text{Ar}})\text{Cl}_2]$ and $\text{In}(\text{NNO}^{\text{Ar}}.\text{Li}(\text{THF})_3)\text{Cl}_2$. Attempts to reduce these complexes using a hydride source were unsuccessful, instead yielding the corresponding indium(III) hydride species $[\text{Li}(\text{THF})_4][\text{In}(\text{NON}^{\text{Ar}})\text{H}_2]$ and $\text{In}(\text{NNO}^{\text{Ar}}.\text{Li}(\text{THF})_3)\text{H}_2$, respectively. Reduction of the (NON^{Ar})-supported indium(III) chloride complexes using alkali reducing agents allowed access to the diindane $[\text{In}(\text{NON}^{\text{Ar}})]_2$, featuring an In-In single bond, and the first example of an anionic N-heterocyclic indene. The latter species is isovalent with N-heterocyclic carbenes and is a potential pre-cursor for indium-metal bonding formation. In addition, this compound is of interest as a source of nucleophilic indium.

Finally, Chapter 6 provides a summary of the results presented in this thesis and a brief overview of the future direction of this field of research.

Abbreviations

2c2e	2-centre-2-electron
AINSE	Australian Institute of Nuclear Science and Engineering
ANSTO	Australian Nuclear Science and Technology Organisation
Ar	2,6-diisopropylphenyl, 2,6- <i>i</i> Pr ₂ C ₆ H ₃
Ar'	2,6-dimethylphenyl, 2,6-Me ₂ C ₆ H ₃
Ar [‡]	2,6-(CHPh ₂) ₂ -4- <i>t</i> BuC ₆ H ₂
Ar [#]	2,6-mes ₂ C ₆ H ₃
BDI	β-diketiminate
μ	Bridging
br	Broad
CAAC	Cyclic alkyl(amino) carbene
ΔT	Change in temperature
δ	Chemical shift (ppm)
Cp	C ₅ H ₅
Cp*	C ₅ Me ₅
CSD	Cambridge Structural Database
CV	Cyclic Voltammetry
Cy	Cyclohexyl
DFT	Density Functional Theory
ΔE _{s-p}	Difference in energy between valence s- and p-orbitals
DTDA	1,2,3,5-dithiadiazolyl
EPR	Electron Paramagnetic Resonance
Et	Ethyl
Hz	Hertz, s ⁻¹
HMBC	Heteronuclear Multiple Bond Correlation
HOMO	Highest Occupied Molecular Orbital
<i>i</i> Pr	<i>iso</i> -propyl
IR	Infra-red

<i>J</i>	Coupling constant
kcal	Kilocalories
kJ	Kilojoules
LUMO	Lowest Occupied Molecular Orbital
<i>m</i> -	meta
Me	Methyl
mes	Mesityl, 2,4,6-Me ₃ C ₆ H ₂
NHC	N-heterocyclic carbene
NMR	Nuclear Magnetic Resonance
(NNO ^R)	RN{Me ₂ SiO}{Me ₂ SiN(R)}
(NON ^R)	(O{SiMe ₂ N(R)} ₂)
<i>n</i> Bu	<i>n</i> -Butyl
<i>o</i> -	ortho
<i>p</i> -	para
<i>p</i> -tolyl	4-MeC ₆ H ₄
p*	empty p-orbital
%V _{Bur}	Percent buried volume
Ph	Phenyl
s	Singlet
SET	Single Electron Transfer
Sept	Septet
SOMO	Singly Occupied Molecular Orbital
Ω	Solid Angle
TEMPO	2,2,6,6-tetramethylpiperidin-1-yl)oxyl
Ter-phenyl/Ter	2,6-aryl ₂ C ₆ H ₃
<i>t</i> Bu	<i>tert</i> -butyl
THF	Tetrahydrofuran
θ	Tolman Cone Angle
UV	Ultraviolet
λ	Wavelength

Table of Contents

Acknowledgements	I
Abstract	III
Abbreviations.....	VI
Table of Contents	VIII
Chapter 1. General Introduction	1
1.1. The Physical and Chemical Properties of the Heavy p-Block Elements.....	1
1.1.1. Size	1
1.1.2. Energy of Frontier Orbitals and Relative Bond Strengths	2
1.1.3. The Inert Pair Effect	2
1.2. Heavy p-Block Metal Hydrides.....	4
1.3. Low Oxidation State Heavy p-Block Elements	5
1.3.1. Synthetic Routes to Low Oxidation State Compounds.....	6
1.4. Sterically Demanding Ligands	7
1.4.1. Bulky Amide ligands.....	8
1.4.2. Di(amido) Ligands	9
1.4.3. Coordination Chemistry of the (NON ^R)-Ligand.....	9
1.5. Assessing the Steric Bulk of a Ligand	11
1.5.1. Percent Buried Volume (%V _{Bur})	12
1.5.2. Solid Angle and G-parameter	13
1.5.3. Limitations and Considerations	14
Chapter 2. Synthesis of Low Oxidation State Bismuth Species	15
2.1. Introduction	15
2.1.1. Bimetallic and Polymetallic Low Oxidation State Bismuth Compounds	15
2.1.2. Monometallic Low Oxidation State Bismuth Compounds	17
2.2. Chapter Outline.....	19
2.3. Result and Discussion	20
2.3.1. Synthesis and Characterisation of Bismuth(III) Chloride Compounds	20
2.3.2. Synthesis and Characterisation of [Bi(NON ^R)] _n	33
2.3.3. Synthesis and Characterisation of Bismuth(I) Species	43
2.4. Conclusion.....	53

2.5.	Experimental	55
2.5.1.	Synthesis of Bismuth(III) Chloride Compounds	55
2.5.2.	Synthesis of Bismuth(II) Compounds.....	59
2.5.3.	Reduction of Bismuth(II) Species.....	62
Chapter 3.	Reactivity of Low Oxidation State Bismuth Species	64
3.1.	Introduction	64
3.1.1.	Oxidative Reactivity with R'-X (X = halogen, R' = H, alkyl, aryl, halogen).....	65
3.1.2.	Oxidative Reactivity with Chalcogens.....	65
3.1.3.	Reactivity with TEMPO	67
3.1.4.	Reactivity with Metal Complexes	67
3.2.	Chapter Outline.....	68
3.3.	Results and Discussion	69
3.3.1.	Reactivity of Bi(II) Species with Halogen Containing Reagents.....	69
3.3.2.	Reactivity of Bi(II) Species with Chalcogens	76
3.3.3.	Reactivity of Bi(II) Species with TEMPO.....	90
3.3.4.	Reactivity of Bi(II) Species with White Phosphorus (P ₄).....	95
3.3.5.	Reactivity of Bi(II) Species with Unsaturated Substrates	102
3.4.	Conclusion.....	109
3.5.	Experimental.....	109
3.5.1.	Synthesis of Bismuth(III) Halogen Compounds	109
3.5.2.	Synthesis of Bismuth(III) Chalcogenides.....	113
3.5.3.	Synthesis of Bismuth(III) TEMPOxide Species	117
3.5.4.	Reactivity of Bismuth(II) Species with White Phosphorus (P ₄)	119
3.5.5.	Reactivity of Bismuth(II) Species with Unsaturated Substrates.....	121
Chapter 4.	Synthesis of Low Oxidation State Antimony Species	122
4.1.	Introduction	122
4.1.1.	Bimetallic and Polymetallic Low Valent Antimony [†]	122
4.1.2.	Monometallic Low Valent Antimony.....	124
4.2.	Chapter Outline.....	126
4.3.	Results and Discussion	127
4.3.1.	Synthesis of Antimony(III) Chloride Species	127
4.3.2.	Synthesis of Low Oxidation State Antimony Compounds.....	133

4.3.3.	Reactivity of Reduced Antimony Species with White Phosphorus (P_4)	149
4.4.	Conclusion.....	151
4.5.	Experimental.....	152
4.5.1.	Synthesis of Antimony(III) Chloride Species	152
4.5.2.	Reactivity of $Sb(NON^R)Cl$ with $LiHBEt_3$	154
4.5.3.	Reactivity of Sb(II) Compounds with White Phosphorus (P_4)	157
Chapter 5.	Synthesis of Low Oxidation State Indium Species.....	159
5.1.	Introduction	159
5.1.1.	Low Oxidation State Indium Compounds.....	159
5.1.2.	N-heterocyclic Group 13 Compounds	161
5.1.3.	Indium Hydrides	165
5.2.	Chapter Outline.....	166
5.3.	Results and Discussion	167
5.3.1.	Synthesis of Indium(III) Halide Species.....	167
5.3.2.	Synthesis of Indium(III) Hydride Species	171
5.3.3.	Reduction of $[In(NON^{Ar})Cl_2]^-$ with Group 1 Metals.....	177
5.4.	Conclusion.....	181
5.5.	Experimental	182
5.5.1.	Synthesis of Indium(III) Halides	182
5.5.2.	Synthesis of Indium(III) Hydrides.....	183
5.5.3.	Synthesis of Reduced Indium Species	184
Chapter 6.	Summary and Outlook.....	186
Chapter 7.	Appendix.....	192
7.1	General Experimental Details	193
7.2	Supplementary Figures	194
7.3	Crystallographic Details	209
References	219
Publications in Support of this Thesis.....		232

Chapter 1. General Introduction

1.1. The Physical and Chemical Properties of the Heavy p-Block Elements[†]

The coordination chemistry of the main group elements has received significant interest in recent years, due in part to the development of systems capable of demonstrating transition metal-like reactivity.¹ For example, the emergence of systems capable of activating H-H and C-H bonds, and a range of unsaturated small molecules (e.g. CO₂, CO) has been demonstrated for several main group metal systems.² Among these species, the most common elements investigated are those in the second and third rows of the periodic table (e.g. Mg, Ga, Ge).³ In contrast, the molecular chemistry of the heavy p-block metals (defined herein as being those with 5s/p and 6s/p valence electrons) is significantly under-represented in the literature, due in part to the low stability often associated with complexes featuring these elements.⁴

The heavy p-block elements differ from their lighter congeners in both their physical and chemical properties. This is most evident in the bulk phase, where the lighter elements generally behave as non-metals while the heavier elements exhibit metallic properties. Some of the major differences between the heavier and lighter p-block elements are highlighted below.

1.1.1. Size

The 'size' of an element (corresponding to the mean distance of the valence orbitals from the nucleus of an atom) has a large influence on the coordination chemistry and reactivity of the element. The most striking difference between the heavy p-block elements and their lighter congeners is the increase in size as the groups are descended. This is illustrated by increases in the atomic radius (Table 1.1)⁵ for the heavier p-block elements compared to the lighter

[†] Due to significant differences in the chemical properties, the chalcogens (group 16 elements) and halogens (group 17 elements) are not included in this discussion.

elements. This allows the heavier elements to accommodate greater coordination numbers. In addition, the amount of steric protection required to kinetically stabilise reactive species also increases (Section 1.4).

Table 1.1. Atomic Radii (Å) of the p-Block Elements^a

Group 13		Group 14		Group 15	
Al	1.18 (100)	Si	1.11 (100)	P	0.98 (100)
Ga	1.36 (115)	Ge	1.25 (113)	As	1.14 (116)
In	1.56 (132)	Sn	1.45 (131)	Sb	1.33 (136)
Tl	1.56 (132)	Pb	1.54 (139)	Bi	1.43 (151)

^a numbers in brackets correspond to % of the radius for the lightest element listed in the group.

1.1.2. Energy of Frontier Orbitals and Relative Bond Strengths

According to valence bond theory, the concept of ‘orbital overlap’, may be used as a qualitative assessment of the degree to which overlapping valence orbitals form bonding interactions. The effectiveness of this overlap is dictated by both the relative energy and spatial arrangement of the valence orbitals. Similar valence orbital energies and spatial arrangements often result in more favourable overlap and stronger bonding interactions.⁶

The frontier orbitals of the heavy p-block elements (5s/p and 6s/p orbitals) are higher energy and more diffuse than those of their lighter congeners, resulting in energy and spatial mismatches between the heavier elements and lighter elements. This contributes to weaker bonding interactions between the heavier p-block elements and lighter elements.

1.1.3. The Inert Pair Effect

First coined in the 1930s, the term ‘inert pair effect’ refers to the tendency of the heavy p-block elements to retain the valence s-electrons as a non-bonding lone pair and is evidenced by a difference in the relative stability of the oxidation states in the heavier elements compared to their lighter congeners.⁶ For example, while molecular aluminium is most commonly found in the +3 oxidation state, the +1 oxidation state is generally favoured for thallium.⁷

The accepted explanation for the chemical inertness of these electrons is attributed to a combination of relativistic effects and thermodynamic factors. Upon descending the p-block, the difference in energy between the valence ns and np ($n = 5$ or 6) orbitals (ΔE_{s-p}) increases dramatically. This is partly caused by relativistic effects, where the charge of the nucleus (Z) increases dramatically down the groups resulting in the velocity of the $1s$ electrons approaching the speed of light causing them to contract closer to the nucleus and leading to an overall contraction of the ns orbitals ($n = 2 - 6$).⁸ In contrast, the np orbitals ($n = 2 - 6$) are significantly less contracted and are relatively unaffected by the increased nuclear charge leading to a greater ΔE_{s-p} . A larger ΔE_{s-p} results in a greater energy barrier to hybridisation and promotes retention of the ns electrons as a non-bonding lone pair. To utilise the ns electrons in bonding, the energy of bond formation must exceed the energy required for hybridisation. However, bonding interactions between the heavy p-block elements and the lighter p-block elements are often too weak to exceed this threshold. The summation of these factors results in preferential retention of the chemically inert valence s electrons in the heavier p-block elements.

Apart from the chemical stability, contributions of the lone pair to the stereochemistry of the metal centre is common among the heavier p-block elements. The cause of this stereochemical activity is still unconfirmed.⁹ Despite the relatively large energy separation and different spatial distribution of the ns/np orbitals, the stereoactivity of the lone pairs was originally thought to correspond to sp mixing of $5s-5p$ and $6s-6p$ states of the metal centre (i.e. a non-bonding orbital with partial p-character).¹⁰ However, recent theoretical work has suggested that the stereochemical properties of the lone pair may be dependent on the ligands bound to the metal centre,¹¹ while other studies have suggested stereochemically active lone pairs may arise due to unfavourable interactions between antibonding metal ns /ligand np molecular orbitals.¹² In general, the influence of the stereochemically active lone pair decreases down the periodic table group and with increasing coordination number.

1.2. Heavy p-Block Metal Hydrides

Much of the work on p-block metal hydrides (defined herein as species containing a M-H bond, M = metal) has focussed on the lighter elements (e.g. Al and Ga), while the heavier elements have been largely neglected.¹³ This is due in part to the loss of thermal stability in the M-H bond down the periodic table. For example, AlH_3 is stable at temperatures up to 105 °C,¹⁴ while GaH_3 and InH_3 decompose rapidly at temperatures above -33 °C and -90 °C, respectively.¹⁵ Thallium(III) hydride has not been reported, presumably due to its low stability.

The thermodynamic stability of M-H bonds involving the heavier p-block elements has been calculated to be similar to the corresponding M-CH₃ bond, which are ubiquitous in this area of chemistry, suggesting that the thermal instability is not due to an inherent weakness in the bond.¹⁶ In contrast to alkyl groups, H^- tends to form bridging interactions between multiple metal centres, making associative decomposition pathways more favourable (Figure 1.1).¹³ This is further enhanced for the heavier p-block metals, which have an increased tendency to form bridging interactions resulting from a weaker/longer M-H bond. As such, much of the research surrounding the isolation of heavy main group metal hydrides is centred on the use of sterically demanding ligands capable of preventing the formation of bridging interactions. Limiting the propensity for hydride compounds to participate in M-H-M bridges is proposed to increase the energy barrier to associative decomposition pathways (Figure 1.1, a and b).¹³

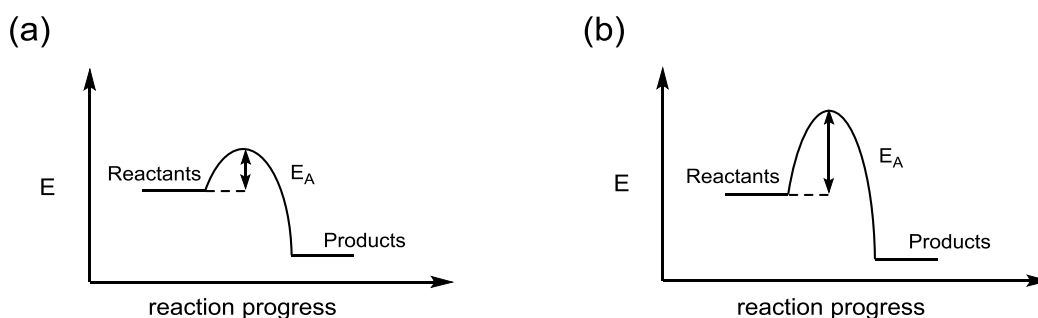
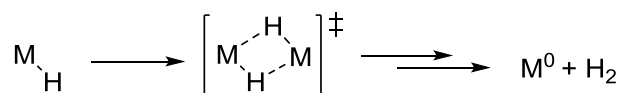


Figure 1.1. Proposed associative decomposition pathway for metal hydrides and representative plot of the reaction coordinate for sterically unprotected (a) and protected (b) metal hydrides.

1.3. Low Oxidation State Heavy p-Block Elements

The assignment of oxidation states is an important concept in chemistry, and plays a vital role in predicting the expected reactivity of a species. While the transition metals have multiple readily accessible oxidation states due to their partially filled d-orbitals, the main group elements are generally found in one or two common oxidation states.¹ Compounds that contain main group elements in oxidation states lower than the common oxidation states (e.g. group 13, +1 and +2; group 14, +1; group 15, +1 and +2) are of interest as synthetic targets due to their attractive physicochemical properties and their potential applications as reducing agents in small molecule activation and catalysis.² For example, magnesium(I) species $[(\text{BDI}^{\text{Ar}^{\text{S}}})\text{Mg}]_2$ (Figure 1.2, Ar^{S} = mes (**1.1**) or 2,6-*i*Pr₂C₆H₃ (Ar, **1.2**)), which contain an unsupported Mg-Mg bond, are versatile reducing agents for both organic and inorganic substrates resulting in cleavage of the Mg-Mg bond and formation of a Mg(II) species.¹⁷

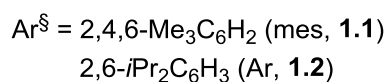
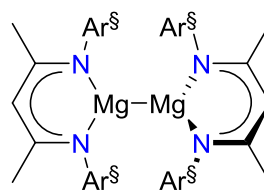


Figure 1.2. Common magnesium(I) reducing agents.

Within the last 40 years many well-defined examples of heavy p-block elements in low oxidation states have been investigated.^{1, 18} Among this growing compound class, molecules featuring homonuclear metal-metal single, double and triple bonds have been the major focus.³ Low oxidation state heavy p-block metal species featuring no covalent M-M bonding, instead comprised of non-bonding electrons centred on the heavy main group element (*i.e.* compounds featuring main group element centred lone pairs or radicals), have also been reported. However, these species are less common and typically require electronic and steric stabilisation to prevent dimerization / M-M bond formation.

The stability of low oxidation state heavy p-block metal species is often limited, due in part to facile disproportionation to metallic M^0 and the element in the common oxidation states. This decomposition is thought to proceed through an associative mechanism involving the close association of metal centres, similar to that described for heavy p-block metal hydride species (Figure 1.1).³

1.3.1. Synthetic Routes to Low Oxidation State Compounds

Access to low oxidation state compounds can be achieved through several pathways. The most common method for the synthesis of these species is by reduction of metal halides using a reducing agent (e.g. potassium), giving a reduced metal centre in addition to a potassium salt (Figure 1.3, Pathway 1). Another common route to reduced p-block metal species involves the addition of a hydride source (e.g. LiAlH_4) to a metal halide species, and is believed to occur through initial formation of a metal hydride intermediate followed by the room temperature

homolysis of the M-H bond to give the reduced heavy p-block metal species and hydrogen gas (Pathway 2). This route has been observed for tin, lead, antimony and bismuth, which form weak M-H bonds. While bismuth and lead hydrides are unstable, tin and antimony hydride species incorporating bulky ancillary ligands are stable, preventing access to low oxidation state species via this pathway. Both pathways will be employed in this thesis as possible routes to low oxidation state main group metal compounds.

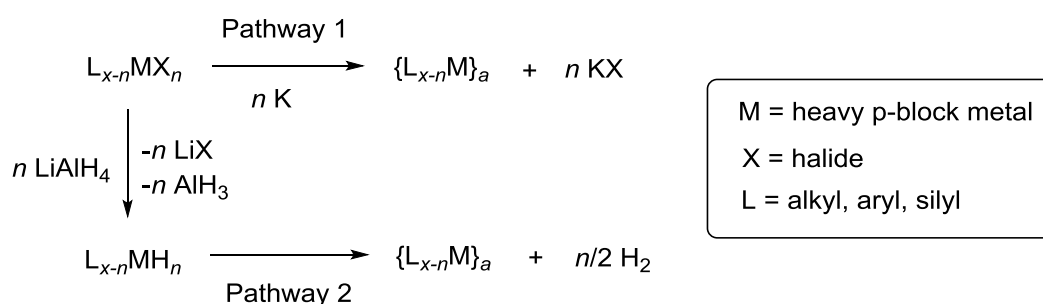


Figure 1.3. Common synthetic pathways to reduced heavy p-block metal complexes.

1.4. Sterically Demanding Ligands

Sterically demanding ligands play a key role in the stabilisation of reactive heavy p-block complexes. Monoanionic ligands dominate this area of the literature, with bulky monodentate aryl ligands (Figure 1.4, **I** and **II**), and bidentate *N,N'*-chelating amidinate (**III**), guanidinate (**IV**) and β -diketiminate (**V**) ligands among the most commonly employed.¹⁹ The latter three cases are versatile ancillary ligands as they benefit from the chelate effect, are relatively easy to synthesise and can be readily modified to fine-tune the steric and electronic properties of the ligand by changing the R/R'/R'' substituents. The most striking difference between **III/IV** and **V** is the number of atoms in the metallacycle formed upon *N,N'*-chelation to a metal centre. While **III** and **IV** form 4-membered metallacycles, **V** forms a 6-membered metallacycle. This has a significant effect on the ring strain and relative position of the nitrogen substituents (assuming ideal angles of 120° about the nitrogen atom) to the metal centre, with the N-substituents of **V** projected further forward from the metal centre to give greater steric protection of the metal centre.

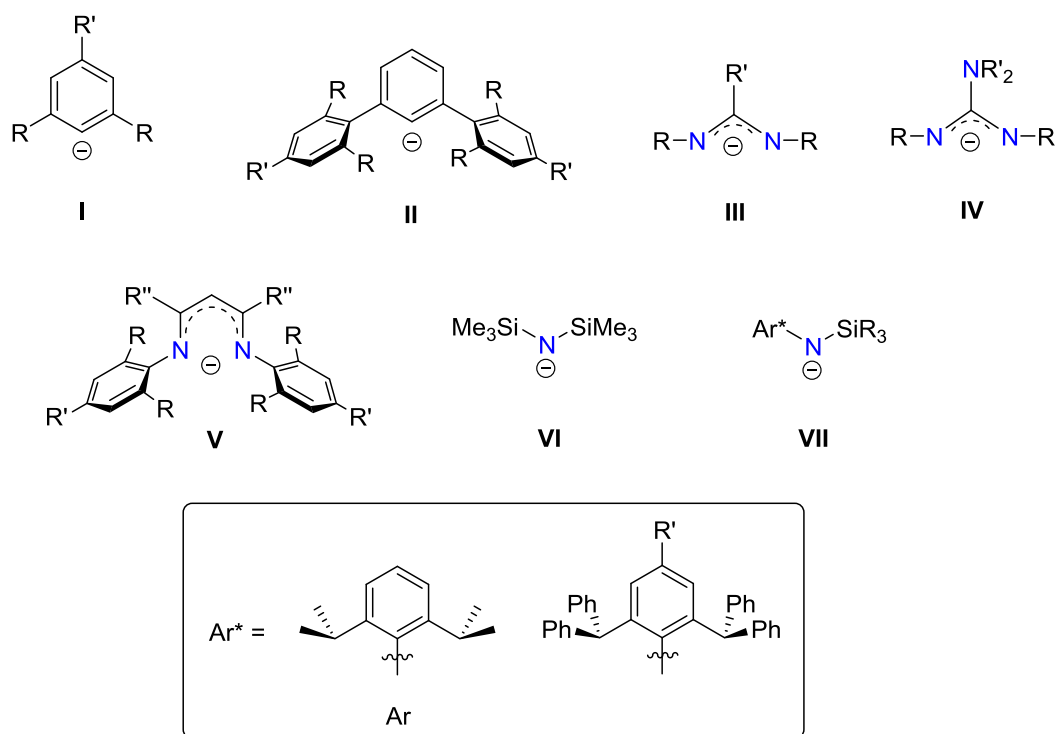


Figure 1.4. Examples of common sterically demanding monoanionic ligands. R/R'/R'' = alkyl or aryl.

1.4.1. Bulky Amide ligands

Metal complexes supported by monoanionic amide ligands $[\text{NR}_2]^-$ have a long history in main group metal chemistry and are now ubiquitous in coordination chemistry.²⁰ Amides of the form $[\text{N}(\text{R})(\text{R}')]^-$ (R / R' = alkyl, aryl, silyl etc.) have received considerable attention due to the ability to tune the steric and electronic properties of the ligand through manipulation of the R and R' substituents. The bis(trimethylsilyl)amide ligand $[\text{N}(\text{SiMe}_3)_2]^-$ (Figure 1.4, **VI**) pioneered much of the early metal amide chemistry due to its simple synthesis, steric bulk and lack of β -hydrogens.²¹ The requirement of greater steric protection to stabilise increasingly reactive species has contributed to the recent emergence of monoanionic amide ligands featuring bulky aryl substituents of the form $[\text{N}(\text{Ar}^*)(\text{SiR}_3)]^-$ (**VII**, R = Me, *i*Pr, Ph; $\text{Ar}^* = 2,6\text{-}i\text{Pr}_2\text{C}_6\text{H}_3$ (Ar), 2,6-(CHPh₂)₂-4-R'C₆H₂, R' = Me, *i*Pr, *t*Bu (Ar^\ddagger)).²²

1.4.2. Di(amido) Ligands

Like the *N,N'*-chelating ligands **III-V**, dianionic di(amido) ligands provide attractive scaffolds as versatile ligands with tunable steric and electronic properties. The di(amido)silyl ligand $[\text{Me}_2\text{Si}\{\text{NR}\}_2]^{2-}$ (Figure 1.5, **VIII**) has been used extensively in the coordination chemistry of main group elements, including by our group.²³ Upon *N,N'*-chelation to a metal centre, this ligand forms a planar 4-membered metallacycle resembling the amidinate and guanidinate systems **III** and **IV**.

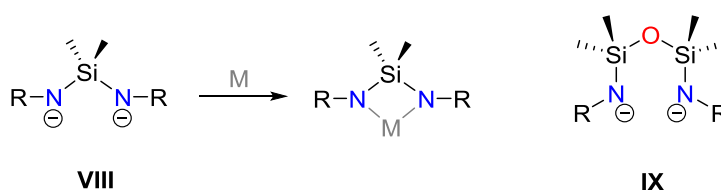


Figure 1.5. Di(amido) ligands $[\text{Me}_2\text{Si}\{\text{NR}\}_2]^{2-}$ (**VIII**) and $[\text{O}\{\text{SiMe}_2\text{N(R)}\}_2]^{2-}$ (**IX**).

1.4.3. Coordination Chemistry of the (NON^R)-Ligand

Di(amido)siloxane ligands $[\text{O}\{\text{SiMe}_2\text{N(R)}\}_2]^{2-}$ (abbrev. $[(\text{NON}^{\text{R}})]^{2-}$, **IX**)[†] are closely related to **VIII**, and have been used extensively as versatile ligands in transition metal and actinide chemistry.²⁴ Despite the only significant difference being the inclusion of a siloxane backbone, these ligands display different coordination properties. Firstly, the inclusion of an oxygen atom in the backbone introduces the potential for a number of different bonding modes (Figure 1.6, **A – F**). A survey of the Cambridge Structural Database (CSD) reveals the distribution of bonding modes in structurally characterised compounds featuring this ligand, showing that *N,N'*-bidentate (**A**) and *N,O,N'*-tridentate chelation (**B**) are the most common.²⁵ In the latter case, examples are limited to oxophilic metal centres (e.g. U, Cr, and Mg). In contrast, there have been no reports of tridentate coordination involving the siloxane oxygen in bridging bonding modes (e.g. **F**).

[†] IUPAC name: *N,N'*-(1,1,3,3-tetramethyldisiloxane-1,3-diyl)bis{N-(alkyl/aryl)amide}

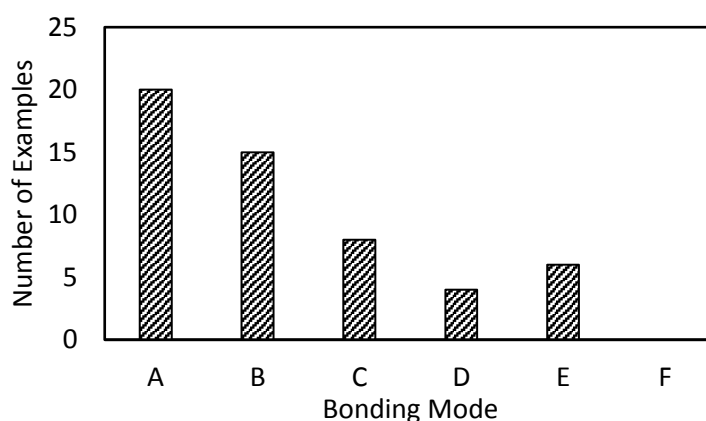
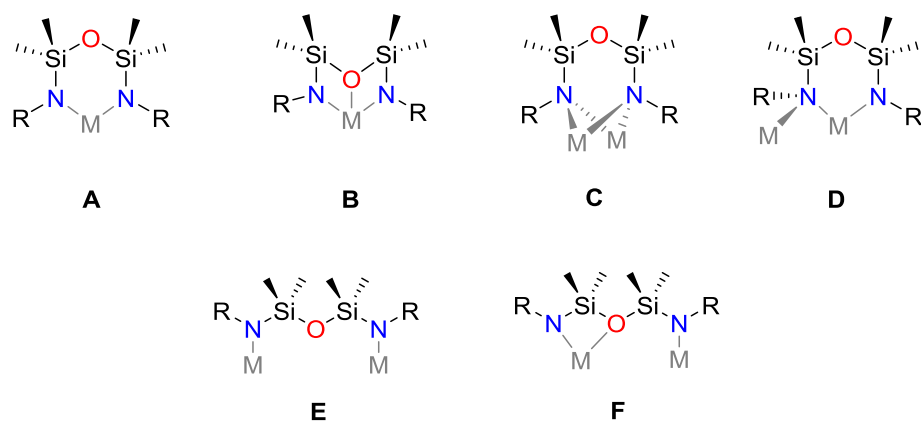


Figure 1.6. Several possible bonding modes for **IX** (top) and their frequency in the literature (bottom).

Secondly, upon chelation to a metal centre through an *N,N'*-bidentate bonding mode (**A**), a 6-membered metallacycle is formed. Analogous to the difference between β -diketiminato and amidinate/guanidinate systems, expansion of the metallacycle formed upon chelation from a 4-membered metallacycle for **VIII** to a 6-membered metallacycle results in forward projection of the nitrogen substituents towards the metal, and greater steric protection of the metal centre. In addition, while **VIII** is locked into a planar 4-membered ring, the metallacycle of **A** is conformationally free, providing a flexible scaffold in which the metallacycle can adopt conformations ranging from chair to boat conformations (Figure 1.7), often adopting intermediate structures (e.g. half-chair, co-planar and twist-boat conformations).

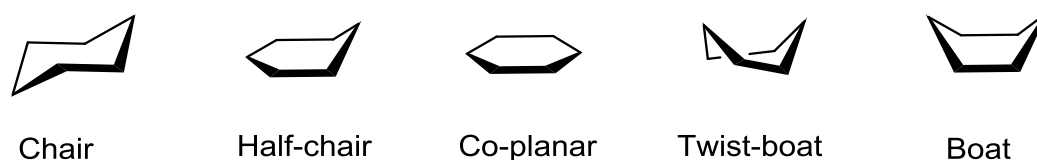


Figure 1.7. Possible conformations of the 6-membered metallacycle for bonding mode A.

Finally, the inclusion of the siloxane functionality in the ligand backbone results in the potential for rearrangement reactions. Leznoff and co-workers noted a retro-Brook rearrangement of the ligand in the dilithium compounds $(\text{NON}^{\text{R}})\text{Li}_2$ ($\text{R} = \text{Ph}$, 2,4,6- $\text{Me}_3\text{C}_6\text{H}_2$ (mes) or 2,6- $i\text{Pr}_2\text{C}_6\text{H}_3$ (Ar)) when stirred in an ethereal solvent (e.g. THF) for an extended period of time (>24 hours). The proposed mechanism for this rearrangement is through nucleophilic attack of an anionic nitrogen atom on one of the Si atoms, resulting in Si-O bond cleavage and Si-N bond formation (Figure 1.8). The ethereal solvent is believed to enhance the nucleophilic character of the anionic N atom by encapsulating the lithium atom and promoting formation of a non-contact ion pair. The product of this rearrangement is the mixed amide/siloxide ligand $[\text{RN}\{\text{Me}_2\text{SiO}\}\{\text{Me}_2\text{SiN}(\text{R})\}]^{2-}$ (abbrev. $[(\text{NNO}^{\text{R}})]^{2-}$). This species has been used as an asymmetric ligand in transition metal and actinide chemistry, with similar coordination modes to those described for $[(\text{NON}^{\text{R}})]^{2-}$.²⁶

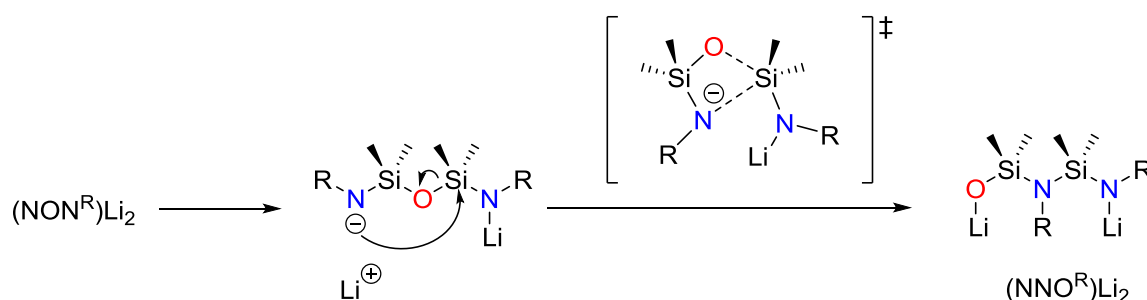


Figure 1.8. Retro-Brook rearrangement of $(\text{NON}^{\text{R}})\text{Li}_2$ to $(\text{NNO}^{\text{R}})\text{Li}_2$.

1.5. Assessing the Steric Bulk of a Ligand

The ability to predict and analyse the effective steric bulk of a ligand system is an invaluable resource and has received significant attention in the field of catalyst design.²⁷ As such,

standardised parameters which allow accurate comparison of the bulk offered by different ligands have been developed. The steric influence of a ligand is comprised of two key components: 1) the overall size of the ligand and 2) the shape of the ligand, both of which must be accounted for in order to accurately represent the steric effect of the ligand.

One of the most common steric descriptors discussed in chemistry is Tolman's cone angle (θ , Figure 1.9a), which was initially used to describe the effective size of phosphine ligands at transition metal, but has since been applied to other ligand systems.²⁸ However, this measurement assumes unrestricted rotation about the metal-ligand bond, and is not an accurate descriptor of ligand shape for many ligand systems (e.g. chelating ligands).

Two parameters which describe the size of a ligand regardless of shape, and have been widely applied in coordination chemistry, are the buried volume ($\%V_{\text{Bur}}$)²⁹ and the solid-angle (Ω)/G-parameter.³⁰

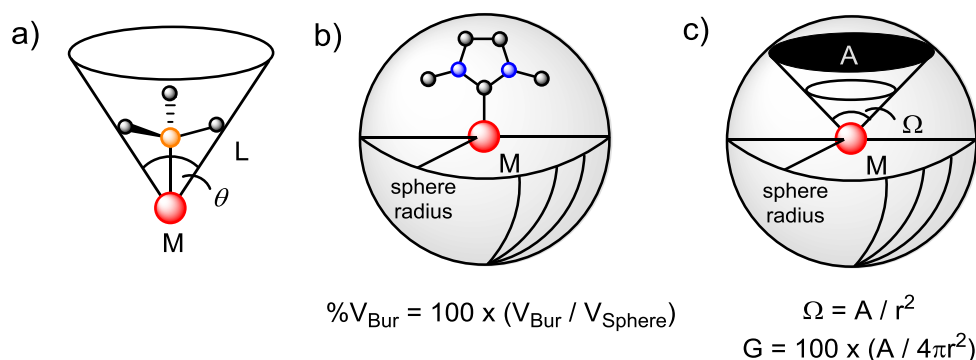


Figure 1.9. Graphical representations of the Tolman cone angle (a), the percent buried volume (b) and the solid angle (Ω) /G-parameter (c).

1.5.1. Percent Buried Volume ($\%V_{\text{Bur}}$)

The percent buried volume ($\%V_{\text{Bur}}$) is a single value parameter that describes the local environment within a sphere of a specified radius (r) about the metal centre (Figure 1.9b). The volume of each atom is calculated based on its Bondi radius³¹ and the total volume occupied by atoms within the pre-defined sphere (excluding the central metal atom) is calculated (V_{Bur}),

with the %V_{Bur} corresponding to the relative volume of the atoms occupying the sphere compared to the total volume of the sphere ($V_{\text{Bur}}/V_{\text{Sphere}} \times 100$).

The %V_{Bur} can be easily calculated from coordinates obtained from X-ray crystal structure data using the Sambvca2.0 web-based software, allowing its widespread use in the chemical literature.²⁹ The most common classes of ligand investigated using this parameter are N-heterocyclic carbenes (NHC) and phosphines, with strong correlations observed between %V_{Bur} and the commonly used Tolman cone angles for both (coefficient of determination (R^2) = 0.96 – 0.981).²⁷ This parameter has also been used to describe other ligand systems, including bidentate *N,N'*-chelating ligands.³²

1.5.2. Solid Angle and G-parameter

The solid angle (Ω) is an important geometric measurement describing the angle that includes a given area on the surface of a sphere. In chemistry terms, the solid angle measures the area of the shadow that a ligand casts on a sphere surrounding the molecule if the metal centre is treated as a light source (measured in steradians, Figure 1.9c), and may be considered as a cone angle which does not assume unrestricted rotation about the metal-ligand bond.³⁰

The G-parameter (which is derived from the solid angle) describes the area of the shadow (A) as a percentage of the area of the sphere and is the most common form of this measurement that is used in comparisons of ligand bulk. In general, a larger G-parameter corresponds to greater encumbrance of the metal centre and differs significantly from the %V_{Bur} in that it describes the influence of substituents outside of the local environment of the metal centre. Calculations of the solid angle (Ω) / G-parameter are performed using atomic coordinates obtained from X-ray data and the Solid-G suite of programs, with the effective 'size' of the atoms corresponding to their van der Waals radii.³¹

1.5.3. Limitations and Considerations

Both the percent buried volume ($\%V_{\text{Bur}}$) and solid angle (Ω) / G-parameter are effective measures of steric bulk, and both measure different aspects of the ligand bulk. However, certain limitations on these measurements must be carefully considered. While the use of X-ray coordinates allows for a computationally inexpensive method for calculating these parameters, X-ray structures often provide only a snapshot of the lowest energy structures and conformations. Therefore, values corresponding to conformationally flexible systems should only be used qualitatively and these values should not be discussed in terms of solution-state structures. Both values are useful quantitative measures for rigid ligand systems and give valuable information about the steric bulk provided by the ligand. While the $\%V_{\text{Bur}}$ value measures the local environment about the metal (within a specified radius), steric bulk outside of this range is not included in the calculation of the parameter. In contrast, the G-parameter includes contributions to the encumbrment of the metal centre that exist outside of this range (e.g. long range $M\cdots\text{aryl}$ interactions).

Despite these limitations, these parameters remain useful tools for the comparison of steric bulk provided by different ligand systems, and will be employed for comparative purposes in this thesis. The $\%V_{\text{Bur}}$ and G values contained within this thesis have been determined exclusively for the di(amido) ligands, with the volume of the metal centre (for $\%V_{\text{Bur}}$) and contributions from secondary ligands not included.

Chapter 2. Synthesis of Low Oxidation State Bismuth Species

2.1. Introduction

2.1.1. Bimetallic and Polymetallic Low Oxidation State Bismuth Compounds

With an electron configuration of $[\text{Xe}]4f^{14}5d^{10}6s^26p^3$, the chemistry of molecular bismuth is dominated by the +3 and +5 oxidation states, formed through loss of the 6p and 6s/p electrons, respectively. Only within the last 35 years have well characterised examples of bismuth in the less common +1 and +2 oxidation states been reported, despite initial reports of bismuth in the +2 oxidation state appearing as early as 1934 with the observation of a violet-red substance proposed to be tetramethyldibismuthane, $\{\text{BiMe}_2\}_2$.³³ Well defined examples of diorganobismuth(II) species $\{\text{BiR}_2\}_2$ ($\text{R} = \text{Me}, \text{Et}, \text{SiMe}_3$) were not reported until 1982,³⁴ with a structural report the following year ($\text{R} = \text{Ph}$) confirming the formation of a molecular dimer with a Bi-Bi single bond (Figure 2.1).³⁵ Since these seminal discoveries, the number of reduced bismuth species containing homonuclear Bi-Bi single bonds that have been reported has increased dramatically. Among these examples are the monoorganobismuth(I) compounds $\{\text{BiR}\}_n$ ($n = 3, 4, 5$) forming cyclic Bi_n cores (Figure 2.1).³⁶

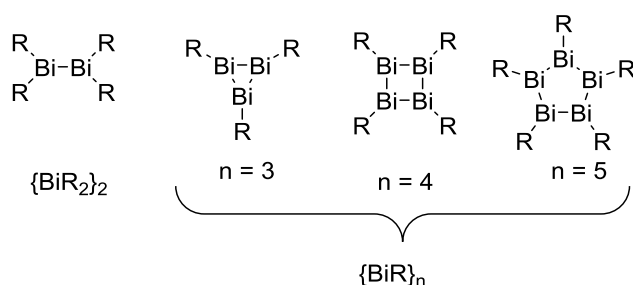


Figure 2.1. General structures for low oxidation state bismuth compounds featuring homonuclear Bi-Bi single bonds.

Within the last 30 years, multiply bonded low-valent main group metal/metalloid species have received significant interest.^{1, 4} The first structurally authenticated dibismuthene $[\text{Bi}(\text{2,4,6-}(\text{CH}(\text{SiMe}_3)_2)_3\text{C}_6\text{H}_2)]_2$ (**2.1**),³⁷ reported in 1997, featured a short Bi=Bi bond (2.821(1) Å) and utilised bulky ancillary ligands to kinetically stabilise the double bond. Since this discovery, examples of dibismuthenes stabilised by bulky aryl (**2.2 – 2.4**),³⁸ ferrocenyl (**2.5**),³⁹ boryl (**2.6**),⁴⁰ phosphide (**2.7**)⁴¹ and gallyl (**2.8** and **2.9**)⁴² ligands have been reported. In addition, salts containing the unusual naked $[\text{Bi}_2]^{2-}$ ion have been reported, which can be considered isoelectronic and isostructural to dioxygen.⁴³ The Bi=Bi bond distances in these complexes occupy a narrow range (2.7957(5) – 2.8701(5) Å), and are on average approximately 6 – 7% shorter than standard Bi-Bi single bonds.

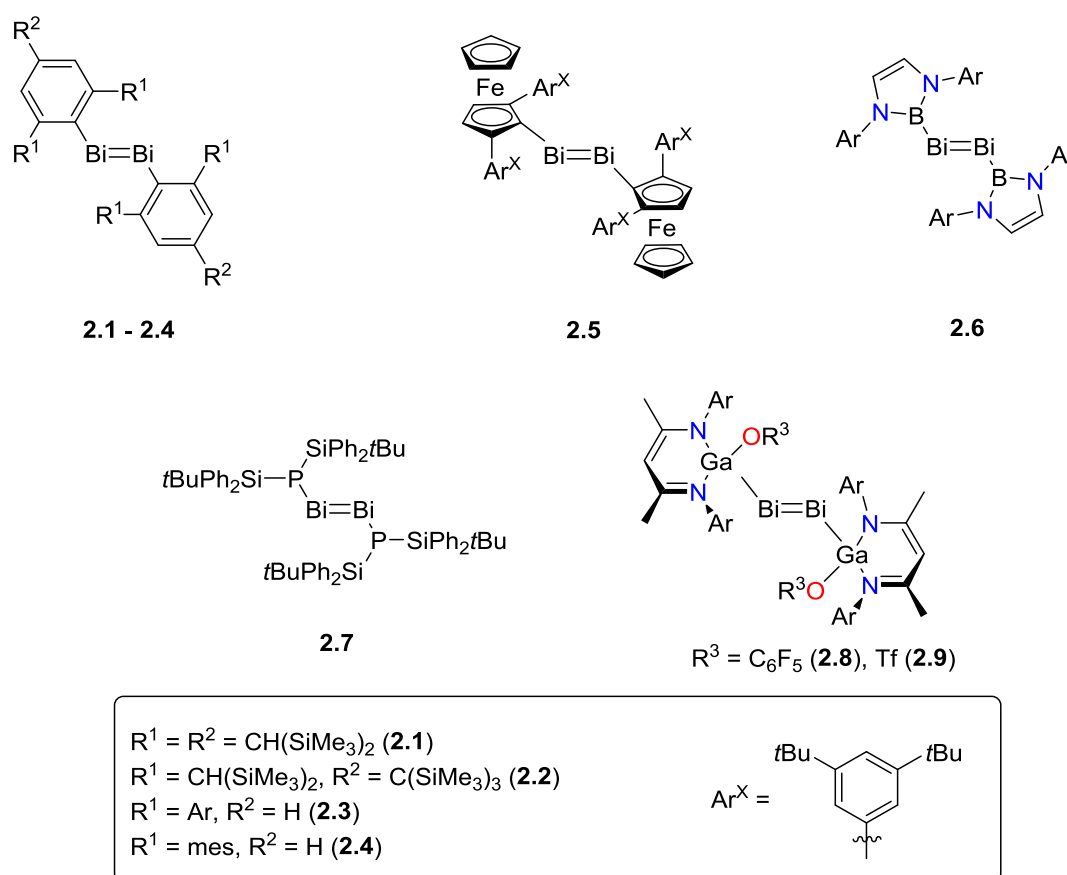


Figure 2.2. Structurally characterised dibismuthenes supported by bulky ligands.

2.1.2. Monometallic Low Oxidation State Bismuth Compounds

Monometallic low oxidation state bismuth(I) compounds (RBi:), and bismuth(II) compounds ($\text{R}_2\text{Bi}^\bullet$), in which there are no covalent Bi-Bi interactions, are rare. Until recently, the investigation of these transient species were limited to IR spectroscopy, requiring the use of low temperature (2-10K) matrix isolation techniques.⁴⁴ In 2010, Dostál and co-workers reported the first room temperature stable monometallic organobismuth(I) compound $\text{Bi}(\text{2,6-(MeC=NAr')}_2\text{C}_6\text{H}_3)$ ($\text{Ar}' = \text{2,6-Me}_2\text{C}_6\text{H}_3$) (Figure 2.3, **2.10**).⁴⁵ The solid-state structure of **2.10** confirmed the monomeric complex, featuring a 3-coordinate bismuth centre with two coplanar imine $\text{N} \rightarrow \text{Bi}$ interactions. The remarkable thermal stability (decomp. $> 250^\circ\text{C}$) of this species was attributed to both the steric influence of the bulky Ar' substituents and the strong, almost covalent, $\text{N} \rightarrow \text{Bi}$ interaction. The role of the latter was further realised during the extension of this synthesis to other N,C,N- and N,C- pincer ligands (**2.11 – 2.13**), confirming the role of strong $\text{n}_\text{N} \rightarrow \text{p}^*_{\text{Bi}}$ ($\text{p}^* = \text{empty p-orbital}$) interactions on the stability of the bismuthinidene.⁴⁶ Calculations showed that delocalisation of the p-type lone pair of the bismuth atom over the NBiC moiety results in aromatic character in the BiC_3N ring(s). In contrast, the weakly donating amino-substituted N,C- chelating ligand $\text{2-(CH}_2\text{NEt}_2\text{)-4,6-}t\text{Bu}_2\text{C}_6\text{H}_2$ promotes Bi=Bi bond formation in **2.14**.

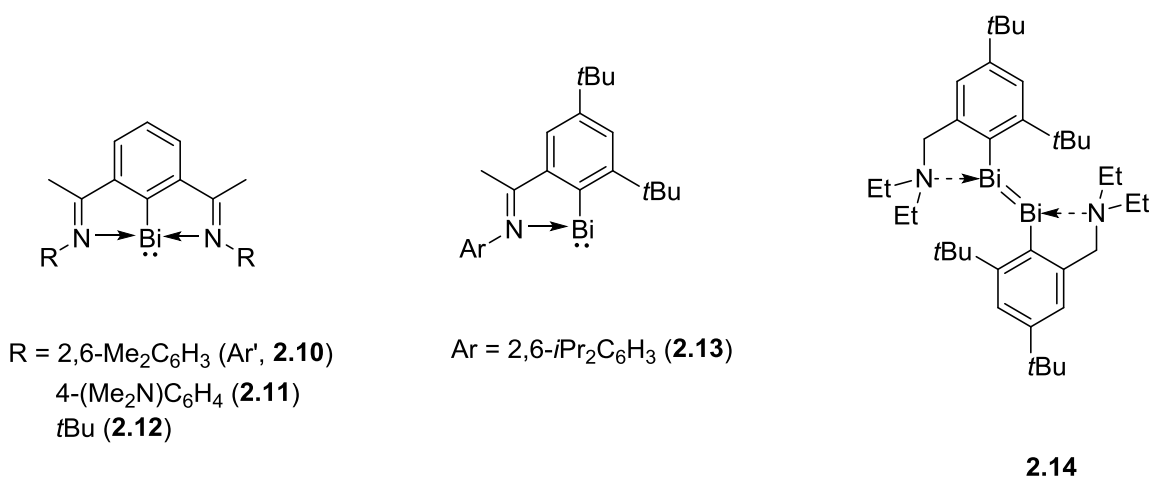
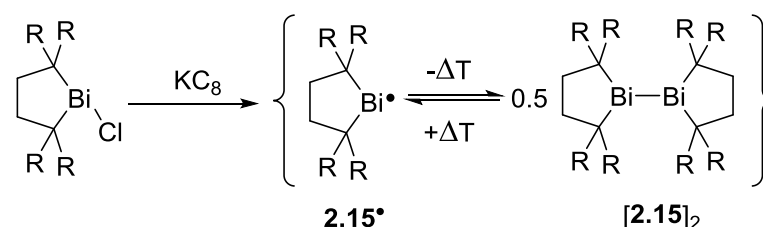


Figure 2.3. Monometallic bismuthinidines and bimetallic dibismuthane supported by N,C,N- and N,C- ligands.

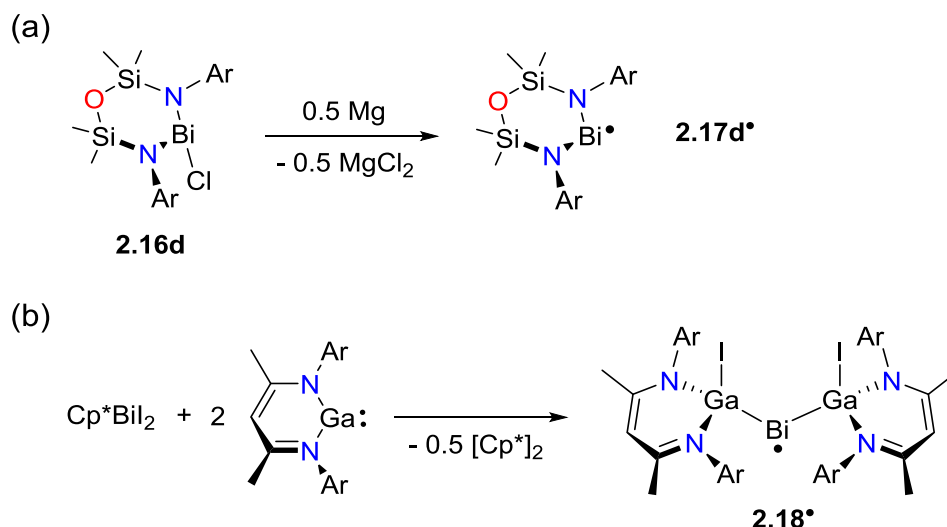
In 2014, Ishida, Iwamoto and co-workers reported the solution-state characterisation of the organobismuth(II) radical $\bullet\text{Bi}(\text{C}(\text{SiMe}_3)_2\text{CH}_2)_2$ (Scheme 2.1, **2.15•**), obtained by reduction of the corresponding bismuth(III) chloride with potassium graphite (KC_8).⁴⁷ However, attempts to crystallise this species were unsuccessful due to dimerisation in the solid-state, instead giving the dibismuthane $[\text{2.15}]_2$. Further investigation revealed that these species exist in an equilibrium in solution, with formation of **2.15•** at ambient temperature and dimerisation to $[\text{2.15}]_2$ at lower temperatures. The lack of an observable EPR spectrum and the inability to characterise **2.15•** in the solid-state demonstrated that this ligand system is not suitable for the isolation of a stable radical species.



Scheme 2.1. Synthesis and reversible radical coupling of **2.15•**. R = SiMe₃.

More recently, we reported the synthesis of the remarkably stable mononuclear bismuth(II) species $\bullet\text{Bi}(\text{NON}^{\text{Ar}})$ (**2.17d•**, ($\text{NON}^{\text{Ar}} = \text{O}\{\text{SiMe}_2\text{N}(\text{Ar})\}_2$, Ar = 2,6-*i*Pr₂C₆H₃), formed by reduction of the corresponding bismuth(III) chloride **2.16d** using magnesium (Scheme 2.2a).⁴⁸ In contrast to **2.15•**, $\bullet\text{Bi}(\text{NON}^{\text{Ar}})$ retains its radical character in the solid-state and at low temperatures in the solution-state. The electronic structure of **2.17d•** was probed using EPR spectroscopy, magnetic moment measurements, UV-visible spectroscopy and density functional theory (DFT), showing a predominantly metal-centred radical species with approximately 90% of the spin density in a p-type orbital on the bismuth. This indicates that spin delocalisation plays a minimal role in the stabilisation of this radical species. A subsequent report by Schulz and co-workers demonstrated that the bismuth radical $\bullet\text{Bi}\{\text{Ga}(\text{I})(\text{BDI}^{\text{Ar}})\}_2$ (**2.18•**, $\text{BDI}^{\text{Ar}} = \{\text{N}(\text{Ar})(\text{CMe})\}_2\text{CH}$, Ar = 2,6-*i*Pr₂C₆H₃) can be isolated, formed by the reaction of $\text{Bi}(\text{Cp}^*)\text{I}_2$ with gallium(I) species $:\text{Ga}(\text{BDI}^{\text{Ar}})$ (Scheme 2.2b).⁴⁹ **2.18•** was identified in the solid-

state, with DFT and EPR revealing a predominantly metal centred radical with approximately 80% of the spin density in a p-type orbital on the bismuth and significant delocalisation on to the gallium centres (approximately 16 %).



Scheme 2.2. Synthesis of **2.17d•** and **2.18•**.

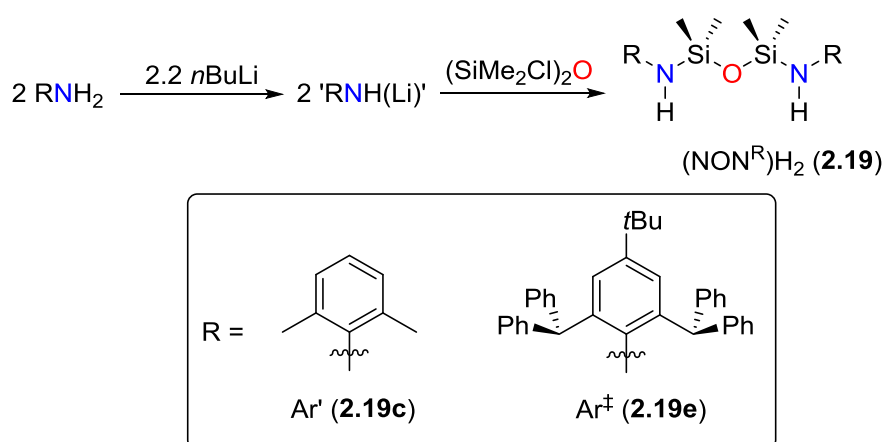
2.2. Chapter Outline

The coordination chemistry of the di(amido)siloxane ligand $[(\text{NON}^{\text{R}})]^{2-}$ (**IX**, discussed in Chapter 1) has been explored extensively for the transition metals, lanthanides and actinides. In contrast, investigations utilising this versatile framework at main group metal centres are limited. We have previously reported the synthesis and characterisation of the bismuth(II) radical species $\bullet\text{Bi}(\text{NON}^{\text{Ar}})$ (**2.17d•**) which displays remarkable stability due to the steric encumbrance imposed by the bulky Ar substituents. This chapter expands on this work, and reports an investigation into the influence of modification of the nitrogen substituents of the (NON^{R}) -framework on the nature of the reduced bismuth species. The investigation of ligands containing diverse steric and electronic profiles will be achieved using alkyl (*t*Bu, **a**) and aryl (Ph (**b**), 2,6-Me₂C₆H₃ (Ar', **c**), 2,6-*i*Pr₂C₆H₃ (Ar, **d**), 2,6-(CHPh₂)₂-4-*t*BuC₆H₂ (Ar[‡], **e**)) substituents. The preparation of bismuth(III) chloride compounds, Bi(NON^R)Cl, followed by their reduction using either Mg or a hydride source was envisaged as a viable pathway towards the targeted reduced bismuth species.

2.3. Result and Discussion

2.3.1. Synthesis and Characterisation of Bismuth(III) Chloride Compounds

The synthesis of $(\text{NON}^{\text{R}})_2$ ($\text{R} = t\text{Bu}$ (**2.19a**), Ph (**2.19b**), 2,6-*i*Pr₂C₆H₃ (Ar , **2.19d**)) has previously been reported in the literature.^{24e, 50} Extension of the synthetic procedure for $(\text{NON}^{\text{Ar}})_2$ to other primary anilines allowed the isolation of the novel derivatives $(\text{NON}^{\text{Ar}'})_2$ (**2.19c**) and $(\text{NON}^{\text{Ar}^\ddagger})_2$ (**2.19e**) (where $\text{Ar}' = 2,6\text{-Me}_2\text{C}_6\text{H}_3$ and $\text{Ar}^\ddagger = 2,6\text{-(CHPh}_2)_2\text{-4-}t\text{BuC}_6\text{H}_2$) as a colourless oil and colourless solid, respectively (Scheme 2.3).



Scheme 2.3. Synthesis of **2.19c** and **2.19e**.

The ^1H NMR spectra of **2.19c** and **2.19e** show a single high field resonance for the SiMe_2 protons (δ_{H} 0.09 and 0.14, respectively). The NH resonances appear at δ_{H} 2.55 and 2.39, respectively, similar to other reported $(\text{NON}^{\text{R}})_2$ compounds.^{24e, 50} In addition, the ^1H NMR spectrum of **2.19c** contains a single sharp singlet corresponding to the *o*-Me protons with a relative integral of 1 : 1 (SiMe_2 : *o*-Me), while key resonances for **2.19e** appear at δ_{H} 1.08 (CMe_3) and 6.32 (CHPh_2). Crystallisation of **2.19e** from THF yielded colourless crystals, which were examined by X-ray crystallography (Figure 2.4). **2.19e** crystallises as the bis-THF adduct in the $P2_1/n$ space group with half a molecule in the asymmetric unit related by a two-fold rotation axis. The N-atoms form a staggered conformation about the SiO_2 core (N1-Si1-Si1'-N1' torsion = $166.24(9)^\circ$). The molecule of THF hydrogen bonds to the NH proton, with a

relatively short N \cdots O2 distance (3.054(3) Å), within the range typically attributed to moderate strength H-bonding (2.5 – 3.2 Å).⁵¹ This is a rare example of a THF molecule participating in hydrogen bonding and the only structurally characterised example of hydrogen bonding between THF and an NH unit.

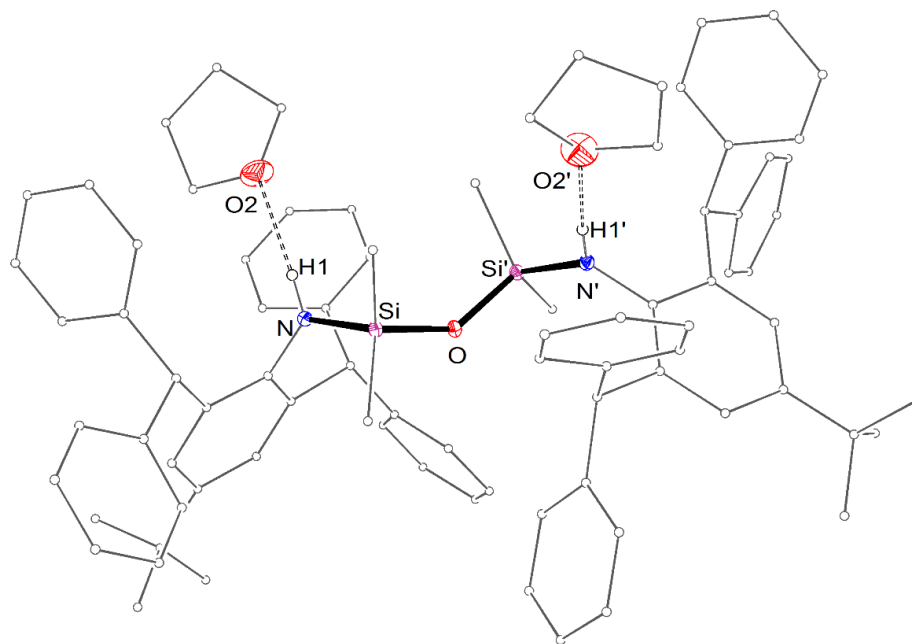
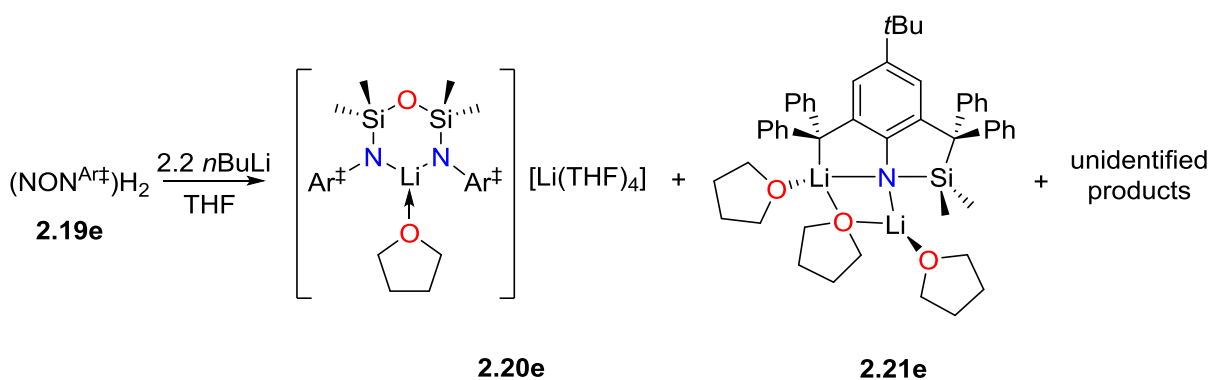


Figure 2.4. Molecular structure of **2.19e** (thermal ellipsoids displayed at 30% probability level, symmetry relationship (') = 1.5-x, y, 0.5-z). Carbon atoms are displayed in wireframe format and selected hydrogen atoms are omitted for clarity. Selected bond lengths (Å) and angles (°): N-Si 1.715(1), Si-O 1.6360(6), N \cdots O2 3.054(3), N-H 0.89(2), O2 \cdots H 2.17(2); N-Si-O 112.8(1), Si-N-O2 122.2(7), C1-N-O2 112.5(1), Si-O-Si' 139.7(1), N-H1 \cdots O2 175(2).

We have previously reported that the reaction of '(NON^{Ar})Li₂' and BiCl₃ gives Bi(NON^{Ar})Cl (**2.16d**) in moderate yields (58 %).⁴⁸ While a few compounds of the type (NON^R)M₂ (M = group 1 metal) have been isolated,⁵² we found it more convenient to generate '(NON^R)Li₂' *in-situ* through the addition of 2 equiv. *n*BuLi to **2.19a-d** in Et₂O and use it as a solution/suspension assuming 100% conversion. However, due to the poor solubility of **2.19e** in Et₂O and the potential for lithiation at the acidic CHPh₂ hydrogen atoms in the presence of excess *n*BuLi, *in-situ* generation of the dilithium salt was avoided and the isolation of '(NON^{Ar†})Li₂' was

attempted. Upon addition of *n*BuLi to a THF solution of **2.19e**, an immediate colour change was observed from colourless to red. The ^1H NMR spectrum of an aliquot of the crude reaction mixture showed formation of a complex mixture of products. Concentration of the solution and storage at $-30\text{ }^\circ\text{C}$ yielded a mixture of colourless crystals of $[\text{Li}(\text{THF})_4][(\text{NON}^{\text{Ar}\ddagger})\text{Li}(\text{THF})]$ (**2.20e**, Scheme 2.4) and red crystals of $[\text{Li}(\text{THF})(\mu\text{-THF})][\text{N}(2\text{-}(\text{CPh}_2\text{SiMe}_2)\text{-4-}t\text{Bu-6-}(\text{C}\{\text{Li}(\text{THF})\}\text{Ph}_2)\text{C}_6\text{H}_2)]$ (**2.21e**). The ^1H NMR spectrum of the crystal mixture revealed a 1 : 4 ratio of **2.20e** : **2.21e** based on the integration of the SiMe_2 peaks (δ_{H} 0.48 and 0.10, respectively). Further purification by recrystallization from Et_2O gave a clean sample of **2.21e** (crop 1) and an enriched sample of **2.20e** (crop 2).



Scheme 2.4. Synthesis of **2.20e** and **2.21e**.

X-ray crystallography was used to elucidate the solid-state structures of **2.20e** and **2.21e**. The crystal structure of **2.20e** (Figure 2.5) shows an outer-sphere ion-pair with the asymmetric unit containing a half molecule located on a 2-fold rotation axis defined by the $\text{Li1}\cdots\text{O1}$ vector. The anionic component consists of a lithium atom chelated by a $(\text{NON}^{\text{Ar}\ddagger})$ -ligand, and is balanced by a THF solvated lithium cation. The $(\text{NON}^{\text{Ar}\ddagger})$ -ligand chelates the lithium atom with a large bite angle ($118.5(2)^\circ$) and standard Li-N bond distances ($1.962(3)\text{ \AA}$). The backbone siloxane does not participate in the chelation as has been observed for other oxophilic metals (e.g. Mg, U),^{48, 53} with the $\text{Li1}\cdots\text{O1}$ distance ($3.138(4)\text{ \AA}$) and N1-Si1-O1 angles ($110.43(9)^\circ$) indicative of a $\kappa_2\text{-N,N'}$ -bidentate bonding mode (Figure 1.6, **A**). A single THF molecule is also bound to the Li atom of the anionic component (Li-O $1.968(5)\text{ \AA}$) to give a highly encumbered metal centre.

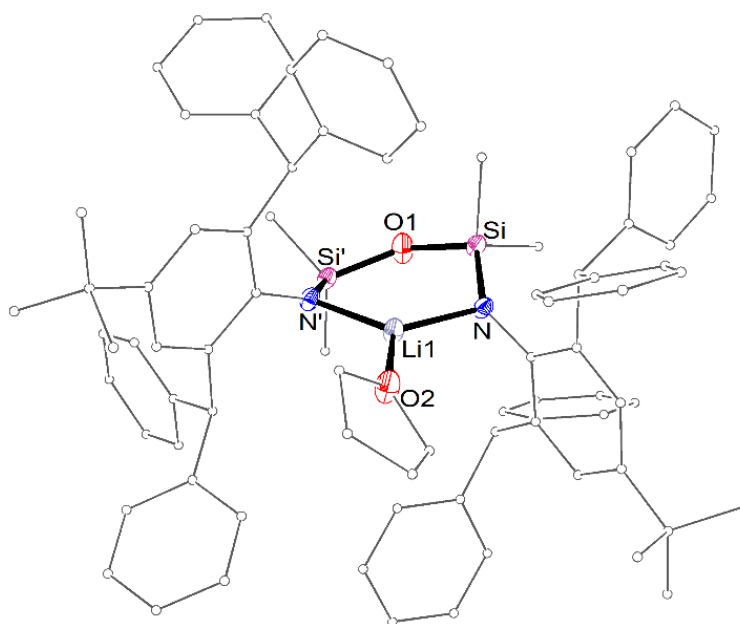


Figure 2.5. Molecular structure of **2.20e** (thermal ellipsoids displayed at 30% probability level, symmetry relationship (') = 1-x, y, 0.5-z). The cationic $[\text{Li}(\text{THF})_4]^+$ component and hydrogen atoms are omitted. Carbon atoms are displayed in wireframe format and hydrogen atoms are omitted for clarity. Selected bond lengths (Å) and angles (°): Li1-N 1.962(3), Li1-O2 1.968(5), Li1...O2 3.138(4), Li2-O3 1.919(6), Li2-O4 1.932(5); N-Li-N' 118.5(2), N1-Si-O1 110.43(9), Si-O-Si' 141.2(1).

The solid-state structure of **2.21e** also revealed formation of a dilithium complex, with two crystallographically independent, but essentially identical, molecules in the asymmetric unit (Figure 2.6). The lithium atoms adopt contrasting bonding modes, with Li1/3 chelated through a $\kappa_2\text{-N,C}$ -bidentate bonding mode, while Li2/4 are coordinated in a monodentate fashion by the nitrogen atom. Despite the different coordination modes, the Li-N distances occupy a narrow range (1.996(3) – 2.038(3) Å). The Li-C distances (Li1-C24 2.315(3) Å; Li3-C62 2.326(3) Å) are similar to those observed in $(\text{Ph}_3\text{C})\text{Li}(\text{OEt}_2)_2$ (2.306(7) Å)⁵⁴ and in related $\kappa_2\text{-N,C}$ -chelated lithium compounds (2.393(7) – 2.390(6) Å).⁵⁵ The average angle about the carbanion centre (C24/62) is 118.6°, significantly larger than that expected for a tetrahedral carbon centre (ideal angle = 109°), suggesting the complex is better described as a contact-ion pair, with significant delocalisation of the negative charge into the aromatic substituents to give a planar carbanion

and results in Si-O bond cleavage and Si-C bond formation (Figure 2.7). The reaction with an additional equivalent of *n*BuLi deprotonates the other *CHPh*₂ group to give **2.21e** as the product. This mechanism draws parallels to the proposed mechanism for the retro-Brook rearrangement to form the (NNO^R)-ligand (Figure 1.8), which involves nucleophilic attack of an anionic nitrogen on the SiMe₂ to cleave a Si-O bond in the presence of THF.^{26b} The influence of THF in this rearrangement is significant, and is believed to be the result of THF-induced formation of a separated ion-pair, increasing the nucleophilicity of the amide anion. No retro-Brook rearrangements were observed in non-donor solvents. To avoid the possible complications caused by THF, subsequent lithiations of **2.19e** were performed in toluene to give an orange suspension, stirred for 12 hours at room temperature and used *in-situ*.

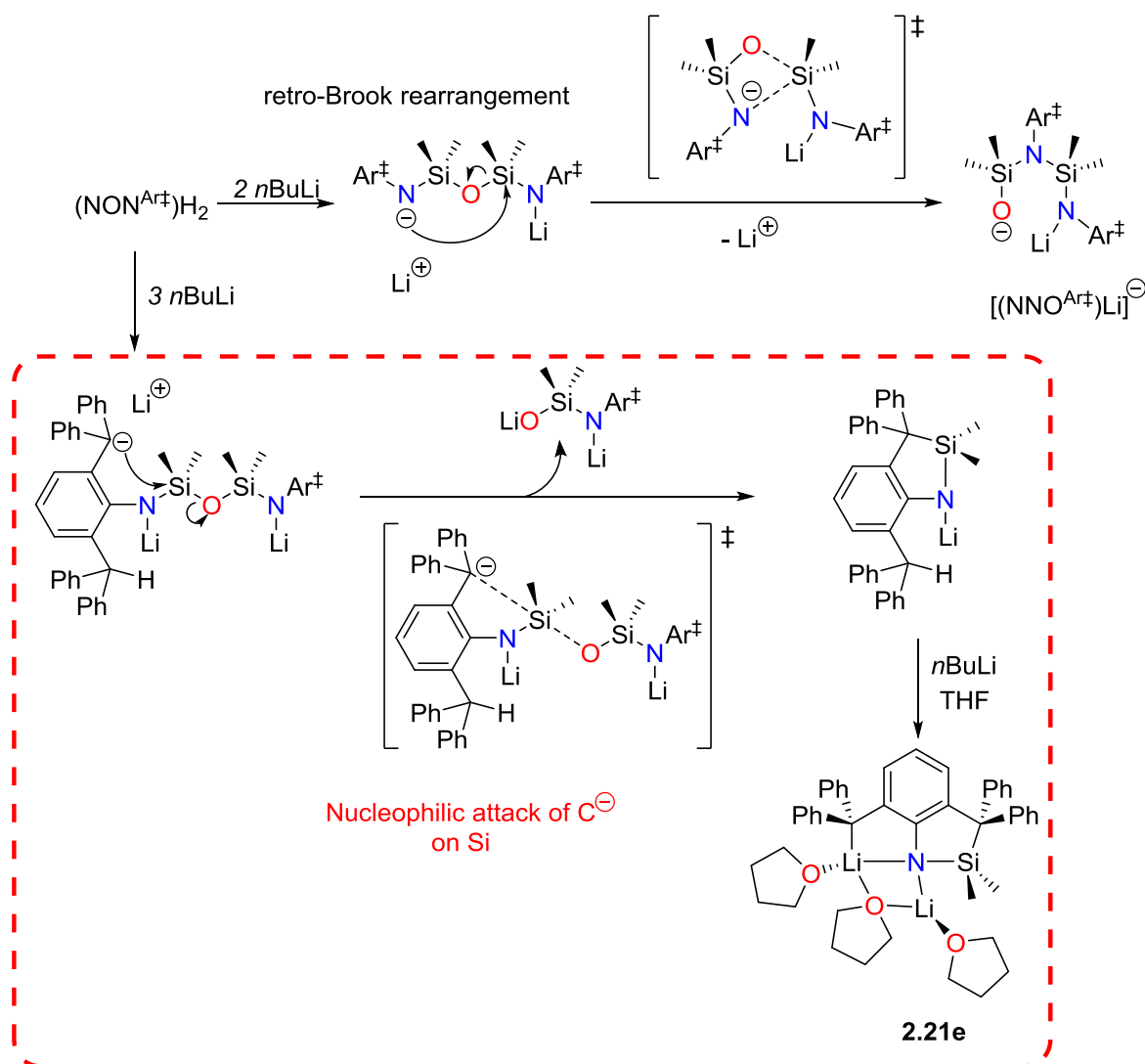
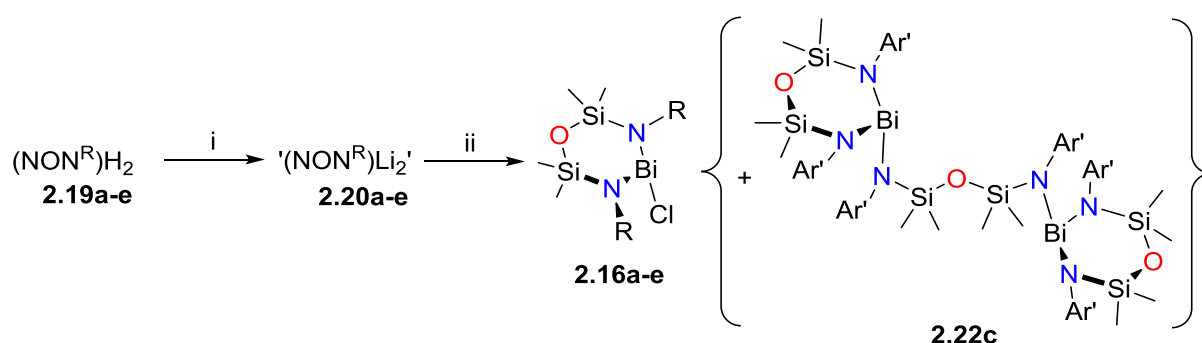


Figure 2.7. Possible mechanism for formation of **2.21e**.

The stoichiometric reaction of '(NON^R)Li₂' with BiCl₃ gave the corresponding Bi(NON^R)Cl (R = *t*Bu (**2.16a**), Ph (**2.16b**), Ar' (**2.16c**),[†] Ar[‡] (**2.16e**)) compounds with varying efficiency (Scheme 2.5). The synthesis of **2.16a** and **2.16b** proceed as expected to give yellow crystals, in moderate yields after work-up (54 % and 55 %, respectively). In contrast, attempts to isolate **2.16c** were hindered by the formation and co-crystallisation of {Bi(NON^{Ar'})₂(μ-NON^{Ar'})} (**2.22c**) in an approximate 1 : 1 ratio. Recrystallisation of the crystal mixture allowed for samples enriched in **2.16c** (crop 2) and **2.22c** (crop 1), allowing analysis by NMR spectrometry. However, complete separation of the components was not achieved, preventing the acquisition of accurate elemental analysis data. Attempts to prevent the formation of **2.22c** by performing the reaction at low temperature (-78 °C) were unsuccessful, with similar results to the room temperature procedure obtained.



Scheme 2.5. Synthesis of **2.16a-e** and **2.22c**. i) 2.2 *n*BuLi, Et₂O (**2.19a-d**) or toluene (**2.19e**), ii) BiCl₃, Et₂O. R = *t*Bu (**a**), Ph (**b**), Ar' (**c**), Ar (**d**), Ar[‡] (**e**).

The reaction of **2.20e** with BiCl₃ in toluene at -30 °C proceeds with a significant colour change from orange to deep red, with concomitant formation of a fine black precipitate which is inseparable from the reaction mixture by filtration. Removal of the volatile components *in vacuo* followed by extraction into hexane and filtration through celite gives a clear red solution. Concentration of the solution and storage at room temperature resulted in the formation of yellow crystals of **2.16e** (53% yield) over 24 hours.

[†] The solid-state structure of **2.16c** was previously obtained within our group, however, no other data was obtained.

The ^1H NMR spectra for **2.16a-e** show resonances consistent with chelation of the (NON^{R})-ligand to a pyramidal bismuth centre to give a C_s -symmetric species, most evident by the presence of two high field singlets corresponding to the inequivalent SiMe_2 protons (**2.16a**, δ_{H} 0.36 and 0.48; **2.16b**, δ_{H} 0.33 and 0.55; **2.16c**, δ_{H} 0.17 and 0.59; **2.16e**, δ_{H} -0.01 and 0.24). The ^1H NMR spectra of **2.16c** and **2.16e** also show inequivalent environments for the *o*-Me (δ_{H} 2.46 and 2.73) and CHPh_2 (δ_{H} 6.47 and 6.88) resonances, respectively. This asymmetry is also observed in the ^{13}C NMR spectra, showing two sets of high field resonances for the SiMe_2 carbon atoms (δ_{C} **2.16a**, 6.2 and 7.7; **2.16b**, 2.4 and 3.8; **2.16c**, 3.0 and 5.4; **2.16e**, 4.8 and 5.1). In contrast, the ^1H NMR spectrum for the ($\text{NON}^{\text{Ar'}}$)-bridged species **2.22c** shows three high field singlets corresponding to the SiMe_2 protons (δ_{H} 0.16, 0.34 and 0.57) and three singlets with equivalent integrals corresponding to the *o*-Me protons (δ_{H} 1.90, 2.31 and 2.70).

The solid-state structures of **2.16a**, **2.16b**, **2.16e** and **2.22c** were determined using X-ray crystallography, confirming the formation of the bismuth(III) chlorides $\text{Bi}(\text{NON}^{\text{R}})\text{Cl}$ (Figure 2.8, Table 2.1) and ($\text{NON}^{\text{Ar'}}$)-bridged co-product $\{\text{Bi}(\text{NON}^{\text{Ar'}})\}_2(\mu\text{-NON}^{\text{Ar'}})$ (Figure 2.11), respectively. Significant disorder in the Bi and Cl atoms of **2.16b** precludes discussion of bond lengths and angles, however the connectivity is unambiguous (Appendix 7.2, Figure S2.1). During the process of our investigations into this area of chemistry, we also isolated a polymorph of the previously reported compound **2.16d** which crystallises in the C2/c space group from hexane (denoted as **2.16d'**, Figure S2.2).

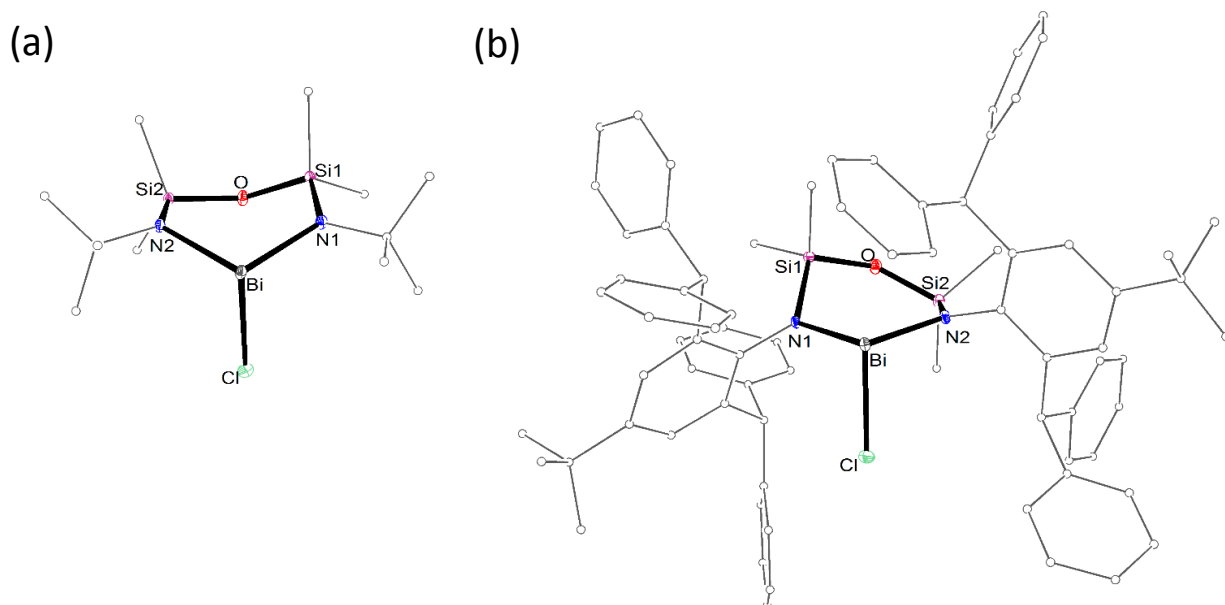


Figure 2.8. Molecular structure of **2.16a** (a) and **2.16e** (b) (thermal ellipsoids displayed at 30% probability level). Hydrogen atoms, solvent molecules and the minor component of disorder in **2.16b** are omitted. Carbon atoms are displayed in wireframe format for clarity. See Table 2.1 for selected bond lengths (Å) and angles (°).

In all cases, the (NON^R)-ligand in the bismuth(III) chlorides chelates the bismuth atom with a κ_2 -*N,N'*-bonding mode to give a 6-membered metallacycle. The conformation of the metallacycle varies significantly with the different R-substituents, ranging from boat and twist-boat conformations in **2.16a** and **2.16b**, respectively, to half-chair and chair conformations in the more sterically encumbered **2.16d'** and **2.16e**. The N-Bi-N bite angles (**2.16a**, 103.6(1)°; **2.16d'**, 98.7(1)°; **2.16e**, 99.0(1)°) and Bi···O distances (**2.16a**, 3.266(3) Å; **2.16d'**, 3.534(3) Å; **2.16e**, 3.513(3) Å) are consistent with a κ_2 -*N,N'*-bidentate coordinated (NON^R)-ligand with variations in the distances and angles attributed to conformational differences. The Bi-N distances (**2.16a**, 2.130(3) and 2.153(3) Å; **2.16d'**, 2.139(3) and 2.144(3) Å; **2.16e**, 2.176(3) and 2.149(3) Å) vary with the R-substituent, but are within the range observed for bismuth amide species Bi(NR₂)₃ (R = Me, Ph, SiMe₃; range 2.155(4) – 2.257(3) Å).⁵⁷ The remaining coordination site is occupied by a chloride atom to give a 3-coordinate metal centre with a pyramidal geometry (sum of angles at bismuth, $\Sigma(\angle\text{Bi})$, range 289.11° – 298.77°). The Bi-Cl

distances (**2.16a**, 2.6105(11) Å; **2.16d'**, 2.5374(10) Å; **2.16e**, 2.4841(11) Å) differ significantly, caused by different extended solid-state structures. The Bi-Cl bonds in **2.16a** and **2.16d'** are considerably longer than those in **2.16c-e** (range 2.4841(11) – 2.512(2) Å). Elongation of the Bi-Cl bond in **2.16a** and **2.16d'** coincides with the presence of short intermolecular Bi \cdots Cl contacts in the solid-state. **2.16a** forms a double-stranded ladder-like polymeric structure in the solid-state (Figure 2.9) with two intermolecular Bi \cdots Cl contacts (3.7424(11) and 3.7823(12) Å) between symmetry related 'Bi(NON^{tBu})Cl' units. While the bond lengths in **2.16b** cannot be discussed, the solid-state structure also features a double-stranded polymeric chain linked by long range Bi \cdots Cl contacts. However, the Bi-Cl \cdots Bi vectors of the chains have an opposite directionality (180°) resulting in the formation of an inverse ladder-like structure. The solid-state structure of **2.16d'** forms a dimer linked by a Bi \cdots Cl contacts (3.5476(11) Å). **2.16c** and **2.16d** also form dimer structures in the solid-state. However, these are linked by long range Bi \cdots aryl π -interactions.^{48, 58} In contrast, **2.16e** exists as a monomer, likely a reflection of the greater steric protection of the bismuth provided by the bulky aryl group.

The Bi \cdots Cl interactions in **2.16a** and **2.16d'** can be described using $\Delta_{\text{Bi-Cl}}(1)$ (for **2.16a** only) and $\Delta_{\text{Bi-Cl}}(2)$, the difference between the Bi-Cl distances and the intra- and inter-chain Bi \cdots Cl contacts, respectively. Both values are similar for **2.16a** ($\Delta_{\text{Bi-Cl}}(1)$: 1.132 Å, $\Delta_{\text{Bi-Cl}}(2)$: 1.172 Å), consistent with similar strength Bi \cdots Cl contacts. In contrast, the Bi \cdots Cl contact in **2.16d'** is significantly stronger ($\Delta_{\text{Bi-Cl}}(2)$: 1.010 Å).

Table 2.1. Selected Bond Lengths (Å) and Angles (°) for **2.16a**, **2.16d'** and **2.16e**.

	2.16a	2.16d'	2.16e
Bi-N1	2.130(3)	2.139(3)	2.176(3)
Bi-N2	2.153(3)	2.144(3)	2.149(3)
Bi...O	3.266(3)	3.534(3)	3.513(3)
Bi-Cl	2.6105(11)	2.5374(10)	2.4841(11)
Bi...Cl(1)	3.7424(11)	—	—
Bi...Cl(2)	3.7823(12)	3.5476(11)	—
$\Delta_{\text{Bi-Cl}}(1)$	1.132	—	—
$\Delta_{\text{Bi-Cl}}(2)$	1.172	1.010	—
N1-Bi-N2	103.6(1)	98.7(1)	99.0(1)
N1-Bi-Cl	97.5(1)	101.0(1)	94.5(1)
N2-Bi-Cl	97.6(1)	93.4(1)	98.4(1)

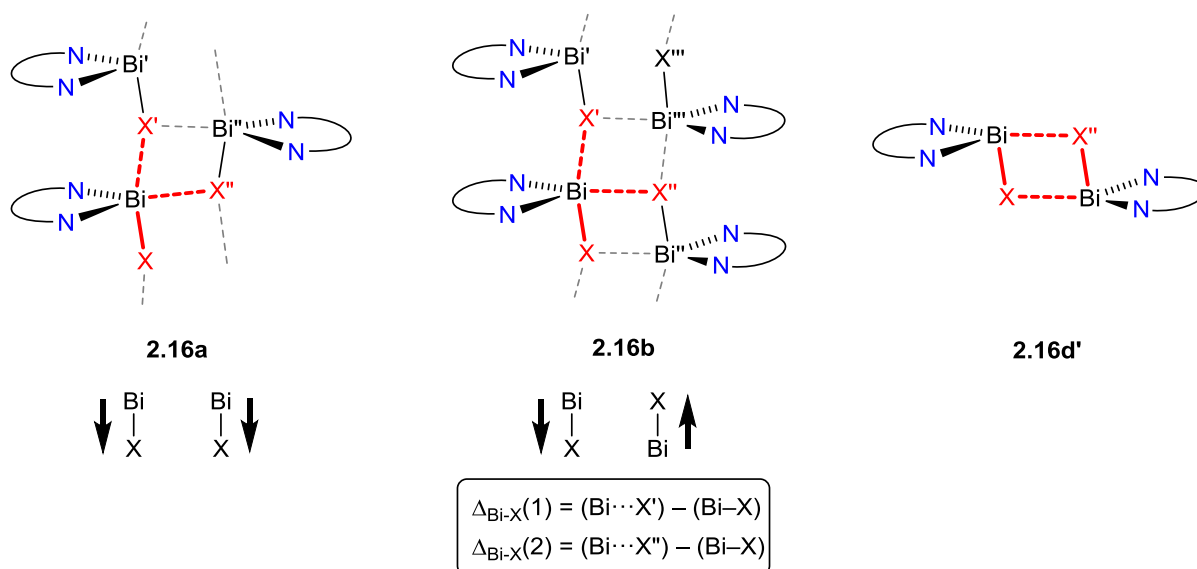


Figure 2.9. Schematic representation of the extended structures of **2.16a**, **2.16b** and **2.16d'**.

The steric parameters, %V_{Bur} and the G parameter, were calculated using atomic coordinates obtained from the X-ray crystal structures and were used to investigate the effect of changing the R-substituent on the encumbrance of the bismuth centre (Section 1.5). In order to allow calculation of the (NON^R)-ligand bulk regardless of the variable nature of the Bi-Cl bond, the contribution of the chloride atoms to the encumbrance of the bismuth was excluded from the calculations. The influence of crystal packing and long range interactions on the conformation of the ligand limits quantitative discussion of these measurements, particularly for the polymeric structure of **2.16a**, which displays long range Bi...Cl interactions.

The %V_{Bur} and G parameters (Table 2.2 and Figure S2.3) show the expected trend in steric bulk of the (NON^R)-ligand ($t\text{Bu} \approx \text{Ar}' < \text{Ar} < \text{Ar}^\ddagger$). While both the %V_{Bur} and G parameter for **2.16a** and **2.16c** are comparable (**2.16a**, %V_{Bur} = 53.8 %, G = 49.5 %; **2.16c**, %V_{Bur} = 51.6 %, G = 48.5 %), the distribution of steric bulk differs considerably, illustrated by the topographical plots of steric encumbrance (Figure 2.10), which shows that much of the bulk in **2.16a** is localised around the *t*Bu groups while the Ar' derivative provides greater steric protection above and below the bismuth. This reflects the limitations of using single value parameters to describe the steric encumbrance of the metal centre. Significant increases in both parameters are observed for the Ar (%V_{Bur} = 57.0 and 58.7 %, G = 57.9 % in both cases) and Ar[‡] derivatives (%V_{Bur} = 64.6 %, G = 71.5 %), reflecting the ability of the (NON^R)-framework to provide a platform for wide-ranging bulk through simple modifications to the nitrogen substituents. It is noteworthy that, despite the differences in the solid-state structures of **2.16d** and its polymorph **2.16d'**, the calculated steric parameters are reasonably consistent, suggesting that these parameters are tolerant of differences in the extended structures. Large differences between the %V_{Bur} and G parameter in **2.16e** are caused by the large percentage of the ligand that exists outside of the defined coordination sphere of the bismuth ($r = 3.5 \text{ \AA}$).

Table 2.2. Steric parameters for Bi(NON^R)Cl (**2.16**, R = *t*Bu (**a**), Ar' (**c**), Ar (**d** and **d'**), Ar[±](**e**)).^a

	2.16a	2.16c ⁵⁸	2.16d ⁴⁸	2.16d'	2.16e
%V _{Bur} (%) ^b	53.8	51.6	57.0	58.7	64.6
G parameter (%) ^c	49.5	48.5	57.9	57.9	71.5

^aBi and Cl atoms are omitted from the calculations. ^bCalculated using the SambVca 2 software for a sphere with *r* = 3.5 Å and hydrogen atoms included.²⁹ ^cCalculated using the Solid-G suite of programs.³⁰

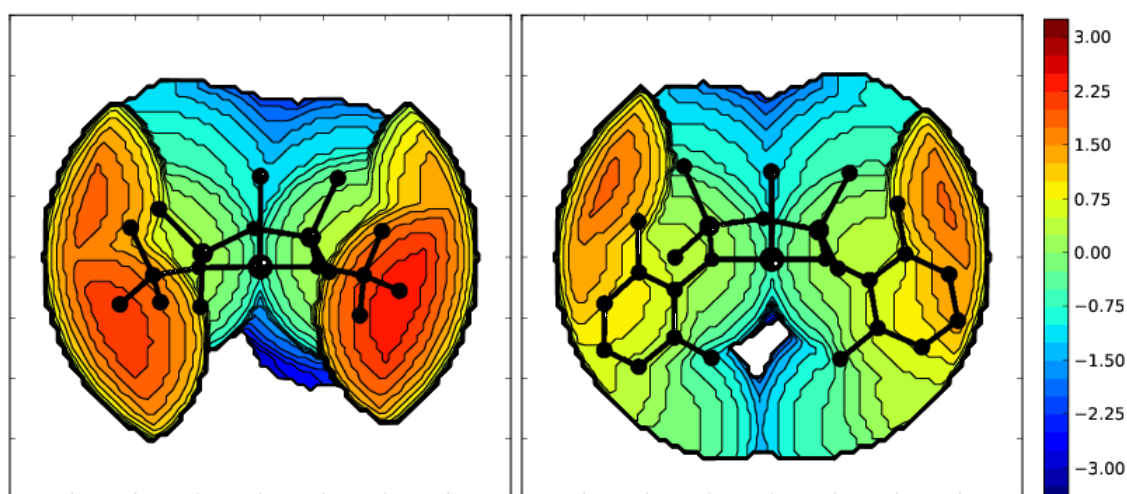


Figure 2.10. Topographical representation of the %V_{Bur} bulk distribution of the (NON^R)-ligand in **2.16a** (left) and **2.16c** (right). Coloured sections correspond to the depth of bulk (red (3.00) corresponds to forward projection, blue (-3.00) corresponds to bulk behind the metal centre). The volume corresponding to the bismuth and chloride atoms are omitted.

The solid-state structure of **2.22c** shows two bismuth centres bridged by a (NON^{Ar'})-ligand (Figure 1.6, bonding mode **E**). Each bismuth atom is chelated by a second (NON^{Ar'})-ligand, which bonds in a κ_2 -*N,N'*-bidentate fashion with standard bite angles (99.2(1)° and 98.2(1)°) and Bi-N bond distances (2.168(2) – 2.188(3) Å). The metallacycles adopt half-chair conformations, with the siloxane oxygen atom sitting 0.449(3) and 0.458(3) Å below the least squares plane defined by the co-planar BiN₂Si₂ atoms. Despite the different bonding modes, there is no difference between the bridging Bi-N bond distances (Bi1-N3 2.185(3) Å; Bi2-N4, 2.188(3) Å) and those of the chelating ligand. The Ar' substituents of the bridging ligand are staggered almost 180° about the Bi1-N3 and Bi2-N4 bonds from the centre of the chelating

(NON^{Ar})-ligand (178.6(2)° and 178.0(2)°, respectively), preventing steric clashes between the nitrogen substituents.

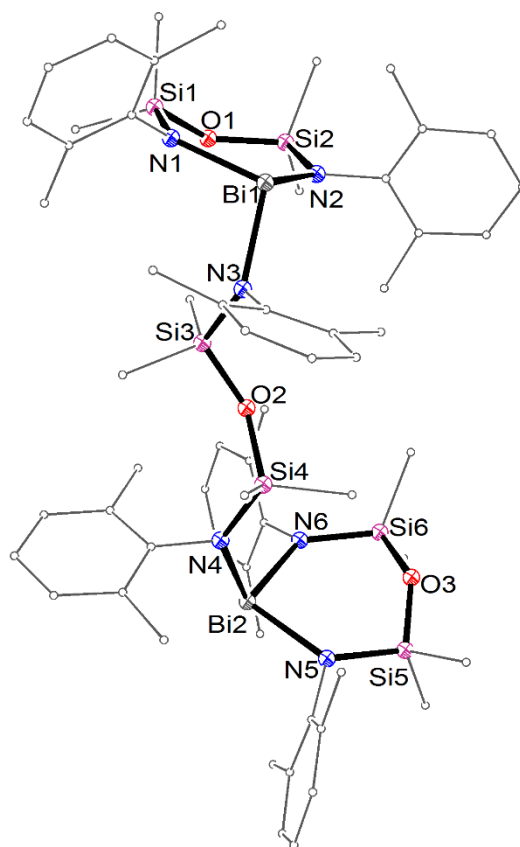


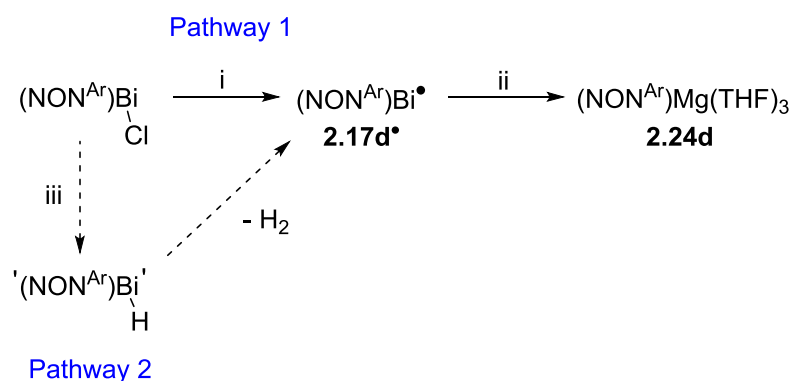
Figure 2.11. Molecular structure of **2.22c** (thermal ellipsoids displayed at 30% probability level). Carbon atoms are displayed in wireframe format and hydrogen atoms are omitted for clarity. Selected bond lengths (Å) and angles (°): Bi-N1 2.188(3), Bi1-N2 2.188(2), Bi1-N3 2.185(3), Bi2-N4 2.188(3), Bi2-N5 2.168(2), Bi2-N6 2.169(2), Bi1···O1 3.500(2), Bi2···O3 3.520(2); N1-Bi1-N2 99.2(1), N5-Bi2-N6 98.2(1), N1-Bi1-N3 104.2(1), N2-Bi1-N3 105.2(1), N4-Bi2-N5 104.2(1), N4-Bi2-N6 104.9(1).

2.3.2. Synthesis and Characterisation of [Bi(NON^R)]_n

We have previously reported the synthesis and characterisation of the bismuth(II) radical species •Bi(NON^{Ar}) (**2.17d•**), obtained from the reduction of **2.16d** using magnesium (Scheme 2.6, Pathway 1).⁴⁸ However, this method was susceptible to over-reduction, whereby the (NON^{Ar})-ligated magnesium species Mg(NON^{Ar})(THF)₃ (**2.23d**) is obtained after stirring the

reaction mixture for 48 hours at room temperature. Therefore, we explored alternative pathways to generate **2.17d•**. Bismuth(III) hydrides are extremely rare, with only one example characterised in the solid-state, requiring two sterically demanding 2,6-mes₂C₆H₃ substituents to kinetically stabilise the labile Bi-H bond (Section 1.2).⁵⁹ In contrast, attempts to isolate bismuth(III) hydride species R₂BiH (R = CH₂tBu, CH(SiMe₃)₂, mes) and RBiH₂ (R = CH₂SiMe₂, CH₂tBu) instead gave the reduced bismuth species {BiR₂}₂ and {BiR}_n (n = 3, 5), respectively. Bi-H bond homolysis was inferred as a key step in the reaction pathway, with H₂ formed as a by-product.⁶⁰

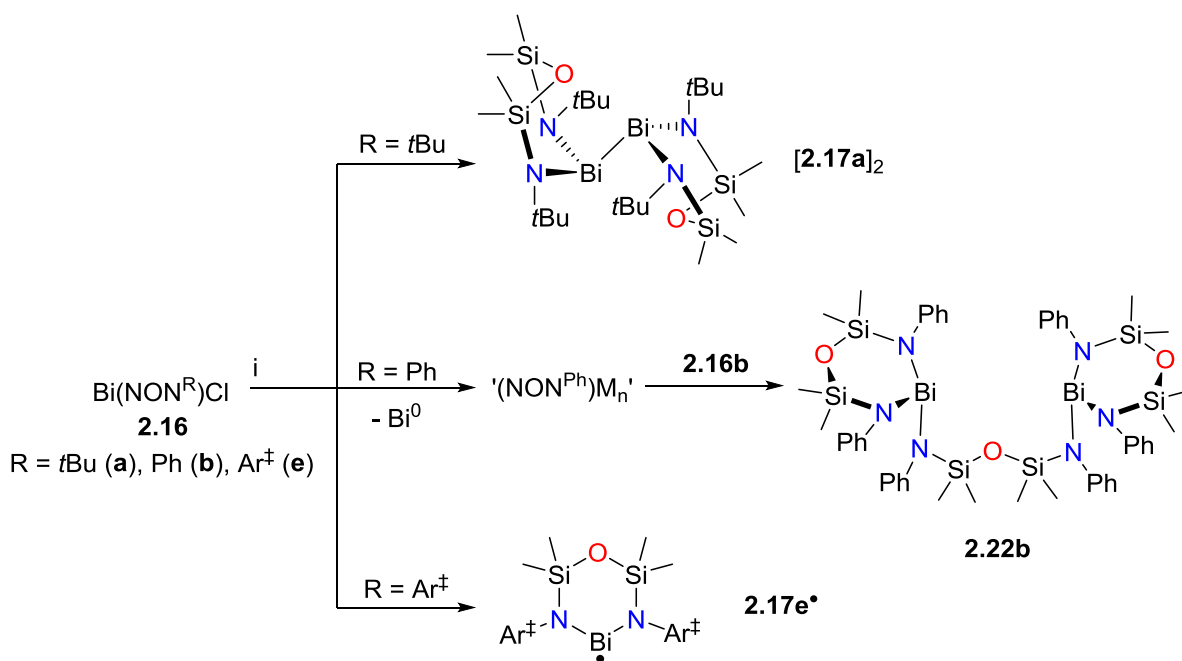
The reaction of **2.16d** with one equivalent of the THF-soluble LiHBEt₃ at -78 °C gives a yellow solution. When the solution was allowed to warm to -30 °C a deep red solution was obtained, which was retained as the solution warmed to room temperature. Deep red crystals of **2.17d•** were obtained in moderate yields (56 %) after work-up, with the reaction presumably proceeding via an intermediate bismuth(III) hydride species, 'Bi(NON^{Ar})H' (Pathway 2). While yields were comparable to those obtained using pathway 1, the reaction proceeds significantly quicker with no evidence of over-reduction.



Scheme 2.6. Synthetic pathways for the isolation of **2.17d•**. i) 0.5 Mg, THF/Et₂O; ii) Mg, THF/Et₂O; iii) LiBEt₃H, THF/Et₂O.

The reactions of **2.16a**, **2.16b** and **2.16e** with either LiHBEt₃ (1 equiv.) or Mg metal (0.5 equiv.) give differing results depending on the nitrogen substituent. The reactions of the tBu and Ar⁺ derivatives, **2.16a** and **2.16e**, with LiHBEt₃ (1 equiv.) or Mg (0.5 equiv.) proceed to give the

corresponding reduced bismuth species $[\text{Bi}(\text{NON}^{\text{R}})]_n$ ($\text{R} = t\text{Bu}$, $n = 2$ (**2.17a**), $\text{R} = \text{Ar}^{\ddagger}$, $n = 1$ (**2.17e**)) as dark orange and deep red crystals after work-up, respectively (Scheme 2.7). In contrast, the attempted reduction of **2.16b** proceeded with the formation of large amounts of black precipitate and a colourless solution, from which colourless crystals of $\{\text{Bi}(\text{NON}^{\text{Ph}})\}_2(\mu\text{-NON}^{\text{Ph}})$ (**2.22b**) were obtained. A sensible synthetic pathway for the formation of **2.22b** has been proposed, whereby transmetalation to form an intermediate $(\text{NON}^{\text{Ph}})\text{-M}_n$ ($\text{M} = \text{Li}$, $n = 2$; $\text{M} = \text{Mg}$, $n = 1$) occurs, followed by the *in-situ* reaction with **2.16b**. To confirm that this is a viable pathway, the reaction of isolated $\text{Mg}(\text{NON}^{\text{Ph}})(\text{THF})_3$ (Figure S2.4, **2.23b**) with **2.16b** was attempted on an NMR scale with **2.22b** identified as the major product (>95%) using ^1H NMR spectroscopy.



Scheme 2.7. Reduction of $\text{Bi}(\text{NON}^{\text{R}})\text{Cl}$. i) LiHBEt_3 , $\text{THF}/\text{Et}_2\text{O}$ or Mg , Et_2O .

The ^1H and ^{13}C NMR spectra of **2.22b** are reminiscent of those previously described for **2.22c**, showing three SiMe_2 resonances (δ_{H} 0.09, 0.18 and 0.34; δ_{C} 3.0, 3.7, 4.7) with a relative integration of 1 : 1 : 1 (for the ^1H NMR data). The solution-state NMR data of $[\text{2.17a}]_2$ also indicate the presence of a diamagnetic species, with two sharp SiMe_2 resonances (δ_{H} 0.43 and 0.45) and a single CMe_3 environment (δ_{H} 1.41) observed in the ^1H NMR spectrum. These data

are consistent with a C_s -symmetric metal environment with chelation of the (NON^{tBu})-ligand to a pyramidal bismuth centre, and are consistent with formation of a dibismuthane in solution. In contrast, the ^1H NMR spectrum of **2.17e•** showed paramagnetically shifted resonances spanning the range δ_{H} -2.31 to +12.78, similar to those observed for **2.17d•**. The Evans' method was used to confirm the solution-state paramagnetism, giving a solution-state magnetic moment ($2.0 \pm 0.1 \mu_{\text{B}}$) (Figure S2.6) consistent with the presence of a single unpaired electron (calc'd $1.73 \mu_{\text{B}}$) per molecule of **2.17e•**. Attempts to investigate the energetics of dibismuthane formation using variable temperature (VT) NMR spectroscopy were unsuccessful, with no observable change in the ^1H NMR spectra upon heating/cooling solutions of [**2.17a**]₂ and **2.17e•** over the temperature range -70 °C to +70 °C, suggesting a very different energy profile between the two species. Similar results were also obtained for the bismuth radical **2.17d•**, indicating large differences in the energetics for the reduced bismuth species with respect to Bi-Bi bond formation. These results contrast the dialkylbismuth radical **2.15•**, which readily dimerises to form the dibismuthane [**2.15**]₂ at low temperatures (Section 2.1).⁴⁷

UV-visible spectroscopy shows that the deep red colour of **2.17e•** corresponds to transitions at 441 nm ($\epsilon = 865 \text{ mol}^{-1}\text{dm}^3\text{cm}^{-1}$) and 490 nm ($\epsilon = 790 \text{ mol}^{-1}\text{dm}^3\text{cm}^{-1}$, Figure 2.12). Analogous transitions were observed in the UV-visible spectrum of **2.17d•** and were assigned to transitions involving the singly occupied molecular orbital (SOMO) using time-dependent (TD) DFT (417 nm, $6p(\text{Bi}) \rightarrow \pi(\text{C-C})$ transition; 482 nm, $n(\text{N}) \rightarrow 6p(\text{Bi})$ transition).⁴⁸ In contrast, a single absorbance is observed in this region at 435 nm ($\epsilon = 350 \text{ mol}^{-1}\text{dm}^3\text{cm}^{-1}$) in the UV-visible spectrum of [**2.17a**]₂.

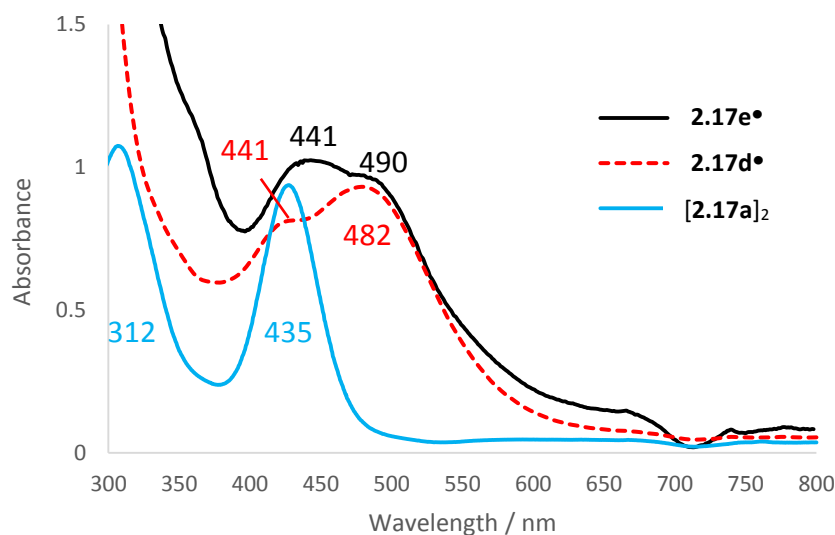


Figure 2.12. Electronic absorption spectrum of **[2.17a]₂** (blue, solid), **2.17d•** (red, dotted) and **2.17e•** (black, solid). λ_{max} / nm (ϵ / mol⁻¹dm³cm⁻¹): **[2.17a]₂**, 312 (390) and 435 (350); **2.17d•**, 417 (946) and 482 (1000); **2.17e•**, 441 (865), 490 (790).

Single crystal X-ray diffraction was used to determine the solid-state structures of **2.22b**, **[2.17a]₂** and **2.17e•**. The solid-state structure of **2.22b** confirms formation of the (NON^{Ph})-bridged bimetallic species {Bi(NON^{Ph})₂(μ -NON^{Ph})} (Figure 2.13). The asymmetric unit contains half a molecule of **2.22b**, which sits on a 2-fold rotation axis. The three-coordinate bismuth atoms are each chelated by one (NON^{Ph})-ligand in a κ_2 -N,N'-bidentate fashion, with a bridging (NON^{Ph})-ligand occupying the remaining coordination sites (Figure 1.6, E). As in **2.22c**, the Bi-N bond lengths do not differ significantly between the chelating and bridging (NON^{Ph})-ligands (Bi-N1 2.179(2), Bi-N2 2.166(2), Bi-N3 2.168(2) Å). In contrast to the structure of **2.22c**, where the Ar' substituents of the bridging (NON^R)-ligand and '(NON^{Ar'})Bi' unit occupy opposite sides of the Bi-N_{bridge} bond (Ct_{BiN2}-Bi-N_{bridge}-Ar', 178.55° and 178.20°, Ct_{BiN2} = centroid defined by Bi, N1/3 and N2/4), the analogous Ph substituent occupies the same side of the Bi-N3 bond as the Bi(NON^{Ph}) fragment (Ct_{BiN2}-Bi-N_{bridge}-Ph, 7.29°). This is likely due to the decreased bulk at the nitrogen substituent allowing rotation about the Bi-N3 bond, and ultimately results in an eclipsed arrangement of the bismuth atoms about the bridging (NON^{Ph})-ligand in **2.22b** (Figure 2.14).

Despite the bismuth atoms being relatively close, the Bi...Bi distance (3.9614(7) Å) is outside the range of standard Bi-Bi bonds (2.990(2) – 3.1821(3) Å).⁶¹ Bi...aryl contacts (Bi...Ct_{C11'-C16'} 3.483(3) Å) between Bi and a phenyl of the symmetry related 'Bi(NON^{Ph})' unit are within the threshold defined for Bi(lone pair)...π(arene) interactions in [BiCl₃.C₆H_{6-n}Me_n] compounds (3.168(7) – 3.751(8) Å)⁶², consistent with ring-slipped (0.49 Å) Bi...aryl interactions, and may play a role in stabilising the unexpected arrangement of bismuth atoms about the bridging (NON^{Ph})-ligand.

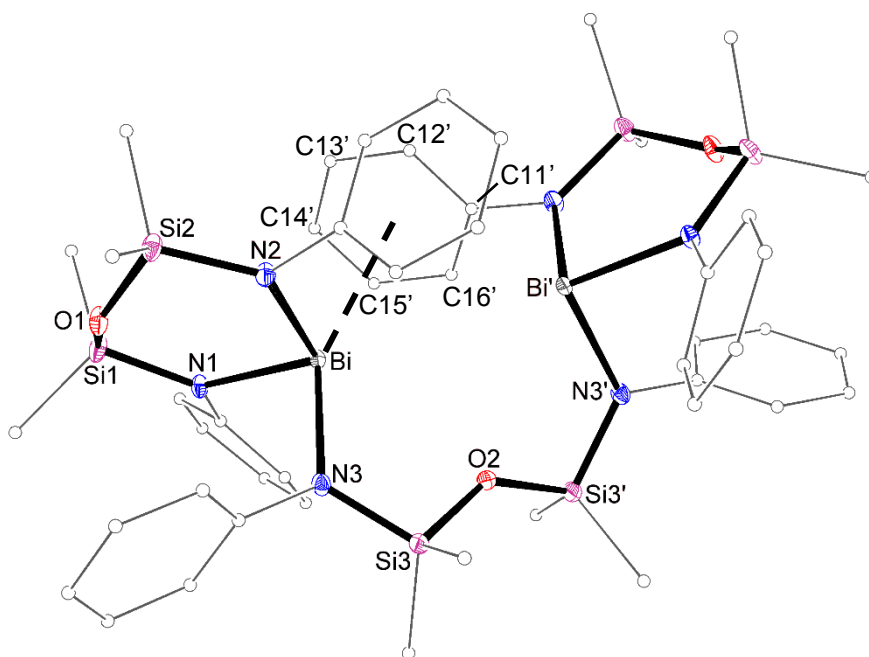


Figure 2.13. Molecular structure of **2.22b** (thermal ellipsoids displayed at 30% probability level, symmetry relationship (') = -x, y, 0.5-z). Hydrogen atoms and a toluene solvent molecule are omitted. Carbon atoms are displayed in wireframe format for clarity. Selected bond lengths (Å) and angles (°): Bi-N1 2.179(2), Bi-N2 2.166(2), Bi-N3 2.168(2), Bi...Ct_{C11-C16} 3.483(3); N1-Bi-N2 99.67(8), N1-Bi-N3 95.66(8), N2-Bi-N3 97.61(8), {BiN1N2} : {BiN1N2}' interplanar angle 81.99.

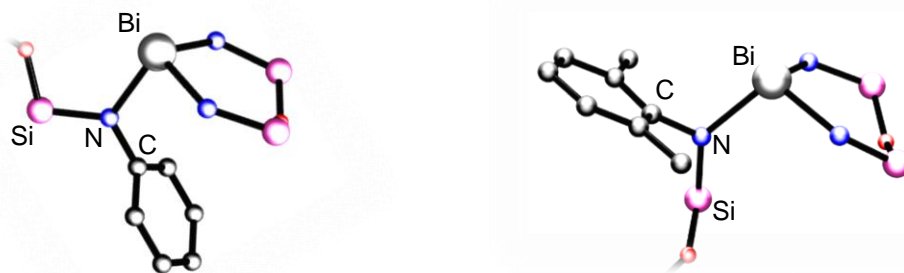


Figure 2.14. Relative arrangements of chelating and bridging (NON^{R})-ligands in **2.22b** (left) and **2.22c** (right).

The X-ray structure of $[\mathbf{2.17a}]_2$ confirms formation of the dibismuthane $[\text{Bi}(\text{NON}^{\text{tBu}})]_2$ in the solid-state (Figure 2.15). The bismuth atoms are crystallographically inequivalent and have a pyramidal geometry ($\Sigma(\angle\text{Bi})$: Bi1, 286.57° ; Bi2, 287.82°) with a (NON^{tBu})-ligand coordinated in a $\kappa_2\text{-}N,N'$ -bidentate fashion to give 6-membered metallacycles. The metallacycles form boat conformations which coincide with Bi \cdots O contacts (Bi1 \cdots O2 3.330(2) Å, Bi2 \cdots O1 3.274(2) Å) between the bismuth atoms and siloxane oxygen atom of the opposing ' $\text{Bi}(\text{NON}^{\text{tBu}})$ ' unit, and may contribute to the stability of the Bi-Bi core. The Bi-N distances (range 2.188(3) – 2.199(3) Å) are long compared to the bismuth(III) chloride **2.16a** (2.130(3) and 2.153(3) Å), consistent with formation of a reduced bismuth species and a larger Bi(II) atom. The Bi-Bi bond distance (3.0201(5) Å) is unexceptional and within the standard range recorded for dibismuthines (2.990(2) – 3.1821(3) Å).⁶¹

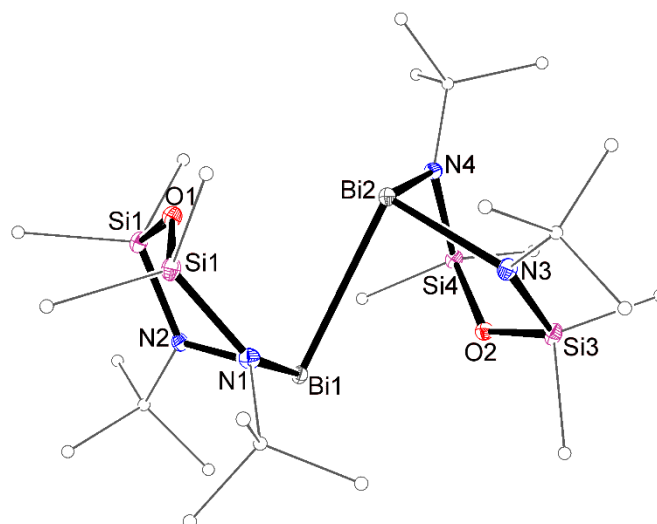


Figure 2.15. Molecular structure of **[2.17a]₂** (thermal ellipsoids displayed at 30% probability level). Hydrogen atoms are omitted. Carbon atoms are displayed in wireframe format for clarity. Selected bond lengths (Å) and angles (°): Bi1–Bi2 3.0201(5), Bi1–N1 2.199(3), Bi1–N2 2.194(3), Bi2–N3 2.188(3), Bi2–N4 2.191(3), Bi1···O2 3.330(2), Bi2···O1 3.274(2); N1–Bi1–N2 99.8(1), N3–Bi2–N4 96.5(1), N2–Bi1–N3 97.61(8), {BiN1N2} : {Bi2N3N4} interplanar angle 25.35.

The solid-state structure of **2.17e•** was obtained in two different monoclinic space groups. Crystals were grown from either hexane or Et₂O to give data in the *C2/c* and *P2₁/n* space groups, respectively (Figure 2.16). In the *C2/c* structure, the asymmetric unit consists of half a molecule of •Bi(NON^{Ar†}) on a two-fold rotation axis defined by the Bi···O vector, while in the latter case, the unit cell contains poorly resolved Et₂O solvate molecules that have been treated as a diffuse contribution to the overall scattering without specific atom positions by SQUEEZE/PLATON,⁶³ allowing discussion of the 'Bi(NON^{Ar†})' unit of interest. Both structures show a two-coordinate bismuth centre chelated by the (NON^{Ar†})-ligand. The Bi–N bond distances (*C2/c*, Bi–N 2.208(2) Å; *P2₁/n*, Bi–N1 2.179(5), Bi–N2 2.180(5) Å) differ slightly for the different space groups, owing to large conformational differences in the six-membered metallacycles (*C2/c*, Half-chair; *P2₁/n* Twist-boat).

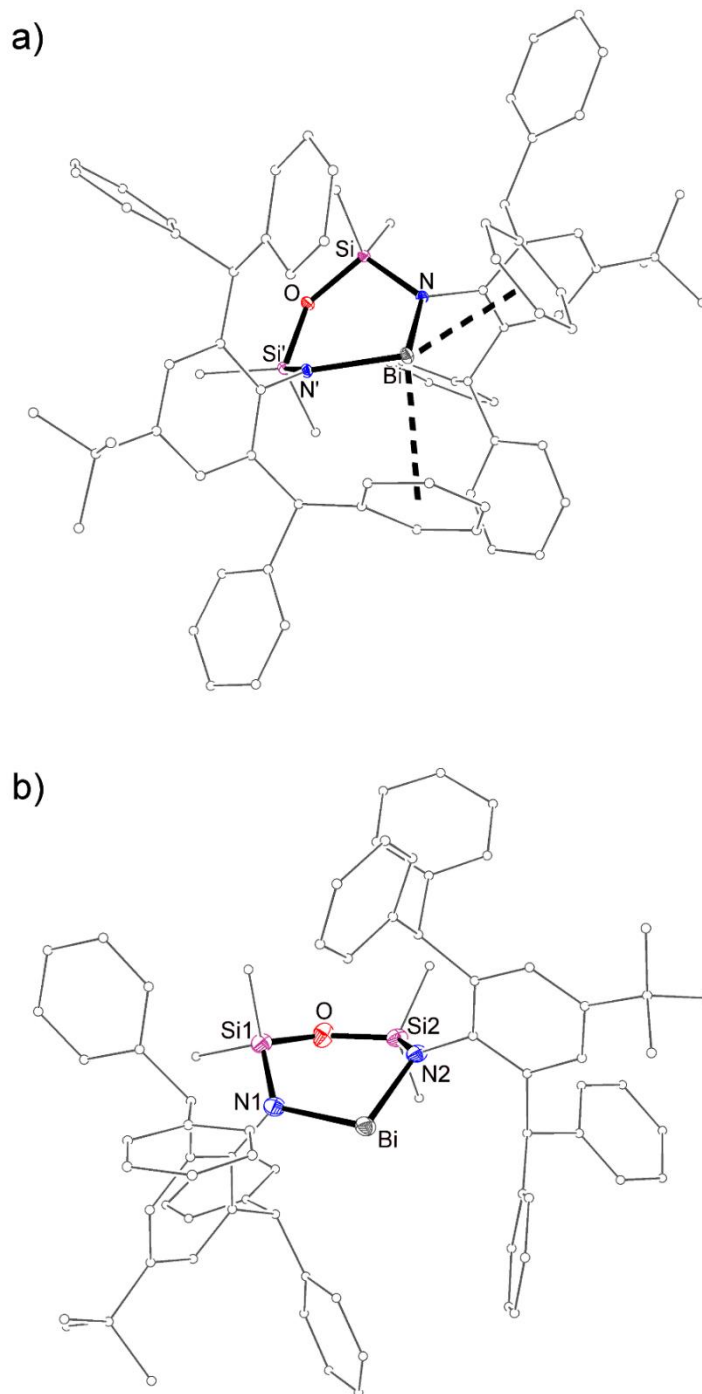


Figure 2.16. Molecular structure of **2.17e•** in the $C2/c$ (a) and $P2_1/n$ (b) space groups (thermal ellipsoids displayed at 30% probability level, symmetry relationship ($'$) = 1-x, y, 1.5-z). Hydrogen atoms are omitted. Carbon atoms are displayed in wireframe format for clarity. Selected bond lengths (Å) and angles (°): **$C2/c$** Bi-N 2.208(2), Bi-Ct_{C8-C13} 3.513(1); N1-Bi-N2 92.26(9). **$P2_1/n$** Bi-N1 2.179(5), Bi-N2 2.180(5); N1-Bi-N2 97.0(2).

The conformation of the six-membered metallacycle and the orientation of the CHPh_2 groups are the only major differences between the two structures and result in significant differences in the steric protection provided by the $(\text{NON}^{\text{Ar}\ddagger})$ -ligand. Two symmetry related phenyl groups form intramolecular $\text{Bi}\cdots\text{aryl}$ interactions ($\text{Bi}\cdots\text{Ct}_{\text{C8-C13}}$ 3.51 Å), with distances within the threshold defined for $\text{Bi}(\text{lone pair})\cdots\pi(\text{arene})$ interactions in $[\text{BiCl}_3\cdot\text{C}_6\text{H}_{6-n}\text{Me}_n]$ compounds (3.168(7) – 3.751(8) Å).⁶² In contrast, the shortest $\text{Bi}\cdots\text{aryl}$ interaction in the $P2_1/n$ structure is outside of this range ($\text{Bi}\cdots\text{Ct}_{\text{C54-C59}}$ 4.18 Å).

The influence of the position of the phenyl groups on the local steric encumbrance of the bismuth centre can be demonstrated by calculating the percent buried volume ($\%V_{\text{Bur}}$)²⁹ and G-parameter (Section 1.5)³⁰ of the complex in the two crystal structures (Figure 2.17 and Table 2.3). To allow for direct comparison to the (NON^{Ar}) -ligand, these values have also been calculated for **2.17d**. As expected, both structures of **2.17e** ($C2/c$ $\%V_{\text{Bur}}$ = 77.6 %, G = 85.8 %; $P2_1/n$ $\%V_{\text{Bur}}$ = 66.2 %, G = 75.6 %) have a noticeable increase in steric encumbrance relative to **2.17d** ($\%V_{\text{Bur}}$ = 57.9 %, G = 59.5 %). However, the large difference in $\%V_{\text{Bur}}$ and G-parameter between the two structures of **2.17e** reflect the influence that the arrangement of the phenyl substituents has on the steric bulk provided by the ligand. As both conformations were observed in the solid-state, and the solid-state structure often represents the lowest energy conformation, this work suggests that the two conformations that generate very different local environments at Bi are energetically similar. The other conclusion that may be drawn from this structural study is that, while initial thoughts may be that increased bulk will deactivate the bismuth centre, the $(\text{NON}^{\text{Ar}\ddagger})$ -ligand may provide wide-ranging fluxional steric bulk which may allow it to accommodate further derivatisation at the bismuth centre.

Table 2.3. Steric Parameters for **2.17d•**, **2.17e•-C2/c** and **2.17e•-P2₁/n**.

	%V _{Bur} ^a	G parameter ^b	Equivalent Cone Angle (°) ^b
2.17e• – C2/c	77.6	85.75	271.3
2.17e• – P2₁/n	66.2	75.63	241.7
2.17d•	57.9	59.47	201.8

^aCalculated using the SambVca2 application using radius = 3.5 Å, Volume of Bi excluded from calculations.²⁹ ^bCalculated using the Solid-G suite of programs.³⁰

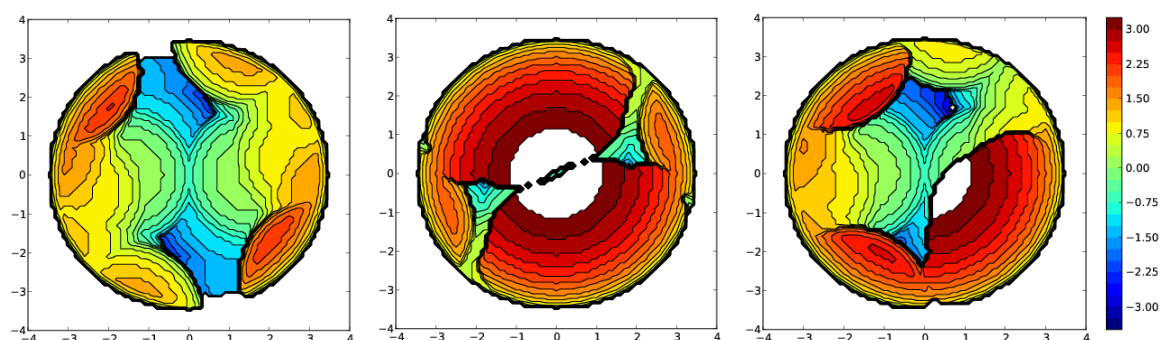


Figure 2.17. Graphical representations of the %V_{Bur} showing the distribution of steric encumbrment of the bismuth centre for **2.17d•** (left), **2.17e•-C2/c** (middle) and **2.17e•-P2₁/n** (right). Coloured sections correspond to the depth of bulk (red (3.00) corresponds to forward projection, blue (-3.00) corresponds to bulk behind the metal centre). The volume corresponding to the bismuth atom is excluded.

2.3.3. Synthesis and Characterisation of Bismuth(I) Species

Cyclic voltammetry (performed by A. Kilpatrick, University of Sussex) was used to examine the redox chemistry of **2.17d•**, using [(*n*Bu)₄N][PF₆] as the electrolyte and THF as the solvent, and was performed under an atmosphere of argon (Figure 2.18). Although oxidation to Bi(III) is expected to be a facile process, oxidative survey scans showed only ligand based oxidation (+0.84 V) rather than the Bi(II)/Bi(III) couple. In contrast, the reductive survey scans showed two cathodic waves at -1.74 V (Figure 2.18, **A**) and -2.50 V (**B**), both assigned to one-electron reduction processes based on the limiting current values. Subsequent oxidative scans

performed after **B** showed irreversible oxidation at -1.03 V (**C**), characteristic of a ‘stripping process’ in which elemental Bi(0) deposited onto the electrode surface undergoes oxidation to form Bi(III).⁶⁴ This process was not observed if the oxidative scans were performed immediately after **A**. Therefore, process **A** was assigned to the Bi(II)/Bi(I) couple, while process **B** was assigned a second one-electron reduction to give Bi(0).

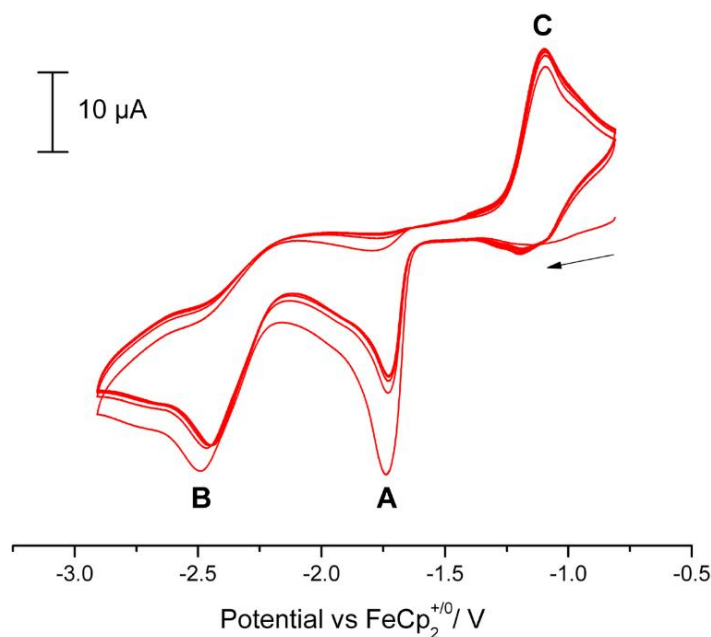
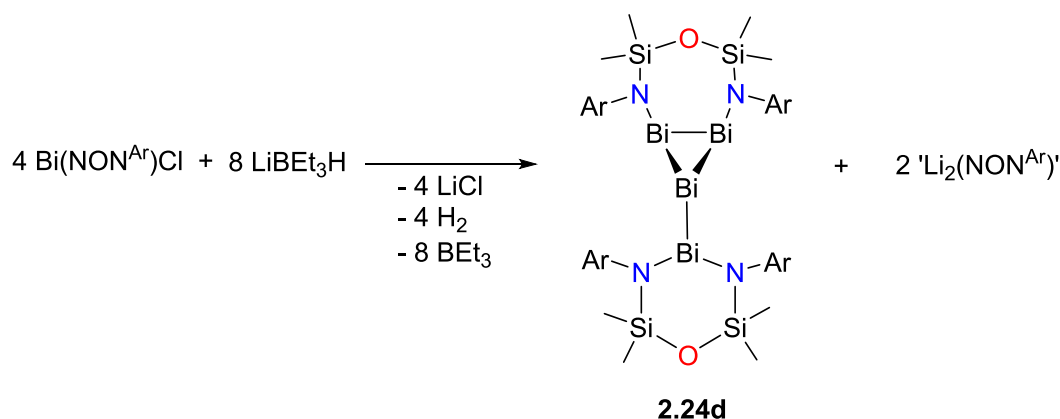


Figure 2.18. Overlaid CV scans (5 cycles) for **2.17d•** in THF/0.1 M [*n*Bu₄N][PF₆], scan rate 100 mVs⁻¹.

These results demonstrate that Bi(I) compounds may be accessible through further reduction of the bismuth(II) species. The potential for this type of reactivity was further realised when on one occasion, a small number of black crystals were obtained from the reaction of **2.16d** and LiBEt₃H, which were analysed using single crystal X-ray diffraction and confirmed to be the Bi₄-cluster Bi₄(NON^{Ar})₂ (**2.24d**). The formation of this species was unexpected, however, a balanced chemical equation can be proposed on the basis of the starting materials and products (Scheme 2.8). The formation of ‘Li₂(NON^{Ar})’ and rearrangement to form ‘(NNO^{Ar})Li₂’ was supported by the isolation of colourless crystals of [Li(THF)₄][Li(NNO^{Ar}.BEt₃)] (**2.25d**, Figure S2.5) from the mother liquor. Unfortunately, disorder in the solvent molecules bound

to the lithium atoms prevents discussion of bond lengths and angles. However, the connectivity of the ion-pair is unambiguous.



Scheme 2.8. Proposed synthetic pathway to **2.24d**.

The solid-state structure of **2.24d** revealed a Bi_4 core ligated by two (NON^{Ar}) -ligands. One (NON^{Ar}) -ligand chelates a bismuth centre, while the other bridges two adjacent bismuth atoms (Figure 2.19). Despite the different coordination modes, the Bi-N distances are essentially equivalent (Bi1-N1 2.224(11) Å, Bi1-N2 2.208(11) Å, Bi4-N3 2.217(11) Å, Bi4-N4 2.194(11) Å) and are on average slightly longer than those observed for the bismuth radical **2.17d•** (2.173(3) and 2.172(5) Å). The Bi-Bi distances (Bi1-Bi2 3.0932(8) Å, Bi1-Bi3 3.009(1) Å, Bi1-Bi3 3.002(1) Å, Bi3-Bi4 3.007(1) Å) are consistent with single bonds and are within the range reported for dibismuthanes (2.990(2) – 3.1821(3) Å). Structurally characterised Bi_3 triangles are rare, only occurring in polycyclic mixed-metal cluster compounds and zintl ion clusters.⁶⁵ The internal angles of the Bi_3 triangle are close to 60° (Bi1-Bi2-Bi3 59.15(2)°, Bi1-Bi3-Bi2 61.94(2)°, Bi2-Bi1-Bi3 58.92(2)°), with an exocyclic bismuth atom (Bi4) almost perpendicular to the Bi_3 triangle (Bi1-Bi3-Bi4 82.13(3)°, Bi2-Bi3-Bi4 93.97(3)°). The sum of angles about the bismuth atoms ($\Sigma(\angle\text{Bi})$: Bi1, 273.96°; Bi2, 268.64°; Bi3, 238.04°; Bi4, 296.0°) differ significantly. If an idealised ‘conventional’ hybridisation model is used, we would expect the angles about the bismuth to vary from 109° for sp^3 -hybridisation to 180° for an sp system, while no hybridisation (i.e. p-orbitals) would result in 90° angles about the bismuth (i.e. $\Sigma(\angle\text{Bi}) = 270^\circ$). While this basic model can be used to describe the bonding in Bi1, Bi2 and Bi4, the extremely

acute angles about Bi3 cannot be described using this model. Wade's rules for bonding in cluster compounds are also unable to describe the bonding in **2.24d** (i.e. $[\text{Bi}_4]^{4+}$), and the Bi-Bi bonds may indicate metallic bonding character with some form of delocalisation of electrons. Investigations into the bonding between the bismuth atoms in **2.24d** using DFT are ongoing.

Although this structural motif is unprecedented for bismuth, similar arrangements have been observed for the lighter group 15 (P, As and Sb) complexes $[(\text{CAAC})\text{P}_4\{\text{CH}_2(\text{CH}_3)\text{C}=\text{CCH}_2(\text{CH}_3)\}]$ (CAAC = cyclicalkyl(amino)carbene),⁶⁶ $[(\text{Cp}_2\text{Zr})\text{P}_4\{\text{P}(\text{SiMe}_3)_2\}_2]$ (Cp = cyclopentadiene, C_5H_5),⁶⁷ $(\text{Ter})_2\text{Cl}_2\text{P}_4$ (Ter = 2,6-dimesitylphenyl),⁶⁸ $[(\text{mes}_2\text{Si-Simes}_2)_2(\text{As}_4)]$ ⁶⁹ and $[(\text{L}^1\text{Mg})_4\text{Sb}_4]$ ($\text{L}^1 = i\text{Pr}_2\text{NC}[\text{N}(2,6-i\text{Pr}_2\text{C}_6\text{H}_3)]_2$),⁷⁰ respectively. In contrast to the reported Sb_4 complex, which was described as a $[\text{Sb}_4]^{4-}$ anion balanced by four Mg^+ counter-ions, **2.24d** is more accurately described as $[\text{Bi}_4]^{4+}$ due to the difference in electronegativity between Bi and N. The oxidation states of the bismuth atoms can be assigned on the basis of electronegativities and homolytic cleavage of Bi-Bi bonds, in which Bi1 and Bi2 are formally in the +1 oxidation state, while Bi4 is in the +2 oxidation state and Bi3 is zero-valent. Unfortunately, rapid decomposition of **2.24d** in solution at room temperature, shown by loss of the dark colour and formation of an insoluble precipitate over several minutes, precludes characterisation by NMR spectroscopy. However, elemental analysis is consistent with the assignment by X-ray crystallography.

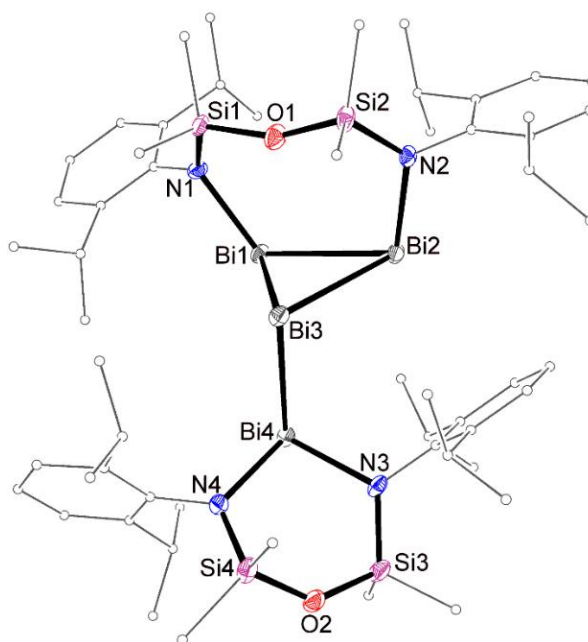


Figure 2.19. Molecular structure of **2.24d** (thermal ellipsoids displayed at 30% probability level). Hydrogen atoms and minor components of disorder are omitted. Carbon atoms are displayed in the wireframe format for clarity. Selected bond lengths (Å) and angles (°): Bi1-Bi2 3.0932(8), Bi1-Bi3 3.009(1), Bi1-Bi3 3.002(1), Bi3-Bi4 3.007(1), Bi1-N1 2.224(11), Bi2-N2 2.208(11), Bi4-N3 2.217(11), Bi4-N4 2.194(11); Bi1-Bi2-Bi3 59.15(2), Bi1-Bi3-Bi2 61.94(2), Bi2-Bi1-Bi3 58.92(2), Bi1-Bi3-Bi4 82.13(3), Bi2-Bi3-Bi4 93.97(3), N3-Bi4-N4 94.4(4).

The formation of **2.24d** was surprising and prompted us to investigate the reactivity of the bismuth(II) species with other reducing agents. We have previously demonstrated that the reaction of **2.17d•** with 1 equiv. magnesium metal results in the deposition of Bi⁰ and formation of Mg(NON^{Ar})(THF)₃ (**2.23d**).⁴⁸ The heterogeneous nature of the reaction with magnesium metal and the potential for transmetallation of the ligand clearly complicate the reduction process. Magnesium(I) species [Mg(BDI^{Ar^S})]₂ (Ar^S = mes (**1.1**), Ar (**1.2**)) are attractive as soluble and relatively mild reducing agents and have previously been used to activate small organic molecules and access rare low valent metal species.^{17b} The addition of 0.5 equiv. of **1.1** or **1.2** to a stirring solution of **2.17d•** results in an immediate colour change to give a purple solution. The latter reaction yielded purple crystals after work-up which were highly air and temperature sensitive.

The ^1H NMR spectrum of a solution of the purple crystals revealed two high field resonances (δ_{H} -0.17 and -0.05), corresponding to the SiMe_2 protons. In addition, a sharp singlet, corresponding to a γ -proton of a BDI backbone was observed at δ_{H} 4.80. The integrals of these peaks (6 : 6 : 1) is consistent with a 1 : 1 ratio of '(NON^{Ar})Bi' and '(BDI^{Ar})Mg', leading us to tentatively suggest formation of a species containing a Bi-Mg bond. However, analysis of the crystals by X-ray diffraction identified the species as the dibismuthene compound $[(\text{BDI}^{\text{Ar}})\text{Mg}(\mu\text{-NON}^{\text{Ar}})\text{Bi}]_2$ (**2.26d**, Figure 2.20), containing a Bi=Bi double bond (2.8604(8) Å). The solid-state structure is consistent with the NMR data, showing formation of a Mg/Bi-heterometallic species. However, the core of the molecule contains a homometallic Bi=Bi double bond, where each bismuth atom is supported by κ_1 -N-coordination of a (NON^{Ar})-ligand, which form bridges to 'Mg(BDI^{Ar})(THF)' units. **2.26d** crystallises in the $P2_1/n$ space group with half a molecule in the asymmetric unit, related by an inversion centre to form the dibismuthene. As with all reported unsupported dibismuthenes, the ligands sit trans across the double bond, with the nitrogen atom almost perpendicular to the Bi=Bi bond (Bi-Bi'-N1' 91.14(6)°). The Bi-N bond distance (2.218(2) Å) is significantly longer than those in **2.17d**, consistent with a larger Bi(I) atom. The formation of a dibismuthene instead of higher oligomers is unexpected, usually requiring extremely bulky ligands to accomplish. However, the aryl substituent of N1' eclipses Bi (Bi-Bi'-N1'-C1' 1.86(5)°), resulting in close contacts between Bi and C_{tC1'-C6'} (3.334(1) Å), consistent with a Bi...aryl interaction. This may play a role in stabilising the double bond and preventing oligomerisation. The bonds about the magnesium centre are unexceptional, with a standard Mg-N2 distance (2.034(3) Å) and slightly asymmetric bonding mode between the Mg and β -diketiminato ligand (Mg-N3 2.085(3) Å, Mg-N4 2.168(3) Å).

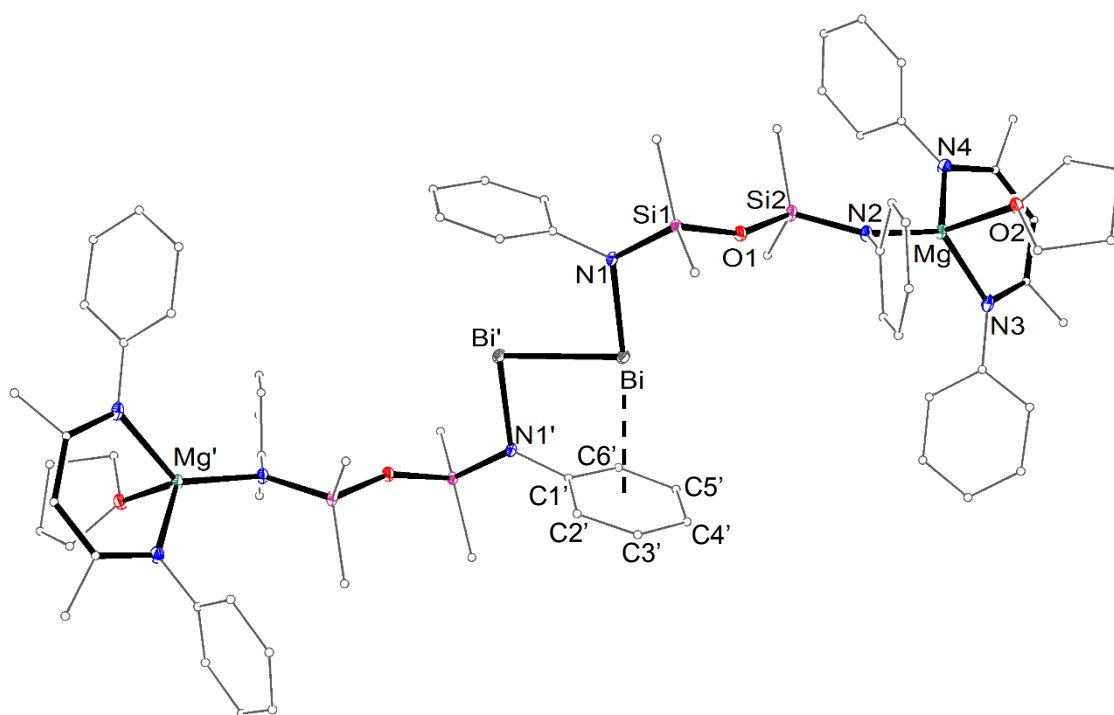
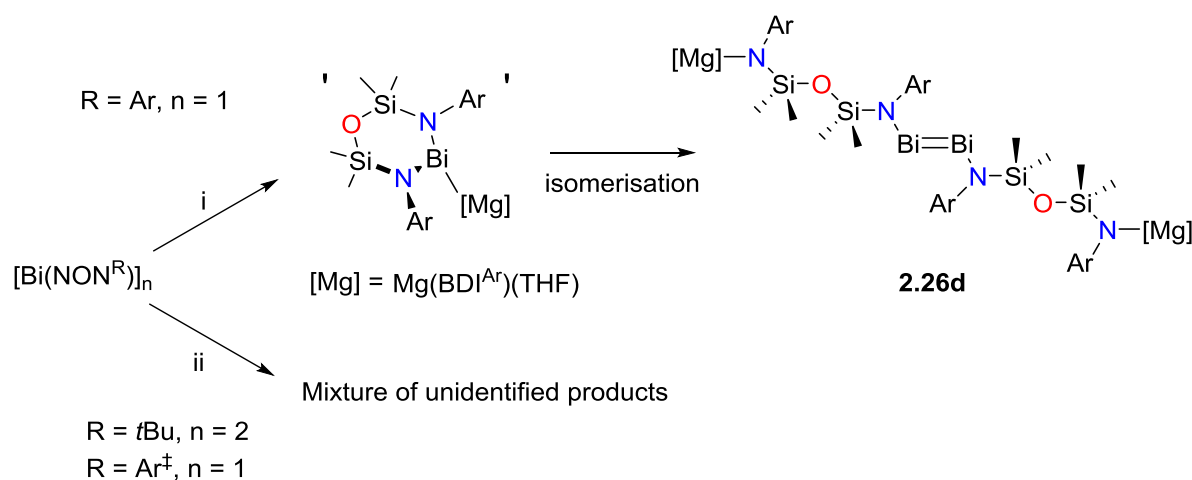


Figure 2.20. Molecular structure of **2.26d** (thermal ellipsoids displayed at 30% probability level, symmetry relationship (') = 2-x, -y, 1-z). Hydrogen atoms and *i*Pr groups of the Ar substituents are omitted. Carbon atoms are displayed in wireframe format for clarity. Selected bond lengths (Å) and angles (°): Bi=Bi 2.8604(8), Bi-N1 2.218(2), Bi-Ct_{C1'-C6'} 3.334(1), Mg-N2 2.034(2), Mg-N3 2.085(3), Mg-N4 2.168(3), Mg-O2 2.062(2); Bi-Bi'-N1' 91.14(6), Bi-Bi'-N1'-C1' 1.86(5), N3-Mg-N4 95.6(1).

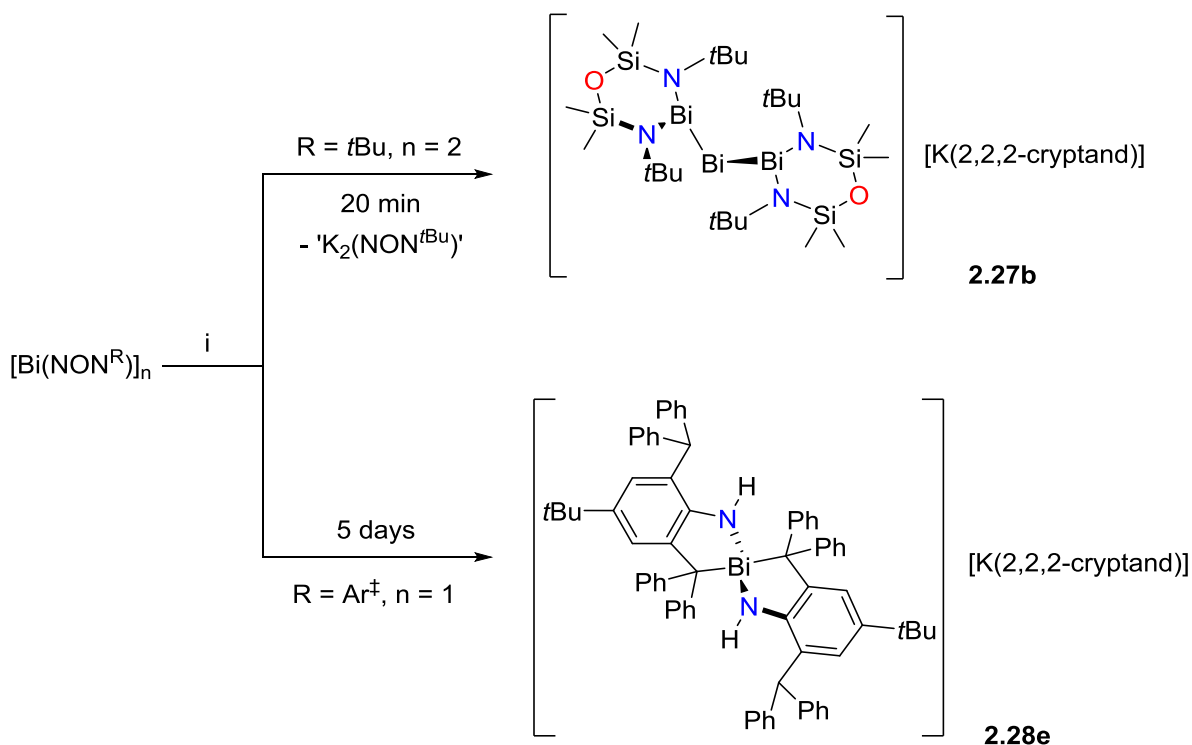
The formation of **2.26d** may occur as a rearrangement from a magnesium bismuthide isomer (Scheme 2.9), although we have no evidence for such an intermediate. The attempted reduction of [**2.17a**]₂ or **2.17e**• using 0.5 equiv. **1.1** or **1.2** proceeded with formation of significant quantities of black solid. Unfortunately, the ¹H NMR spectrum of the reaction mixtures revealed the formation of a complex and intractable mixture of products.



Scheme 2.9. Reduction of bismuth(II) species with magnesium(I) reagents. i) 0.5 **1.2**, THF/toluene. ii) 0.5 **1.1** or **1.2**, THF/toluene.

Efforts to reduce [**2.17a**]₂, **2.17d**• and **2.17e**• using a mixture of potassium metal and 2,2,2-cryptand also met with varied success. The reaction between [**2.17a**]₂ and a pre-mixed suspension of K/2,2,2-cryptand in C₆D₆ results in a slight colour change to dark yellow in addition to the formation of a black precipitate. Removal of the precipitate by filtration followed by allowing the reaction mixture to sit at room temperature for 20 minutes yielded a small number of extremely air and temperature sensitive crystals which were analysed by X-ray diffraction and identified as the tribismuthane [K(2,2,2-cryptand)][Bi₃(NON^{tBu})₂] (Scheme 2.10, **2.27b**). The formation of this compound presumably proceeds with concomitant formation of 'K₂(NON^{tBu})', although this species was not identified in the reaction mixture. The reaction of **2.17d**• with a pre-mixed suspension of K/2,2,2-cryptand in C₆D₆ gives thermally unstable red crystals after 30 minutes at room temperature. Attempts to identify the crystals using X-ray crystallography were unsuccessful due to significant disorder within the crystal lattice. Efforts to solve the data revealed tantalising glimpses of a related Bi₃-core structure, however, the poor quality of the data and significant disorder in the crystal lattice hindered the proposal of a conclusive and valid model. In contrast, the reaction of **2.17e**• with K/2,2,2-cryptand under identical conditions did not yield crystals within a short timeframe. Leaving the reaction mixture at room temperature for an extended period of time (5 days) resulted in

the formation of black crystals, identified as the decomposition product **2.28e** using X-ray crystallography. Attempts to analyse either of the reaction products by ^1H NMR spectroscopy were unsuccessful, with rapid decomposition of **2.27b** at room temperature and the low solubility of **2.28e** in C_6D_6 preventing NMR analysis.



Scheme 2.10. Reactivity of bismuth(II) species with K/2,2,2-cryptand. i) K, 2,2,2-cryptand, C_6D_6 .

The solid-state structure of **2.27b** revealed a non-contact ion-pair (Figure 2.21). The complex sits on a special position, with the two halves of the molecule related by a 2-fold rotation axis defined by the central $\text{Bi}_2 \cdots \text{K}$ vector. The anionic component contains an unprecedented Bi_3 chain supported by $(\text{NON}^{\text{tBu}})$ -ligands and is balanced by a potassium cation encapsulated by the cryptand ligand. The $(\text{NON}^{\text{tBu}})$ -ligands chelate the terminal bismuth atoms in a $\kappa_2\text{-N,N}'$ -bidentate fashion, with an acute bite angle ($89.7(2)^\circ$) that coincides with long Bi-N distances ($2.231(6)$ and $2.234(5)$ Å) compared to those in **[2.17a]₂** (avg. 2.195 Å). The internal bismuth atom of the Bi_3 chain is a rare example of a 2-coordinate bismuth centre and has a bent geometry, while the terminal bismuth atoms are pyramidal ($\Sigma(\angle\text{Bi}): 301.3^\circ$). The acute Bi1-

Bi2-Bi1' angle ($78.0(1)^\circ$) is surprising, but may be explained by a lack of hybridisation for Bi2 in addition to increased repulsive interactions between the bonding electrons and the lone pair. The Bi1-Bi2 bond distance ($2.9605(5) \text{ \AA}$) is short, outside the range for a standard Bi-Bi single bond ($2.990(2) - 3.1821(3) \text{ \AA}$). The Bi1...Bi1' distance ($3.7280(6) \text{ \AA}$) is also outside of this range and suggests no strong bonding interactions are present between Bi1 and Bi1'. The boat conformation adopted by the (NON^{*t*Bu})-ligands result in relatively close Bi2...O1 contacts ($3.662(6) \text{ \AA}$), shorter than the sum of the van der Waals radii (3.82 \AA).

The core $[\text{Bi}_3]^{3+}$ unit is unprecedented in bismuth chemistry, however, an analogous arrangement of atoms has been observed in phosphorus and antimony species $[\text{P}_3\text{R}_4]^-$ ($\text{R} = i\text{Pr}$ or $t\text{Bu}$) and $[\text{Sb}_3(\text{R})_4]^-$ ($\text{R} = t\text{Bu}$ or Ph).⁷¹ Interestingly, these species also show short P-P and Sb-Sb bonds. Computational studies investigating the nature of the bonding interaction between the bismuth atoms and the location of the negative charge are ongoing.

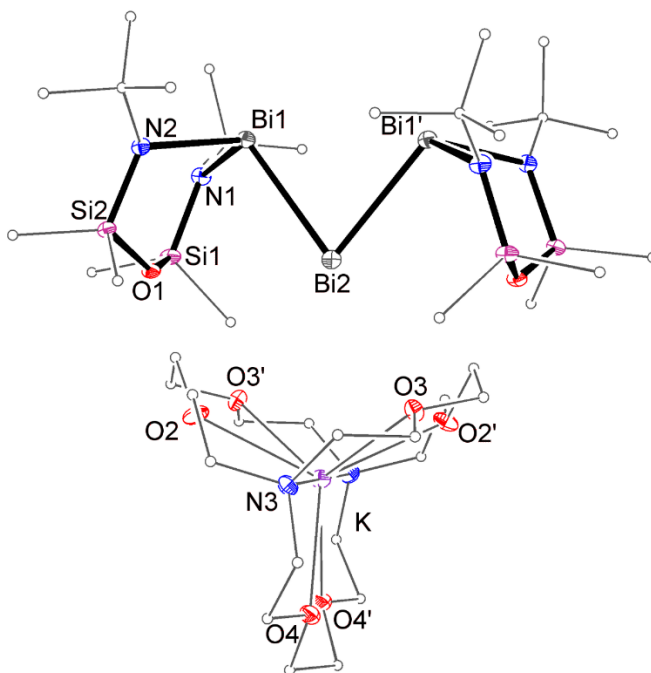


Figure 2.21. Molecular structure of **2.27b** (thermal ellipsoids displayed at 30% probability level, symmetry relationship (') = $1-x, y, 0.5-z$). Hydrogen atoms are omitted. Carbon atoms are displayed in wireframe format for clarity. Selected bond lengths (\AA) and angles ($^\circ$): Bi1-Bi2

2.9605(4), Bi1-N1 2.234(6), Bi1-N2 2.231(6), Bi2...O1 3.662(6); N1-Bi1-N2 89.7(2), Bi1-Bi2-Bi1' 78.04(2), Bi2-Bi1-N1 103.6(1), Bi2-Bi1-N2 108.0(1).

The solid-state structure of **2.28e** reveals a non-contact ion pair (Figure 2.22). The anionic component features a four-coordinate bismuth(III) centre, chelated by two bidentate *N,C*-ligands and balanced by a cryptand encapsulated potassium cation. The bismuth centre has a disphenoidal (see-saw) geometry, with the nitrogen atoms occupying the equatorial sites (N1-Bi-N2 94.62(7)°) and the carbon atoms in axial positions (C7-Bi-C43 156.78(7)°). Accordingly, the Bi-N distances (Bi-N1 2.204(2) Å, Bi-N2 2.173(2) Å) are standard, while the Bi-C bonds are long (Bi-C7 2.590(2) Å, Bi-C43 2.555(2) Å) compared to standard Bi-C bonds, as would be expected for axial ligands. The *N,C*-ligand bite angles are acute (N1-Bi-C7 70.63(7)°, N2-Bi-C43 72.26(8)°), with the ligands almost perpendicular to each other (BiN1C7 : BiN2C43 interplanar angle: 85.41(7)°). The C-C-C angles around the carbanion centres (avg. 115.6°) are significantly larger than is expected for a tetrahedral carbon centre (ideal angle: 109°), suggesting the Bi-C interaction is better described as a contact ion-pair, with the negative charge of the carbanion stabilised by the aromatic substituents, analogous to the ligand decomposition product **2.21e** (Figure 2.7).

2.4. Conclusion

This chapter describes the synthesis of a range of unprecedented and rare low oxidation state bismuth compounds supported by the (NON^R)-ligand. A series of bismuth(III) chlorides Bi(NON^R)Cl (R = *t*Bu (**2.16a**), Ph (**2.16b**), Ar' (**2.16c**), Ar (**2.16d**), Ar⁺ (**2.16e**)) were prepared from the corresponding pre-ligand (NON^R)H₂ and the steric environment of the bismuth centre was investigated using the %V_{Bur} and G parameters. Analogous to the reduction of **2.16d**, the reduction of **2.16a** and **2.16e** using either LiHBEt₃ or Mg metal gave the corresponding bismuth(II) species in the form of the dibismuthane [Bi(NON^{*t*Bu})]₂ (**[2.17a]**) or the bismuth radical species •Bi(NON^{Ar⁺}) (**2.17e•**). Further reduction of the bismuth(II) species, in addition to the bismuth radical species •Bi(NON^{Ar}) (**2.17d•**), was achieved using various reducing

agents, giving a number of interesting low oxidation state bismuth compounds. These include the first example of a mixed oxidation state bismuth compound containing Bi(II), Bi(I) and Bi(0) in the same unit (**2.24d**), and the first structurally characterised species containing a Bi₃-chain (**2.27b**). A key step in the formation of these products involves cleavage of Bi-N bond(s).

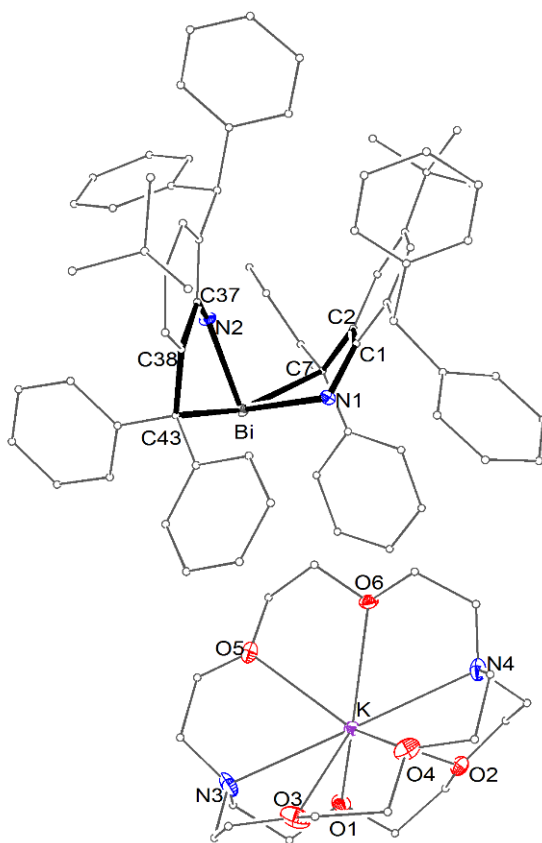


Figure 2.22. Molecular structure of **2.28e** (thermal ellipsoids displayed at 30% probability level). Et₂O solvent molecule and hydrogen atoms are omitted. Carbon atoms are displayed in wireframe format for clarity. Selected bond lengths (Å) and angles (°): Bi-N1 2.204(2), Bi-N2 2.173(2), Bi-C7 2.590(2), Bi-C43 2.555(2); N1-Bi-C7 70.63(7), N2-Bi-C43 72.26(8), C7-Bi-C43 156.78(7), N1-Bi-N2 94.62(7).

2.5. Experimental

See Appendix 7.1 for general experimental details.

2.5.1. Synthesis of Bismuth(III) Chloride Compounds

Synthesis of (NON^{Ar'})H₂ (2.19c)

2.19c was made following the literature procedure for **2.19d**, using 4.0 g of Ar'⁺NH₂ (0.033 mol), 18.2 mL of a 2.0 M solution of *n*BuLi in hexane (0.036 mol) and 3.1 mL of O(SiMe₂Cl)₂ (0.016 mol). **2.19c** was isolated as a pale yellow oil. Yield 5.95 g, 78 %. ¹H NMR (C₆D₆, 300 MHz): δ 7.01 (d, *J* = 7.5, 4H, *m*-C₆H₃), 6.88 (t, *J* = 7.5, 2H, *p*-C₆H₃), 2.22 (s, 12H, *o*-Me₂), 0.09 (s, 12H, SiMe₂). ¹³C{¹H} NMR (C₆D₆, 75 MHz): δ 142.9, 131.9, 128.7, 122.5 (C₆H₃), 19.9 (*o*-Me₂), 0.8 (SiMe₂). MS: *m/z* (M + H)⁺ 373.2124 (Calcd 373.2126).

Synthesis of (NON^{Ar±})H₂ (2.19e)

A solution of *n*BuLi (4.1 mL, 2M in cyclohexane, 8.2 mmol) was added drop wise to a stirring suspension of Ar[±]NH₂ (3.56 g, 7.4 mmol) in toluene (30 mL) at -78 °C resulting in an immediate colour change from pale yellow to orange/red. The suspension was allowed to warm to room temperature and stirred for 4 hours followed by the dropwise addition of O(SiMe₂Cl)₂ (0.72 mL, 3.7 mmol) at -78 °C. After allowing the suspension to warm to room temperature and stirring overnight, a brown solution was formed. Removal of the volatiles *in vacuo* gave a colourless solid, which was suspended in hot toluene and the precipitates removed by filtration to give a clear brown solution. Removal of the volatiles *in vacuo* gave an off white solid which was recrystallized from THF to give colourless crystals of **2.19e**·(THF)₂. Yield 2.90 g, 72 %. ¹H NMR (C₆D₆, 600 MHz): δ 7.30 – 7.00 (m, 44H, C₆H₅ and C₆H₂), 6.32 (s, 4H, CHPh₂), 3.60 (m, 3H*, THF-CH₂), 2.39 (s, 2H, NH), 1.44 (m, 3H*, THF-CH₂), 1.08 (s, 18H, CMe₃), 0.14 (s, 12H, SiMe₂). ¹³C{¹H} NMR (C₆D₆, 150 MHz): δ 146.1, 144.9, 141.2, 139.6, 130.0, 128.6, 126.6, 126.4 (C₆H₂ and C₆H₅), 67.8 (THF-CH₂), 53.1 (CHPh₂), 34.5 (CMe₃), 31.4 (CMe₃), 25.8 (THF-CH₂), 1.0 (SiMe₂). MS: *m/z* (M + H)⁺ 1093.5871 (Calcd 1093.5887). *partial loss of THF under vacuum during sample preparation

*Synthesis of $[Li(NON^{Ar\ddagger})(THF)][Li(THF)_4]$ (**2.20e**) and $Li(THF)(\mu-THF)[N(2-(CPh_2SiMe_2)-4-tBu-6-(C\{Li(THF)\}Ph_2)C_6H_2)]$ (**2.21e**)*

A solution of *n*BuLi (0.8 mL, 2M in cyclohexane, 1.54 mmol) was added dropwise to a stirring solution of **2.19e** (0.80 g, 0.73 mmol) in THF (10 mL) at -30 °C resulting in an immediate colour change from pale yellow to blood red. The solution was allowed to warm to room temperature and stirred for 2 hours followed by concentration to 2 mL. Storage of the solution at -30 °C gave a mixture of colourless crystals of **2.20e** and red crystals of **2.21e**. Fractional recrystallisation of the mixture from Et₂O gave an enriched sample of **2.20e** (crop 1) and a clean sample of **2.21e** (crop 2, yield 0.31 g, 28%). ¹H NMR (C₆D₆, 300 MHz): δ **2.20e***: 7.45 – 6.90 (m, 24H, C₆H₅ and C₆H₂), 6.64 (s, 4H, CHPh₂), 3.12 (m, 12H, THF-CH₂) 1.16 (s, 38H, THF-CH₂ and CMe₃), 0.48 (s, 12H, SiMe₂). **2.21e**: 7.67 (d, 1H, *J* = 2.1, C₆H₂), 7.62 (d, 4H, *J* = 7.4, C₆H₅), 7.42 (d, 4H, *J* = 7.8, C₆H₅), 7.35 – 7.28 (m, 1H, C₆H₅), 7.24 (t, 4H, *J* = 7.8, C₆H₅), 7.12-7.03 (m, 4H, C₆H₅), 6.98 (t, 4H, *J* = 7.8, C₆H₅), 6.23 (t, 2H, *J* = 7.8, C₆H₂), 3.18 (m, 12H, THF-CH₂), 1.25 (s, 9H, CMe₃), 1.21 (br, 12H, THF-CH₂), 0.10 (s, 6H, SiMe₂). ¹³C{¹H} NMR (C₆D₆, 75 MHz): δ **2.20e***: 159.0, 152.8, 147.6, 140.4, 136.9, 126.0, 116.9, 112.0 (C₆H₅ and C₆H₂), 52.9, 52.7 (CHPh₂), 34.2 (CMe₃), 32.1 (CMe₃), 25.0 (br, THF-CH₂), 5.7 (SiMe₂). **2.21e**: 148.2, 146.1, 141.0, 137.9, 131.1, 130.4, 130.2, 130.0, 129.3, 124.7, 124.4, 117.1, 112.1 (C₆H₅ and C₆H₂), 79.9 (CPh₂), 68.2 (THF-CH₂), 32.2 (CMe₃), 31.7 (CMe₃), 25.6 (br, THF-CH₂), 1.8 (SiMe₂). *identified from a mixture of **2.20e** and **2.21e** and subtraction of the peaks corresponding to **2.20e**.

*Synthesis of $Bi(NON^{tBu})Cl$ (**2.16a**)*

A solution of *n*BuLi in hexane (2.5 mL of a 1.6 M solution, 4.0 mmol) was added dropwise to a stirring solution of (NON^{tBu})H₂ (0.50 g, 1.81 mmol) in hexane (7 mL) at -30 °C. The resulting suspension was allowed to warm to room temperature and stirred for 2h. The suspension was added dropwise to a stirring suspension of freshly sublimed BiCl₃ (0.57 g, 1.81 mmol) in Et₂O (10 mL), followed by stirring for 3h. Unreacted BiCl₃ and decomposition products were removed by filtration through celite to give a yellow solution. Concentration and storage of

the solution at -30 °C yielded yellow needles of **2.16a** after 24 hours. Yield 0.51 g, 54 %. ^1H NMR (C_6D_6 , 300 MHz): δ 1.19 (s, 18H, CMe_3), 0.55, 0.33 (s, 6H, SiMe_2). $^{13}\text{C}\{^1\text{H}\}$ NMR (C_6D_6 , 75 MHz): δ 53.8 (CMe_3), 37.3 (CMe_3), 7.7, 6.2 (SiMe_2). Facile decomposition of **2.16a** prevented accurate elemental analysis.

*Synthesis of $\text{Bi}(\text{NON}^{\text{Ph}})\text{Cl}$ (**2.16b**)*

A solution of $n\text{BuLi}$ in hexane (3.3 mL of a 2.0 M solution, 6.7 mmol) was added dropwise to a stirring solution of $(\text{NON}^{\text{Ph}})\text{H}_2$ (1.0 g, 3.2 mmol) in hexane (7 mL) at -30 °C. The resulting suspension was allowed to warm to room temperature and stirred for 2h. The suspension was added dropwise to a stirring suspension of freshly sublimed BiCl_3 (1.0 g, 3.2 mmol) in Et_2O (10 mL), followed by stirring for 3h. Unreacted BiCl_3 and decomposition products were removed by filtration through celite to give a yellow solution. Concentration and storage of the solution at -30 °C yielded yellow blocks of **2.16b** after 24 hours. Yield 0.98 g, 55 %. ^1H NMR (C_6D_6 , 600 MHz): δ 7.16* (br, 4H, C_6H_5), 6.98 (br, 4H, C_6H_5), 6.87 (br, 2H, $p\text{-C}_6\text{H}_5$) 0.48, 0.36 (s, 6H, SiMe_2). $^{13}\text{C}\{^1\text{H}\}$ NMR (C_6D_6 , 75 MHz): δ 146.4, 129.7, 127.7, 124.25 (C_6H_5), 3.8, 2.4 (SiMe_2).

*overlapping with the solvent resonance

*Synthesis of $\text{Bi}(\text{NON}^{\text{Ar'}})\text{Cl}$ (**2.16c**) and $\{\text{Bi}(\text{NON}^{\text{Ar'}})\}_2(\mu\text{-NON}^{\text{Ar'}})$ (**2.22c**)*

A solution of $n\text{BuLi}$ in hexane (1.88 mL of a 1.6 M solution, 3.0 mmol) was added dropwise to a stirring solution of $(\text{NON}^{\text{Ar'}})\text{H}_2$ (0.50 g, 1.34 mmol) in hexane (7 mL) at -30 °C. The resulting suspension was allowed to warm to room temperature and stirred for 4 h. The suspension was added dropwise to a stirring suspension of freshly sublimed BiCl_3 (0.42 g, 1.34 mmol) in Et_2O (10 mL), followed by stirring for 18 h in the absence of light. Unreacted BiCl_3 and decomposition products were removed by filtration through celite to give an orange solution. Concentration and storage of the solution at -30 °C for 24 h yielded a small number of pale yellow crystals comprised mainly of the bridged species **2.22c**. Yield 0.055 g, 8.1 %. Further concentration of the mother liquor and storage at -30 °C gave colourless crystals predominantly consisting of **2.16c**. Yield 0.027 g, 3.3 %. **2.16c**: ^1H NMR (C_6D_6 , 300 MHz): δ 7.07

(br, 4H, *m*-C₆H₃), 6.82 (t, *J* = 7.8, 2H, *p*-C₆H₃), 2.73, 2.46 (s, 6H, *o*-Me₂), 0.59, 0.17 (s, 6H, SiMe₂). ¹³C{¹H} NMR (C₆D₆, 75 MHz): δ 142.3, 139.9, 137.8, 129.5, 129.2, 125.7 (C₆H₃), 20.9, 20.5 (*o*-Me₂), 5.4, 3.0 (SiMe₂). ²⁹Si NMR (C₆D₆, 100 MHz) δ -5.2. **2.22c**: ¹H NMR (C₆D₆, 300 MHz) δ 7.15 (m, 4H, *p*-C₆H₃), 6.96* (d, *J* = 7.8, 4H, *m*-C₆H₃), 6.83 (d, *J* = 7.8, 8H, *m*-C₆H₃), 6.66* (t, *J* = 7.8, 2H, *p*-C₆H₃), 2.70, 2.31, 1.90* (s, 12H, *o*-Me₂), 0.57, 0.34*, 0.16 (s, 12H, SiMe₂). ¹³C{¹H} NMR (C₆D₆, 75 MHz): δ 143.4*, 141.1, 139.5, 136.0*, 129.6, 129.1, 125.4, 124.9* (C₆H₃), 22.1*, 20.3, 20.2 (*o*-Me₂), 5.3, 3.8*, 2.4 (SiMe₂). ²⁹Si NMR (C₆D₆, 100 MHz) δ -7.7, -12.5*. *resonances corresponding to the bridging ligand.

Synthesis of Bi(NON^{Ar†})Cl (**2.16e**)

A suspension of Li₂(NON^{Ar†}) (1.36 g, 0.92 mmol) in toluene (10 mL, generated *in-situ* from *n*BuLi and **2.19e**) was added dropwise to a stirring suspension of BiCl₃ (0.29 g, 0.92 mmol) in toluene (10 mL) at -30 °C to give a red solution and black precipitate. Removal of the volatiles *in vacuo* gave a thick oil which was extracted with hexane (10 mL) and filtered through celite to give a clear red solution. Concentration of the reaction mixture to 3 mL and storage at room temperature resulted in the slow formation of the yellow crystals of **2.16e** after 24 hours. Yield 0.65 g, 53 %. Anal. Calcd. for C₇₆H₇₈BiClN₂OSi₂ (1566.39): C, 71.69; H, 6.31; N, 1.79 %. Found: C, 71.62; H, 6.39; N, 2.07 %. (Calculated with partial loss of toluene from crystals – 2.5 toluene molecules included). ¹H NMR (C₆D₆, 600 MHz): δ 7.73 (br, 4H, C₆H₂ and C₆H₅), 7.64 (br, 2H, C₆H₂ and C₆H₅), 7.38 (br, 4H, C₆H₂ and C₆H₅), 7.30 – 7.00 (m, 34H, C₆H₂ and C₆H₅), 6.88 (s, 2H, CHPh₂), 6.47 (s, 2H, CHPh₂), 1.05 (s, 18H, CMe₃), 0.24, -0.01 (s, 6H, SiMe₂). ¹³C{¹H} NMR (C₆D₆, 150 MHz): δ 147.9, 147.5, 146.7, 146.1, 145.5, 145.2, 142.3, 140.4, 131.5, 131.0, 130.7, 130.4, 129.5, 128.6, 128.5, 127.1, 126.9, 126.5, 126.3 (C₆H₅ and C₆H₂), 51.6, 50.8 (CHPh₂), 34.2 (CMe₃), 31.4 (CMe₃), 5.1, 4.8 (SiMe₂).

2.5.2. Synthesis of Bismuth(II) Compounds

Alternative synthesis of •Bi(NON^{Ar}) (2.17d•)

A solution of LiHBEt₃ in THF (0.93 mL of a 1.0 M solution, 0.93 mmol) was added dropwise to a stirring solution of **2.16d** (0.75 g, 1.0 mmol) in Et₂O (40 mL) at -78 °C. The resulting solution was allowed to warm to room temperature resulting in a colour change from yellow to deep red in addition to the formation of a black precipitate. Removal of the volatiles *in vacuo*, followed by extraction into Et₂O (20 mL) and filtration through celite gave a clear deep red solution. Concentration and storage of the filtrate at -30 °C yielded deep red crystals of **2.17d•** after 24 hours. Yield 0.36 g, 56 %.

Synthesis of {Bi(NON^{Ph})}₂(μ-NON^{Ph}) (2.22b)

Method 1:

A solution of LiHBEt₃ in THF (0.81 mL of a 1.0 M solution, 0.81 mmol) was added dropwise to a stirring solution of **2.16b** (0.45 g, 0.81 mmol) in Et₂O (10 mL) at -30 °C. The resulting suspension was allowed to warm to room temperature, resulting in the formation of large amounts of black solid and a colourless solution. Removal of the volatiles *in vacuo*, followed by extraction into hexane (10 mL) and filtration through celite gave a clear colourless solution. Concentration and storage of the solution at -30 °C colourless crystals of **2.22b** after 24 hours. Yield 0.074 g, 20 %.

Method 2:

Solid magnesium turnings (0.0046 g, 0.18 mmol) were added to a solution of **2.16b** (0.20 g, 0.38 mmol) in Et₂O (10 mL). The resulting suspension was stirred over 3 hours to give a black solid and colourless solution. Removal of the volatiles *in vacuo*, extraction into 4 mL toluene and filtration through celite gave a clear colourless solution, which, when cooled to -30 °C for 24h gave colourless crystals of **2.22b**. Yield 0.056 g, 33 %. ¹H NMR (C₆D₆, 600 MHz): δ 7.25 (t, 4H, *J* = 7.5, C₆H₅), 7.17 – 7.01 (m, 20H, C₆H₅), 6.92 (t, 4H, *J* = 7.5, C₆H₅), 6.83 (t, 2H, *J* = 7.5,

C₆H₅), 0.34, 0.18, 0.09 (s, 12H, SiMe₂). ¹³C{¹H} NMR (C₆D₆, 75 MHz): δ 148.6, 148.2, 131.2, 129.7, 128.3, 127.6, 124.2, 123.1 (C₆H₅), 4.1, 3.1, 2.4 (SiMe₂).

Synthesis of [Bi(NON^{tBu})]₂ (**[2.17a]**)

Method 1:

A solution of LiHBEt₃ in THF (0.55 mL of a 1.0 M solution, 0.55 mmol) was added dropwise to a stirring solution of **2.16a** (0.31 g, 0.60 mmol) in Et₂O (20 mL) at -78 °C. The resulting suspension was allowed to warm to room temperature and stirred for 1h. Removal of the volatiles *in vacuo*, followed by extraction into Et₂O (10 mL) and filtration through celite gave a dark orange/red solution. Concentration and storage of the solution at -30 °C yielded dark orange/red crystals of **[2.17a]**₂ after 24 hours. Yield 0.16 g, 60 %.

Method 2:

Solid magnesium turnings (0.009 g, 0.37 mmol) were added to a solution of **2.16a** (0.40 g, 0.77 mmol) in Et₂O (10 mL). The resulting suspension was stirred over 24 hours to give a orange/red suspension. Removal of the volatiles *in vacuo*, extraction into 10 mL hexane and filtration through celite gave a clear orange/red solution, which, when cooled to -30 °C for 24h gave dark orange/red crystals of **[2.17a]**₂. Yield 0.20 g, 54 %. Melting Point: 162-164 °C (decomp. >180 °C). Anal. Calcd. For C₂₄H₆₀Bi₂N₄O₂Si₂ (966.34): C, 29.81; H, 6.25; N, 5.79 %. Found: C, 30.39; H, 6.36; N, 5.73%. ¹H NMR (C₆D₆, 300 MHz): δ 1.40 (s, 18H, CMe₃), 0.45, 0.43 (s, 6H, SiMe₂). ¹³C{¹H} NMR (C₆D₆, 75 MHz): δ 54.5 (CMe₃), 37.5 (CMe₃), 9.2, 6.9 (SiMe₂).

Synthesis of •Bi(NON^{Ar†}) (**(2.17e•)**)

Method 1:

A solution of LiHBEt₃ in THF (0.19 mL of a 1.0 M solution, 0.19 mmol) was added dropwise to a stirring solution of **2.16e** (0.25 g, 0.19 mmol) in Et₂O (20 mL) at -70 °C. The resulting suspension was allowed to warm to room temperature and stirred for 1h to give a colour change from yellow to red. Removal of the volatiles *in vacuo*, followed by extraction into Et₂O

(10 mL) and filtration through celite gave a clear red solution. Concentration and storage of the solution at -30 °C yielded red crystals of **2.17e•** after 24 hours. Yield 0.13 g, 53 %.

Method 2:

Solid magnesium turnings (0.009 g, 0.37 mmol) were added to a solution of **2.16e** (1.0 g, 0.75 mmol) in Et₂O (10 mL). The resulting suspension was stirred over 72 hours to give a deep red suspension. Removal of the volatiles *in vacuo*, extraction into 10 mL hexane and filtration through celite gave a clear red solution, which, when cooled to -30 °C gave red crystals of **2.17e•**. Yield 0.64 g, 66 %. Anal. Calcd. for C₇₆H₇₈BiN₂OSi₂ (1300.62): C, 70.18; H, 6.05; N, 2.15 %. Found: C, 70.12; H, 6.20 N, 2.33 %.

Synthesis of Mg(NON^{Ph})(THF)₃ (2.23b)

The addition of a solution of Mg(*n*Bu)₂ in hexane (1.27 mL of a 1.0 M solution, 1.27 mmol) to a stirring solution of **2.19b** (0.40 g, 1.27 mmol) in hexane (5 mL) results in formation of a white precipitate. The resulting suspension was stirred for 1h at room temperature, followed by the addition of a few drops of THF and hot filtration through celite to give a clear colourless solution. Storage of the solution at room temperature for 24 hours yielded colourless crystals of **2.23b**. Yield 0.70 g, 84 %. ¹H NMR (C₆D₆, 600 MHz): δ 7.22 (t, 4H, *J* = 7.2, *m*-C₆H₅), 6.76 (t, 2H, *J* = 7.2, *p*-C₆H₅) 6.70 (d, 4H, *J* = 7.2, *o*-C₆H₅), 3.56 (m, 13H*, THF-CH₂) 1.26 (m, 13H*, THF-CH₂), 0.56 (s, 12H, SiMe₂). ¹³C{¹H} NMR (C₆D₆, 150 MHz): δ 157.7, 129.4, 121.6, 114.4 (C₆H₅), 68.9, 25.4 (THF-CH₂), 3.0 (SiMe₂).

*Residual THF from solvent

Synthesis of (NON^{Ar±})Pb – used for the diamagnetic correction in the magnetic moment measurements of 2.17e• (Figure S2.6)

A solution of *n*BuLi (0.27 mL of a 2.0M solution in cyclohexane, 0.54 mmol) was added dropwise to a solution of **2.19e** (0.40 g, 0.27 mmol) in toluene (10 mL). After stirring for 12h at room temperature, this suspension was added dropwise to a suspension of PbCl₂ (0.075 g, 0.27 mmol) in Et₂O (10 mL). The resulting suspension was stirred vigorously for 24 hours

followed by filtration through celite and concentration to 3 mL. Storage of the yellow solution at -30 °C for 24 hours yields yellow crystals of (NON^{Ar†})Pb. Yield 0.23 g, 66 %. ¹H NMR (C₆D₆, 600 MHz): δ 7.36 (d, 8H, *J* = 7.5, *o*-C₆H₅), 7.34 (s, 4H, C₆H₂), 7.19 – 7.13 (m, 8H, C₆H₅), 7.08 – 7.03 (m, 12H, C₆H₅), 7.01 (t, 8H, *J* = 7.5, *m*-C₆H₅), 6.88 (t, 4H, *J* = 7.5, *p*-C₆H₅), 6.67 (s, 4H, CHPh₂), 1.09 (s, 18H, CMe₃), 0.28 (s, 12H, SiMe₂). ¹³C{¹H} NMR (C₆D₆, 150 MHz): δ 148.5, 145.0*, 144.2, 141.7, 130.6*, 129.1, 128.6, 128.4, 127.4, 126.7, 126.5, (C₆H₅ and C₆H₂), 51.3 (CHPh₂), 34.0 (CMe₃), 31.7 (CMe₃), 4.9 (SiMe₂). *two overlapping resonances

2.5.3. Reduction of Bismuth(II) Species

Synthesis of Bi₄(NON^{Ar})₂ (2.24d) and [Li(THF)₄][Li(NNO.BEt₃)] (2.25d)

A solution of LiHBEt₃ in THF (0.25 mL of a 1.0 M solution, 0.25 mmol) was added dropwise to a stirring solution of **2.16d** (0.15 g, 0.206 mmol) in Et₂O (10 mL) at -78 °C, which was stirred for 30 minutes and then allowed to warm to room temperature resulting in the formation of a deep red/purple suspension. Filtration of the suspension through celite gives a red/purple suspension, followed by concentration to ~3 mL and storage at -30 °C for 3 weeks resulting in the formation of a small number of black crystals of **2.24d**. Further concentration of the mother liquor and storage at -30 °C yielded a small number of colourless crystals of **2.25d**. This result was not reproducible despite repeated attempts using varying quantities of LiHBEt₃ (0.9 – 2.2 equiv.) and letting the solution stir at -78 °C for longer periods of time (up to 4 hours). **2.24d**: Anal. Calcd. for C₅₆H₉₂Bi₄N₄O₂Si₄ (1801.64): C, 37.33; H, 5.15; N, 3.11 %. Found: C, 37.17; H, 5.02 N, 3.26 %.

Synthesis of [(BDI^{Ar})Mg(NON^{Ar})Bi]₂ (2.26d)

A solution of [Mg(BDI^{Ar})]₂ (**1.2**, 0.075 g, 0.085 mmol) in toluene (5 mL) was added dropwise to a stirring solution of **2.17d•** (0.11 g, 0.16 mmol) in toluene (5 mL), resulting in an immediate colour change from red to purple. The resulting purple suspension was stirred for 10 minutes at room temperature, filtered through celite and concentrated to *ca.* 1 mL. Storage of this solution at -30 °C for 48 hours gave a temperature sensitive amorphous purple solid. Single

crystals of **2.26d** suitable for X-ray diffraction were obtained by recrystallisation from a mixture of THF/hexane (1:9). Yield 0.058 g, 30 %. ^1H NMR (C_6D_6 , 600 MHz): δ 7.16 – 7.07 (m, 8H, C_6H_3), 7.01 (d, 2H, $J = 7.5$, C_6H_3), 6.98 (d, 2H, $J = 7.5$, C_6H_3), 6.88 (t, 1H, $J = 7.5$, C_6H_3), 6.39 (t, 1H, $J = 7.5$, C_6H_3), 4.80 (s, 1H, $\gamma\text{-CH}$), 3.79, 3.65 (sept, 2H, $J = 7.5$, CHMe_2), 3.19, 2.95 (br, 2H, CHMe_2), 1.47 (s, 6H, CMe), 1.40 – 0.94 (m, 48H, CHMe_2), -0.05, -0.17 (s, 6H, SiMe_2). $^{13}\text{C}\{^1\text{H}\}$ NMR (C_6D_6 , 150 MHz): δ 171.6 ($\gamma\text{-C}$), 161.5, 149.0, 146.1, 144.2, 144.2, 142.7, 126.4, 126.0, 124.6, 124.3, 123.8, 121.1 (C_6H_3), 96.6 (CMe), 28.3, 29.1, 27.9, 27.7, 26.6, 25.9, 24.9, 24.8, 24.4 (CHMe_2 , CHMe_2 and CMe), 6.6, 2.6 (SiMe_2).

*Synthesis of $[\text{K}(2,2,2\text{-cryptand})][\text{Bi}_3(\text{NON}^{t\text{Bu}})_2]$ (**2.27a**)*

A suspension of K (0.0026 g, 0.068 mmol) and 2,2,2-cryptand (0.025 g, 0.068 mmol) in C_6D_6 (0.5 mL) was added to a solution of **[2.17a]₂** (0.032 g, 0.034 mmol) in C_6D_6 (0.5 mL), giving a dark yellow solution and small amount of black solid. The suspension was filtered through celite and the reaction mixture was allowed to sit for 20 minutes in a NMR tube fitted with a Young's tap, giving several dark crystals of **2.27a** which were analysed using X-ray diffraction. These crystals were highly air, moisture and temperature sensitive, and readily decomposed to a black solid, preventing analysis by NMR. Yield not measured, several crystals obtained.

*Synthesis of **2.28e***

A suspension of K (0.0029 g, 0.076 mmol) and 2,2,2-cryptand (0.029 g, 0.076 mmol) in C_6D_6 (0.5 mL) was added to a solution of **2.17e•** (0.050 g, 0.038 mmol) in C_6D_6 (0.5 mL), giving a dark yellow solution and small amount of black solid. The suspension was filtered through celite and the reaction mixture was allowed to sit for 5 days giving dark crystals of **2.28e** which were analysed using X-ray diffraction. Poor solubility in hydrocarbon solvents precluded analysis by NMR spectroscopy.

Chapter 3. Reactivity of Low Oxidation State Bismuth Species

Bismuth Species

3.1. Introduction

The reactivity of low oxidation state bismuth species is under-represented in the literature compared to other p-block metal systems. Dibismuthanes $\{\text{BiR}_2\}_2$ (R = alkyl or aryl) are highly reactive compounds capable of activating a wide range of substrates (e.g. electrophiles, nucleophiles, atmospheric oxygen and free radicals).⁷² In contrast, the reactivity of dibismuthenes $\{\text{BiR}\}_2$ is relatively unexplored. The weakness of the Bi-Bi (and Bi=Bi) bond has been demonstrated by their reactivity with halogens, chalcogens and transition metals. These reactions are proposed to proceed through homolytic cleavage of the Bi-Bi/Bi=Bi bond prior to reaction with the substrate, forming a highly reactive bismuth radical intermediate in the former case. Evidence for this bond homolysis includes the reversible exchange reactions with distibanes $\{\text{SbR}_2\}_2$ and diarsanes $\{\text{AsR}_2\}_2$ resulting in formation of species containing Bi-Sb and Bi-As bonds, respectively (Figure 3.1),⁷³ in addition to rearrangement reactions of *cyclo*- Bi_n compounds in solution (Section 2.1).^{60a}

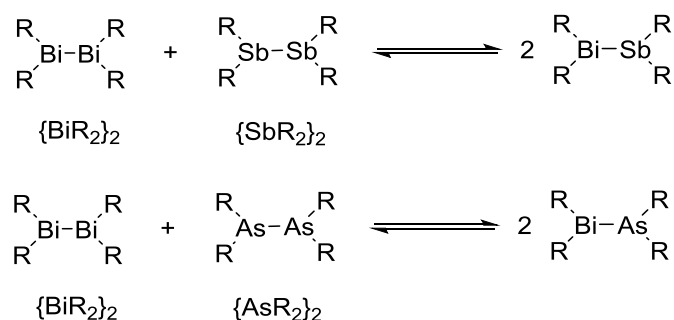


Figure 3.1. Exchange reactions between dibismuthanes and distibanes/diarsanes.

3.1.1. Oxidative Reactivity with R'-X (X = halogen, R' = H, alkyl, aryl, halogen)

Early investigations into the reactivity of low oxidation state bismuth compounds examined the oxidative addition of iodine (I_2), alkyl/aryl bromides ($R'Br$, $R' = CCl_3, CH_2Ph, CPh_3, Ph$) and HCl to tetramethyldibismuthane $\{BiMe_2\}_2$, resulting in cleavage of the Bi-Bi bond.^{34a, 74} The reaction between $\{BiMe_2\}_2$ and iodine gave a mixture of Me_2BiI , $MeBiI_2$, BiI_3 and metallic bismuth, while the oxidative addition of $R'Br$ resulted in formation of a mixture of Me_2BiBr and Me_2BiR' (Figure 3.2). Similarly, the reaction of $\{BiMe_2\}_2$ with HCl was proposed to give a mixture of Me_2BiCl and Me_2BiH . However, the latter species was not confirmed in the reaction mixture, presumably due to rapid decomposition at room temperature.

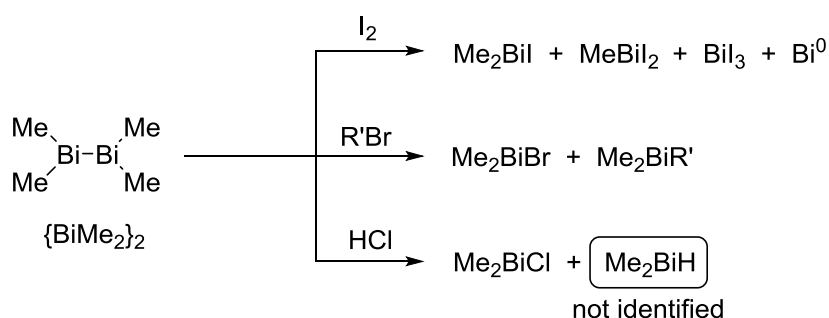


Figure 3.2. Oxidation of dibismuthanes with halogen sources. $R' = CCl_3, CH_2Ph, CPh_3, Ph$.

3.1.2. Oxidative Reactivity with Chalcogens

The reactivity of Bi-Bi bonds with atmospheric oxygen has been demonstrated for tetraalkyldibismuthanes $\{BiR_2\}_2$ ($R = Me, nPr, mes$), giving the corresponding bis(bismuthanyl) oxide $R_2Bi-O-BiR_2$ (**3.1**, Figure 3.3).⁷⁵ In contrast, when $R = 2,6-(Me_2NCH_2)C_6H_3$, a peroxide bridged species featuring an intact $[O_2]^{2-}$ fragment held between two BiR_2 units can be isolated at $-30\text{ }^\circ\text{C}$ (**3.2**).⁷⁶ However, this species is unstable and quickly converts to $R_2Bi-O-BiR_2$ at room temperature. Dibismuthanes also react cleanly with elemental sulfur, selenium and tellurium, proceeding with cleavage of the Bi-Bi bond and formation of the chalcogen insertion products $R_2Bi-E-BiR_2$ ($E = S, Se, Te$; $R = \text{alkyl or aryl}$).⁷⁷ The Bi-Bi bonds in dibismuthanes can also be

cleaved by reaction with dichalcogenides $\{R'E\}_2$ ($E = S, Se, Te$), giving the corresponding Bi-E bonded species R_2Bi-ER' (**3.3**).⁷⁸

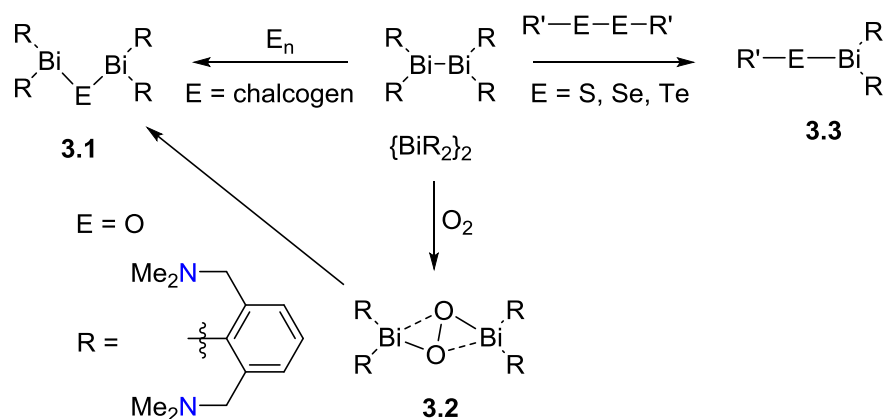


Figure 3.3. Oxidation of dibismuthanes with chalcogen containing species.

The reaction of dibismuthenes $\{BiAr^{\text{II}}\}_2$ ($Ar^{\text{II}} = 2,6\text{-CH}(\text{SiMe}_3)_2\text{-4-RC}_6\text{H}_2$, $R = \text{CH}(\text{SiMe}_3)_2$ (**2.1**) or $\text{C}(\text{SiMe}_3)_3$ (**2.2**)) with chalcogens was demonstrated to form various group 15/16 heterocyclic compounds, depending on the chalcogen substrate (Figure 3.4).^{38a, 79} The reaction with atmospheric oxygen results in formation of the 1,3-dioxo-2,4-dibismetane **3.4**, while the reaction with sulfur (S_8) resulted in the formation of 1,2,4-trithia-3,5-dibismolane **3.5** as the major product and the corresponding reaction with Se or $Te=P(nBu)_3$ resulted in formation of the selenadibismuthane and telluradibismuthane compounds **3.6** and **3.7**, respectively.

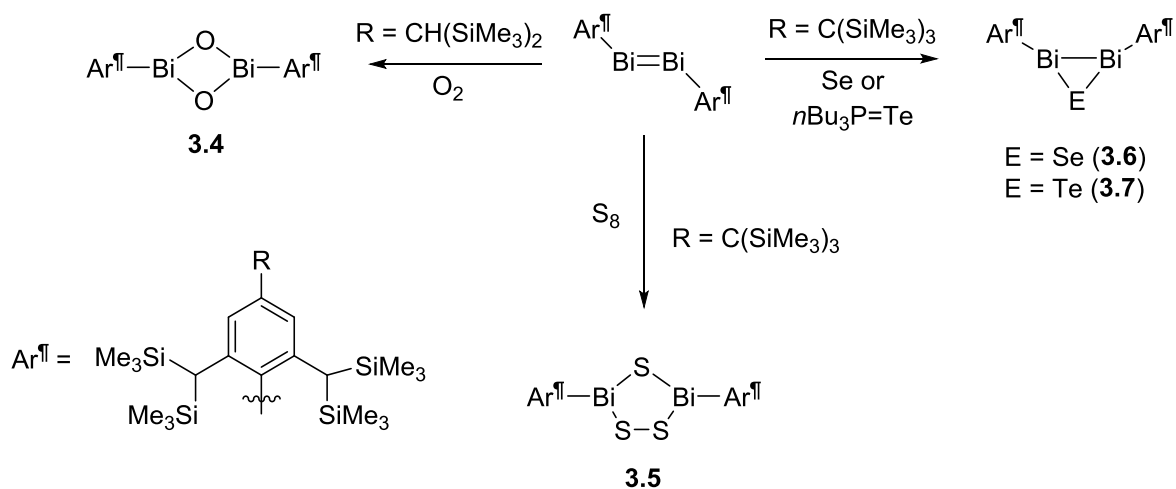


Figure 3.4. Oxidation of dibismuthenes with chalcogen substrates.

3.1.3. Reactivity with TEMPO

2,2,6,6-tetramethylpiperidin-1-yl)oxyl (TEMPO) is a stable nitroxyl radical commonly used in the trapping of radical intermediates and as an initiator in radical polymerisation.⁸⁰ Recent reports have also highlighted the potential to use TEMPO as a ligand (as either neutral TEMPO• or the anionic TEMPOxide, [TEMPO][−]),⁸¹ a one electron oxidant at zero- and low-valent elements (e.g. group 1 metals, Si, Ge, Sn)⁸² or to access single electron transfer (SET) chemistry involving E-H bonds (E = Al, P, Ga, Ge, Mg).⁸³

Dibismuthane [**2.15**]₂ was demonstrated to exist as a loosely associated species in an equilibrium with its monomeric form **2.15**• in solution (Section 2.1.2).⁴⁷ The reactivity of this mixture with TEMPO results in formation of the bismuth(III) TEMPOxide species **3.8**, which was isolated in the solid-state (Figure 3.5). The reaction was observed to be reversible in solution, with the presence of TEMPO• detected in solution by EPR spectroscopy.

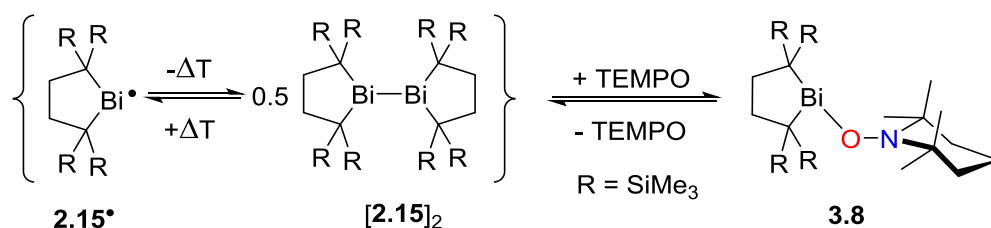


Figure 3.5. Reversible reactivity of **2.15**•/[**2.15**]₂ with TEMPO.

3.1.4. Reactivity with Metal Complexes

The reactivity of dibismuthanes with metal species has demonstrated their potential as (pre)ligands. Transition metal carbonyl compounds M₂(CO)_n (M = Fe, n = 9; M = Co, n = 8, M = Mo, n = 10) and {CpM(CO)₃}₂ (M = Cr, Mo, W) react with dibismuthanes, resulting in cleavage of the Bi-Bi bond and formation of species containing M-Bi bonds (Figure 3.6, **3.9** – **3.12**).⁸⁴ In contrast, the addition of {BiEt₂}₂ to group 13 trialkyls (Al(*t*Bu)₃ and Ga(*t*Bu)₃) results in coordination of the dibismuthane to the group 13 elements through the lone-pair of the bismuth (Figure 3.7, **3.13**).⁸⁵ More recently, Schulz and co-workers reported the insertion of low oxidation state Al(I) and Ga(I) metal centres into the Bi-Bi bond of {BiEt₂}₂ (**3.14**).⁸⁶ While

the reaction with aluminium(I) was irreversible, the reaction with the gallium(I) derivative was observed to be a temperature dependent equilibrium.

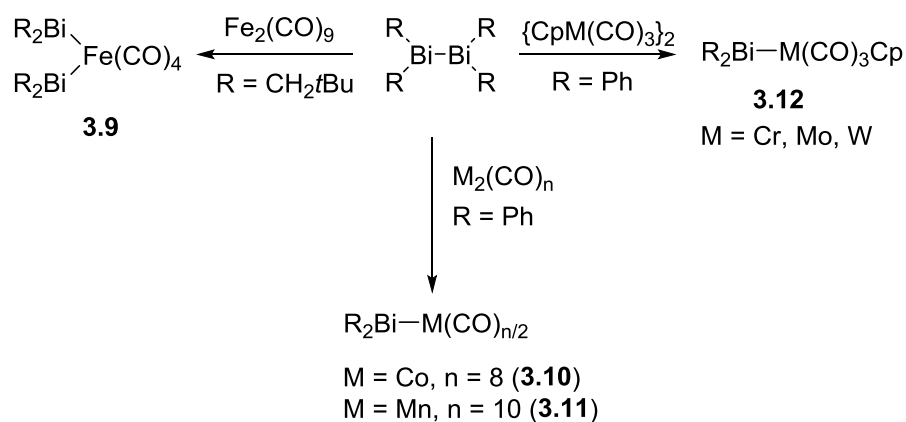


Figure 3.6. Reactivity of dibismuthanes with transition metal carbonyl complexes

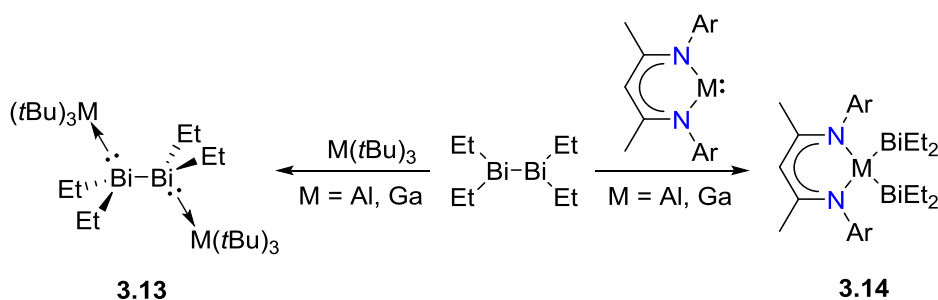


Figure 3.7. Reactivity of tetraethyldibismuthane with group 13 metal compounds. Ar = 2,6-*i*Pr₂C₆H₃.

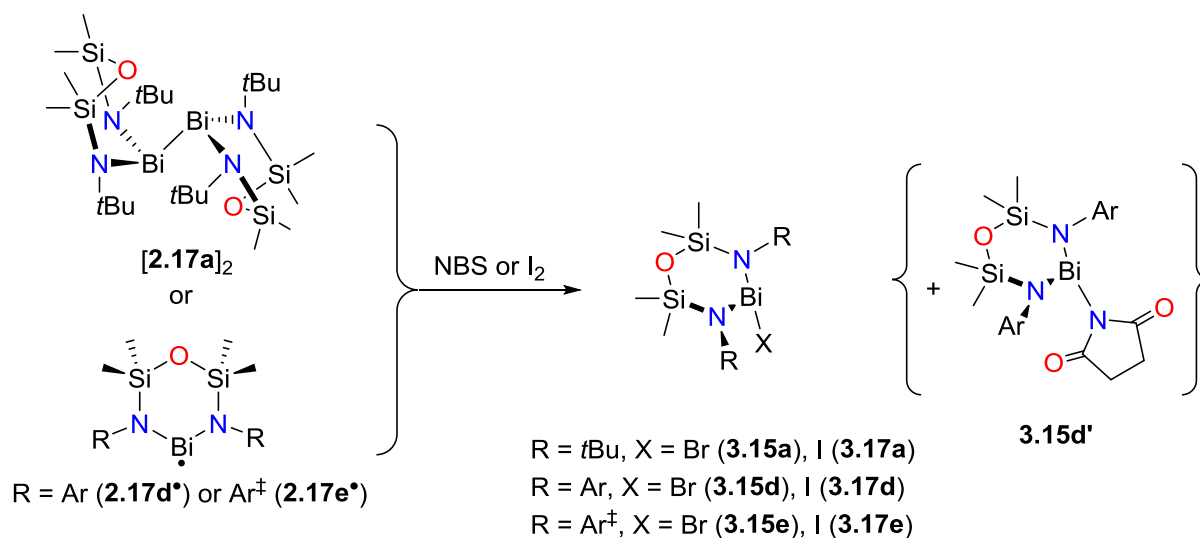
3.2. Chapter Outline

The aim of the work described herein was to explore the reactivity of the bismuth(II) compounds [**2.17a**]₂, **2.17d**• and **2.17e**• synthesised in chapter 2. While [**2.17a**]₂ is a dibismuthane, **2.17d**• and **2.17e**• are bismuth centred radicals. It is anticipated that these species will be highly reactive and provide a platform for unprecedented reactivity. Initial experiments target established reactivity (e.g. halogen containing compounds, chalcogens, TEMPO) to provide insight into whether the nature of the reduced bismuth species influences its reactivity. This is to be followed by investigations into the reactivity of reduced bismuth species with previously unexplored substrates.

3.3. Results and Discussion

3.3.1. Reactivity of Bi(II) Species with Halogen Containing Reagents

The oxidative addition of halogen reagents to the reduced bismuth species was investigated using a halide radical source. *N*-Bromosuccinimide (NBS) is commonly used in organic chemistry as a convenient source of Br[•], while elemental iodine provides I[•] through facile homolysis of the I-I bond. Addition of NBS to [2.17a]₂ and 2.17e[•] proceeds to afford the desired Bi(III) compounds Bi(NON^R)Br (R = *t*Bu (3.15a), Ar[†] (3.15e)) in low to moderate yields (30 – 40 %) as yellow crystalline solids after work-up (Scheme 3.1). In contrast, the corresponding reaction with 2.17d[•] gave colourless co-crystals which were identified as an approximate 1 : 1 mixture of the desired product Bi(NON^{Ar})Br (3.15d) and Bi(NON^{Ar})(N{C(O)CH₂})₂ (3.15d', Figure S3.1) using X-ray crystallography; the latter compound contains the *N*-bound succinimide ligand. However, the poor quality of the X-ray data and significant disorder in the crystal structure prevents any further discussion. In order to allow comparison of the spectroscopic and structural data, an independently synthesized sample of 3.15d was isolated from the reaction of K₂(NON^{Ar})(Et₂O)₂ (3.16d, Figure S3.2) with BiBr₃. The reactions of [2.17a]₂, 2.17d[•] or 2.17e[•] with I₂ proceeds cleanly to afford the corresponding bismuth(III) iodide Bi(NON^R)I (R = *t*Bu (3.17a), Ar (3.17d), Ar[†] (3.17e)) in good yields as orange crystals (70 – 85 %).



Scheme 3.1. Synthesis of bismuth(III) bromides and iodides $\text{Bi}(\text{NON}^{\text{R}})\text{X}$.

The room temperature ^1H NMR spectra of all of the $\text{Bi}(\text{NON}^{\text{R}})\text{X}$ compounds are consistent with a pyramidal bismuth centre chelated by a (NON^{R}) -ligand, demonstrated by the presence of two singlets corresponding to the SiMe_2 protons (δ_{H} : **3.15a**, 0.32 and 0.56; **3.15d**, 0.18 and 0.61; **3.15e**, -0.02 and 0.23; **3.17a**, 0.31 and 0.55; **3.17d**, 0.17 and 0.60; **3.17e**, -0.02 and 0.24). While most of these resonances are sharp, the ^1H NMR spectrum of **3.17e** shows broadened resonances. At elevated temperatures the SiMe_2 resonances of **3.17e** coalesce, forming a sharp singlet at 65 °C (δ_{H} 0.03). This is consistent with formation of an averaged $\text{C}_{2\text{h}}$ symmetric species. The Gibbs free energy (ΔG^\ddagger) for this process was estimated from the coalescence temperature ($T_{\text{c}} = 312 \text{ K}$) and maximum peak separation ($\Delta\nu = 78 \text{ Hz}$) to give a ΔG^\ddagger value of 60.8 kJ mol^{-1} . Analogous behaviour is noted for **3.15e** at elevated temperatures, however, a significantly higher coalescence temperature is observed ($T_{\text{c}} = 331 \text{ K}$), indicative of a higher energy process ($\Delta\nu = 77 \text{ Hz}$, $\Delta G^\ddagger = 67.2 \text{ kJ mol}^{-1}$). This type of behaviour has also been observed in the related bismuth(III) chloride $\text{Bi}\{(\text{NAr})_2\text{SiMe}_2\}\text{Cl}$ and can be explained by a similar set of possible processes involving an averaged $\text{C}_{2\text{h}}$ symmetry (Figure 3.8).^{23c} The energetics of this process appear to correspond to increased steric bulk of the (NON^{R}) -ligand, suggesting that the observed fluxional behaviour is not due to an intermolecular process (e.g. intermolecular halogen exchange, pathway C). In addition, this process is more favourable for the

weaker/longer Bi-I bond compared to the Bi-Br (and Bi-Cl) bond, and may indicate rapid, reversible inversion of the pyramidal bismuth through a planar transition state (e.g. pathway A) or through Bi-X bond cleavage and recombination (pathway B). However, no fluxional processes were observed for bismuth(III) halides involving the smaller (NON^{R})-ligand systems (which have a greater tendency to form elongated Bi-X bonds with intermolecular $\text{Bi}\cdots\text{X}$ interactions, Section 2.3.1). The fluxional behaviour in **3.15e** and **3.17e** may correspond to enhanced stabilisation of a transition state/intermediate by the ($\text{NON}^{\text{Ar}^\ddagger}$)-ligand (e.g. stabilisation of a cation intermediate through $\text{Bi}\cdots\text{aryl}$ interactions).

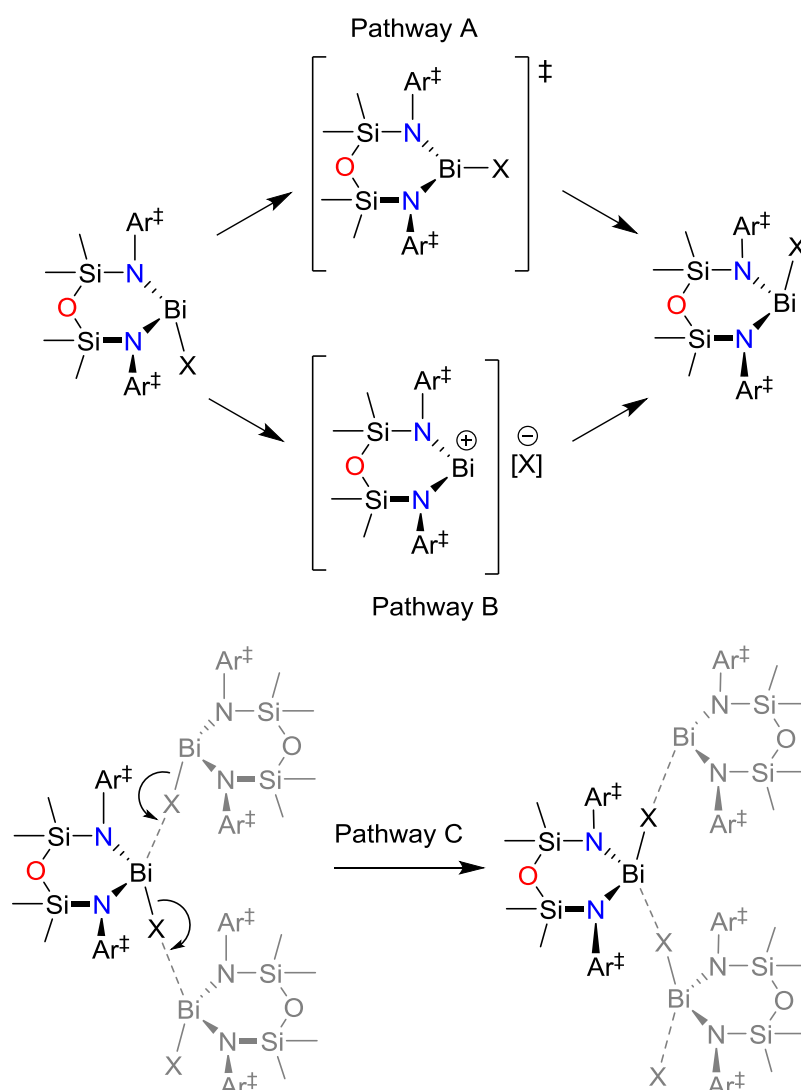


Figure 3.8. Possible solution-state behaviour explaining the observed C_{2h} symmetry of **3.15e** and **3.17e** at high temperatures.

The solid-state structures of the bismuth halide species were determined using single crystal X-ray diffraction (Figure 3.9, Figure 3.10 and Table 3.1), confirming the formation of $\text{Bi}(\text{NON}^{\text{R}})\text{X}$ ($\text{X} = \text{Br}, \text{I}$). **3.15a** and **3.15d** are isomorphous to their chloride analogues **2.16a** and **2.16d'**. In all cases, the (NON^{R}) -ligand chelates a pyramidal bismuth centre ($\Sigma(\angle \text{Bi})$: **3.15a**, 297.8° ; **3.15d**, 295.15° ; **3.15e**, 296.59° ; **3.17a**, 295.18° ; **3.17d**, 296.02° ; **3.17e**, 299.30°), with an associated halide. The Bi-N distances for *t*Bu and Ar substituted species (range $2.129(4) \text{ \AA}$ - $2.158(6) \text{ \AA}$) are generally shorter than those in the corresponding Bi(II) species ($[\text{2.17a}]_2$ range $2.188(3) \text{ \AA}$ to $2.199(3) \text{ \AA}$; **2.17d**• $2.173(4) \text{ \AA}$ and $2.172(4) \text{ \AA}$), while the Bi-N distances in **3.15e** and **3.17e** (range $2.181(5) - 2.204(5) \text{ \AA}$) are similar to those of **2.17e**• ($2.179(5)$, $2.180(5)$ and $2.208(2) \text{ \AA}$). A short $\text{Bi}\cdots\text{aryl}$ ($\text{Bi}\cdots\text{C}_{\text{C71-C76}} 3.328(2) \text{ \AA}$) contact between the bismuth atom and a CHPh_2 substituent is also present in solid-state structure of **3.15e**.

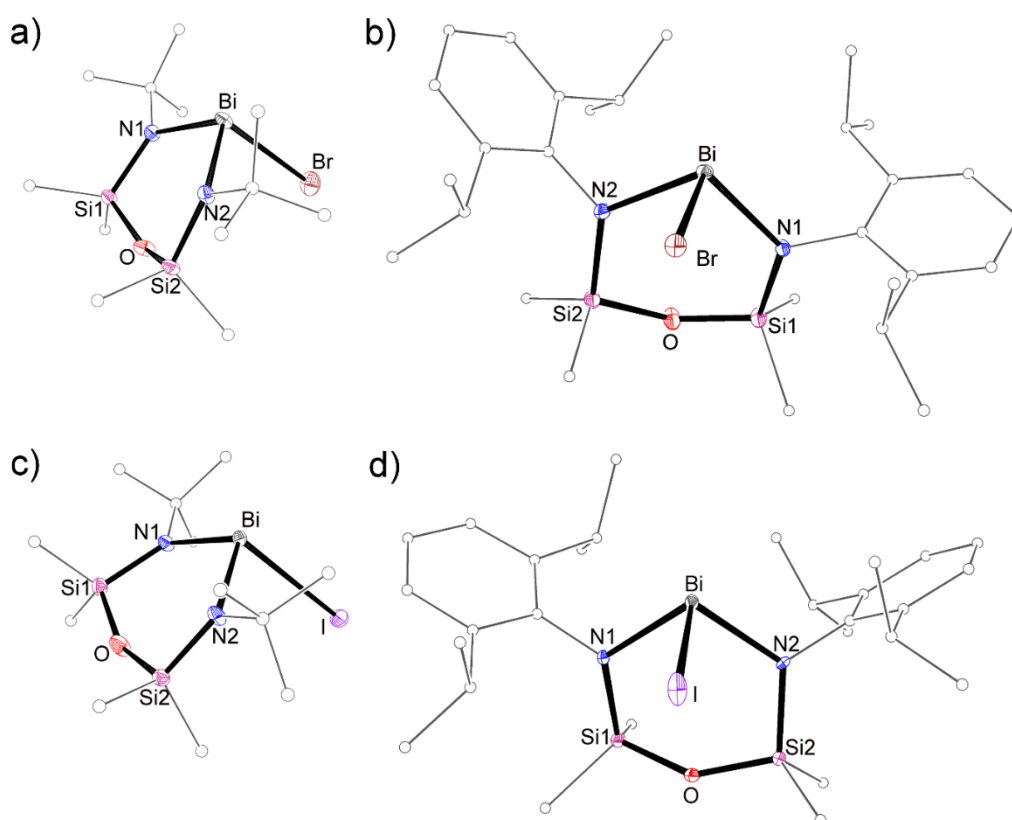


Figure 3.9. Molecular structure of **3.15a** (a), **3.15d** (b), **3.17a** (c) and **3.17d** (d) (thermal ellipsoids displayed at 30% probability level). Hydrogen atoms are omitted, and carbon atoms are displayed in wireframe format for clarity. Selected bond lengths and angles are reported in Table 3.1.

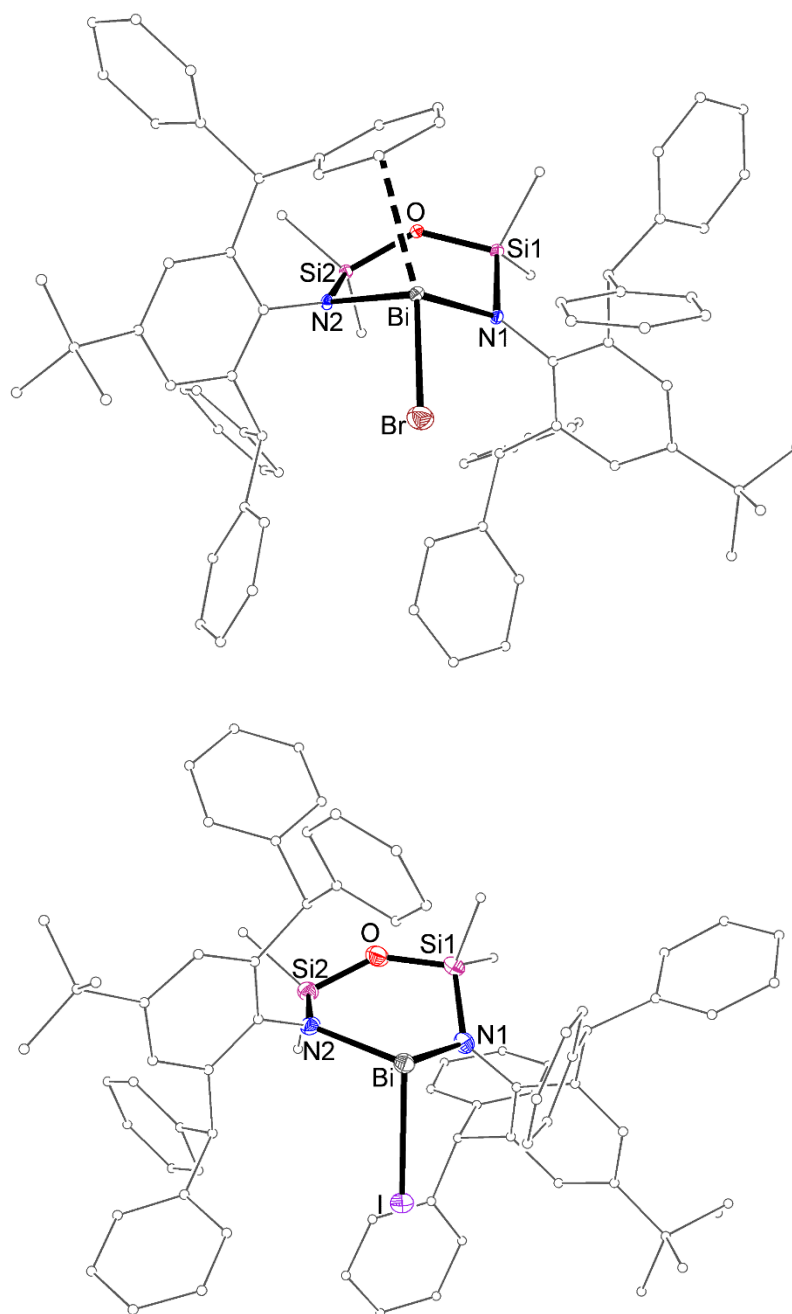


Figure 3.10. Molecular structure of **3.15e** (top) and **3.17e** (bottom) (thermal ellipsoids displayed at 30% probability level). Hydrogen atoms and the minor component of disorder are omitted. Carbon atoms are displayed in wireframe format for clarity. Selected bond lengths and angles are reported in Table 3.1.

Table 3.1. Selected Bond Lengths (Å) and Angles (°) for Bi(NON^R)X (X = Br, I).

3.15a			
Bi-N1	2.129(4)	Bi···Br(2)	3.7798(8)
Bi-N2	2.143(6)	$\Delta_{\text{Bi-X}}(1)$	0.859
Bi-Br	2.7764(8)	$\Delta_{\text{Bi-X}}(2)$	1.004
Bi···O	3.259(4)	N1-Bi-N2	103.98(8)
Bi···Br(1)	3.6348(8)	$\Sigma(\angle \text{Bi})$	297.8
3.17a			
Bi-N1	2.135(4)	Bi···I(2)	3.8805(5)
Bi-N2	2.139(6)	$\Delta_{\text{Bi-X}}(1)$	0.047
Bi-I	3.2464(4)	$\Delta_{\text{Bi-X}}(2)$	0.634
Bi···O	3.453(4)	N1-Bi-N2	104.8(2)
Bi···I(1)	3.2935(4)	$\Sigma(\angle \text{Bi})$	295.18
3.15d			
Bi-N1	2.139(2)	Bi···Br(1)	3.6446(6)
Bi-N2	2.145(2)	$\Delta_{\text{Bi-X}}(1)$	0.964
Bi-Br	2.6806(6)	N1-Bi-N2	100.02(9)
Bi···O	3.499(2)	$\Sigma(\angle \text{Bi})$	295.15°
3.17d			
Bi-N1	2.146(6)	Bi···O	3.304(6)
Bi-N2	2.158(6)	N1-Bi-N2	99.5(2)
Bi-I	2.8782(7)	$\Sigma(\angle \text{Bi})$	296.02°
3.15e			
Bi-N1	2.198(3)	Bi···O	2.978(3)
Bi-N2	2.199(4)	N1-Bi-N2	98.4(1)
Bi-Br	2.5786(6)	$\Sigma(\angle \text{Bi})$	296.59
Bi···Ct _{C71-C76}	3.328(2)		
3.17e			
Bi-N1	2.204(5)	Bi···O	3.453(4)
Bi-N2	2.181(5)	N1-Bi-N2	98.5(2)
Bi-I	2.8412(6)	$\Sigma(\angle \text{Bi})$	299.3

The nature of the Bi-X interaction differs considerably with both halogen and nitrogen substituent. The Bi-X bonds in the Ar and Ar[†] derivatives (Bi-Br, 2.6805(3) (**3.15d**) and 2.5786(6) Å (**3.15e**); Bi-I, 2.8783(7) (**3.17d**) and 2.8412(6) Å (**3.17e**)) are within the broad range found for related structures containing a three-coordinate bismuth centre with a terminal bromide or iodide ligand (Bi-Br, range 2.5895(4) – 2.696(2) Å; Bi-I, range 2.8302(10) – 2.9209(4) Å).^{40, 87} In contrast, the Bi-X bonds in **3.15a** (2.7764(7) Å) and **3.17a** (3.2464(4) Å) are long and are outside of their respective ranges. As noted for the corresponding bismuth chlorides, the degree of intermolecular Bi...X interaction is greater for compounds containing the (NON^{tBu})-ligand. This trend is mirrored for the heavier halogenide analogues, with **3.15a** (3.6348(8) and 3.7798(8) Å) and **3.17a** (3.2935(4) and 3.8805(5) Å) forming a ladder-like arrangement of parallel chains linked through Bi...X interactions with symmetry related molecules (Figure 3.11). However, the Bi-X...Bi vectors of the chains have opposite directionalities resulting in the formation of an inverse-ladder structure in **3.17a**, similar to **2.16b**. In contrast, **3.15d** exists as a dimer in the solid-state, linked through two Bi...X contacts (3.6446(6) Å). Analogous to the bismuth(III) chloride species **2.16a** and **2.16d'**, the Bi...X interactions in **3.15a**, **3.15d** and **3.17a** can be described using $\Delta_{\text{Bi-X}}(1)$ and $\Delta_{\text{Bi-X}}(2)$, the difference between Bi-X and the intra- and inter-chain Bi...X distances, respectively. The $\Delta_{\text{Bi-X}}(1)$ and $\Delta_{\text{Bi-X}}(2)$ values (**3.15a**, 0.859 and 1.004 Å, respectively; **3.17a**, 0.047 and 0.634 Å, respectively; **3.15d**, $\Delta_{\text{Bi-X}}(2) = 0.964$ Å) follow the general trend Cl > Br > I, most pronounced for $\Delta_{\text{Bi-X}}(1)$ in **3.17a** (0.047 Å), with a difference of only +1.4%. Therefore this compound is best described as the contact ion-pair [Bi(NON^{tBu})] [I] (Figure 3.11).

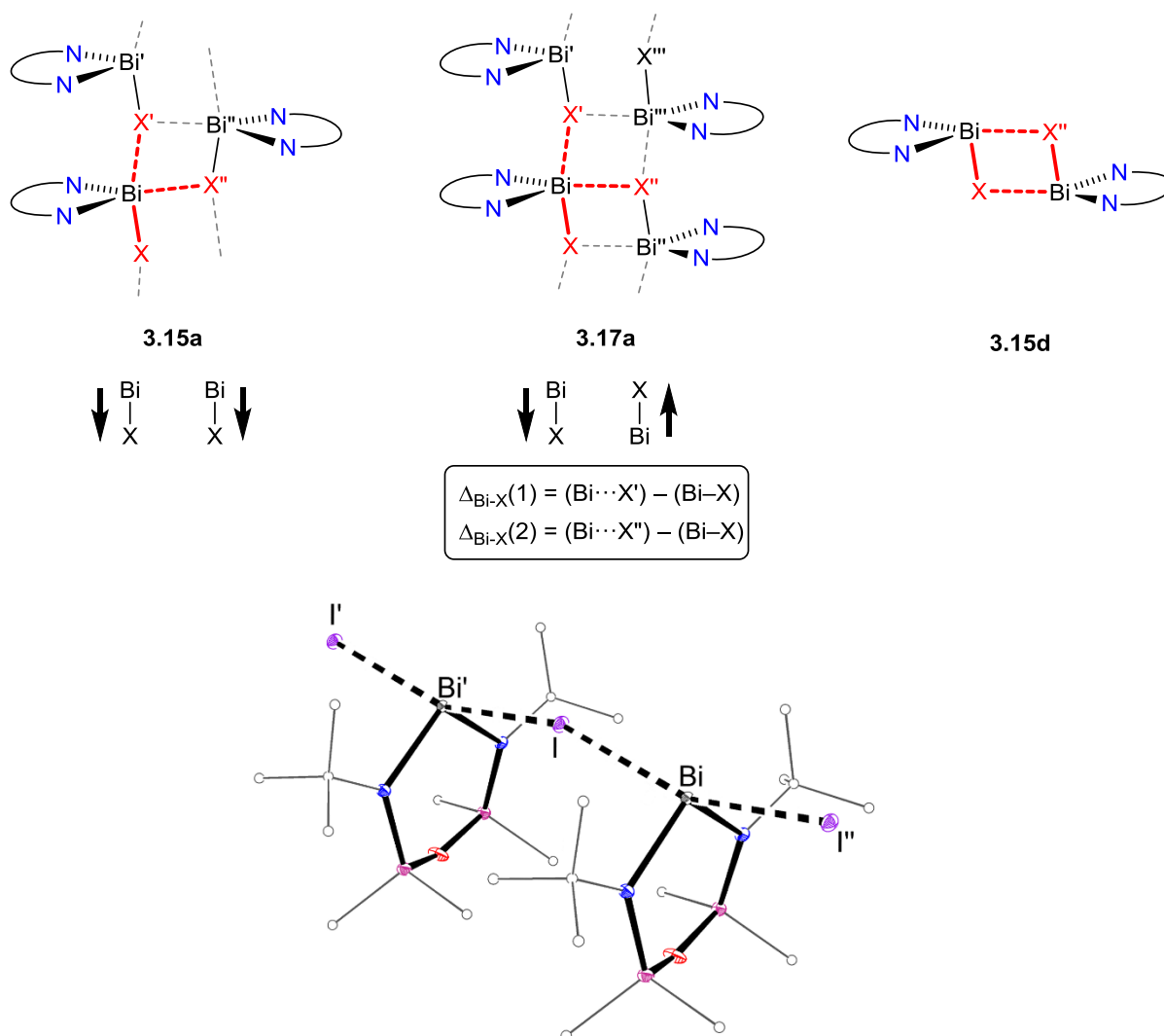


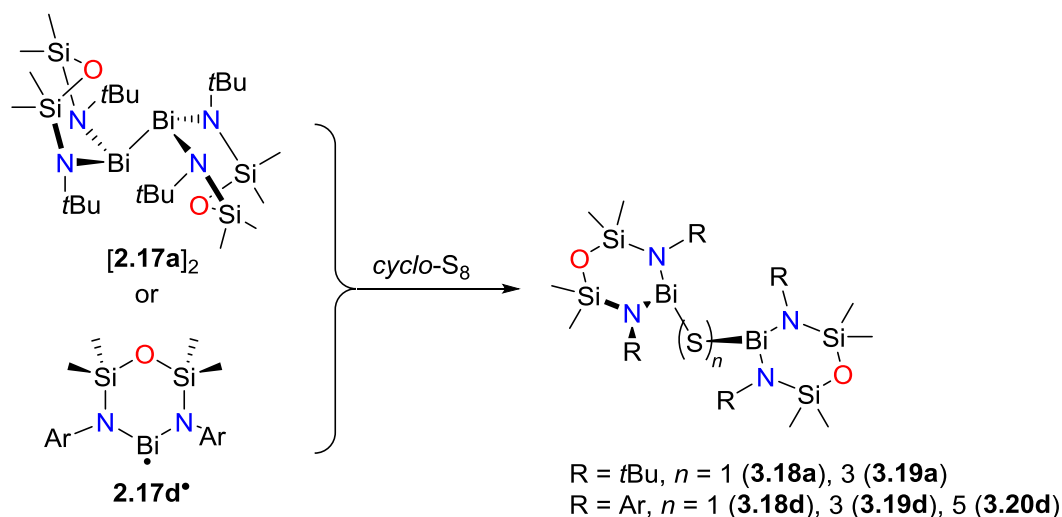
Figure 3.11. Schematic representation of the extended solid-state structures in **3.15a**, **3.17a** and **3.15d** (top) and contact ion-pair structure of **3.17a** (bottom).

3.3.2. Reactivity of Bi(II) Species with Chalcogens

3.3.2.1. Sulfur

The reactions of **[2.17a]₂** and **2.17d•** with S₈ proceed with an immediate colour change from dark orange (**[2.17a]₂**) or deep red (**2.17d•**) to give yellow solutions (Scheme 3.2). In both cases, a mixture of products is reproducibly formed, evident by the presence of several (NON^R)-ligand environments in the normal range for diamagnetic compounds in the ¹H NMR spectra of the crude reaction mixtures. Attempts to isolate pure crystalline products from the mixtures were unsuccessful, instead yielding crystalline mixtures of products of the general

form $[\text{Bi}(\text{NON}^{\text{R}})]_2(\mu\text{-S}_n)$. The monosulfide-bridged compounds $[\text{Bi}(\text{NON}^{\text{R}})]_2(\mu\text{-S})$ (**3.18a**, $\text{R} = t\text{Bu}$; **3.18d**, $\text{R} = \text{Ar}$) are likely the major components of each mixture (determined by analysis of the unit cells of a number of crystals (sample size ~ 20) from the crystal mixture), with the trisulfide $[\text{Bi}(\text{NON}^{\text{R}})]_2(\mu\text{-S}_3)$ (**3.19a**, $\text{R} = t\text{Bu}$; **3.19d**, $\text{R} = \text{Ar}$) present as the secondary component. The pentasulfide $[\text{Bi}(\text{NON}^{\text{Ar}})]_2(\mu\text{-S}_5)$ (**3.20d**) was also confirmed for the Ar-derivative.



Scheme 3.2. Reaction of $[\mathbf{2.17a}]_2$ and $\mathbf{2.17d}^\bullet$ with *cyclo-S*₈.

The solid-state structures of the bridging sulfide species $[\text{Bi}(\text{NON}^{\text{R}})]_2(\mu\text{-S}_n)$ were determined using X-ray diffraction, confirming the presence of bimetallic species linked by $\mu_2\text{-S}_n$ ligands. The structures of **3.18a** and **3.18d** confirm chelation of the (NON^{R}) -ligand to the bismuth atoms, with a bent $\text{Bi}_2(\mu\text{-S})$ core (Figure 3.12). The Bi-S distances (**3.18a**, 2.5619(12) and 2.5267(15) Å; **3.18d**, 2.5349(8) and 2.5281(8) Å) are within the range of literature values seen for other *bis*-(bismuthanyl)sulfanes (range 2.505(3) – 2.601(1) Å).⁸⁸ The Bi-S-Bi angle of **3.18a** (96.27(4)°) is comparable to the corresponding angles observed in compounds of the type $[\text{R}_2\text{Bi}]_2(\mu\text{-S})$ ($\text{R} = \text{CH}(\text{SiMe}_3)_2$, 92.48(4)°; $\text{R} = 2\text{-(CH}_2\text{NMe}_2)\text{C}_6\text{H}_4$, 98.17(3)°; *mes*, 98.73(2)°). In contrast, the corresponding angle in **3.18d** (110.97(3)°) is considerably larger, and is closer to the Bi-S-Bi angles in the *bis*-(di(amido)bismuthanyl)sulphide $[\text{Bi}(1,8\text{-(NSiMe}_3)_2\text{C}_{10}\text{H}_6)]_2(\mu\text{-S})$ (112.89(3)° and 113.46(3)°), which has an intermolecular secondary Bi-S contact. However, no secondary contacts are observed in the solid-state structure of **3.18d**, suggesting the large Bi-

S-Bi angle is due to the increased steric bulk around the bismuth atoms. The Bi-N distances of **3.18a** (Bi1-N: 2.145(3) and 2.158(4) Å; Bi2-N: 2.169(3) and 2.147(4) Å) occupy a narrow range, consistent with symmetric coordination of the (NON^{tBu})-ligand to the bismuth, while the corresponding distances in **3.18d** (Bi1-N: 2.195(3) and 2.164(3) Å; Bi2-N: 2.193(3) and 2.161(3) Å) indicate asymmetric coordination of the (NON^{Ar})-ligand. According to Breunig's conformation classification,^{88b} these compounds can be described as *syn-syn* (**3.18a**) and near *syn-syn* (**3.18d**) based on the relative assumed positions of the bismuth lone pairs (lp) if they are considered stereochemically active (Table 3.2), similar to the near *syn-syn* arrangements observed for [BiR₂]₂(μ-E) (R = mesityl, E = S, Se; R = CH(SiMe₃)₂, E = S, Te).

The solid-state structures of [Bi(NON^R)]₂(μ-S₃) (R = *t*Bu (**3.19a**) and Ar (**3.19b**)) confirm the presence of a [S₃]²⁻ ligand linking two bismuth centres. While **3.19a** crystallises cleanly (Figure 3.13a), **3.19d** co-crystallised with one molecule of the contaminant Bi(NON^{Ar})Cl (**2.16d**)[†] in the unit cell (Figure S3.3). The presence of both **3.19d** and **2.16d** in the crystal structure is unambiguous. However, due to the poor quality of the data, bond lengths and angles of these species cannot be discussed in detail. **3.19a** crystallises in the *I*2/a space group, with the asymmetric unit comprised of half of a molecule of [Bi(NON^{tBu})]₂(μ-S₃), which sits on a special position (2-fold rotation axis). Growing the asymmetric unit reveals a core unit containing two (NON^{tBu})-chelated bismuth centres linked by a (μ₂-S₃)-ligand. The Bi-S distance (2.592(2) Å) is standard for a single bond, with a Bi-S-S angle of 92.0(1)°. The S-S distance (2.062(3) Å) and S-S-S angle (107.0(2)°) are consistent with sulfur-sulfur single bonds.⁸⁹

[†] Present as an impurity (<5%) in the **2.17d** starting material

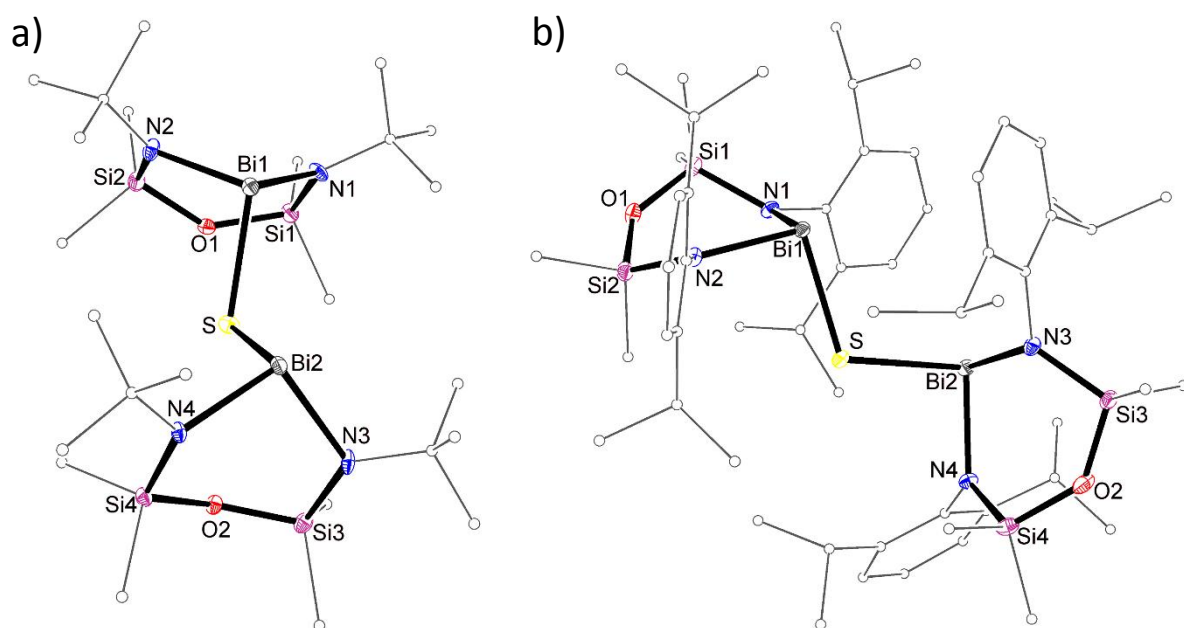


Figure 3.12. Molecular structure of **3.18a** (a) and **3.18d** (b) (thermal ellipsoids displayed at 30% probability level). Hydrogen atoms are omitted. Carbon atoms are displayed in wireframe format for clarity. Selected bond lengths (Å) and angles (°): **3.18a**, Bi1-S 2.562(1), Bi2-S 2.527(1), Bi1-N1 2.145(3), Bi1-N2 2.159(4), Bi2-N3 2.170(4), Bi2-N4 2.147(4), Bi1...O1 3.137(3), Bi2...O2 3.135(3); Bi1-S-Bi2 96.27(4), N1-Bi1-N2 97.1(1), N3-Bi2-N4 96.7(1), $\Sigma(\angle \text{Bi1})$ 295.5, $\Sigma(\angle \text{Bi2})$ 294.9. **3.18d**, Bi1-S 2.5349(8), Bi2-S 2.5281(9), Bi1-N1 2.195(3), Bi1-N2 2.164(3), Bi2-N3 2.193(3), Bi2-N4 2.161(3), Bi1...O1 3.649(3), Bi2...O2 3.568(3); Bi1-S-Bi2 96.27(4), N1-Bi1-N2 97.1(1), N3-Bi2-N4 96.7(1), $\Sigma(\angle \text{Bi1})$ 290.01, $\Sigma(\angle \text{Bi2})$ 290.43.

Table 3.2. Torsion angles and Breunig's conformation classification for Bi-E-Bi (E = S, Se, Te).

Entry	Compound	ϕ Bi-E-Bi-lp ^a		Conformation
		ϕ_1 (°)	ϕ_2 (°)	
1	3.18a	7.8	4.4	<i>syn-syn</i>
2	3.18d	52.1	47.21	near <i>syn-syn</i>
3	3.22a	7.8	4.4	<i>syn-syn</i>
4	3.22d	51.4	46.2	near <i>syn-syn</i>
5	3.23a	7.8	4.3	<i>syn-syn</i>
6	3.23d	40.1	38.7	near <i>syn-syn</i>

^alp = assumed position of the bismuth lone pairs if they are considered stereochemically active

The crystal structure of $[\text{Bi}(\text{NON}^{\text{Ar}})]_2(\mu\text{-S}_5)$ (**3.20d**) confirms formation of a bis(bismuthanyl)pentasulfide species (Figure 3.13b). However, significant disorder in many of the atoms, including three sulfur atoms in the S_5 -chain (two components with approximate occupancies of 0.7:0.3), limits the accuracy of the bond lengths and angles within the S_5 -chain. Therefore, discussion of the bond lengths and angles will be limited to the major component. The bismuth atoms are chelated by (NON^{Ar}) -ligands with standard Bi-N distances (range 2.155(5) – 2.225(5) Å). The Bi-S bond distances (2.575(2) and 2.540(2) Å) are similar to those observed in the previously discussed bismuth sulfide species, while the S-S bond distances (range 1.967(5) – 2.055(6) Å) and S-S-S angles (range 106.7(2)° – 109.0(2)°) are consistent with typical polysulfide bonding interactions. Structurally characterised metal compounds containing μ_2 -bridging pentasulfide ligands are rare but have been reported at antimony and bismuth in the *N,C,N*-pincer stabilised compound $[\text{M}(2,6\text{-(CH}_2\text{NEt}_2)_2\text{C}_6\text{H}_3)]_2(\mu\text{-S}_5)_2$ (M = Sb, Bi).⁹⁰

In contrast to the reactions between $[\mathbf{2.17a}]_2/\mathbf{2.17d}^\bullet$ and S_8 , which remain homogeneous in Et_2O , the reaction of $\mathbf{2.17e}^\bullet$ with S_8 under the same conditions results in the formation of a pale-yellow precipitate. Extraction with hot toluene followed by slow-cooling to room temperature gave yellow crystals of $[\text{Bi}(\text{NON}^{\text{Ar}\ddagger})\text{S}_4]_2$ ($[\mathbf{3.21e}]_2$, Scheme 3.3). The ^1H NMR spectrum confirms that the product is diamagnetic over the temperature range 293 – 333 K, with two SiMe_2 resonances (δ_{H} -0.09 and 0.21) consistent with chelation of the $(\text{NON}^{\text{Ar}\ddagger})$ -ligand to a pyramidal bismuth centre. Elemental analysis is consistent with a ' $\text{Bi}(\text{NON}^{\text{Ar}\ddagger})$ ' unit, plus four sulfur atoms suggesting that the structure may be an extension of those observed in **3.18**-**3.20**, with a bridging ($\mu_2\text{-S}_8$)-ligand. Although rare, this ligand has been structurally characterised for Cu and Ag compounds.⁹¹

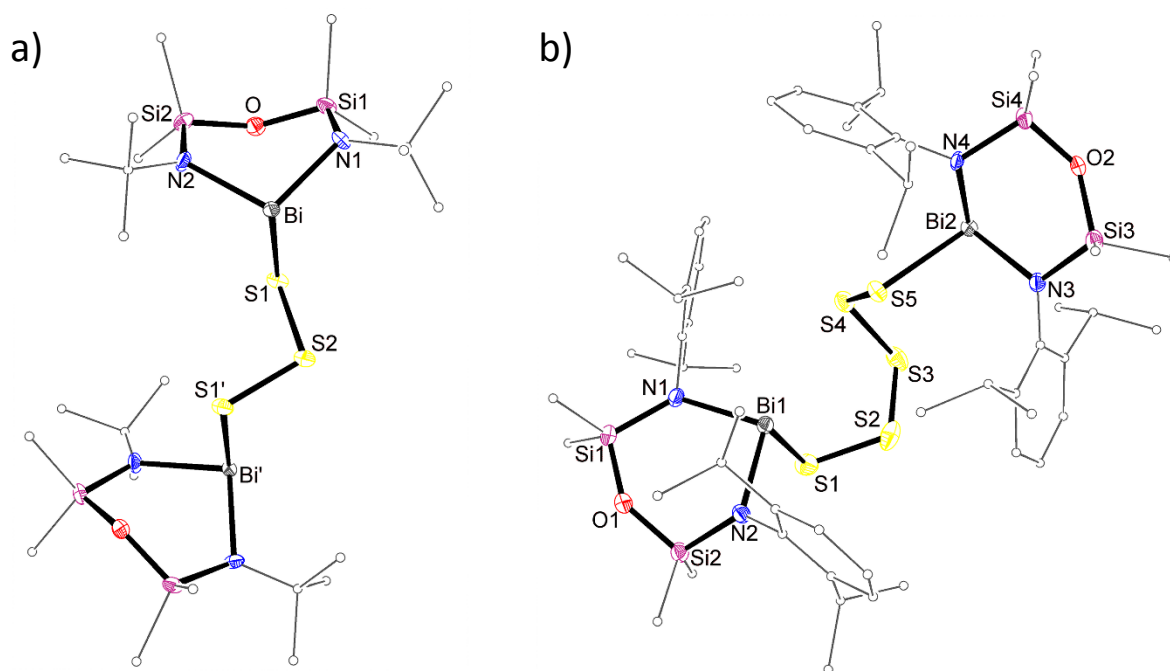
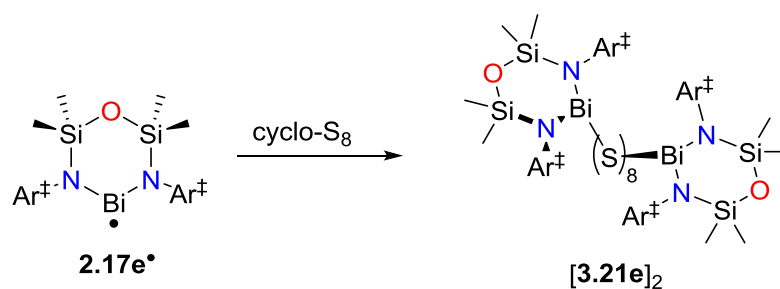


Figure 3.13. Molecular structure of **3.19a** (a) and **3.20d** (b) (thermal ellipsoids displayed at 30% probability level, symmetry equivalent in **3.19a** (') = 1.5-x, y, 1-z). Hydrogen atoms and the minor component of disorder in **3.20d** are omitted. Carbon atoms are displayed in wireframe format for clarity. Selected bond lengths (Å) and angles (°): **3.19a**, Bi-S1 2.592(2), S1-S2 2.062(1), Bi-N1 2.147(6), Bi-N2 2.157(6), Bi...O 3.126(5); Bi-S1-S2 92.0(2), N1-Bi-N2 101.6(2), S1-S2-S21' 107.0(2), $\Sigma(\angle \text{Bi})$ 297.8. **3.20d**, Bi1-S1 2.575(2), Bi2-S5 2.540(2), S1-S2 2.036(3), S2-S3 1.967(5), S3-S4 2.055(6), S4-S5 2.048(4), Bi1-N1 2.174(6), Bi1-N2 2.155(5), Bi2-N3 2.190(5), Bi2-N4 2.23(1), Bi1...O1 3.546(5), Bi2...O2 3.053(8); Bi1-S1-S2 95.1(1), Bi2-S5-S4 99.3(1), S1-S2-S3 109.0(2), S2-S3-S4 106.7(2), S3-S4-S5 108.5(2), N1-Bi1-N2 98.4(2), N3-Bi2-N4 93.2(4), $\Sigma(\angle \text{Bi1})$ 294.5, $\Sigma(\angle \text{Bi2})$ 284.1.



Scheme 3.3. Synthesis of **[3.21e]₂**.

X-ray diffraction was used to determine the solid-state structure, revealing two ‘Bi(NON^{Ar†})(S₄)’ units related by an inversion centre to form a dimer **[3.21e]₂** (Figure 3.14). The two terminal sulfur atoms of the S₄-chain are disordered over two positions and were freely refined with 51.7:48.3 site occupancy. Despite the disorder, the S–S bond lengths (range 2.021(3) Å – 2.113(3) Å) and angles at sulfur (range 105.1(2)° – 108.2(1)°) are within the range expected for such units. However, the contacts between the symmetry related fragments are inconsistent with a continuous S₈-chain comprising regular S–S bonds. For example, the distances between the symmetry-related sulfur atoms (2.758(4) Å – 3.213(4) Å) are considerably longer than those within the S₄-chain, although they are within the sum of the van der Waals radii (3.60 Å).³¹ The angle between terminal sulfur atoms would also be unreasonable for 2-centre-2-electron (2c2e) S–S bonds, (S3–S4⋯S4' = 64.1(1)°, S3a–S4a⋯S4a' = 65.4(1)°) and is therefore more accurately described as a side-on interaction between four co-planar sulfur atoms. Such intermolecular associations are ubiquitous in the solid-state structures of 1,2,3,5-dithiadiazolyl (DTDA) radical dimers (R-CNSSN•, Figure 3.15), and we postulated that **[3.21e]₂** exists as a dimeric unit linked by pancake bonds.⁹²

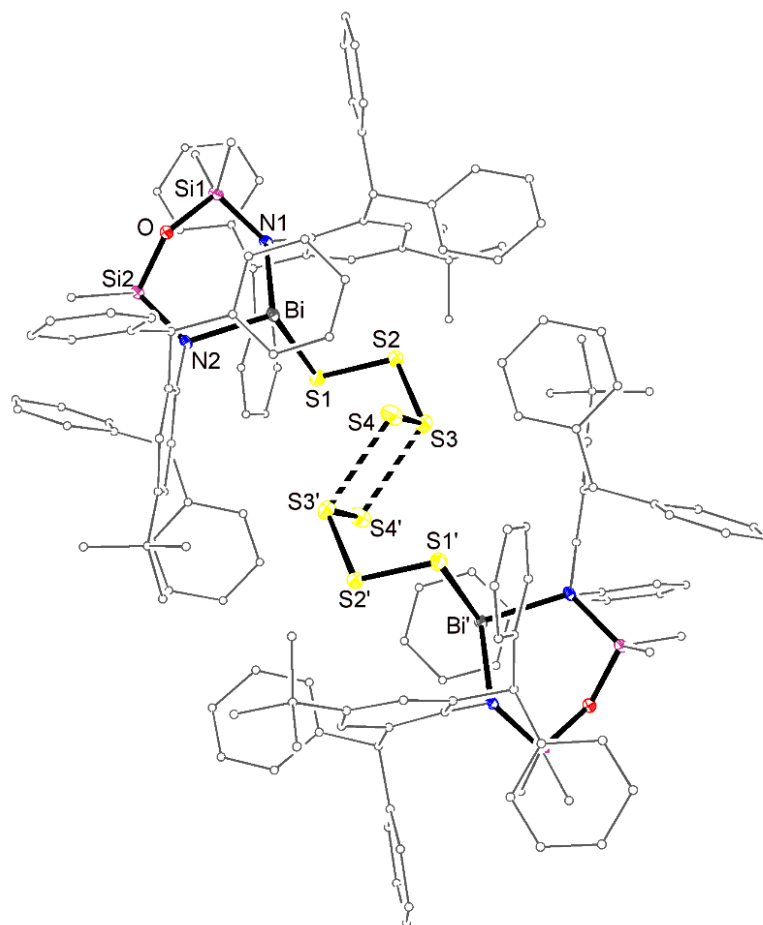


Figure 3.14. Molecular structure of **[3.21e]₂** (thermal ellipsoids displayed at 30% probability level, symmetry equivalent (') = 1-x, 1-y, 1-z). Hydrogen atoms are omitted. Carbon atoms are displayed in wireframe format for clarity. Selected bond lengths (Å) and angles (°): Bi-S1 2.599(1), S1-S2 2.044(2), S2-S3 2.021(3), S3-S4 2.040(4), S2-S3a 2.113(3), S3a-S4a 2.033(4), S3-S4' 2.758(4), S3a-S4a' 3.004(4), Bi-N1 2.217(4), Bi1-N2 2.202(4), Bi...O 3.246(3); Bi1-S1-S2 94.12(6), S1-S2-S3 105.5(1), S2-S3-S4 105.1(2), S2-S3a-S4a 108.2 Bi2-S5-S4 99.3(1), S1-S2-S3 109.0(2), S2-S3-S4 106.7(2), S3-S4-S5 108.5(2), S3-S4-S4' 64.1, S3a-S4a-S4a' 65.4(1), N1-Bi1-N2 98.9(1), $\Sigma(\angle \text{Bi1})$ 296.8.

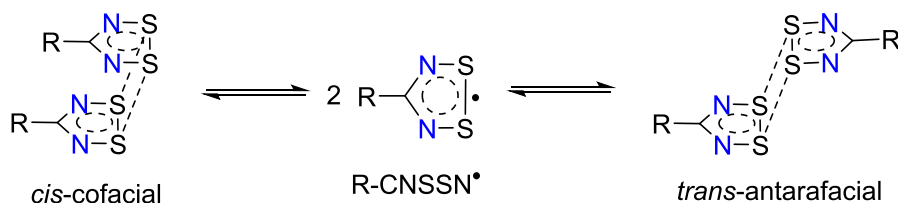


Figure 3.15. Structure of DTDA and two possible dimerization pathways.

Density Functional Theory (DFT, performed by M. Lein, Victoria University of Wellington) was used to analyse the bonding between the S_4 -chains in $[\mathbf{3.21e}]_2$. Comparing the S-S bond lengths determined in the crystal structures to the calculated values for $[\mathbf{3.21e}]_2$ and the monomeric radical, $\text{Bi}(\text{NON}^{\text{Ar}\ddagger})\text{S}_4^\bullet$ ($\mathbf{3.21e}^\bullet$), significant differences can be seen, consistent with electronic reorganisation as the two S_4 -chains interact with each other. The most notable difference is a shortened S3-S4 distance in $\mathbf{3.21e}^\bullet$ (average of two conformations = 1.94 Å) compared to the observed value for $[\mathbf{3.21e}]_2$ (2.037 Å), indicating significant multiple bond character (Wiberg Bond Index = 1.544). The spin density on $\mathbf{3.21e}^\bullet$ was calculated to be located on the three terminal sulfur atoms in the S_4 -chain, with a SOMO consistent with $\mathbf{3.21e}^\bullet$ being described as a π^* radical.

When the two $\mathbf{3.21e}^\bullet$ units dimerise, the two π^* (SOMO) orbitals overlap to form a bonding MO (HOMO-18) with a closed shell singlet configuration (Figure 3.16), consistent with the observed diamagnetic behaviour in solution. The HOMO-18 of $[\mathbf{3.21e}]_2$ is 21.41 kcalmol⁻¹ lower in energy than the SOMO of $\mathbf{3.21e}^\bullet$, promoting retention of the dimer $[\mathbf{3.21e}]_2$ in solution. The LUMO of $[\mathbf{3.21e}]_2$ corresponds to the antibonding combination of π^* (SOMO) fragments similar to the MO's in DTDA's. However, the bond dissociation enthalpy for $[\mathbf{3.21e}]_2$ (47.2 kcalmol⁻¹) is significantly larger than typical values for DTDA's, illustrated by the *cis*-cofacial Ph-CNSSN $^\bullet$ dimer (8.4 kcalmol⁻¹).⁹³

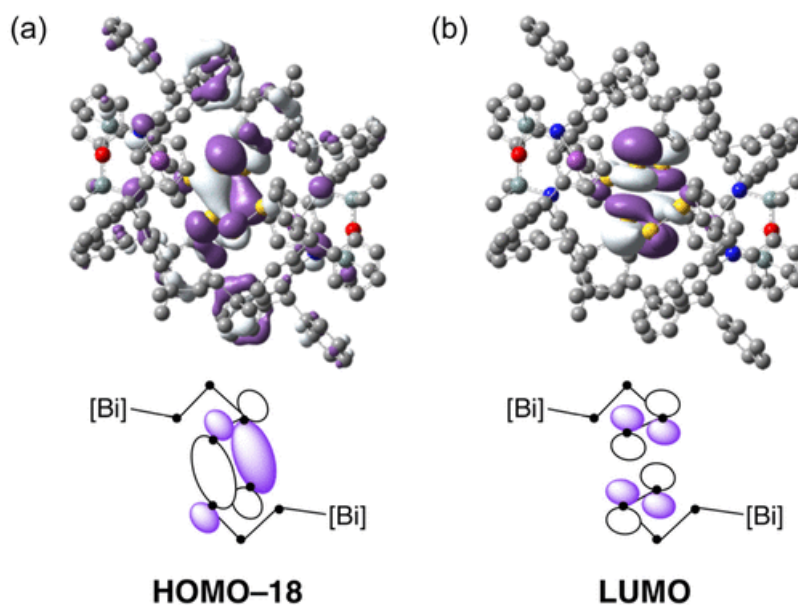


Figure 3.16. Molecular orbital diagrams of $[3.21e]_2$ showing (a) $\pi^*(SOMO)-\pi^*(SOMO)$ bonding interaction (HOMO-18) and (b) antibonding combination (LUMO).

These results are consistent with a stable *trans*-antarafacially bonded dimer $[3.21e]_2$, which can be considered as the first structurally characterised metal complex of an S_4 radical anion. Similar bonding interactions have been observed in transition metal sulfide compounds containing the $[S_2]^- \bullet$ ligand. For example, the supersulfidonickel(II) dimer $[Ni(BDI^{Ar})(S_2)]_2$ (Figure 3.17) features a rectangular S_4 ring with two short S-S bonds ($1.944(2) \text{ \AA}$) and two long S-S bonds ($2.777(2) \text{ \AA}$), with computational analysis revealing that this bonding motif is caused by the dimerization of two $Ni(BDI^{Ar})(S_2) \bullet$ sulfur-centred radical monomers.⁹⁴

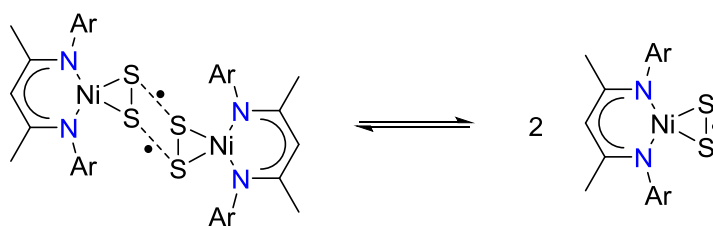
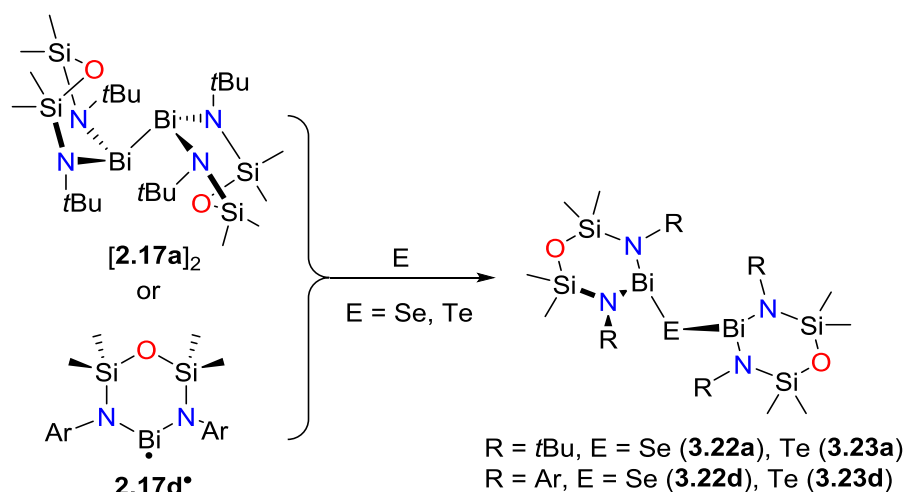


Figure 3.17. Dimerisation of a supersulfidonickel(II) compound.

3.3.2.2. Selenium and Tellurium

The reactions of $[2.17a]_2$ and $2.17d^\bullet$ with excess Se and Te in THF proceed slowly to give the corresponding bis(diamidobismuthanyl)chalcogenanes $[Bi(NON^R)]_2(\mu-E)$ (**3.22a**, R = *t*Bu, E = Se; **3.22d**, R = Ar, E = Se; **3.23a**, R = *t*Bu, E = Te; **3.23d**, R = Ar, E = Te) as analytically pure crystalline materials after work-up (Scheme 3.4). In contrast, no reaction was observed between $2.17e^\bullet$ and Se or Te under the same conditions. The 1H NMR spectra of **3.22a**, **3.22d**, **3.23a** and **3.23d** are all consistent with diamagnetic species which retain the chelating (NON^R) -ligand at a pyramidal metal centre, indicated by the presence of two $SiMe_2$ resonances of equal integration (δ_H **3.22a**, 0.40 and 0.61; **3.22d**, 0.26 and 0.54; **3.23a**, 0.33 and 0.58; **3.23d**, 0.22 and 0.57).



Scheme 3.4. Reaction of $[2.17a]_2$ and $2.17d^\bullet$ with selenium and tellurium.

The solid-state structures of the bis(diamidobismuthanyl)chalcogenanes **3.22a**, **3.22d**, **3.23a** and **3.23d** were determined using X-ray diffraction, confirming two ' $Bi(NON^R)$ ' units linked by a monochalcogenide bridge to give a $Bi_2(\mu_2-E)$ core (Figure 3.18 and Table 3.3). **3.22a** and **3.23a** are isomorphous with their sulfide analogue **3.18a** and the only major differences are in the bond lengths and angles associated with the $Bi-(\mu-E)-Bi$ unit. The crystal structure of **3.22d** has significant disorder, with the bridging selenide and Bi_2 atoms modelled over two positions and freely refined with relative site occupancies of 0.94 : 0.06. Due to the unreliable bond lengths and angles given by the minor component, only data corresponding to the major component

will be discussed. As expected, the Bi-E bond distances (E = Se: **3.22a**, 2.6799(4) and 2.6454(6) Å; **3.22d**, 2.6282(6) and 2.6376(5) Å; E = Te: **3.23a**, 2.877(3) and 2.8507(5) Å; **3.23d**, 2.888(1) and 2.904(1) Å) are significantly longer than the sulfide analogue, increasing with the size of the central chalcogen atom. The Bi-E bond distances align well with the sum of covalent radii (Bi-Se: 2.67 Å, Bi-Te: 2.86 Å) and are comparable to those seen in [Bi(mes)₂]₂(μ-Se) (2.651(1) Å) and [Bi(CH(SiMe₃)₂)₂]₂(μ-Te) (range 2.855(1) – 2.889(1) Å).^{88b, 95} In contrast to the series of compounds [BiEt₂]₂(μ-E) (E = S, Se, Te), no intermolecular Bi...E interactions were observed in the solid-state.⁷⁷ Analogous to the monosulfide insertion products **3.18a** and **3.18d**, the relative arrangement of the 'Bi(NON^R)' units vary from *syn-syn* (**3.22a** and **3.23a**) to near *syn-syn* (**3.22d** and **3.23d**) depending on the nitrogen substituent (Table 3.2, entries 3 – 6).

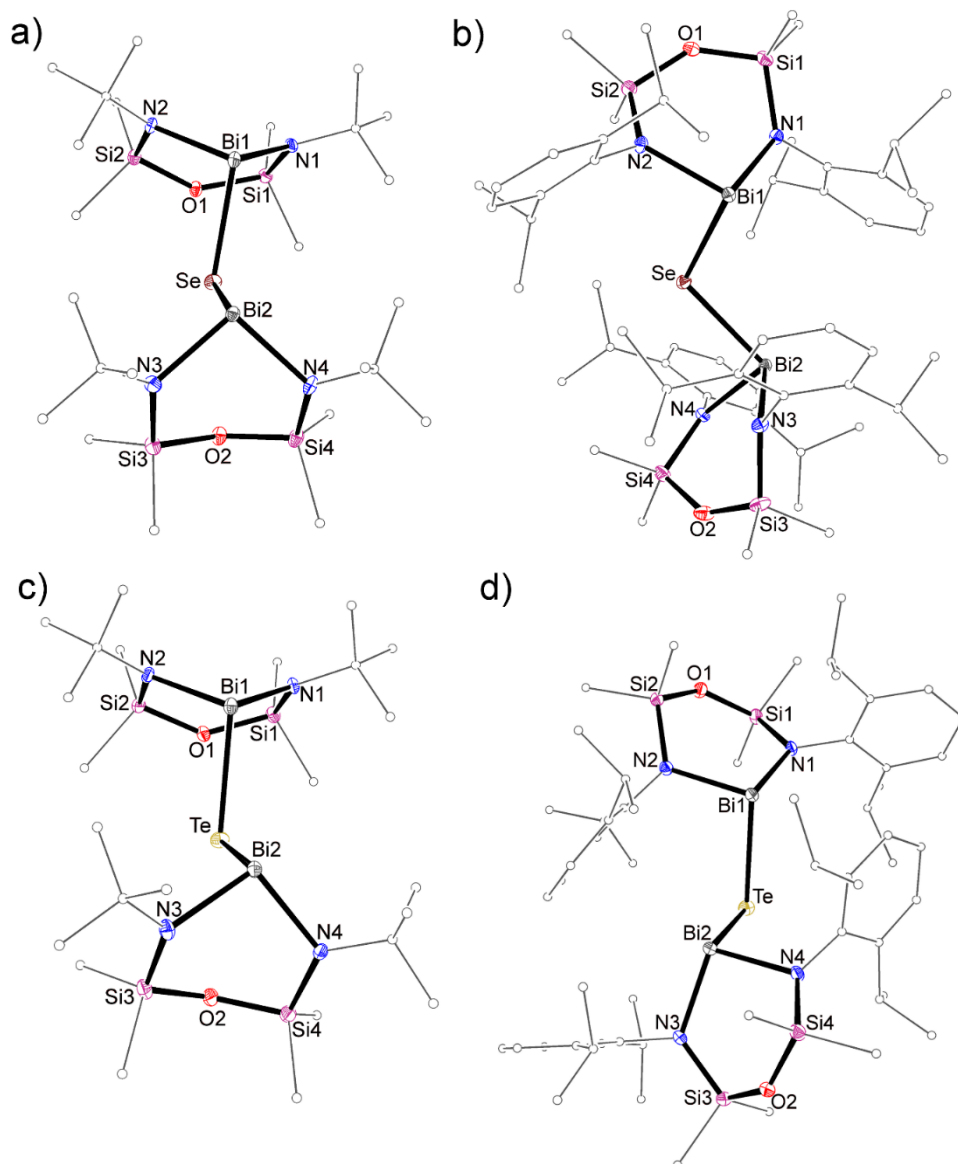


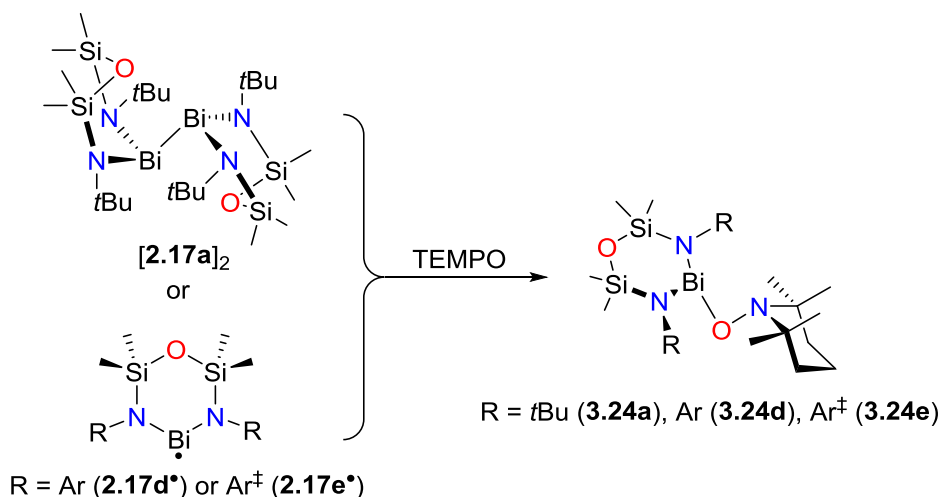
Figure 3.18. Molecular structure of **3.22a** (a), **3.22d** (b), **3.23a** (c) and **3.23d** (d) (thermal ellipsoids displayed at 30% probability level). Hydrogen atoms and minor component of disorder in **3.22d** are omitted. Carbon atoms are displayed in wireframe format for clarity. Selected bond lengths and angles are reported in Table 3.3.

Table 3.3. Selected Bond Lengths (Å) and Angles (°) for [Bi(NON^R)]₂(μ-E) (E = Se, Te).

3.22a			
Bi1-Se	2.6799(4)	Bi2-N4	2.175(3)
Bi2-Se	2.6454(6)	Bi1-Se-Bi2	93.92(1)
Bi1-N1	2.161(3)	N1-Bi1-N2	96.4(1)
Bi1-N2	2.149(3)	N3-Bi2-N4	96.8(1)
Bi2-N3	2.159(3)		
3.22d			
Bi1-Se	2.6282(6)	Bi2-N4	2.169(3)
Bi2-Se	2.6376(5)	Bi1-Se-Bi2	109.63(1)
Bi1-N1	2.194(3)	N1-Bi1-N2	95.4(1)
Bi1-N2	2.171(3)	N3-Bi2-N4	95.8(1)
Bi2-N3	2.200(2)		
3.23a			
Bi1-Te	2.8777(3)	Bi2-N4	2.157(2)
Bi2-Te	2.8507(5)	Bi1-Se-Bi2	90.01(1)
Bi1-N1	2.159(2)	N1-Bi1-N2	96.46(9)
Bi1-N2	2.159(3)	N3-Bi2-N4	96.7(1)
Bi2-N3	2.172(3)		
3.23d			
Bi1-Te	2.888(1)	Bi2-N4	2.212(3)
Bi2-Te	2.904(1)	Bi1-Se-Bi2	88.62(2)
Bi1-N1	2.183(3)	N1-Bi1-N2	94.9(1)
Bi1-N2	2.207(3)	N3-Bi2-N4	95.3(1)
Bi2-N3	2.191(3)		

3.3.3. Reactivity of Bi(II) Species with TEMPO

The reactions of $[2.17a]_2$, $2.17d^\bullet$ or $2.17e^\bullet$ with TEMPO proceed with an immediate colour change from dark orange or deep red to pale yellow ($[2.17a]_2$) or orange ($2.17d^\bullet$ and $2.17e^\bullet$), respectively, giving the corresponding bismuth tempoxide $Bi(NON^R)(OTEMP)$ ($R = tBu$ (**3.24a**), Ar (**3.24d**), Ar^\ddagger (**3.24e**)) as pale yellow or orange crystals after work-up (Scheme 3.5).



Scheme 3.5. Synthesis of $Bi(NON^R)(OTEMP)$.

X-ray diffraction confirmed the identity of **3.24a**, **3.24d** and **3.24e** as monomeric $Bi(NON^R)(OTEMP)$ compounds (Figure 3.19). In all cases, the (NON^R) -ligand chelates the bismuth centre to give a 6-membered metallacycle which approximates to boat (**3.24a** and **3.24e**) or half-chair (**3.24d**) conformations. The Bi-N distances (**3.24a**, 2.163(3); **3.24d**, 2.190(4) and 2.192(4) Å; **3.24e**, 2.252(2) and 2.205(2) Å) are heavily dependent on the R-substituent, with significantly longer Bi-N bonds observed for the Ar^\ddagger derivative compared to the smaller tBu and Ar derivatives. As expected for oxidation of a bismuth centre, the Bi-N distance in **3.24a** is considerably shorter than those in $[2.17a]_2$ (range 2.188(3) – 2.199(3) Å). In contrast, the Bi-N distances of **3.24d** and **3.24e** are longer than their Bi(II) precursors ($2.17d^\bullet$, 2.173(3) and 2.172(5) Å; $2.17e^\bullet$, 2.179(5), 2.180(5) and 2.208(2) Å), and may reflect the increasingly encumbered bismuth centre.

An anionic TEMPOxide ligand completes the coordination sphere of the bismuth to give a three-coordinate metal. The degrees of pyramidalisation of the bismuth centres reveals a trend towards planarity with increasing bulk of the nitrogen substituent ($\Sigma(\angle\text{Bi})$: **3.24a**, 287.7°; **3.24d**, 299.4°; **3.24e**, 304.1°). The Bi-O distances of the TEMPOxide ligand (**3.24a**, 2.111(3) Å; **3.24d**, 2.129(3) Å; **3.24e**, 2.164(2) Å) are comparable to that reported for the bismuth(III) TEMPOxide **3.8** (2.146(5) Å), increasing as the bismuth centre becomes more sterically encumbered. The pyramidalization of the TEMPO nitrogen atom ($\Sigma(\angle\text{N})$: **3.24a**, 331.8°; **3.24d**, 333.5°; **3.24e**, 334.8°) indicates single-electron reduction of the TEMPO radical to the [TEMPO]⁻ anion.⁸¹ The TEMPOxide Bi-O-N angles (**3.24a**, 105.6(2)°; **3.24d**, 100.3(3)°; **3.24e**, 104.5(2)°) are larger than those typically found in $\kappa^2\text{O},\text{N}$ -bound nitroxyl ligands (range 67.2° – 89.4°), confirming monodentate coordination of TEMPO through the oxygen atom.⁸¹

The ¹H NMR spectra of **3.24a**, **3.24d** and **3.24e** are strikingly different. The ¹H NMR spectrum of **3.24a** in C₆D₆ shows two sharp singlets for the SiMe₂ protons (δ_{H} 0.43 and 0.55), consistent with coordination of the (NON^tBu)-ligand to a pyramidal bismuth centre. A broad singlet at δ_{H} 1.32 corresponding to CMe₂ protons suggests rapid ring flipping of the C₅N ring of the TEMPOxide in the solution-state. In contrast, the ¹H NMR spectra for **3.24d** and **3.24e** in C₇D₈ each show a single broad or sharp SiMe₂ resonance (δ_{H} 0.41 (very broad) and 0.08 (sharp), respectively) at room temperature. No paramagnetic shifting of peaks was observed, suggesting the presence of a fluxional diamagnetic species. Variable temperature (VT) ¹H NMR spectroscopy was used to investigate the solution-state behaviour of **3.24d** (Figure S3.4a). Cooling the NMR sample (in C₇D₈) to 263 K splits the SiMe₂ resonance into two sharp singlets (δ_{H} 0.34 and 0.55), analogous to the room temperature ¹H NMR spectrum of **3.24a**. At higher temperatures, a single sharp resonance is observed (313 K, δ_{H} 0.41), similar to that observed in the ¹H NMR spectrum of **3.24e** and consistent with an energetically accessible fluxional process ($\Delta G^\ddagger = 60.8 \text{ kJmol}^{-1}$) which may be dependent on the bulk of the nitrogen substituent. These data are indicative of an averaged C_{2h} symmetric species at higher temperatures, analogous to that observed for Bi(NON^{Ar})X (X = Br (**3.15e**), I (**3.17e**)) and can be explained by

a number of possible pathways (Figure S3.4b), including rapid cleavage and recombination of the Bi-O bond or energetically accessible pyramidal inversion at the bismuth centre.

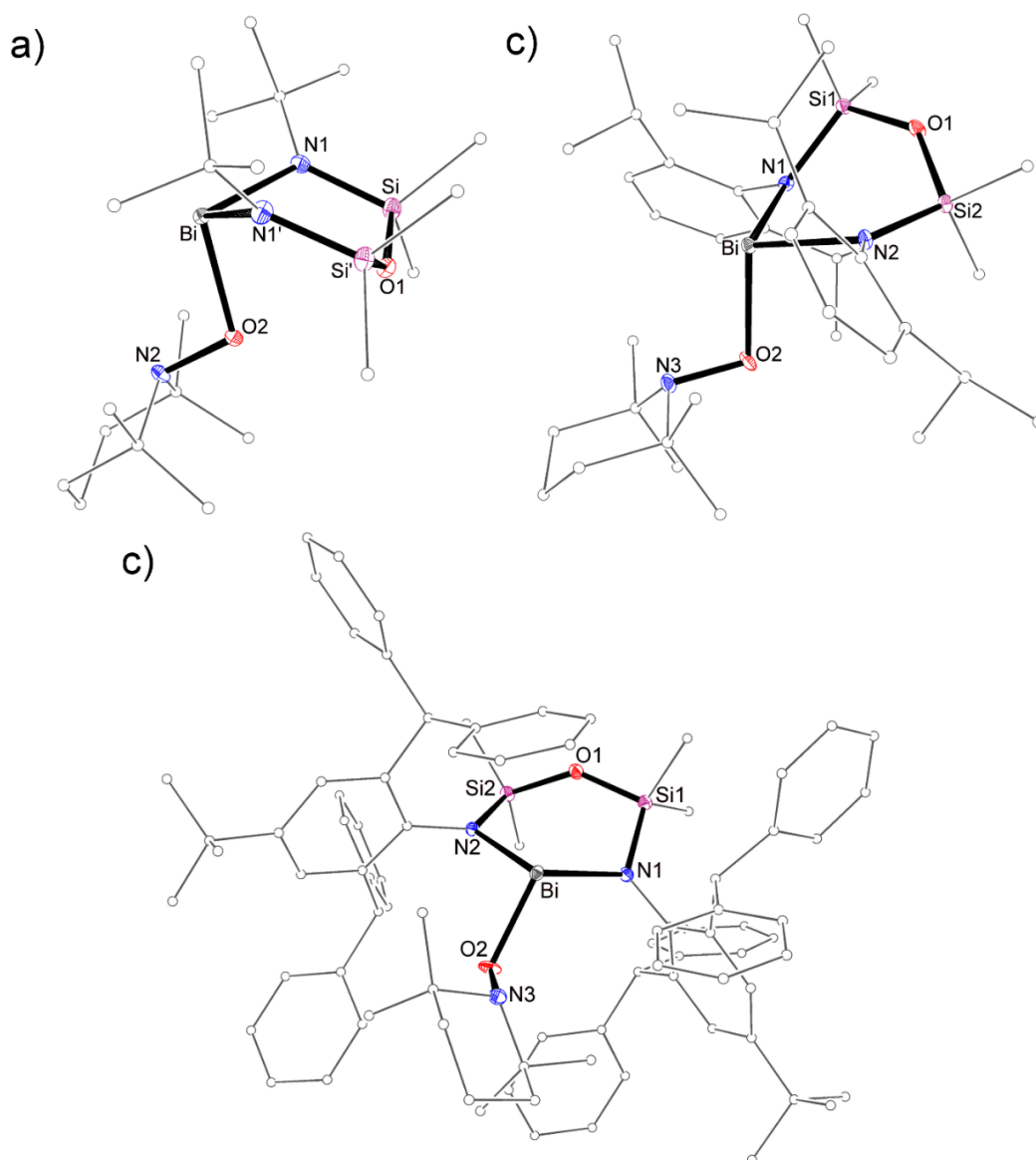


Figure 3.19. Molecular structure of **3.24a** (a), **3.24d** (b) and **3.24e** (c) (thermal ellipsoids displayed at 30% probability level, symmetry equivalent for **3.24a** (') = $x, 1.5-y, z$). Hydrogen atoms are omitted. Carbon atoms are displayed in wireframe format for clarity. Selected bond lengths (Å) and angles (°): **3.24a** Bi-N1 2.163(3), Bi-O1 2.111(3), O2-N2 1.448(4); N1-Bi-N1' 96.72(8), Bi-O2-N2 105.6(2). **3.24d** Bi-N1 2.192(4), Bi-N2 2.190(4), Bi-O2 2.129(4), O2-N3 1.467(5); N1-Bi-N2 93.8(2), Bi-O2-N3 100.3(2). **3.24e** Bi-N1 2.252(2), Bi-N2 2.205(2), Bi-O2 2.164(2), O2-N3 1.478(3); N1-Bi-N2 98.14(9), Bi-O2-N3 104.5(1).

Hill and co-workers recently reported the catalytic coupling of TEMPO and phenylsilanes to generate silylethers using a magnesium hydride catalyst.^{83b} The proposed catalytic cycle for this process involves the reaction of the magnesium hydride with TEMPO in a single electron transfer (SET) process, followed by Mg-O/Si-H σ -bond metathesis to regenerate the magnesium hydride species. We have demonstrated that the bismuth(III) hydrides 'Bi(NON^R)H' are unstable at ambient temperature (Section 2.3.2), releasing hydrogen gas and generating reduced bismuth species spontaneously. A similar catalytic process to the Mg example was envisaged whereby Bi-O/Si-H σ -bond metathesis (Figure 3.20, **A**), followed by rapid decomposition of the 'Bi(NON^R)H' (**B**) and subsequent radical coupling with TEMPO (**C**) result in the catalytic dehydrosilylation of TEMPO. An alternative plausible reaction pathway involves SET reactivity with the intermediate bismuth(III) hydride to generate the bismuth(III) TEMPOxide species (**B'**). However, the low stability of bismuth hydride species makes this pathway unlikely.

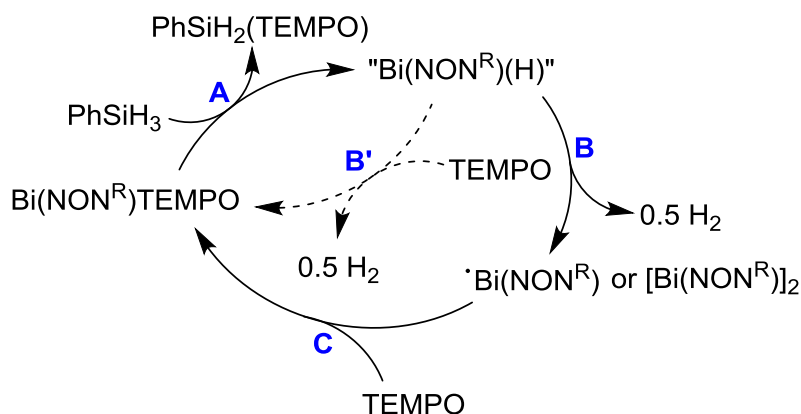
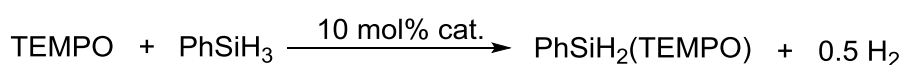


Figure 3.20. Catalytic cycle for the coupling of TEMPO and silanes using [Bi(NON^R)]_n.

Initial experiments confirmed the reaction of **2.24a**, **2.24d** or **2.24e** with phenylsilane (PhSiH₃) proceeds at 70 °C in a sealed NMR tube, generating PhSi(H)₂(OTEMP) (δ_{H} 5.44) and the reduced bismuth species [**2.17a**]₂, **2.17d**• and **2.17e**•, respectively. Extension of this reactivity to a catalytic regime using a 1 : 1 mixture of PhSiH₃ and TEMPO• with 10mol% **2.17d**• showed

slow formation of a mixture of $\text{PhSi(H)}_2(\text{OTEMP})$ and $\text{PhSi(H)}(\text{OTEMP})_2$ (Table 3.4). However, harsh conditions were required to obtain appreciable turnover (75 % conversion, 70 °C, 15 days). No reaction was observed under the same conditions in the absence of **2.17d•**. Monitoring the reaction over time shows sole formation of $\text{PhSi(H)}_2(\text{TEMPO})$ as the initial product (30% conversion, 7 days), after which $\text{PhSi(H)}_2(\text{TEMPO})$ is present in sufficient quantities to act as the silane substrate, resulting in the formation of both $\text{PhSi(H)}_2(\text{TEMPO})$ and $\text{PhSi(H)}(\text{TEMPO})_2$ over the final 8 days (Figure S3.5).

The corresponding reaction with **[2.17a]₂** was notably slower (30% conversion, 70 °C, 15 days), with no formation of $\text{PhSi(H)}(\text{TEMPO})_2$, while **2.17e•** is considerably faster (65% conversion, 70 °C, 6 days) with a 3 : 1 ratio of $\text{PhSi(H)}_2(\text{TEMPO})$: $\text{PhSi(H)}(\text{TEMPO})_2$ (Figure S3.6 and S3.7). These results were unexpected and contrast typical reactivity patterns where steric bulk deactivates catalysts. In general, radical coupling reactions are rapid, and therefore the rate determining step for this process is likely to be the Bi-O/Si-H σ -bond metathesis step (**A**), evidenced by the ^1H NMR spectra showing $\text{Bi}(\text{NON}^{\text{R}})(\text{TEMPO})$ as the catalytic resting state. A qualitative assessment of the catalysis suggests that improved reaction rates may correspond to weaker Bi-O bonds for the more encumbered bismuth centres in **3.24d** and **3.24e**. This is the first example of redox-based catalysis by bismuth and establishes the viability of SET reactivity in catalytic applications for future investigations in this area.

Table 3.4. Catalytic activity of bismuth(II) species for the coupling of phenylsilane and TEMPO at 70 °C.

Catalyst (10mol%)	Conversion (%) ^a			Time (days)
	$\text{PhSi(H)}_2(\text{TEMPO})$	$\text{PhSi(H)}(\text{TEMPO})_2$	Total	
[2.17a]₂	30	0	30	15
2.17d•	50	25	75	15
2.17e•	49	16	65	6

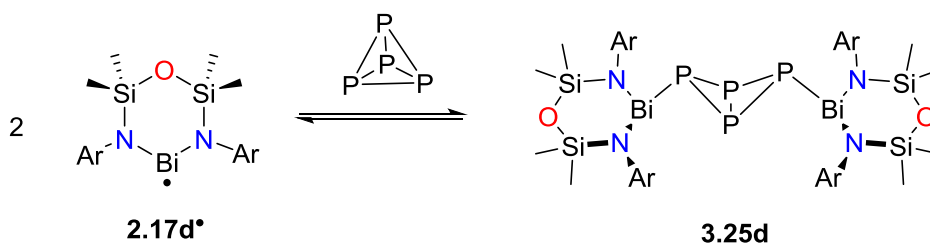
^adetermined by the relative integration of the $H_n\text{Si}$ resonances in the ^1H NMR spectrum. See Figures S3.5-S3.7 for plots of conversion over time.

3.3.4. Reactivity of Bi(II) Species with White Phosphorus (P₄)

The activation of white phosphorus (P₄) is of continued interest as an entry into organophosphorus compounds. Group 13 (Al, Ga, In, Tl) and group 14 (Si, Ge, Sn) metalloids/metals have been demonstrated to activate P₄, forming M-P bonds under mild conditions.⁹⁶ In contrast, there have been no reports of group 15 metalloids/metals (As, Sb, Bi) demonstrating similar reactivity.⁹⁷ Inspired by the reactivity of phosphinyl radicals with P₄,⁹⁸ we sought to explore the analogous reactivity with reduced bismuth species.

The addition of P₄ to the low valent bismuth species **[2.17a]₂**, **2.17d•** and **2.17e•** give surprisingly different results. In the case of **[2.17a]₂** and **2.17e•**, no reaction was observed, even when the reaction mixture was heated to 70 °C and excess (10 equiv.) P₄ was added, with only starting materials isolated from the reaction mixture. This was confirmed by monitoring the reaction mixture using ¹H and ³¹P NMR spectroscopy. In contrast, **2.17d•** reacts with P₄, forming orange-red crystals of the bimetallic compound [Bi(NON^{Ar})]₂(P₄) (**3.25d**) after work-up. This was confirmed using X-ray crystallography and elemental analysis. The ¹H NMR spectrum of an isolated sample of **3.25d** at room temperature showed resonances consistent with a diamagnetic species with a pyramidal bismuth centre chelated by a (NON^{Ar})-ligand (SiMe₂, δ_H 0.47 and 0.26). Significant paramagnetic resonances corresponding to **2.17d•** were also present in the ¹H NMR spectrum. The ³¹P NMR spectrum shows two mutually coupled triplets of an A₂B₂ system at δ_P 107.2 and 350.3 (*J*_{PP} = 164 Hz), in addition to a singlet at δ_P 521.2 corresponding to P₄. The relative quantities of **2.17d•** / P₄ and **3.25d** vary with temperature, indicating an equilibrium in solution (*K*_{eq} = 1.5 × 10³ M⁻² at 293 K). These data are consistent with reversible activation of a single P-P bond in the P₄ tetrahedron to give the tetraphosphabicyclo[1.1.0]butane-bridged bimetallic compound **3.25d** (Scheme 3.6). ¹H and ³¹P NMR spectra were measured over the temperature range -40 °C to +40 °C (Figure S3.8 and S3.9), showing the solution contains predominantly **3.25d** at low temperatures (below 0 °C) and **2.17d•** / P₄ at higher temperatures (above 30 °C). A Van't Hoff plot of the ³¹P data gives

$\Delta H^\circ = -64.8 \text{ kJmol}^{-1}$ and $\Delta S^\circ = -154.6 \text{ JK}^{-1}\text{mol}^{-1}$, showing that the activation is exothermic, with a reduction in the entropy at low temperature as **3.25d** is formed.



Scheme 3.6. Reversible activation of P_4 using **2.17d•**.

The solid-state structure of **3.25d** was determined using X-ray diffraction (Figure 3.21). The asymmetric unit contains half a molecule which sits on a 2-fold rotation axis and contains poorly resolved Et_2O solvate molecules that have been treated as a diffuse contribution to the overall scattering without specific atom positions by SQUEEZE/PLATON⁶³ to allow discussion of the unit of interest. The crystal structure of **3.25d** confirmed two ' $\text{Bi}(\text{NON}^{\text{Ar}})$ ' units anchored by a bridging $\mu, \eta\text{-}1\text{:}1\text{-P}_4$ moiety. This structural motif is rare, but has been observed in a number of other metal systems,⁹⁸⁻⁹⁹ including one main group metal example using tin.¹⁰⁰ The Bi-N distances (Bi-N1 2.189(4); Bi-N2 2.192(4) Å) indicate symmetrical coordination of the (NON^{Ar})-unit to a pyramidal bismuth centre ($\Sigma(\angle \text{Bi})$: 288.73°). The Bi-P distance (2.675(1) Å) is significantly longer than the sum of covalent radii for Bi and P (2.55 Å),¹⁰¹ but is within the range observed in bridging bismuth(III) phosphides (2.609(3) – 2.693(5) Å).¹⁰² The relatively weak Bi-P bond may account for the reversibility observed in the solution-state. The P-P distances (P1-P2 2.209(2); P1-P2' 2.223(2); P2-P2' 2.179(2) Å) are standard for single bonds, forming constrained P_3 triangles with acute internal angles nearing 60° (P1-P2-P2' 60.87(6)°; P1-P2'-P2 60.25(6)°; P2-P1-P2' 58.88(6)°). The degree of pyramidalisation for P1 and P2 (252.5° and 198.7°, respectively) indicate highly unfavourable geometries, consistent with the highly strained ring structure. The relative arrangement of the ' $(\text{NON}^{\text{Ar}})\text{Bi}$ ' units about the central P_4 core can be described using an analogous classification to the mono-chalcogenide

insertion products (Section 3.3.2), giving a *syn-syn* arrangement with a Bi-P1-Bi'-lp (lp = assumed position of the lone pair on bismuth) torsion angle of 17.8°.

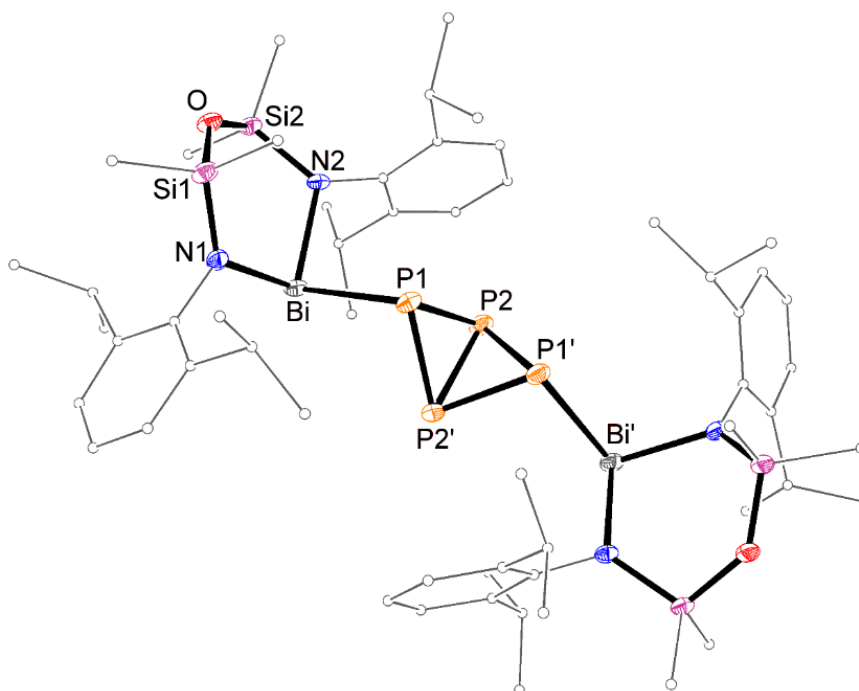


Figure 3.21. Molecular structure of **3.25d** (thermal ellipsoids displayed at 30% probability level, symmetry equivalent (') = 1-x, y, 1.5-z). Hydrogen atoms are omitted, and carbon atoms are displayed in wireframe format for clarity. Selected bond lengths (Å) and angles (°): Bi-P1 2.675(1), P1-P2 2.223(2), P2-P2' 2.179(2), Bi-N1 2.169(4), Bi-N2 2.192(4); Bi-P1-P2 96.88(6), N1-Bi-N2 95.2(1), P1-P2-P2' 60.25(6), P2-P1-P2' 58.88(6).

The reversible activation of P_4 has previously been observed in the germanium(II) system $\text{GeAr}^\#_2$ ($\text{Ar}^\# = 2,6\text{-mes}_2\text{C}_6\text{H}_3$) upon exposure to UV light, caused by a transition from the HOMO (Ge-P bonding) to the LUMO (Ge...P antibonding).¹⁰³ The UV-visible spectrum of **3.25d** (Figure S3.10), obtained at -40 °C, shows a peak at 405 nm, in addition to absorptions from radical **2.17d•**. Time dependent DFT calculations (performed by M. Lein, Victoria University of Wellington) revealed three electronic transitions contribute to this absorption, each of them associated with excitation from the HOMO (Bi-P bonding, $\text{P1}\cdots\text{P1}'$ antibonding) to the

LUMO+1 (Bi...P antibonding, P1-P1' bonding), and suggests that photolysis may play a role in the observed reversibility of the reaction.

Further functionalisation of the P_4 unit is an attractive goal. Bertrand and co-workers showed that stabilised carbenes can be used to ring open P_4 leading to its fragmentation or aggregation into various polyphosphide species depending on the steric and electronic properties of the carbene.^{66, 104} A common intermediate in the formation of these species is the diphosphene **3.26** (Figure 3.22), formed through the cleavage of two P-P bonds. Although this intermediate has not been isolated, the reactive species has been trapped using 2,3-dimethyl-1,4-butadiene or an additional equivalent of an electrophilic carbene.⁶⁶

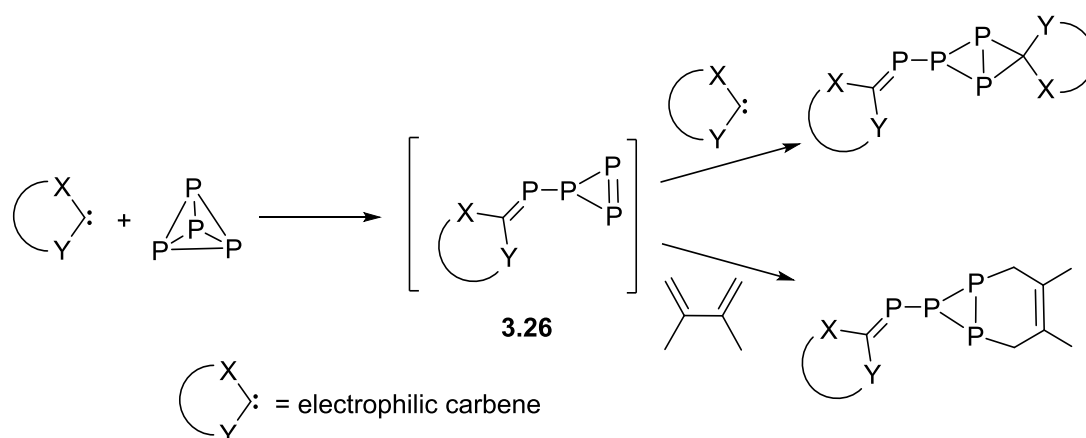
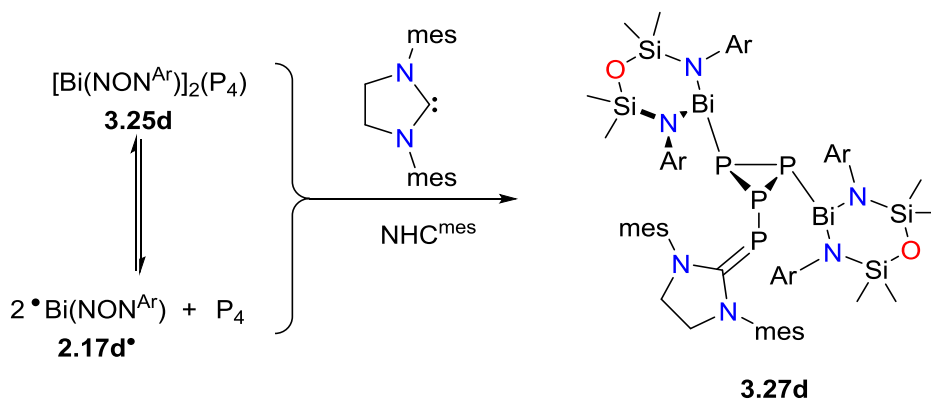


Figure 3.22. Activation of P_4 by electrophilic carbenes and trapping of the intermediate species **3.26**.

We sought to exploit this versatile reactivity in the co-functionalisation of the P_4 -unit in **3.25d**. However, the reversible activation of P_4 by **2.17d•** complicates this step, with both **3.25d** and P_4 present in solution.[†] The reaction of **3.25d** with 1 equiv. of the saturated N-heterocyclic carbene $(\text{CH}_2\text{N}(\text{mes}))_2\text{C}:$ (NHC^{mes} , $\text{mes} = 2,4,6\text{-Me}_3\text{C}_6\text{H}_2$) in C_6D_6 results in formation of a dark red solution, from which red crystals of $[\text{Bi}(\text{NON}^{\text{Ar}})]_2(\text{P}_4)(\text{NHC}^{\text{mes}})$ (**3.27d**) were obtained after work-up (Scheme 3.7).

[†] Exists as a mixture of **3.25d**, **2.17d•** and P_4 in solution.



Scheme 3.7. Synthesis of **3.27d**.

^1H , ^{13}C and ^{31}P NMR spectroscopy revealed the formation of a new diamagnetic species. The ^1H NMR spectrum of **3.27d** is complicated, showing 8 equal integral SiMe_2 resonances (δ_{H} 0.05, 0.06, 0.10, 0.29, 0.34, 0.55, 0.64 and 0.85) and 8 equal integral CHMe_2 resonances (δ_{H} 3.52, 3.63, 3.97, 4.02, 4.08, 4.13, 4.25 and 4.39) indicating a highly asymmetric compound featuring at least two different (NON^{Ar}) -ligand environments (Figure S3.11). Resonances corresponding to the NHC mesityl substituent also display a high degree of asymmetry, with three singlets for the C_6H_2 protons (δ_{H} 6.22, 6.60 and 6.67 with a relative integral of 1:1:2, respectively) consistent with restricted rotation of one mesityl substituent and unrestricted rotation of the other. The ^1H - ^{29}Si HMBC spectrum (Figure S3.12) shows four distinct ^{29}Si environments with coupling between two SiMe_2 proton resonances and each $^{29}\text{SiMe}_2$ resonance. The ^{31}P NMR spectrum shows 4 inequivalent phosphorus environments with an ABCD system (Figure 3.23, Table 3.5).

Table 3.5. ^{31}P NMR spectral data for **3.27d**.

	δ_{P}	Splitting Pattern	J_{PP} (Hz)
A	-0.65	ddd	300, 210 and 18
B	-141.0	ddd(overlap)	215, 200 and 18
C	-153.0	dt	215, 200 and 146
D	-189.7	ddd	300, 200 and 146

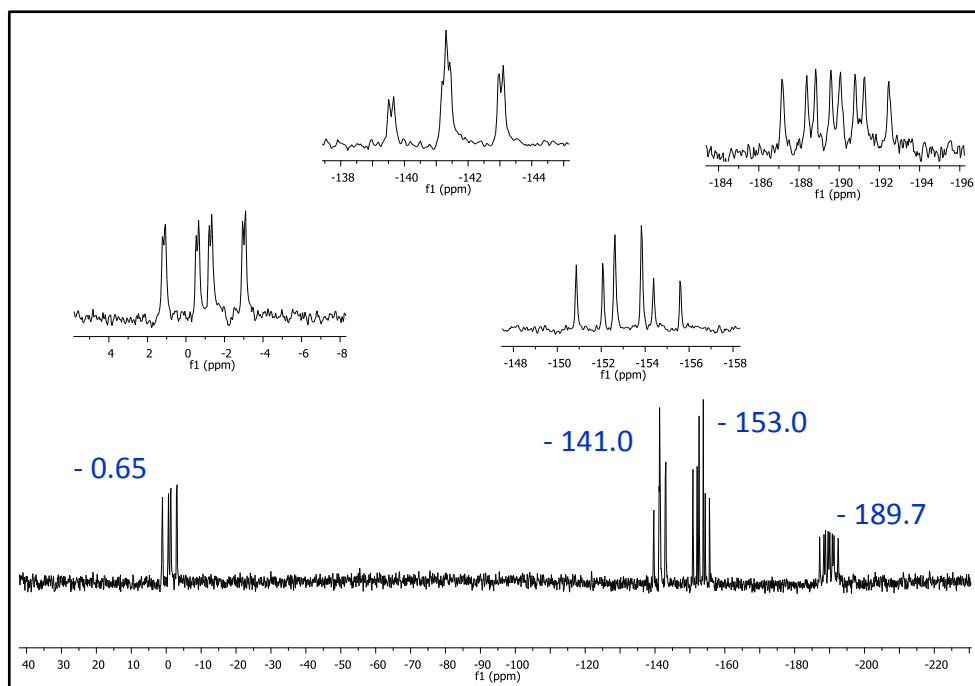


Figure 3.23. ^{31}P NMR spectrum of **3.27d**.

Single crystal X-ray diffraction was used to determine the solid-state structure of **3.27d** (Figure 3.24), showing two ' $\text{Bi}(\text{NON}^{\text{Ar}})$ ' units and one NHC^{mes} ligand bound to an extremely hindered central P_4 unit. The P_4 core exists as a P_3 triangle with an exocyclic phosphorus and is reminiscent of the Bi_4 cluster **2.24d** (Section 2.2.6). The structure is consistent with the high degree of asymmetry observed in the NMR spectra, with the ' $(\text{NON}^{\text{Ar}})\text{Bi}$ ' unit and the exocyclic phosphorus atom either on the same side (*cis*-) or opposite sides (*trans*-) of the P_3 ring, resulting in two distinct environments for the ' $(\text{NON}^{\text{Ar}})\text{Bi}$ ' units. The P-P distances are all consistent with single bonds, occupying a narrow range (2.198(2) – 2.235(2) Å). The internal angles of the P_3 triangle are close to 60° (P1-P2-P3 60.68(5) $^\circ$, P1-P3-P2 59.05(5) $^\circ$, P2-P1-P3 60.27(5) $^\circ$) with the exocyclic phosphorus atom (P4) sitting almost perpendicular to the plane of the P_3 triangle (P1-P3-P4 102.05(6) $^\circ$, P2-P3-P4 89.19(6) $^\circ$). The Bi-P distances (Bi1-P1 2.6682(11) Å; Bi2-P2 2.6963(11) Å) are similar to those observed in **3.25d**. The Bi-N distances are consistent with symmetric coordination at Bi2 (Bi2-N3 2.192(4) Å, Bi2-N4 2.204(4) Å), however, large differences between the Bi1-N1 and Bi1-N2 distances (2.267(4) and 2.181(4) Å, respectively) indicate asymmetric coordination, likely due to the extremely hindered metal

centre. The relative position of the (NON^{Ar})-ligands are offset from each other by 76.2° (measured as the rotation of the (NON^{Ar})-ligand about the Bi···Bi vector) and are staggered with respect to each other (BiN₂ : BiN₂ interplanar angle: 55.0°). The C57-P4 distance (1.775(5) Å) is typical for a double bond, within the standard range observed for NHC=P interactions (1.727(2) – 1.813(4) Å).

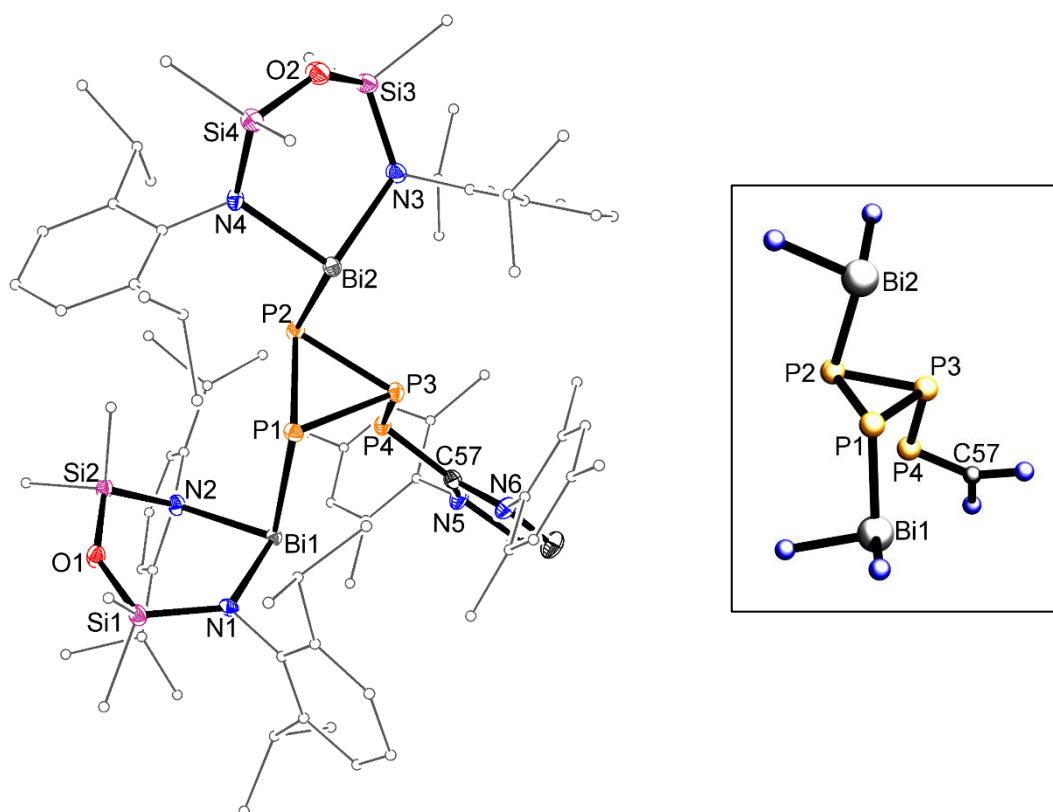


Figure 3.24. Molecular structure of **3.27d** (thermal ellipsoids displayed at 30% probability level) and structure of the core P₄ unit. Hydrogen atoms and two hexane solvent molecules are omitted. Selected carbon atoms are displayed in wireframe format for clarity. Selected bond lengths (Å) and angles (°): Bi1-P1 2.668(1), Bi2-P2 2.696(1), P1-P2 2.198(2), P1-P3 2.235(2), P2-P3 2.226(2), P3-P4 2.221(1), P4=C57 1.775(5), Bi1-N1 2.267(4), Bi1-N2 2.181(4), Bi2-N3 2.192(4), Bi2-N4 2.204(4); Bi1-P1-P2 109.77(5), Bi1-P1-P3 96.92(5), Bi2-P2-P1 85.80(5), Bi2-P2-P3 85.63(4), N1-Bi1-N2 99.0(1), N3-Bi2-N4 94.3, P1-P2-P3 60.68(5), P1-P3-P2 59.05(5) P1-P3-P4 102.05(6), P2-P1-P3 60.27(5), P2-P3-P4 89.19(6), P3-P4-C57 107.2(2), P1-P2-P3 60.68(5), P2-P1-P2' 58.88(6).

The formation of **3.27d** may occur with initial P_4 activation by NHC^{mes} to generate intermediate **3.26**, followed by $P=P$ bond activation by two molecules of **2.17d•** (Figure 3.25a). Evidence for such a mechanism was obtained from the independent reaction of P_4 with NHC^{mes} , followed by addition of the **2.17d•** after 4h at room temperature. A large driving force for the reactivity of the $P=P$ bond in **3.26** is the relief of the unfavourable constrained geometry of the P_3 ring system. Regardless, the activation of $P=P$ double bonds by main group elements is rare and has only been demonstrated for the lighter elements.¹⁰⁵ For example, Yamashita and co-workers recently reported the activation of the $P=P$ bond in the diphosphenes $\{PR\}_2$ ($R = 2,4,6-tBu_3C_6H_3$ or $B\{N(Ar)CH_2\}_2$) using $nBuLi$, forming an anionic diphosphane species balanced by a lithium cation (Figure 3.25b), likely proceeding through nucleophilic attack of a carbanion.^{105b}

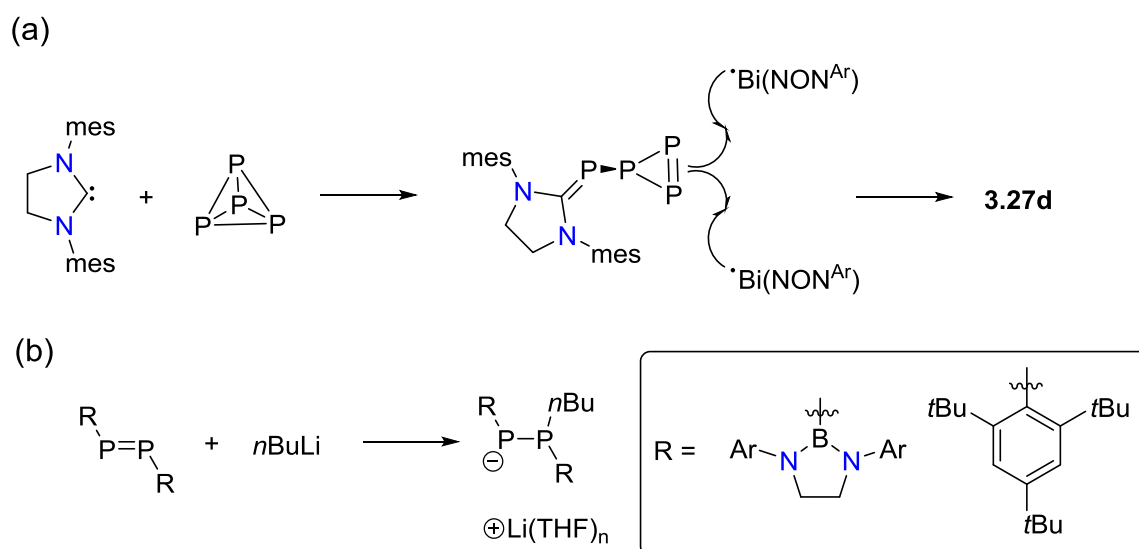


Figure 3.25. (a) Possible mechanism for the formation of **3.27d**. (b) Reaction of $nBuLi$ with diphosphenes $\{PR\}_2$.

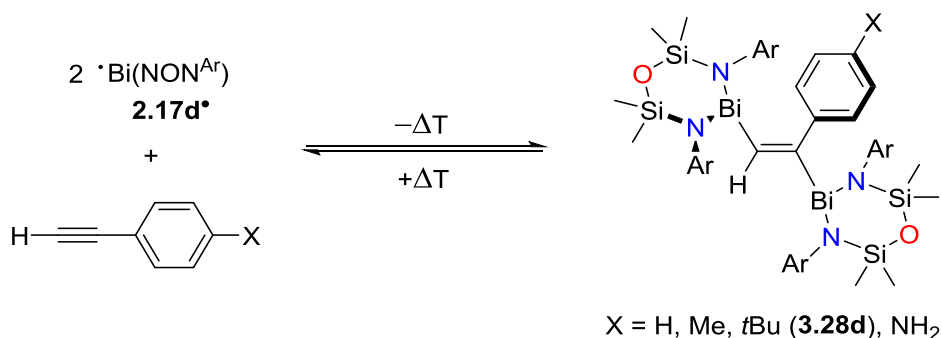
3.3.5. Reactivity of Bi(II) Species with Unsaturated Substrates

The activation of unsaturated substrates is widespread in low valent metal chemistry and has been demonstrated for many elements of the periodic table.³ However, the only examples of the activation of unsaturated substrates by a heavy low valent group 15 element is the anti-addition of reduced antimony species $(SbPh_2)_2$ and $(SbPh)_6$ to alkynes to give the alkene

bridged distibanylation products *trans*-(SbPh₂)₂(HC=CHR) (R = Ph, 4-FC₆H₄), *trans*-(SbPh₂)₂(PhC=CHR) (R = C≡CPh) and [SbPh(MeO₂CC=CCO₂Me)]_n,¹⁰⁶ respectively, and the activation of the C=O bond of 1,4-benzoquinone using {Bi(4-MeC₆H₄)₂}₂ to give {Bi(4-MeC₆H₄)₂}(1,4-O₂C₆H₄).^{78a} However, in the latter example, the solid-state structure was not determined, with characterisation limited to ¹H NMR spectroscopy, mass spectrometry and elemental analysis.

The activation of alkynes using reduced bismuth species was initially investigated. No reaction was observed by ¹H NMR spectroscopy when phenylacetylene was added to an NMR sample of [2.17a]₂ or 2.17e•. In contrast, the ¹H NMR spectrum of a mixture of phenylacetylene and 2.17d• indicates the formation of a diamagnetic species with four SiMe₂ resonances of equal integration (δ_H 0.16, 0.20, 0.29 and 0.47) and a sharp low field singlet at δ_H 10.50 corresponding to C=CH shifted significantly downfield compared to the that observed for *trans*-(SbPh₂)₂(PhC=CH) (~7.2 ppm). Unfortunately, crystals of the reaction product(s) were not obtained. Changing the substituent at the *para*-position of the aromatic ring of the alkyne (i.e. HC≡C(C₆H₄-4-X), X = Me, *t*Bu, NH₂) resulted in similar behaviour in the ¹H NMR spectrum, again forming a diamagnetic species with four high field singlets corresponding to the SiMe₂ protons (δ_H: 0.14, 0.21, 0.30 and 0.49 (X = Me or *t*Bu (3.28d)); 0.01, 0.10, 0.32 and 0.45 (X = NH₂)). These data are consistent with the dibismuthanylation of the C≡C bond (Scheme 3.8). The product from the reaction involving the *para*-*t*Bu derivative, [Bi(NON^{Ar})]₂(HC=C(C₆H₄-4-*t*Bu)) (3.28d), was isolated as a yellow crystalline solid from THF. ¹H NMR spectroscopy of the isolated sample of 3.28d revealed the spontaneous formation of 2.17d• and HC≡C(C₆H₄-4-*t*Bu) over time. VT NMR spectroscopy revealed that the relative quantities of these species vary with temperature, indicating the presence of an equilibrium in solution. This is consistent with the reversible activation of the C≡C bond of the terminal alkyne (Scheme 3.8). The ¹H NMR spectrum was measured over the temperature range -60 °C to +50 °C, showing almost complete formation of 3.28d below -40 °C and significant dissociation to 2.17d• and HC≡C(C₆H₄-4-*t*Bu) above +40 °C. A Van't Hoff plot of the data (Figure S3.13) was used to

determine the thermodynamic values of $\Delta H^\circ = -14.8 \text{ kJmol}^{-1}$ and $\Delta S^\circ = -27.22 \text{ JK}^{-1}\text{mol}^{-1}$. The reversible activation of $\text{C}\equiv\text{C}$ multiple bonds using p-block metals is rare, but has previously been reported for a number of low valent Sn, Al and Ga compounds.¹⁰⁷ However, the latter two examples required a redox active bis(imino)acetonaphthalene (bian) ligand in order for the reversible addition to occur.



Scheme 3.8. Reversible activation of terminal alkynes by **2.17d•**.

X-ray diffraction confirmed the identity of **3.28d** as the bis(bismuthanyl)alkene $[\text{Bi}(\text{NON}^{\text{Ar}})]_2(\text{HC}=\text{C}(\text{C}_6\text{H}_4\text{-4-}t\text{Bu}))$ (Figure 3.26). The asymmetric unit contains one molecule of **3.28d** in addition to five THF molecules which, due to the poor quality of the data, were modelled isotropically. The solid-state structure of **3.28d** features two bismuth atoms anchored *trans* to each other through an alkene linkage, analogous to the structure of the bis(antimony)alkenes $[\text{SbPh}_2]_2(\text{HC}=\text{C}(\text{C}_6\text{H}_4\text{-4-X}))$ ($\text{X} = \text{H}$; $\text{X} = \text{F}$). However, the Bi1-C57-C58-Bi2 torsion angle (152.95°) is significantly smaller than the analogous torsion angle seen for the bis(antimony)alkenes ($\text{X} = \text{H}$, $178.8(3)^\circ$; $\text{X} = \text{F}$, $167.0(3)^\circ$), and is likely caused by a non-coplanar Bi-C₂-Bi core (Bi2 sits $0.965(6) \text{ \AA}$ out of the plane defined by Bi1, C57 and C58). The Bi1-C57 and Bi2-C58 distances ($2.287(6)$ and $2.321(5) \text{ \AA}$, respectively) are standard for single bonds, within the range observed in trialkyl bismuth compounds BiR_3 (range $2.23(3) - 2.347(3) \text{ \AA}$), while the C57-C58 distance ($1.325(7) \text{ \AA}$) indicates a standard $\text{C}=\text{C}$ double bond (1.34 \AA). The angles about C57 and C58 range between $113.9(3)^\circ$ and $125.0(5)^\circ$ to give planar carbon atoms ($\Sigma(\angle\text{C}): 360^\circ$), consistent with sp^2 -hybridisation of the carbon centres. Both bismuth atoms

are pyramidal ($\Sigma(\angle\text{Bi})$: Bi1, 296.53°; Bi2, 301.07°) and chelated by (NON^{Ar})-ligands with $\kappa_2\text{-N,N'}$ -bidentate coordination (N-Bi-N bite angles = 93.85(15)° and 98.77(16)°) featuring long Bi-N distances (2.181(4) – 2.233(4) Å) compared to **2.16d**, and are even longer than those of the Bi(II) radical **2.17d•**.

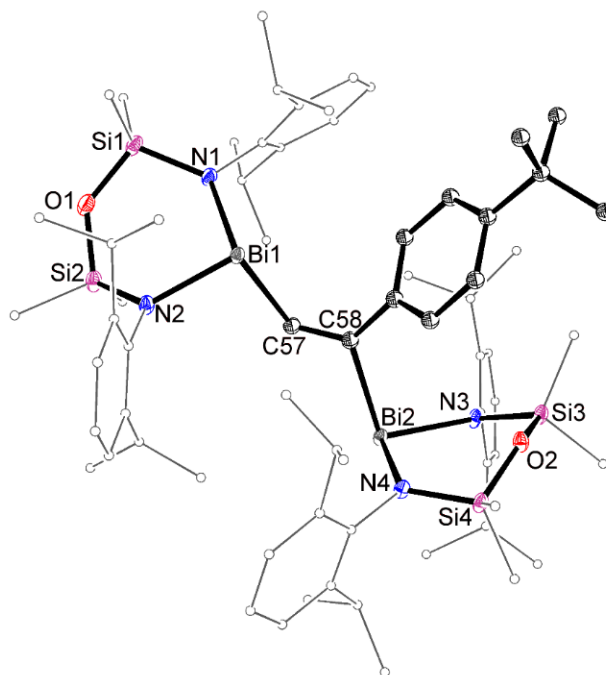


Figure 3.26. Molecular structure of **3.28d** (thermal ellipsoids displayed at 30% probability level). Hydrogen atoms and solvent molecules (5 x THF) are omitted. Carbon atoms are displayed in wireframe format for clarity. Selected bond lengths (Å) and angles (°): Bi1-N1 2.209(4), Bi1-N2 2.181(4), Bi2-N3 2.201(5), Bi2-N4 2.233(4), Bi1-C57 2.287(6), Bi2-C58 2.321(5), C57=C58 1.325(7); N1-Bi1-N2 93.85 (3), N3-Bi2-N4 98.77(16), Bi1-C57-C58 118.2(3), Bi2-C58-C57 113.9(3).

In order to extend the scope of this reactivity, the addition of various alkynes to the reduced bismuth species was attempted and monitored using ^1H NMR spectroscopy. However, terminal aliphatic alkynes $\text{HC}\equiv\text{CR}$ ($\text{R} = n\text{Bu}$, $t\text{Bu}$), terminal silyl-substituted alkynes ($\text{R} = \text{SiMe}_3$, $\text{Si}(i\text{Pr})_3$) and the internal alkyne diphenylacetylene ($\text{PhC}\equiv\text{CPh}$) are unreactive with the reduced bismuth species [**2.17a**]₂, **2.17d•** and **2.17e•**. This selectivity mirrors that seen for the reduced antimony species, which also did not react with diphenylacetylene and aliphatic alkynes.¹⁰⁶

A simple two-step mechanism for the reversible activation of alkynes has been proposed in Figure 3.27. The observed selectivity of this reaction on the basis of this mechanism may correspond to the ability of the R and R' groups to stabilise the radical character in intermediate species **A**. Alkynes substituted by aromatic R substituents allow delocalisation of the radical character into the aromatic ring, stabilising the radical intermediate. The lack of observed reactivity with diphenylacetylene was surprising given the reactivity of phenylacetylene, and may be caused by destabilisation of the proposed radical intermediate through electron withdrawing inductive effects of the R' phenyl substituent. Initial activation at the terminal alkyne carbon (i.e. R' = H) of a terminal alkyne is also sterically favoured compared to diphenylacetylene (where R' = Ph).

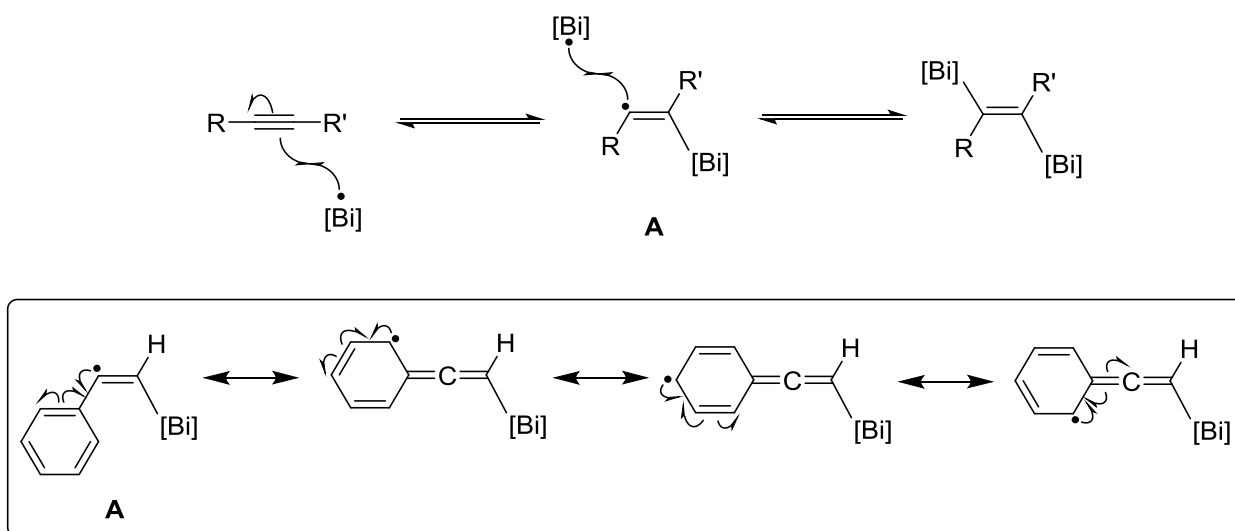
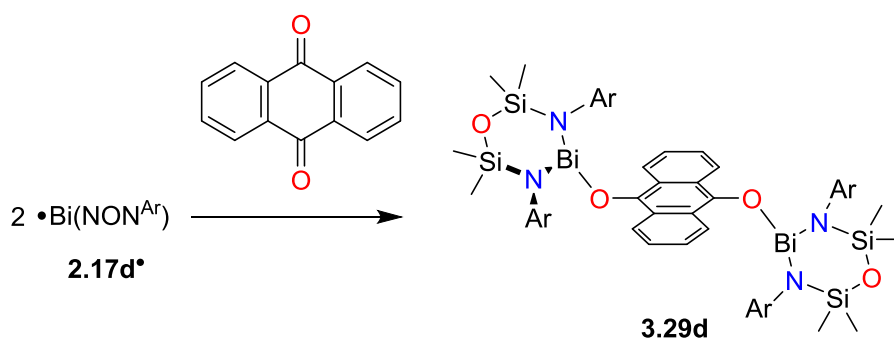


Figure 3.27. Proposed mechanism for the activation of C≡C bonds.

The activation and utilisation of unsaturated heteronuclear C=X bonds (X = O, N, S) is an important area of research.¹⁰⁸ Heterocumulenes are attractive unsaturated substrates due to their isoelectronic relationship with CO₂, while retaining easy working conditions (i.e. liquids). The addition of phenyl isocyanate (PhN=C=O), phenylisothiocyanate (PhN=C=S) and alkyl carbodiimides (RN=C=NR, R = Cy, *i*Pr) to **[2.17a]₂**, **2.17d•** or **2.17e•** did not result in formation of a new species, even after heating to 70 °C for 24 hours. To check for the presence of an equilibrium, excess (10 equiv.) unsaturated substrate was added and the reaction

mixture investigated using ^1H NMR spectroscopy, yielding the same result. Similar results were obtained when investigating the reactivity of the reduced bismuth species with unactivated ketones ($\text{R}_2\text{C}=\text{O}$, $\text{R} = \text{Me}, \text{Ph}$). However, when the dione 9,10-anthraquinone was added to $[\mathbf{2.17a}]_2$, $\mathbf{2.17d}^\bullet$ or $\mathbf{2.17e}^\bullet$, differing results were obtained. No reaction was observed between $[\mathbf{2.17a}]_2$ or $\mathbf{2.17e}^\bullet$ and excess 9,10-anthraquinone. In contrast, the addition of 9,10-anthraquinone to a solution of $\mathbf{2.17d}^\bullet$ results in an immediate colour change to give a dark purple solution, from which purple-red crystals were isolated after work-up (Scheme 3.9). 9,10-anthraquinone (and its monocyclic derivative, 1,4-quinone) is commonly used as radical traps due to the large driving force resulting from formation of a stable aromatic ring system. The ^1H NMR spectrum of the crystals reveals two SiMe_2 resonances (δ_{H} 0.27 and 0.90) and two CHMe_2 resonances (δ_{H} 3.81 and 3.98), consistent with a diamagnetic species with a pyramidal metal chelated by a (NON^{Ar}) -ligand.



Scheme 3.9. Reaction of $\mathbf{2.17d}^\bullet$ with 9,10-anthraquinone.

The solid-state structure of $\mathbf{3.29d}$ confirmed activation of the $\text{C}=\text{O}$ bonds of the 9,10-anthraquinone and consequential formation of the bimetallic species $[\text{Bi}(\text{NON}^{\text{Ar}})]_2(\text{C}_{14}\text{H}_8\text{O}_2)$ ($\mathbf{3.29d}$), containing two crystallographically distinct $\text{Bi}(\text{NON}^{\text{Ar}})$ units linked by a $[\text{C}_{14}\text{H}_8\text{O}_2]^{2-}$ ligand (Figure 3.28). Two Et_2O molecules were also present in the asymmetric unit. The (NON^{Ar}) -ligand chelates the pyramidal bismuth centres (Bi1 , 289.0° ; Bi2 , 285.6°) in a $\kappa_2\text{-}N,N'$ -bidentate bonding mode with standard bite angles ($96.5(1)^\circ$ and $97.0(1)^\circ$). The Bi-O distances (Bi1-O3 $2.144(2)$ Å, Bi2-O6 $2.129(2)$ Å) are long, but within the typical range for bismuth aryloxide species ($2.056(3) - 2.134(4)$ Å).¹⁰⁹ The C-O distances ($1.365(4)$ Å and $1.362(4)$ Å) are

also typical for aryloxide ligands at bismuth (1.359(2) – 1.403(3) Å), while the C-C bond distances in the central C₆ ring occupy a narrow range (1.407(5) – 1.437(4) Å), consistent with delocalisation of electrons over the central aromatic ring. In contrast, the outer C₆ rings of the anthracene moiety each contain two short C=C bonds (1.352(5) – 1.363(5) Å), consistent with minimal delocalisation of the electron density over the outer C₆ rings. The Bi-N distances (Bi1, 2.143(2) and 2.153(2) Å; Bi2, 2.148(2) and 2.143(2) Å) are shorter than those of the Bi(II) species **2.17d**•, consistent with oxidation of the bismuth centre. The BiN₂ least squares planes are staggered by approx. 41.88° (Bi1) and 49.66° (Bi2) with respect to the 9,10-anthraquinolene, presumably in order to alleviate steric clashes between the (NON^{Ar})-ligand and anthracene moieties.

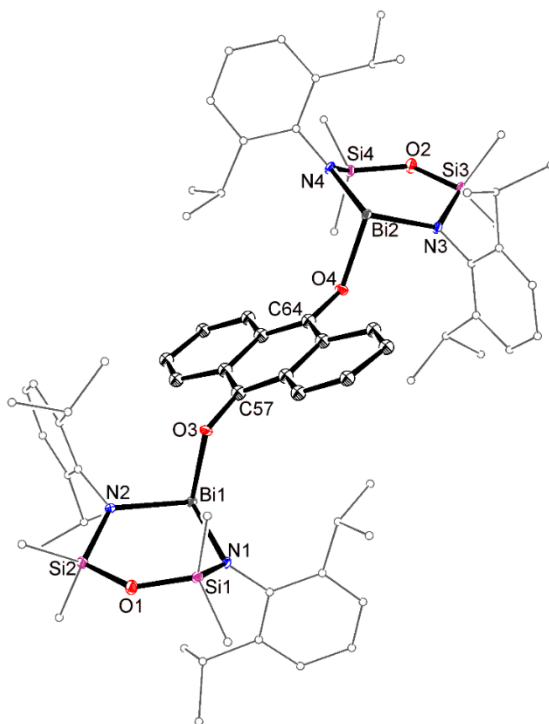


Figure 3.28. Molecular structure of **3.29d** (thermal ellipsoids displayed at 30% probability level). Hydrogen atoms and Et₂O solvent molecules are omitted. Carbon atoms are displayed in wireframe format for clarity. Selected bond lengths (Å) and angles (°): Bi1-N1 2.143(3), Bi1-N2 2.153(2), Bi2-N3 2.147(2), Bi2-N4 2.140(3), Bi1-O3 2.144(2), Bi2-O4 2.129(2), O3-C57

1.365(4), O4-C64 1.362(2); N1-Bi1-N2 96.5(1), N3-Bi2-N4 97.0(1), Bi1-O3-C57 117.3(2), Bi2-O4-C64 122.7(2).

3.4. Conclusion

This chapter describes the reactivity of the bismuth(II) species synthesised in chapter 2 (**[2.17a]₂** and **2.17e•**) and the previously reported bismuth(II) radical **2.17d•**. Initial experiments focussed on established oxidative addition reactions using halogen radical sources (*N*-bromosuccinimide and I₂), and elemental chalcogens to give the corresponding bismuth(III) halides Bi(NON^R)X (X = Br or I) or {Bi(NON^R)₂(E_n)} (E = S, Se, Te; n = 1, 3, 5 or 8), respectively. Of particular note is the reaction of **2.17e•** with sulfur, which gave the S₈-linked species [Bi(NON^{Ar†})(S₄)₂] (**3.21e**), featuring a unique *trans*-antarafacial bonding interaction in the S₈ chain and can be described as a dimer of an [S₄]^{−•} radical. The reactivity of the reduced bismuth species with the stable nitroxyl radical TEMPO proceeds cleanly to give Bi(NON^R)(OTEMP) (R = *t*Bu (**3.24a**), Ar (**3.24d**), Ar[†] (**3.24e**)). These species were demonstrated to be catalysts for the coupling of phenylsilane and TEMPO. When the reduced species were reacted with P₄, terminal aromatic alkynes or 9,10-anthraquinone, divergent reactivity was observed, with no reaction observed between the substrates and **[2.17a]₂/2.17e•** while reversible activation of the substrates (through either P-P or C≡C/C=O bond activation) was achieved using **2.17d•**. The experiments described in this chapter highlight the influence of both the nature of the bismuth(II) species (i.e. bismuth centred radical vs. dibismuthane) and the encumbrance imposed by the ligand on the reactivity of these species.

3.5. Experimental

3.5.1. Synthesis of Bismuth(III) Halogen Compounds

Synthesis of Bi(NON^{tBu})Br (3.15a)

A solution of *N*-bromosuccinimide (0.011 g, 0.062 mmol) in Et₂O (5 mL) was added to a solution of **[2.17a]₂** (0.030 g, 0.031 mmol) in Et₂O (5 mL), resulting in an immediate colour

change to yellow and the formation of a colourless precipitate. Removal the volatiles *in vacuo* followed by extraction into hexane (10 mL) and filtration through celite gave a clear yellow solution. Concentration of the solution to approx. 2 mL followed by storage at -30 °C gave yellow needles of **3.15a**. Yield 0.024 g, 68 %. Anal. Calcd. for C₁₂H₃₀BiBrN₂OSi₂ (563.44): C, 25.58; H, 5.37; N, 4.97 %. Found: C, 25.39; H, 5.42; N, 4.75 %. ¹H NMR (C₆D₆, 600 MHz) δ 1.19 (s, 18H, CMe₃), 0.56, 0.32 (s, 6H, SiMe₂). ¹³C{¹H} NMR (C₆D₆, 150 MHz) δ 53.7 (CMe₃), 36.7 (CMe₃), 7.3, 5.3 (SiMe₂).

Synthesis of Bi(NON^{Ar})Br (**3.15d**)

Method 1:

A solution of K₂(NON^{Ar}).(Et₂O)₂ **3.16d** (0.45 g, 0.64 mmol) in Et₂O (10 mL) was added dropwise to a solution of BiBr₃ (0.29 g, 0.64 mmol) in THF (10 mL). The brown suspension was stirred for 12 hours at room temperature followed by the removal of solvents *in vacuo*. The resulting thick oil was extracted with hexane and filtered through celite to give a red solution. Concentration to approx. 3 mL followed by storage at -30 °C overnight gave yellow crystals of **3.15d**. Yield 0.27 g, 55 %. Anal. Calcd. for C₂₈H₄₆BiBrN₂OSi₂ (771.74): C, 43.58; H, 6.01; N, 3.63 %. Found: C, 43.41; H, 6.24; N, 3.65 %. ¹H NMR (C₆D₆, 600 MHz) δ 7.23, 7.08 (dd, *J* = 7.7 and 1.5, 2H, *m*-C₆H₃), 6.97 (t, *J* = 7.7, 2H, *p*-C₆H₃), 4.22, 3.63 (sept, *J* = 6.9, 2H, CHMe₂), 1.46, 1.29, 1.26, 1.06 (d, *J* = 6.9, 6H, CHMe₂), 0.61, 0.18 (s, 6H, SiMe₂). ¹³C{¹H} NMR (C₆D₆, 150 MHz) δ 151.5, 148.3, 138.0, 126.9, 125.1, 123.8 (Ar-C), 29.1, 29.0, 27.5, 27.4, 25.3, 24.8 (CHMe₂ and CHMe₂), 4.3, 3.2 (SiMe₂).

Method 2:

A solution of *N*-bromosuccinimide (0.009 g, 0.051 mmol) in Et₂O (5 mL) was added to a solution of **2.17d•** (0.035 g, 0.051 mmol) in Et₂O (5 mL), resulting in a gradual colour change

from deep red to yellow. Removal the volatiles *in vacuo* followed by extraction into hexane (10 mL) and filtration through celite gave a clear yellow solution. Concentration of the solution to approx. 2 mL followed by storage at -30 °C gave yellow co-crystals of Bi(NON^{Ar})Br (**3.15d**) and Bi(NON^{Ar})(N{C(O)CH₂})₂ (**3.15d'**).

*Synthesis of Bi(NON^{Ar±})Br (**3.15e**)*

A solution of *N*-bromosuccinimide (0.009 g, 0.051 mmol) in Et₂O (5 mL) was added to a solution of **2.17e•** (0.035 g, 0.051 mmol) in Et₂O (5 mL), resulting in a gradual colour change from deep red to yellow. Removal the volatiles *in vacuo* followed by extraction into hexane (10 mL) and filtration through celite gave a clear yellow solution. Concentration of the solution to approx. 2 mL followed by storage at -30 °C gave yellow crystals of **3.15e**. Yield 0.017 g, 50%. ¹H NMR (C₆D₆, 600 MHz): δ 7.75 – 7.60 (m, 6H, C₆H₂ and C₆H₅), 7.39 – 7.22 (m, 10H, C₆H₂ and C₆H₅), 7.15 – 6.82 (m, 28H, C₆H₂ and C₆H₅), 6.47 (s, 2H, CHPh₂), 1.06 (s, 18H, CMe₃), 0.24, -0.02 (s, 6H, SiMe₂). ¹³C{¹H} NMR (C₆D₆, 150 MHz): δ 147.9, 147.5, 146.7, 146.1, 146.0, 145.7, 145.5, 145.2, 145.1, 143.5, 142.4, 142.3, 141.0, 140.4, 131.6, 131.5, 131.0, 130.7, 130.4, 130.0, 129.7, 127.1, 127.0, 126.8, 126.5, 126.3 (C₆H₅ and C₆H₂), 51.6, 50.8 (CHPh₂), 34.2 (CMe₃), 31.4 (CMe₃), 5.1, 4.6 (SiMe₂).

*Synthesis of K₂(NON^{Ar}).(Et₂O)₂ (**3.16d**)*

KH (0.11 g, 2.73 mmol) was cautiously added to a solution of (NON^{Ar})H₂ (**2.19d**, 0.60 g, 1.24 mmol) in THF (20 mL). After the initial bubbling had slowed, the reaction mixture was heated to 55 °C and stirred for 12 hours, followed by removal of the volatiles *in vacuo* and extraction into Et₂O (20 mL). Filtration through celite followed by concentration to 10 mL and storage at -30 °C gave colourless crystals of **3.16d**. A second crop of crystals was isolated from further concentration of the mother liquor and storage at -30 °C. Yield 0.58 g, 66%. ¹H NMR (C₆D₆, 300

MHz) δ 6.91 (br, 4H, *m*-C₆H₃), 6.39 (br, 2H, *p*-C₆H₃), 3.80 (br, 4H, CHMe₂), 3.27 (m, 8H, OCH₂CH₃), 1.21 (br, 24H, CHMe₂), 1.12 (m, 12H, OCH₂CH₃), 0.45 (s, 12H, SiMe₂). *poor solubility in C₆D₆ prevented collection of ¹³C NMR data.

Synthesis of Bi(NON^{tBu})I (3.17a)

A solution of I₂ (0.013 g, 0.052 mmol) in Et₂O (5 mL) was added dropwise to a stirring solution of [2.17a]₂ (0.050 g, 0.052 mmol) in Et₂O (5 mL) resulting in an immediate colour change to orange. Removal of the volatiles *in vacuo* and extraction into hexane gave an orange solution. Concentration to 0.5 mL and storage at -30 °C overnight gave orange needles of 3.17a. Yield 0.053 g, 83 %. Anal. Calcd. for C₁₂H₃₀BiIN₂OSi₂ (610.44): C, 23.61; H, 4.95; N, 4.59 %. Found: C, 23.37; H, 4.65; N, 4.37%. ¹H NMR (C₆D₆, 600 MHz) δ 1.17 (s, 18H, CMe₃), 0.55, 0.31 (s, 6H, SiMe₂). ¹³C{¹H} NMR (C₆D₆, 150 MHz) δ 54.5 (CMe₃), 36.5 (CMe₃), 7.6, 4.3 (SiMe₂).

Synthesis of Bi(NON^{Ar})I (3.17d)

A solution of I₂ (0.009 g, 0.036 mmol) in Et₂O (5 mL) was added dropwise to a stirring solution of 2.17d• (0.050 g, 0.072 mmol) in Et₂O (5 mL) resulting in an immediate colour change from deep red to orange. Removal of the volatiles *in vacuo* and extraction into hexane gave an orange solution. Concentration to 0.5 mL and storage at -30 °C overnight gave orange crystals of 3.17d. Yield 0.041 g, 73 %. Anal. Calcd. for C₂₈H₄₆BiIN₂OSi₂ (818.74): C, 41.08; H, 5.66; N, 3.42 %. Found: C, 40.97; H, 5.74; N, 3.51 %. ¹H NMR (C₆D₆, 600 MHz) δ 7.21, 7.08 (dd, *J* = 7.7 and 1.5, 2H, *m*-C₆H₃), 6.96 (t, *J* = 7.7, 2H, *p*-C₆H₃), 4.17, 3.59 (sept, *J* = 6.9, 2H, CHMe₂), 1.51, 1.30, 1.26, 1.08 (d, *J* = 6.9 Hz, 6H, CHMe₂), 0.60, 0.17 (s, 6H, SiMe₂). ¹³C{¹H} NMR (C₆D₆, 75 MHz) δ 151.3, 148.2, 137.7, 126.9, 124.9, 123.7 (*Ar-C*), 28.9, 28.6, 27.4, 25.1, 24.5 (CHMe₂ and CHMe₂), 4.5, 3.2 (SiMe₂).

Synthesis of $\text{Bi}(\text{NON}^{\text{Ar}\pm})\text{I}$ (**3.17e**)

A solution of I_2 (0.012 g, 0.046 mmol) in Et_2O (5 mL) was added dropwise to a stirring solution of **2.17e**• (0.120 g, 0.092 mmol) in Et_2O (5 mL) resulting in an immediate colour change from deep red to orange. Removal of the volatiles *in vacuo* and extraction into hexane gave an orange solution. Concentration to 0.5 mL and storage at $-30\text{ }^\circ\text{C}$ overnight gave orange crystals of **3.17e**. Yield 0.091 g, 69 %. ^1H NMR (C_6D_6 , 600 MHz): δ 7.76 (br, 4H, C_6H_2 and C_6H_5), 7.65 (br, 2H, C_6H_2 and C_6H_5), 7.41 – 7.20 (br m, 10H, C_6H_2 and C_6H_5), 7.15 – 7.00 (m, 20H, C_6H_2 and C_6H_5), 6.88 (s, 2H, CHPh_2), 6.47 (s, 2H, CHPh_2), 1.06 (s, 18H, CMe_3), 0.24, -0.02 (br s, 6H, SiMe_2). $^{13}\text{C}\{^1\text{H}\}$ NMR (C_6D_6 , 150 MHz): δ 147.5, 146.1, 142.3, 132.1, 130.7, 129.6, 128.6 (C_6H_5 and C_6H_2), 34.1 (CMe_3), 31.5 (CMe_3), 5.0, 4.2 (SiMe_2). Many resonances not observed due to peak broadening.

3.5.2. Synthesis of Bismuth(III) Chalcogenides

Generation of mixture containing $[\text{Bi}(\text{NON}^{\text{tBu}})]_2(\mu\text{-S})$ (**3.18a**) and $[\text{Bi}(\text{NON}^{\text{tBu}})]_2(\mu\text{-S}_3)$ (**3.19a**)

A suspension of S_8 (0.0076 g, 0.030 mmol) in hexane (5 mL) was added drop wise to a solution of **2.17a**₂ (0.105 g, 0.108 mmol) in hexane (5 mL), resulting in a gradual colour change from orange to yellow over 30 minutes. Concentration of the resulting solution *in vacuo* to ca. 1mL followed by storage at $-30\text{ }^\circ\text{C}$ gave a mixture of yellow crystals of **3.18a** (major ~90 %) and colourless crystals of **3.19a** (minor ~10 %). The crystals were separated by hand under a microscope and analysed by single-crystal X-ray diffraction. Accurate elemental analysis could not be obtained due to the inseparable mixture of products. **3.18a**: ^1H NMR (C_6D_6 , 600 MHz): δ 1.35 (s, 18H, CMe_3), 0.50, 0.35 (s, 6H, SiMe_2). $^{13}\text{C}\{^1\text{H}\}$ NMR (C_6D_6 , 150 MHz): δ 53.5 (CMe_3), 37.4 (CMe_3), 7.4, 6.5 (SiMe_2). **3.19b**: ^1H NMR (C_6D_6 , 600 MHz): δ 1.33 (s, 18H, CMe_3), 0.48, 0.34 (s, 6H, SiMe_2). Insufficient compound was isolated to be analysed by ^{13}C NMR spectroscopy.

Generation of mixture containing $[Bi(NON^{Ar})]_2(\mu-S)$ (**3.18d**), $[Bi(NON^{Ar})]_2(\mu-S_3)$ (**3.19d**) and $[Bi(NON^{Ar})]_2(\mu-S_5)$ (**3.20d**)

A suspension of S_8 (0.0051 g, 0.020 mmol) in hexane (5 mL) was added drop wise to a solution of **2.17d**• (0.101 g, 0.146 mmol) in hexane (5 mL), resulting in a gradual colour change from deep red to yellow over 30 minutes. Concentration of the solution to *ca.* 1 mL followed by storage at -30 °C gave a mixture of yellow blocks (**3.18a**), yellow plates (**3.19a**) and yellow needles (**3.20a**). The crystals were separated by hand under a microscope and analysed by single-crystal X-ray diffraction. Accurate elemental analysis could not be obtained due to the inseparable mixture of products.

Synthesis of $[Bi(NON^{Ar\ddagger})(S_4)]_2$ (**3.21e**)₂

A suspension of S_8 (0.003 g, 0.085 mmol) in toluene (5 mL) was added drop wise to a solution of **2.17e**• (0.10 g, 0.077 mmol) in toluene (5 mL), resulting in a rapid colour change from deep red to yellow and formation of yellow precipitate over 5 minutes. Hot filtration of the suspension gave a clear yellow solution which was allowed to cool to room temperature resulting in a few yellow crystals. Concentration of the solution *in vacuo* followed by storage at -30 °C gave yellow crystals of **3.21e**₂. Yield 0.035 g, 32 %. Anal. Calcd. for $C_{152}H_{156}Bi_2N_4O_2S_8Si_4$ (2857.72): C, 63.89; H, 5.50; N, 1.96 %. Found: C, 64.01; H, 5.70; N, 1.95 %. ¹H NMR (C_6D_6 , 600 MHz): δ 7.82 (d, 8H, *J* = 7.5, *o*- C_6H_5), 7.63 (d, 4H, *J* = 7.5, C_6H_2), 7.19 – 7.13 (m, 46H, C_6H_5) 7.08 – 7.03 (m, 34H, C_6H_5), 6.98 (s, 4H, *m*- C_6H_5), 6.43 (s, 4H, $CHPh_2$), 1.09 (s, 36H, CMe_3), 0.21, -0.09 (s, 12H, $SiMe_2$). ¹³C{¹H} NMR (C_6D_6 , 150 MHz): δ 147.5, 147.3, 146.9, 146.4, 145.9, 143.7, 142.4, 141.3, 131.8, 131.4, 130.8, 130.2, 129.5, 128.5, 126.7, 126.6 (C_6H_5 and C_6H_2), 52.1, 51.1 ($CHPh_2$), 34.3 (CMe_3), 31.7 (CMe_3), 4.6, 4.3 ($SiMe_2$).

*Synthesis of [Bi(NON^{tBu})]₂(μ-Se) (**3.22a**)*

Powdered selenium (0.016 g, 0.21 mmol) was added to a solution of [**2.17a**]₂ (0.040 g, 0.042 mmol) in Et₂O (10 mL) and stirred for 24 hours at room temperature, after which time the volatiles were removed *in vacuo*. Extraction into hexane gave a suspension which was filtered through celite to give an orange solution. Concentration to approx. 1 mL followed by storage at -30 °C overnight gave yellow crystals of **3.22a**. Yield 0.029 g, 65 %. Anal. Calcd. for C₂₄H₆₀Bi₂N₄O₂SeSi₄ (1046.26): C, 27.56; H, 5.78; N, 5.36 %. Found: C, 27.39; H, 5.83; N, 5.25 %. ¹H NMR (C₆D₆, 600 MHz) δ 1.35 (s, 18H, CMe₃), 0.61, 0.40 (s, 6H, SiMe₂). ¹³C{¹H} NMR (C₆D₆, 150 MHz) δ 54.3 (CMe₃), 36.6 (CMe₃), 7.6, 6.9 (SiMe₂).

*Synthesis of [Bi(NON^{Ar})]₂(μ-Se) (**3.22d**)*

Powdered selenium (0.023 g, 0.29 mmol) was added to a solution of **2.17d**• (0.050 g, 0.072 mmol) in Et₂O (10 mL) and stirred for 24 hours at room temperature, after which time the volatiles were removed *in vacuo*. Extraction into hexane gave a suspension which was filtered through celite to give an orange solution. Concentration to approx. 1 mL followed by storage at -30 °C overnight gave orange crystals of **3.22d**. Yield 0.035 g, 67 %. Anal. Calcd. for C₅₆H₉₂BiN₄O₂SeSi₄ (1462.64): C, 45.99; H, 6.34; N, 3.83 %. Found: C, 46.18; H, 6.18; N, 3.96 %. ¹H NMR (C₆D₆, 600 MHz) δ 7.13, 6.98 (d, *J* = 7.5, 2H, *m*-C₆H₃), 6.91 (t, *J* = 7.5, 2H, *p*-C₆H₃), 4.00, 3.65 (sept, *J* = 6.7, 2H, CHMe₂), 1.24 (m, 18H, CHMe₂), 1.07 (d, *J* = 6.7, 6H, CHMe₂), 0.54, 0.26 (s, 6H, SiMe₂). ¹³C{¹H} NMR (C₆D₆, 150 MHz) δ 150.2, 147.1, 140.8, 125.8, 124.8, 124.1 (Ar-C), 27.8, 27.7, 27.5, 27.4, 26.2, 26.0 (CHMe₂ and CHMe₂), 4.1, 3.3 (SiMe₂).

*Synthesis of [Bi(NON^{tBu})]₂(μ-Te) (**3.23a**)*

Powdered tellurium (0.033 g, 0.26 mmol) was added to a solution of [**2.17a**]₂ (0.050 g, 0.052 mmol) in Et₂O (10 mL) and stirred for 78 hours at room temperature, after which time the

volatiles were removed *in vacuo*. Extraction into hexane gave a suspension which was filtered through celite to give a yellow solution. Concentration to approx. 2 mL followed by storage at -30 °C overnight gave yellow crystals of **3.23a**. Yield 0.031 g, 55 %. Anal. Calcd. for $C_{24}H_{60}Bi_2N_4O_2Si_4Te$ (1094.67): C, 26.33; H, 5.52; N, 5.12 %. Found: C, 26.18; H, 5.37; N, 5.01 %. 1H NMR (C_6D_6 , 600 MHz) δ 1.35 (s, 18H, CMe_3), 0.58, 0.38 (s, 6H, $SiMe_2$). $^{13}C\{^1H\}$ NMR (C_6D_6 , 150 MHz) δ 54.6 (CMe_3), 36.0 (CMe_3), 7.3, 5.8 ($SiMe_2$).

*Synthesis of $[Bi(NON^{Ar})]_2(\mu-Te)$ (**3.23d**)*

Powdered tellurium (0.037 g, 0.29 mmol) was added to a solution of **2.17d**• (0.050 g, 0.072 mmol) in Et_2O (10 mL) and stirred for 78 hours at room temperature, after which time the volatiles were removed *in vacuo*. Extraction into hexane gave a suspension which was filtered through celite to give an orange-red solution. Concentration to approx. 1 mL followed by storage at -30 °C overnight gave red crystals of **3.23d**. Yield 0.014 g, 26 %. Anal. Calcd. for $C_{56}H_{92}BiN_4O_2Si_4Te$ (1511.28): C, 44.51; H, 6.14; N, 3.73 %. Found: C, 44.39; H, 6.27; N, 3.73 %. 1H NMR (C_6D_6 , 600 MHz) δ 7.10, 7.02 (dd, $J = 7.6$ and 1.5 , 2H, $m-C_6H_3$), 6.87 (t, $J = 7.6$, 2H, $p-C_6H_3$), 3.89, 3.74 (sept, $J = 6.6$, 2H, $CHMe_2$), 1.28, 1.21, 1.18, 1.14 (d, $J = 6.6$, 6H, $CHMe_2$), 0.57, 0.22 (s, 6H, $SiMe_2$). $^{13}C\{^1H\}$ NMR (C_6D_6 , 150 MHz) δ 150.7, 147.9, 141.5, 125.9, 124.9, 124.0 ($Ar-C$), 29.5, 27.8, 27.6, 27.4, 26.1, 26.0 ($CHMe_2$ and $CHMe_2$), 4.4, 2.7 ($SiMe_2$).

3.5.3. Synthesis of Bismuth(III) TEMPOxide Species

Synthesis of Bi(NON^{tBu})(OTEMP) (3.24a)

A solution of TEMPO (0.049 g, 0.32 mmol) in hexane (5 mL) was added dropwise to a solution of **[2.17a]₂** (0.15 g, 0.16 mmol) in hexane (5 mL) resulting in an immediate colour change from orange-red to pale yellow. The resulting solution was concentrated *in vacuo* to ca. 1 mL and stored at -30 °C overnight to give orange crystals of **3.24a**. Yield 0.164 g, 82 %. Anal. Calcd. for C₃₇H₆₄BiN₃O₂Si₂ (639.78): C, 39.42; H, 7.56; N, 6.57. Found C, 39.43; H, 7.68; N, 6.43. ¹H NMR (C₆D₆, 600 MHz, 298 K): δ 1.48 (br, 4H, CH₂), 1.35 – 1.20 (br, 2H, CH₂), 1.32 (br, 12H, CMe₂) 1.27 (s, 18H, CMe₃), 0.55, 0.43 (s, 6H, SiMe₂). ¹H NMR (C₆D₆, 600 MHz, 333 K): δ 1.48 (d, *J* = 7.6, 4H, CH₂), 1.41 (br, 2H, CH₂) 1.32 (br, 12H, CMe₂) 1.27 (s, 18H, CMe₃), 0.50, 0.41 (s, 6H, SiMe₂). ¹³C{¹H} NMR (C₆D₆, 600 MHz): δ 59.92 (CMe₂), 53.12 (CMe₃), 40.59 (CH₂), 37.29 (CMe₃), 17.63 (CH₂), 8.16, 6.53 (SiMe₂).

Synthesis of Bi(NON^{Ar})(OTEMP) (3.24d)

A solution of TEMPO (0.023 g, 0.15 mmol) in hexane (5 mL) was added dropwise to a solution of **2.17d•** (0.10 g, 0.15 mmol) in hexane (5 mL) resulting in an immediate colour change from deep red to orange. The resulting solution was concentrated *in vacuo* to ca. 1 mL and stored at -30 °C overnight to give orange crystals of **3.24d**. Yield 0.079 g, 64 %. Anal. Calcd. for C₃₇H₆₄BiN₃O₂Si₂ (848.09): C, 52.40; H, 7.61; N, 4.95 %. Found C, 52.36; H, 7.57; N, 5.10 %. ¹H NMR (C₇D₈, 300 MHz, 263 K): δ 7.23 (d, *J* = 7.6, 2H, *m*-C₆H₃)*, 6.93 (t, *J* = 7.6, 2H, *p*-C₆H₃), 4.05, 3.77 (sept, *J* = 6.7, 2H, CHMe₂), 1.62 (d, *J* = 6.7, 6H, CHMe₂), 1.37 (m, 12H, CHMe₂), 1.25 (d, *J* = 6.7, 6H, CHMe₂), 1.11 (br, 6H, CMe₂), 0.91 (br, 6H, CMe₂), 0.55, 0.33 (s, 6H, SiMe₂). ¹H NMR (C₇D₈, 300 MHz, 313 K): δ 7.00 (t, *J* = 7.6 Hz, 2H, *p*-C₆H₃), 3.90 (br, 4H, CHMe₂), 1.48 (br, 12H, CMe₂), 1.28 (d, *J* = 6.7 Hz, 18H, CHMe₂), 0.4 (s, 6H, SiMe₂). ¹³C{¹H} NMR (C₆D₆, 75 MHz): δ 59.9

(CMe₂), 53.1 (CMe₃), 40.6 (CH₂)*, 37.3 (CMe₃), 17.6 (CH₂), 8.2, 6.5 (SiMe₂). *two overlapping resonances.

*Synthesis of Bi(NON^{Ar±})(OTEMP) (**3.24e**)*

A solution of TEMPO (0.025 g, 0.16 mmol) in hexane (5 mL) was added dropwise to a solution of **2.17e•** (0.205 g, 0.16 mmol) in hexane (5 mL) resulting in an immediate colour change from deep red to orange. The resulting solution was concentrated *in vacuo* to ca. 1 mL and stored at -30 °C overnight to give orange crystals of **3.24e**. Yield 0.207 g, 89 %. ¹H NMR (C₇D₈, 600 MHz): δ 7.71 (br, 8H, C₆H₅), 7.58 (s, 4H, C₆H₂), 7.35 (br, 8H, C₆H₅), 7.16 – 7.05 (m, 20H, C₆H₅) 8.60 (br, 2H, *p*-C₆H₃), 6.82 (br, 4H, CHPh₂), 1.48 (br, 12H, CMe₂), 1.51 – 1.00 (m, 18H, CMe₂ and CH₂), 1.18 (s, 18H, CMe₃), 0.08 (s, 12H, SiMe₂). ¹³C{¹H} NMR (C₇D₈, 150 MHz): δ 146.8, 146.1, 145.5, 142.8, 141.7, 140.8, 131.5, 129.9, 127.0, 126.7, 126.1 (C₆H₅ and C₆H₂), 51.0 (CHPh₂), 33.7 (CMe₃), 31.2 (CMe₃), 4.7 (SiMe₂).

Stoichiometric reaction of Bi(NON^R)(OTEMP) with phenylsilane

A J. Young's NMR tube was charged with a solution of Bi(NON^R)(OTEMP) (R = *t*Bu (**3.24a**, 0.04 mmol), Ar (**3.24d**, 0.04 mmol), Ar* (**3.24e**, 0.02 mmol), followed by the addition of a single equivalent of PhSiH₃. The reaction was heated to 70 °C and the ¹H NMR spectrum measured at regular intervals over a 24 hour period.

General procedure for catalysis:

[**2.17a**]₂ (0.011 g, 0.013 mmol), **2.17d•** (0.008 g, 0.013 mmol) or **2.17e•** (0.017 g, 0.013 mmol) was added to a Young's NMR tube containing a mixture of TEMPO (0.020 g, 0.13 mmol) and PhSiH₃ (0.005 g, 0.13 mmol) in C₆D₆ (0.5 mL). The reaction mixture was heated to 70 °C and monitored at regular intervals using ¹H NMR spectroscopy.

3.5.4. Reactivity of Bismuth(II) Species with White Phosphorus (P₄)

Synthesis of [Bi(NON^{Ar})]₂(P₄) (3.25d)

NMR scale:

To a Young's NMR tube charged with **2.17d**• (0.03 g, 0.043 mmol) in C₆D₆ was added P₄ (0.015 g, 0.12 mmol). The mixture was allowed to react for 30 minutes followed by analysis by NMR spectroscopy.

Preparative scale (0.5 equiv. P₄):

A solution of P₄ (0.018 g, 0.15 mmol) in toluene (5 mL) was added to a solution of **2.17d**• (0.20 g, 0.29 mmol) in toluene (5 mL). The deep red solution was stirred for 2 hours, followed by *in vacuo* removal of the volatiles to give an orange powder. Orange/red crystals of **3.25d** were obtained by recrystallization from a mixture of Et₂O and hexane (9:1) at -30 °C. Yield 0.13 g, 60 %. Anal. Calcd. for C₅₆H₉₂Bi₂N₄O₂P₄Si₄ (1506.49): C, 44.62; H, 6.15; N, 3.72 %. Found: C, 44.30; H, 6.05; N, 3.81%. ¹H NMR (C₇D₈, 300 MHz, 233 K): δ 7.25 (d, *J* = 7.2, 4H, C₆H₃), 6.97 (m, 4H, C₆H₃), 6.84 (d, *J* = 7.2, 4H, C₆H₃), 3.95, 3.62 (m, 4H, CHMe₂), 1.61, 1.35, 1.20, 1.13 (d, *J* = 6.5, 12H, CHMe₂), 0.49, 0.24 (s, 12H, SiMe₂). ¹H NMR (C₇D₈, 300 MHz, 298 K): δ 7.29 (m, 4H, C₆H₃), 7.02 (m, 4H, C₆H₃), 6.94 (m, 4H, C₆H₃), 3.92, 3.65 (br, 4H, CHMe₂), 1.60 – 1.05 (m, 48H, CHMe₂), 0.47, 0.26 (s, 12H, SiMe₂). ³¹P{¹H} NMR (C₇D₈, 121 MHz, 233 K): δ -347.5 (t, *J*_{PP} = 164), -110.2 (t, *J*_{PP} = 164). ³¹P{¹H} NMR (C₇D₈, 121 MHz, 298 K): δ -350.3 (t, *J*_{PP} = 164), -107.2 (t, *J*_{PP} = 164). UV-vis (-40 °C): λ (ε): 405 nm (ε not determined as the exact concentration of **3.25d** is unknown).

*Synthesis of [Bi(NON^{Ar})]₂(P₄)(NHC^{mes}) (**3.27d**)*

Method 1: from **3.25d**

A solution of :C{N(Ar)CH₂}₂ (NHC^{mes}, 0.021 g, 0.054 mmol) was added to a solution of **3.25d** (0.081 g, 0.054 mmol) in Et₂O (4 mL), resulting in an immediate colour change from orange to red. Concentration of the solution to ca. 1 mL and storage at -30 °C gave red crystals of **3.27d** after 24 hours. Yield 0.045 g, 44 %.

Method 2: from P₄, NHC^{mes} and **2.17d•**

A solution of C{N(Ar)CH₂}₂ (NHC^{mes}) (0.043 g, 0.11 mmol) in Et₂O (3 mL) was added to a solution of P₄ (0.014 g, 0.11 mmol) in Et₂O (4 mL), giving a blue solution. This solution was stirred at room temperature for 4h followed by addition of a solution of **2.17d•** (0.152 g, 0.22 mmol) in Et₂O (5 mL), resulting in an immediate colour change from blue to red. Concentration of the solution to ca. 3 mL and storage at -30 °C gave red crystals of **3.27d** after 24 hours. Yield 0.076 g, 37 %. ¹H NMR (C₆D₆, 600 MHz): δ 7.45 (d, *J* = 7.2, 1H, C₆H₃), 7.30 – 7.20 (m, 4H, C₆H₃), 7.10 – 6.75 (m, 6H, C₆H₃), 6.87 (t, *J* = 7.2, 1H, C₆H₃), 6.67 (s, 2H, C₆H₂), 6.60, 6.22 (s, 1H, C₆H₂) 4.39, 4.25, 4.12, 4.08, 4.02, 3.98, 3.63, 3.52 (sept, 2H, *J* = 7.2 Hz, CHMe₂), 2.87, 2.80 (m, 2H, CH₂), 2.73 (m, 4H, CH₂), 2.22, 2.18, 2.09 (s, 3H, *o*-Me), 1.90 (d, 3H, *J* = 7.2 Hz, CHMe₂), 1.88 (s, 3H, *o*-Me), 1.56 (m, 12H, CHMe₂ and *o*-Me), 1.50 (d, 6H, *J* = 7.5, CHMe₂), 1.43 (m, 9H, CHMe₂), 1.38, 1.35 1.28 (d, 3H, *J* = 7.5, CHMe₂), 0.86, 0.64, 0.56, 0.34, 0.29, 0.10, 0.06, 0.05 (s, 3H, SiMe₂). ¹³C{¹H} NMR (C₆D₆, 150 MHz): δ 152.4, 150.7, 150.1, 149.6, 148.9, 148.5, 147.8, 146.8, 143.4, 143.1, 142.8, 142.6, 138.4, 137.9, 136.5, 136.0, 134.4, 131.2, 130.9, 130.1, 126.3, 125.5, 125.4, 124.9, 124.8, 124.5, 124.3, 124.0, 123.6, 123.5, 123.0 (C₆H₂ and C₆H₃), 51.1, 48.8 (CH₂), 28.9, 27.9, 27.7, 27.6, 27.5, 27.2, 27.0, 26.9, 26.7, 26.5, 26.0, 25.4, 25.3, 24.0, 21.2, 21.0, 18.6, 18.2, 17.8, 17.1 (CHMe₂, CHMe₂, *p*-Me and *o*-Me), 6.3*, 4.9, 4.0, 3.2, 2.4, 1.5, 1.0 (SiMe₂). ³¹P{¹H} NMR (C₆D₆, 121 MHz): δ -0.65 (ddd, *J*_{PP} = 300, 210 and 18), -141.0 (ddd, *J*_{PP} = 215, 200, 18), -

153.0 (dt, J_{pp} = 215, 200 and 146), -189.7 (ddd, J_{pp} = 300, 200 and 146). *two overlapping resonances

3.5.5. Reactivity of Bismuth(II) Species with Unsaturated Substrates

*Synthesis of [Bi(NON^{Ar})]₂(HC=C(C₆H₄-4-*t*Bu)) (3.28d)*

A solution of 4-*t*Bu-C₆H₄C≡CH (0.003 g, 0.023 mmol) in C₆D₆ (0.5 mL) was added to a J. Young's NMR tube charged with **2.17d•** (0.032 g, 0.046 mmol) in C₆D₆ (0.5 mL). Removal of the volatiles *in vacuo* gives a red oily residue. Addition of THF (*ca.* 1 mL) followed by storage at -30 °C gave yellow crystals of **3.28d**. Yield 0.015 g, 42 %. ¹H NMR (C₆D₆, 600 MHz) δ 10.51 (s, 1H, HC=C), 7.10 – 7.00 (m, 10H, C₆H₃ and C₆H₄), 3.98, 3.87, 3.81, 3.69 (sept, J = 6.6, 2H, CHMe₂), 1.41 (m, 9H, CMe₃), 1.37, 1.31, 1.26, 1.24, 1.15, 1.06, 0.71, 0.54 (d, 6H, J = 6.6, CHMe₂), 0.49, 0.30, 0.21, 0.14 (s, 6H, SiMe₂).

Synthesis of [Bi(NON^{Ar})]₂(C₁₄H₈O₂) (3.29d)

A solution of 9,10-anthraquinone (0.008 g, 0.036 mmol) in THF was added to a solution of **2.17d•** (0.050 g, 0.072 mmol) in Et₂O (0.5 mL). Removal of the volatile components *in vacuo* gave a dark purple residue. Single crystals of sufficient quality for X-ray diffraction were obtained by storage of a concentrated THF / toluene (1 : 1) solution at -30 °C gave purple-red of **3.29d**. Yield 0.023 g, 40 %. ¹H NMR (C₆D₆, 600 MHz) δ 7.15 – 7.0 (m, 16H, C₆H₃ and C₁₄H₈), 6.97 (t, 4H, J = 7.2, *p*-C₆H₃), 3.98, 3.81 (sept, J = 6.8, 4H, CHMe₂), 1.33, 1.19, 1.12, 0.51 (d, J = 6.8, 12H, CHMe₂), 0.90, 0.27 (s, 6H, SiMe₂). ¹³C{¹H} NMR (C₆D₆, 150 MHz): 150.7, 147.0, 133.7, 127.2, 126.4, 123.8 (C₆H₃ and C₁₄H₈*), 28.2, 28.1, 27.7, 25.7, 24.9 (CHMe₂ and CHMe₂), 5.3, 2.5 (SiMe₂). *some aromatic peaks not observed due to poor solubility.

Chapter 4. Synthesis of Low Oxidation State Antimony Species

4.1. Introduction

4.1.1. Bimetallic and Polymetallic Low Valent Antimony[†]

Despite the fact that antimony and bismuth are in the same group of the periodic table, the molecular and bulk properties of these two elements differ considerably.¹¹⁰ Sb-X (X = C, N, O, P etc.) bonding interactions are often significantly more stable than their heavier Bi analogues (Section 1.1) as a result of less diffuse frontier orbitals and reduced core-core repulsion. The inert pair effect also plays a lesser role in the chemistry of antimony compared to bismuth, highlighted by a more prevalent and accessible +5 oxidation state.⁸ However, like bismuth, the chemistry of molecular antimony is dominated by the +3 oxidation state, formed through loss of the 5p electrons. The chemistry of antimony in the +1 and +2 oxidation states is much more developed than bismuth, due in part to the smaller size of antimony (allowing easier kinetic stabilisation) and more the favourable Sb-Sb and Sb-X (X = C, N, O etc.) bond enthalpies.¹¹⁰

Like their bismuth analogues, early reports of low oxidation state antimony compounds featuring Sb-Sb single bonds focussed on distibanes $\{R_2Sb\}_2$ (R = Me, Et, Ph) and oligomeric monoorganoantimony(I) $\{RSb\}_n$ compounds (Figure 4.1a). The relative stability of Sb-Sb and Bi-Bi bonded species is illustrated by the stability of tetramethyldipnictogens $\{Me_2M\}_2$ (M = Sb, Bi). Tetramethyldistibane ($\{Me_2Sb\}_2$) is stable in solution when heated to 100 °C for weeks, whereas $\{Me_2Bi\}_2$ decomposes at 25 °C in hours.⁷³ Similar to their bismuth analogues, monoorganoantimony(I) species $\{RSb\}_n$ commonly oligomerise into compounds featuring several Sb-Sb bonds arranged in a cyclic Sb_n core. The importance of the steric bulk of the R

[†] Although sometimes considered as a 'metalloid', in this thesis we will define antimony as a group 15 metallic element.

substituents on the stability of the different sized rings is highlighted by the bulkier $\text{CH}(\text{SiMe}_3)_2$ and $t\text{Bu}$ substituents resulting in three- and four-membered rings, while the smaller CH_2tBu and Ph substituents allow formation and isolation of the six-membered rings.^{60a, 72, 111} These species are stable in the solid-state, but may rearrange in solution. This was evidenced by a study on $\text{cyclo}-(\text{SbR})_6$ ($\text{R} = o\text{-tolyl}, m\text{-tolyl}$ or $p\text{-tolyl}$) which undergoes spontaneous redistribution in solution to give either the tetramer or pentamer as the major species, depending on the concentration of the solution (Figure 4.1b).¹¹²

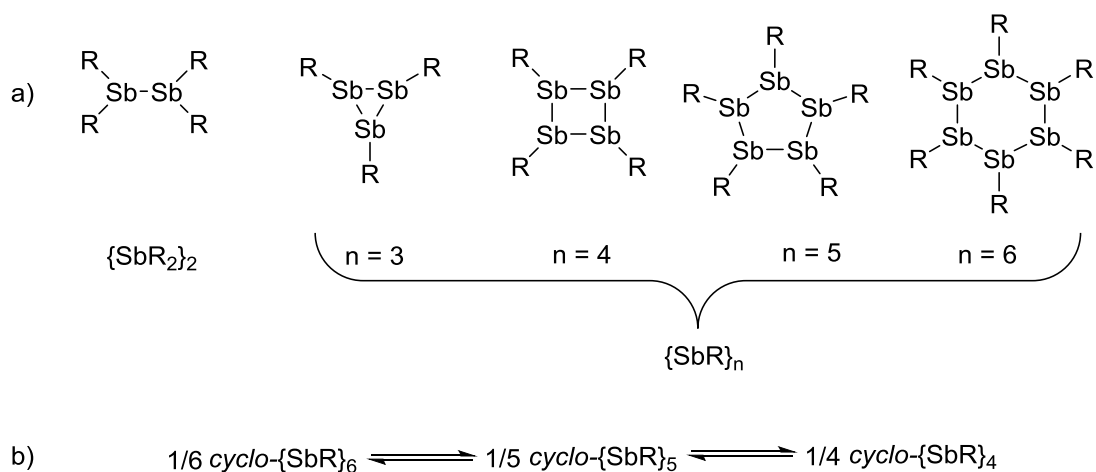


Figure 4.1. (a) General structures for low-valent antimony compounds featuring homonuclear Sb-Sb bonds and (b) Redistribution of $\text{cyclo-}\{\text{SbR}\}_6$ in solution.

Within the last 20 years, the development of ligands capable of providing increased steric bulk has allowed for the isolation of distibene complexes featuring $\text{Sb}=\text{Sb}$ bonds. Despite the apparent increase in $\text{Sb}=\text{Sb}$ and $\text{Sb}-\text{X}$ ($\text{X} = \text{C}, \text{N}, \text{O}, \text{P}$) bond strength compared with bismuth, only 8 unsupported (i.e. not metal stabilised) distibenes have been structurally characterised. Most of these utilise bulky aromatic substituents to stabilise double bond formation and prevent oligomerisation (Figure 4.2, **4.1** to **4.6**),^{38a, 38b, 39, 113} with the only exceptions being the distibenes $[\text{Sb}(\text{N}\{\text{Si}(i\text{Pr})_3\}\text{Ar}^\bullet)]$ (**4.7**)⁴⁰ and $[\text{Sb}\{\text{Ga}(\text{BDI}^{\text{Ar}})(\text{NMe}_2)\}]_2$ (**4.8**),¹¹⁴ which are stabilised by bulky amido- and gallyl-ligands, respectively. The $\text{Sb}=\text{Sb}$ bond distances (2.642(1) – 2.710(1) Å) are 4.4 - 9.5 % shorter than typical Sb-Sb bonds, with the stabilising ligands arranged *trans* about the distibene core.

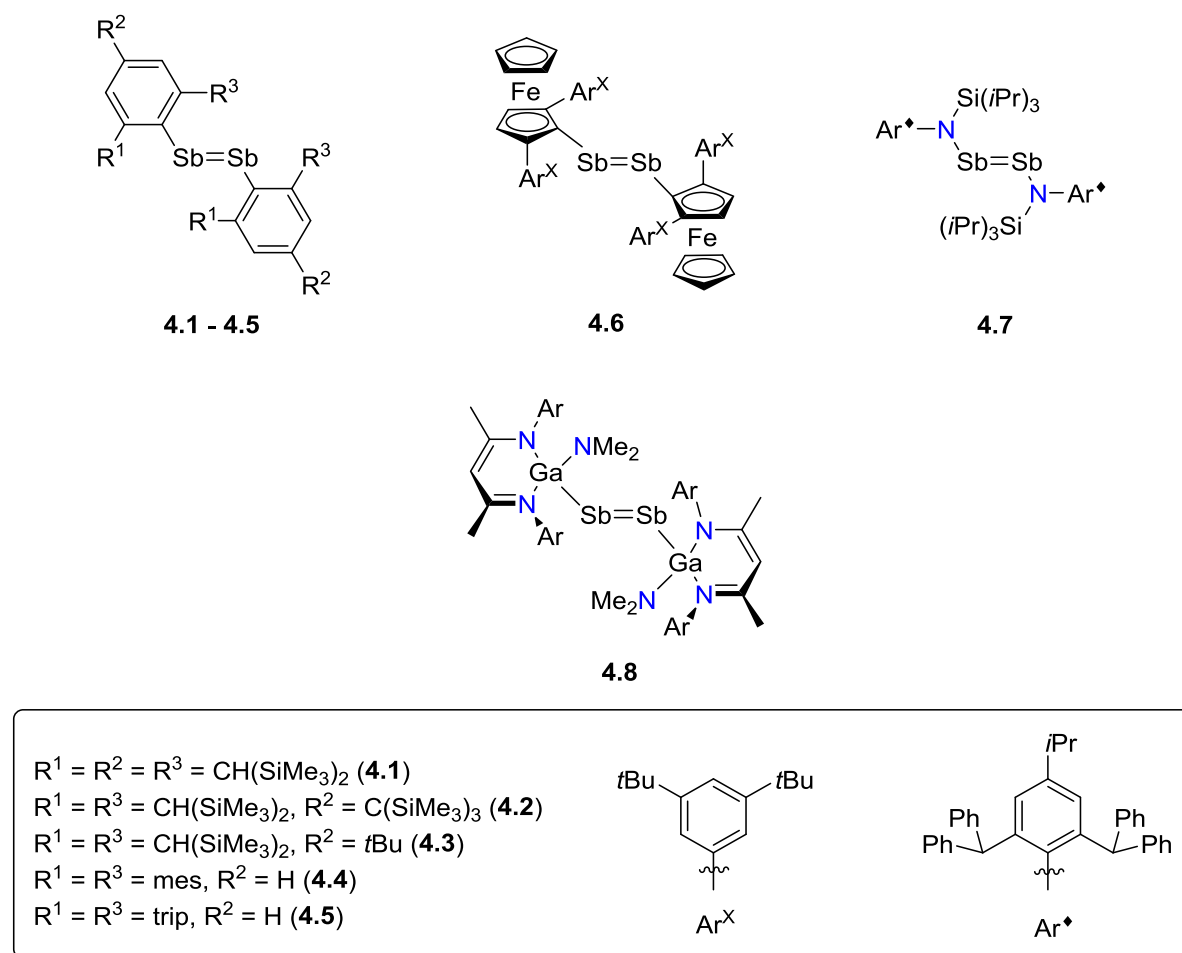


Figure 4.2. Structurally characterised distibenes supported by bulky ligands.

4.1.2. Monometallic Low Valent Antimony

Like their heavier bismuth analogues, stable low valent antimony species with no covalent Sb-Sb bonding interactions are rare. Studies of isolated monomeric antimony(I) species (RSb:) and antimony(II) radicals ($\text{R}_2\text{Sb}^\bullet$) were, until recently, limited to the use of low temperature matrix isolation techniques and IR spectroscopy to investigate their structure and properties.¹¹⁵ While examples of Sb(I) donor atoms coordinated to transition metals, prepared from the *in-situ* release of monomeric RSb: fragments from oligomeric antimony(I) compounds, were reported as early as 1978,¹¹⁶ persistent free (non-coordinated) stibinidenes remain rare. Persistent antimony(II) radicals are also rare, but have been inferred as transient intermediates in the rearrangement of *cyclo*- $\{\text{RSb}\}_n$ ($n = 4$ to 6) species (Figure 4.1b) through homolytic cleavage of the Sb-Sb bonds and subsequent radical coupling to form new Sb-Sb

bonds. In addition, the irradiation of $\{\text{Ph}_2\text{Sb}\}_2$ using UV light was proposed to result in the formation of $\text{Ph}_2\text{Sb}^\bullet$ through homolysis of the Sb-Sb bond, which can be trapped by reaction with alkyl iodides.¹¹⁷

In 2010, Dostál and co-workers reported the isolation of the first neutral[†] stibinidene $\text{Sb}(\text{2,6}-(\text{CH}=\text{NAr}')_2\text{C}_6\text{H}_3)$ ($\text{Ar}' = \text{2,6-Me}_2\text{C}_6\text{H}_3$, Figure 4.3, **4.9**), stabilised by a bulky *N,C,N*-pincer ligand capable of forming strong $n(\text{N})$ to $p^*(\text{Bi})$ interactions to stabilise the monomeric antimony centre.^{45, 90} Following this report, examples of stable stibinidines supported by carbenes (**4.10** and **4.11**) were reported.¹¹⁸ In both cases, two extreme canonical forms are possible: 1) a stibaalkene involving a $\text{Sb}=\text{C}$ bond or 2) a carbene stabilised stibinidene. While the Sb-C(carbene) distances (**4.10**, 2.068(6) Å; **4.11**, 2.082(5) Å) suggest partial double bond character ($\Sigma_{\text{cov}}(\text{Sb-C}) = 2.15$ Å), theoretical studies showed that the Sb-C bond is best described as σ -donation from the carbene to the antimony, with only weak back donation from the antimony lone pair.

Until recently, only two persistent antimony(II) radical species were reported in the literature. While neither could be isolated in the solid-state, EPR analysis was consistent with formation of a radical species. Ishida, Iwamoto and co-workers reported the solution-state characterisation (NMR, EPR and UV-visible spectroscopies) of the antimony(II) radical $\bullet\text{Sb}(\text{C}\{(\text{SiMe}_3)_2\text{CH}_2\}_2)$ (**4.12•**), featuring considerable radical character on the metal centre. However, at low temperatures in solution and in the solid-state, the compound reversibly dimerises to form the distibane [**4.12**]₂, which features a very long Sb-Sb bond (3.0297(4) Å). The other room temperature stable antimony(II) radical species was stabilised by a cyclic(alkyl)amino carbene (CAAC) ligand (**4.13•**).^{118a} Surprisingly, EPR analysis and DFT calculations suggested only minor spin-delocalisation, with over 90% of the spin density on

[†] Examples of ionic stibinidines $[\text{R}_2\text{Sb:}][\text{M}(\text{L})_n]$ (where R = alkyl/aryl, M = group 1 metal, L = donor ligand), where the antimony is formally in the +1 oxidation-state are well known. However, these are excluded from the discussion for simplicity.

the antimony centre. This contrasts other carbene-stabilised main group radicals in which the spin density is localised on the carbene fragment.¹¹⁹

Neither **4.12•** or **4.13•** could be isolated in the solid-state, and were not structurally characterised. Schulz and co-workers recently reported the first structurally authenticated antimony(II) radical species $\bullet\text{Sb}\{\text{Ga}(\text{Cl})(\text{BDI}^{\text{Ar}})\}_2$ (**4.14•**), stabilised by bulky gallyl ligands. This species is surprisingly stable, and can be stored in solution for months at room temperature. DFT was used to show that the unpaired electron is predominantly antimony centred (80 %), with small but significant spin delocalisation onto the adjacent gallium centres (16 %).

4.2. Chapter Outline

The work described in this chapter aims to investigate the low oxidation state chemistry of antimony (i.e. Sb(I) and Sb(II) species) supported by the (NON^R)-ligand. Analogous to chapter 2, the effect of subtle changes to the steric and electronic properties of the (NON^R)-ligand on the reduced antimony species will be investigated. It is anticipated that the different steric and electronic properties provided by the ligands will allow isolation of rare and unprecedented low oxidation state antimony species. A similar pathway to that used in the synthesis of low oxidation state bismuth compounds was envisaged (chapter 2), involving the reduction of a Sb(III) chloride species using LiHBEt₃ or Mg metal as the reducing agent (Figure 1.3, Pathway 1 and 2). While both pathways have been demonstrated as viable routes to reduced antimony compounds, reductions involving antimony halides are typically significantly slower than their bismuth counterparts, due in part to the shorter/stronger Sb-X bonds (X = halide).

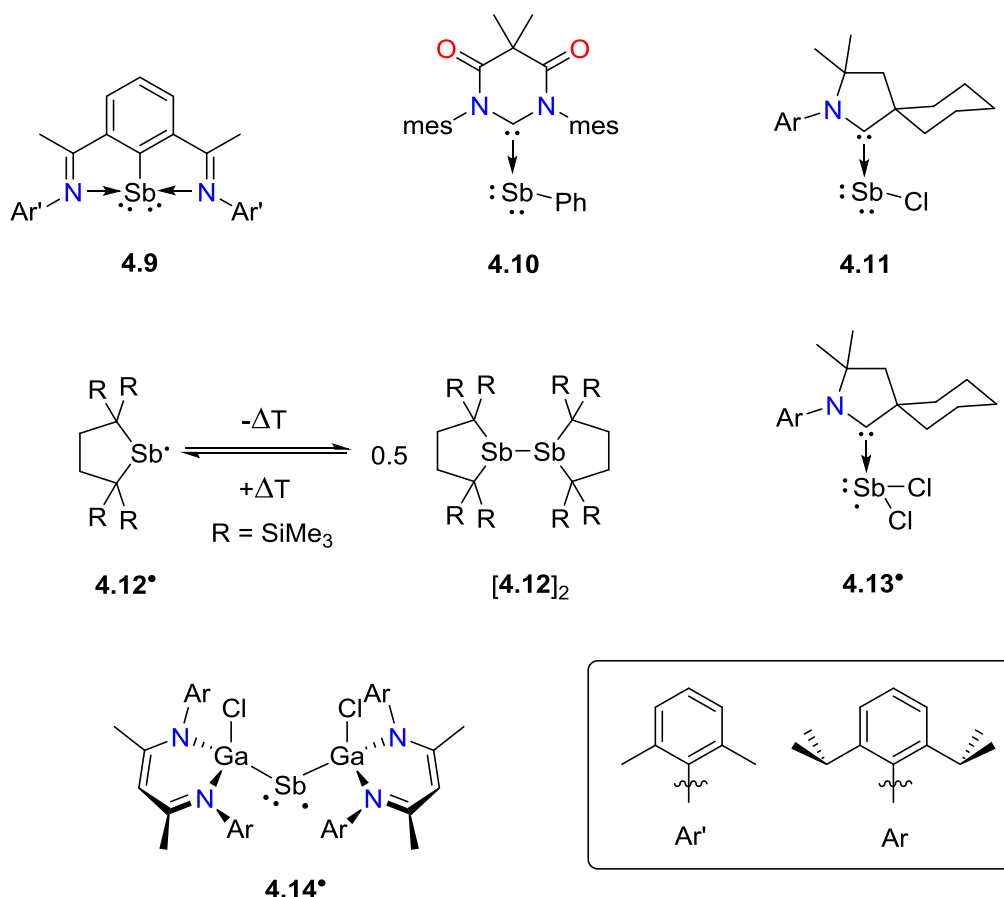


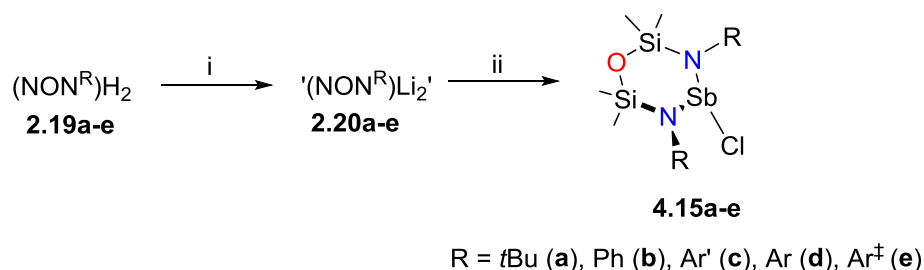
Figure 4.3. Reported monomeric antimony(I) and antimony(II) species.

4.3. Results and Discussion

4.3.1. Synthesis of Antimony(III) Chloride Species

Compounds containing Sb-Cl bonds have been demonstrated to be viable precursors to low oxidation state antimony species using a group 1 metal or Mg as reducing agents. The antimony(III) chlorides Sb(NON^R)Cl (Scheme 4.1, **4.15a-e**, R = *t*Bu (**a**), Ph (**b**), Ar' (**c**), Ar (**d**), Ar[‡] (**e**)) were prepared using similar methods to their bismuth analogues (Section 2.3.1). The addition of the *in-situ* generated '(NON^R)Li₂' salt to SbCl₃ at -30 °C, followed by warming to room temperature and stirring for 12 hours, gave the corresponding antimony(III) chlorides, Sb(NON^R)Cl, in low (for **4.15e**) to high yields (23 – 81 %) as colourless crystals after work-up. In contrast to the synthesis of **2.16c/2.23c**, no evidence of the bridged species

$[(\text{NON}^{\text{Ar}'})\text{Sb}]_2(\text{NON}^{\text{Ar}'})$ was detected in the ^1H NMR spectrum of the crude reaction mixture, allowing for the isolation of pure **4.15c** in good yields.



Scheme 4.1. Synthesis of **4.15a-e**. i) 2.2 $n\text{BuLi}$, Et_2O (**2.19a-d**) or toluene (**2.19e**), ii) SbCl_3 , Et_2O .

The ^1H NMR spectra of **4.15a-e** are similar to their bismuth counterparts. In all cases, the SiMe_2 protons are split into two singlets (δ_{H} : **4.15a**, 0.29 and 0.53; **4.15b**, 0.26 and 0.46; **4.15c**, 0.09 and 0.53; **4.15d**, 0.17 and 0.53; **4.15e**, 0.03 and 0.07) reflecting chelation of the (NON^{R}) -ligand to a pyramidal antimony centre. Two sets of resonances for the *o*-Me (singlet, δ_{H} 2.33 and 2.61) and CHMe_2 (septet, δ_{H} 3.70 and 4.17) protons of **4.15c** and **4.15d**, respectively, are also observed.

The solid-state structures of **4.15a-e** were determined using X-ray crystallography (Figure 4.4 and Table 4.1). The crystal structures of **4.15c** and **4.15e** are isomorphous with the corresponding bismuth analogues, while **4.15a**, **4.15b** and **4.15d** crystallise with a different unit cell to their bismuth counterparts. All of the structures show $\kappa_2\text{-N,N'}$ -bidentate coordination to the pyramidal antimony centre ($\Sigma(\angle\text{Sb})$: $290.9^\circ - 298.9^\circ$), with a relatively narrow distribution of Sb-N distances (2.011(2) – 2.067(3) Å). **4.15a** crystallises with two essentially identical molecules in the unit cell. Both molecules (denoted **4.15a-1** and **4.15a-2**) adopt boat conformations with relatively large N-Sb-N bite angles ($102.22(8)^\circ$ and $102.85(7)^\circ$), similar to those of **4a**. The metallacycles of **4.15b** and **4.15c** both form half-chair conformations, with either a nitrogen (**4.15b**) or antimony (**4.15c**) atom outside the plane of the ring. **4.15d** crystallises with three essentially identical molecules (**4.15d-1**, **4.15d-2** and **4.15d-3**) in the asymmetric unit while **4.15e** co-crystallises with four toluene molecules in the asymmetric unit. The conformations of the metallacycles in **4.15d** and **4.15e** are best

described as twist-boats, with similar bite angles (**4.15d**, 100.24(6)°, 100.38(6)° and 100.34(6)°; **4.15e**, 99.59(12)°).

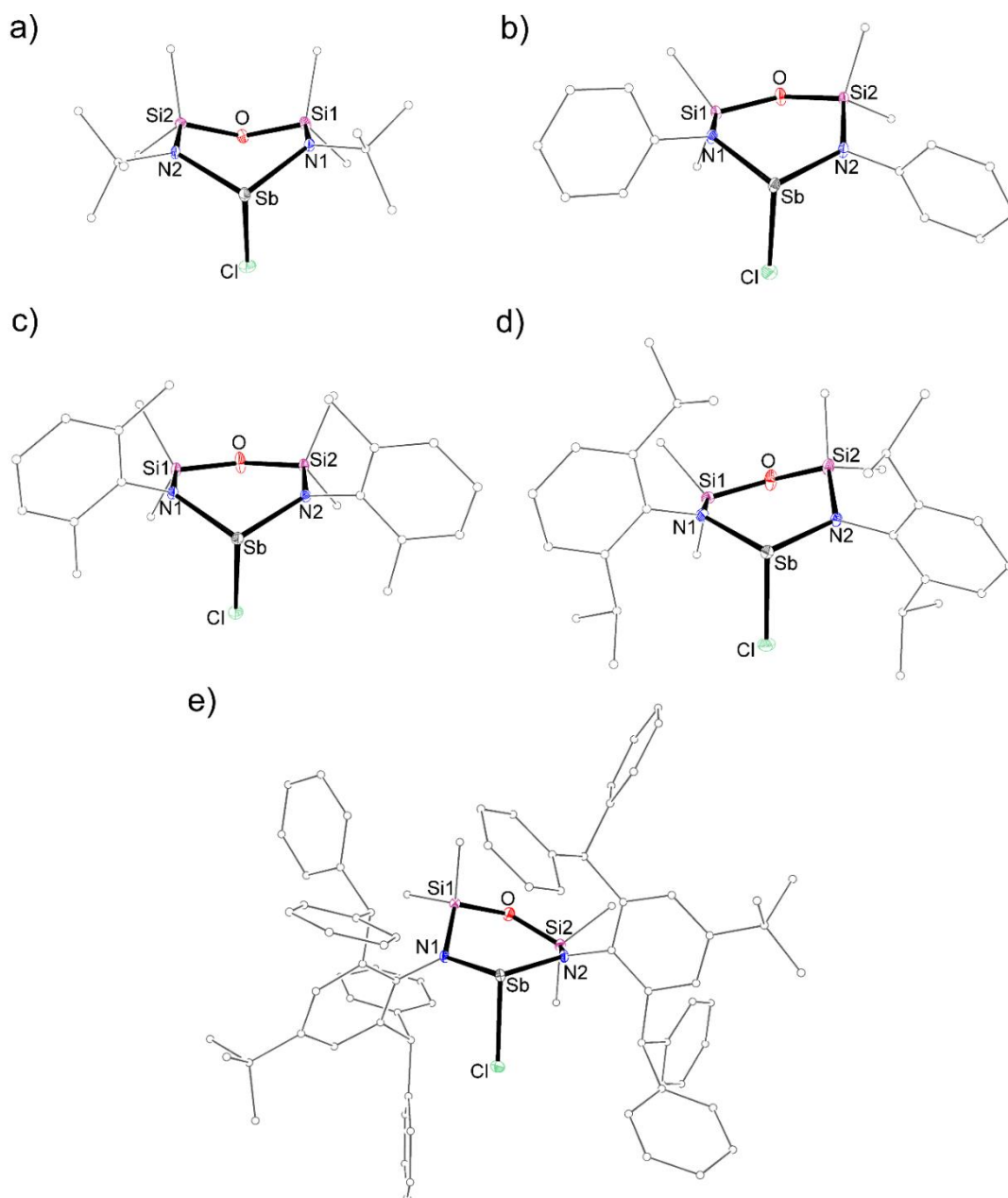


Figure 4.4. Molecular structures of **4.15a-e** (thermal ellipsoids displayed at 30% probability level). Hydrogen atoms, solvent molecules and the minor component of disorder in **4.15b** are omitted and carbon atoms are displayed in wireframe format for clarity. Representative molecules **4.15a-1** and **4.15d-1** are displayed. Selected bond lengths and angles are listed in Table 4.1.

In contrast to their bismuth analogues, the Sb-Cl bond distances in **4.15a-e** occupy a relatively narrow range (2.3941(6) – 2.4433(16) Å). These values are comparable to those observed in the related di(amido)antimony(III) chloride species $\text{Sb}\{\text{N}(\text{Ar})\}_2\text{SiMe}_2\text{Cl}$ and $\text{Sb}(\text{N}\{\text{SiMe}_3\}_2)_2\text{Cl}$ (2.390(2) and 2.405(1) Å), with the longer Sb-Cl bonds corresponding to the *t*Bu (**4.15a**, 2.4286(6) and 2.4378(6) Å) and Ph derivatives (**4.15b**, 2.4433(16) Å).¹²⁰ Investigation of the extended solid-state structures shows that **4.15a** forms single chain polymeric networks linked through long range Sb \cdots Cl interactions (**4.15a-1**, 4.2264(6) Å; **4.15a-2**, 4.1720(5) Å), while **4.15b** forms an inverse double-stranded ladder-like structure previously observed in **2.16b** with two long range Sb \cdots Cl interactions (Figure 4.5): one intra-chain interaction and one inter-chain interaction (3.9126(16) and 4.0727(10) Å, respectively). In contrast, **4.15c** forms a dimer in the solid-state, linked through Sb \cdots aryl interactions (Sb \cdots Ct_{C1'-C6'} 3.4799(13) Å), while both **4.15d** and **4.15e** exist as monomers in the solid-state, with no short intermolecular Sb \cdots Cl or Sb \cdots aryl contacts. The influence of long range Sb \cdots Cl interactions on the strength of the Sb-Cl bond is evidenced by the elongation in the Sb-Cl distances of **4.15a** and **4.15b** compared to **4.15c-e**. Like their bismuth analogues, the Sb \cdots Cl interactions in **4.15a** and **4.15b** can be described using $\Delta_{\text{Sb-Cl}}(1)$ and $\Delta_{\text{Sb-Cl}}(2)$ (for **4.15b** only), the difference between the Sb-Cl distances and the intra- and inter-chain Sb \cdots Cl contacts, respectively. Both values of $\Delta_{\text{Sb-Cl}}(1)$ for **4.15a-1** and **4.15a-2** (1.7978 and 1.7342 Å, respectively) are significantly larger than the $\Delta_{\text{Sb-Cl}}(1)$ value for **4.15b** (1.4693 Å), consistent with a stronger Sb \cdots Cl interaction in **4.15b**. The inter-chain Sb \cdots Cl interaction in **4.15b** ($\Delta_{\text{Sb-Cl}}(2)$, 1.6294 Å) is significantly weaker than the intra-chain interaction, but is still shorter than the contacts observed in **4.15a**. These values are significantly larger than those of **2.16a** and **2.16d'** (Section 2.3.1), consistent with a smaller metal centre with shorter Sb-Cl bonds and less Lewis acidic character.

Table 4.1. Selected Bond Lengths (Å) and Angles (°) for **4.15a-e**.

4.15a			
Sb1-N1	2.011(2)	Sb...Cl(1)	4.2264(6), 4.1720(5)
Sb1-N2	2.036(2)	$\Delta_{\text{Sb-Cl}}(1)$	1.7978, 1.7342
Sb2-N3	2.028(2)	N1-Sb1-N2	103.6(1)
Sb2-N4	2.022(2)	N3-Sb2-N4	102.85(7)
Sb1-Cl1	2.4286(6)	$\Sigma(\angle\text{Sb1})$	298.96
Sb2-Cl2	2.4378(6)	$\Sigma(\angle\text{Sb2})$	298.3
4.15b			
Sb-N1	2.013(3)	$\Delta_{\text{Sb-Cl}}(1)$	1.4693
Sb-N2	2.024(2)	$\Delta_{\text{Sb-Cl}}(2)$	1.6294
Sb-Cl	2.4433(16)	N1-Sb-N2	97.27(10)
Sb...Cl(1)	3.9126(16)	$\Sigma(\angle\text{Sb})$	292.76
Sb...Cl(2)	4.0727(10)		
4.15c			
Sb-N1	2.034(2)	Sb...Ct _{C1'-C6'}	3.4799(13)
Sb-N2	2.031(2)	N1-Sb-N2	99.61(9)
Sb-Cl	2.412(1)	$\Sigma(\angle\text{Sb})$	290.87
4.15d			
Sb1-N1	2.0395(13)	Sb3-Cl3	2.3942(5)
Sb1-N2	2.0265(12)	N1-Sb1-N2	100.24(6)
Sb2-N3	2.0298(12)	N3-Sb2-N4	100.38(6)
Sb2-N4	2.0323(13)	N5-Sb3-N6	100.34(6)
Sb3-N5	2.0251(12)	$\Sigma(\angle\text{Sb1})$	295.67
Sb3-N6	2.0308(12)	$\Sigma(\angle\text{Sb2})$	293.45
Sb1-Cl1	2.3941(6)	$\Sigma(\angle\text{Sb2})$	294.71
Sb2-Cl2	2.3978(6)		
4.15e			
Sb-N1	2.067(3)	N1-Sb1-N2	99.59(12)
Sb-N2	2.038(3)	$\Sigma(\angle\text{Sb})$	294.1
Sb-Cl	2.3973(11)		

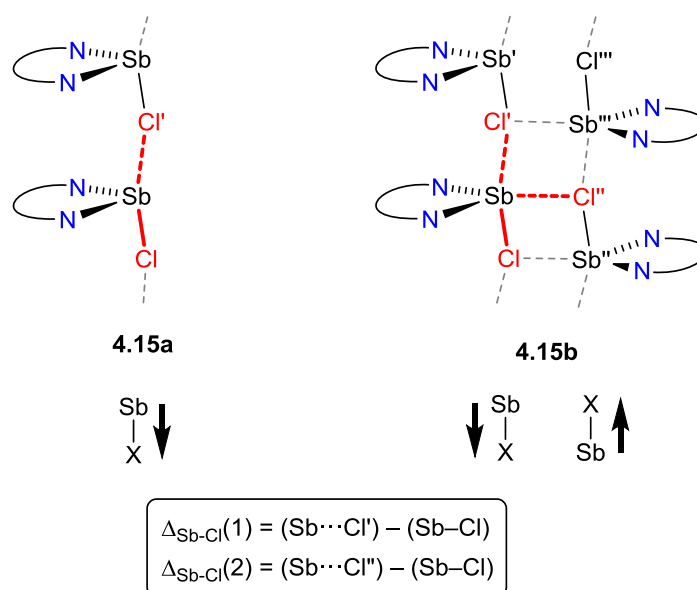


Figure 4.5. Schematic representation of the extended solid-state structures in **4.15a** and **4.15b**.

The steric parameters, %V_{Bur} and G, were calculated for **4.15a-e**. Analogous to the calculations for the bismuth systems discussed in Section 2.3.1, the contribution of the chloride atoms to the encumbrance of the antimony was excluded from the calculations. The %V_{Bur} and G parameters (Table 4.2) show a similar trend to that observed for their bismuth analogues (Section 2.3.1). Unsurprisingly, the Ph derivative is the least sterically protecting ligand (%V_{Bur} = 47.9 %, G = 44.0 %), while the *t*Bu (%V_{Bur} = 56.9 %, G = 52.7 %) and Ar' (%V_{Bur} = 54.4 %, G = 50.7 %) derivatives have similar %V_{Bur} and G values, as was observed for their bismuth analogues. As expected, the antimony centres in the Ar (%V_{Bur} = 61.3 %, G = 60.1 %) and Ar⁺ (%V_{Bur} = 70.0 %, G = 72.1 %) derivatives are significantly more sterically protected.

Table 4.2. Steric parameters for Sb(NON^R)Cl (**4.15a-e**).^a

	4.15a	4.15b	4.15c	4.15d	4.15e
%V _{Bur} (%) ^b	56.9	47.9	54.4	61.3	70.0
G parameter ^c	52.7	44.0	50.7	60.1	72.1

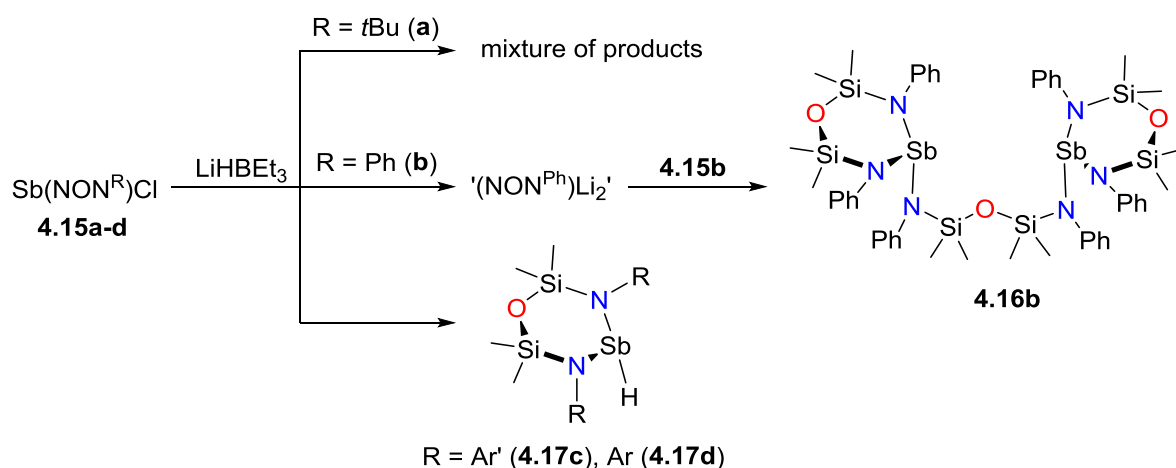
^aSb and Cl atoms are omitted from the calculations. ^bCalculated using the SambVca 2 software for a sphere with *r* = 3.5 Å and hydrogen atoms included.²⁹ ^cCalculated using the Solid-G suite of programs.³⁰

4.3.2. Synthesis of Low Oxidation State Antimony Compounds

4.3.2.1. Attempted Reduction of Antimony(III) Chlorides using LiHBEt₃

We initially sought to reduce the antimony(III) chloride species using a similar route to their bismuth analogues, through generation of the antimony(III) hydride species and subsequent Sb-H homolysis. However, attempts to reduce the antimony(III) chlorides Sb(NON^R)Cl using LiHBEt₃, following the procedure used for the bismuth analogues (Section 2.3.2), were unsuccessful and did not yield the reduced antimony species (Scheme 4.2). While the spontaneous homolysis of Sb-H bonds has been reported as a route to low valent antimony species {tBu₂Sb}₂ and {RSb}_n (R = mesityl, CH₂SiMe₃, 2,6-(Me₂NCH₂)₂C₆H₃),¹²¹ antimony(III) hydrides supported by sterically demanding ligands are typically stable.

The dropwise addition of 1 equiv. LiBEt₃H in THF (1.0 M) to a solution of **4.15a** in Et₂O at -78 °C, followed by slow warming to room temperature results in the formation of large amounts of amorphous black solid and a colourless solution, from which no crystals could be isolated. ¹H NMR analysis of the crude reaction mixture revealed the formation of a complex mixture of products, indicated by multiple ligand environments. The analogous reaction of **4.15b** proceeds similarly, giving a black precipitate and colourless solution. Colourless crystals were isolated from the reaction mixture after work-up and were identified as the (NON^{Ph})-bridged structure {Sb(NON^{Ph})₂(μ-NON^{Ph})} (4.16b) by NMR spectroscopy and X-ray crystallography. A similar mechanism to that proposed for the corresponding bismuth system is suggested, involving initial transmetallation of the ligand followed by salt-metathesis type reactivity (Scheme 2.7). In contrast, the analogous reactions using **4.15c** and **4.15d** gave the corresponding antimony(III) hydrides Sb(NON^R)H (R = Ar' (**4.17c**), Ar (**4.17d**)) as colourless crystals after work-up, while the Ar[†] derivative did not react. Both **4.17c** and **4.17d** are stable in the solid-state and solution-state, and can be heated to 70 °C for 7 days without decomposition or loss of H₂.



Scheme 4.2. Reaction of **4.15a-d** with LiHBET₃.

The ¹H NMR spectrum of **4.16b** is similar to its bismuth analogue **2.22b**, with three SiMe₂ resonances with equal integrals (δ_{H} 0.14, 0.15 and 0.19), consistent with two pyramidal antimony centres each chelated by a (NON^{Ph})-ligand and a bridging (NON^{Ph})-ligand with equivalent SiMe₂ protons. In contrast, the ¹H NMR spectra of **4.17c** and **4.17d** both show two SiMe₂ resonances (δ_{H} **4.17c**, 0.19 and 0.35; **4.17d**, 0.30 and 0.38), with low field singlets corresponding to SbH at δ_{H} 10.90 and 11.34, respectively. These resonances are significantly downfield from typical SbH resonances reported for alkyl and aryl substituted antimony(III) hydrides (δ_{H} 2.12 – 5.09),¹²² suggesting a more deshielded and protic hydrogen atom in **4.17c** and **4.17d**. A possible explanation for the observed difference in the SbH resonance is the increased electron withdrawing influence of the nitrogen atoms (electronegativity = 3.04) compared to carbon (electronegativity = 2.55). The infrared (IR) spectra of **4.17c** and **4.17d** show absorptions at 1804 cm⁻¹ and 1774 cm⁻¹, respectively, comparable to absorptions observed for Sb-H bond stretching modes in R₂SbH and RSbH₂ (R = aryl or alkyl, range 1806 – 1883 cm⁻¹).

X-ray crystallography confirmed the identity of **4.16b** as the (NON^{Ph})-bridged species {Sb(NON^{Ph})}₂(μ -NON^{Ph}) (Figure 4.6). The solid-state structure is isostructural, but not isomorphous, with the bismuth analogue, instead crystallising in the $P\bar{1}$ space group, with two crystallographically distinct antimony centres. Each antimony atom is pyramidal ($\Sigma(\angle\text{Sb})$: Sb1,

296.54°; Sb2, 296.31°) and is chelated by a (NON^{Ph})-ligand with a κ_2 -N,N'-bidentate bonding mode, and coordinated by a (μ_2 -NON^{Ph})-ligand bridging the two atoms with an E-type bonding mode (Figure 1.6). Despite the different coordination modes, the Sb-N bond distances occupy a narrow range (2.037(3) - 2.063(2) Å). Analogous to the structure of **2.22b**, the nitrogen substituents of the bridging ligand eclipse the 'Sb(NON^{Ph})' units (Ct_{SbN2}-Sb-N-Ph torsion angle = 14.6° and 21.5°). The Sb1...Sb2 distance (4.1243(5) Å) is slightly longer than the sum of van der Waals radii (4.0 Å),³¹ suggesting that there is no interaction between the two atoms. In addition, no short Sb...aryl contacts are present in the structure, with the shortest distance (4.1884(13) Å) significantly longer than the average value for Sb...aryl interactions reported in a recent survey of the Cambridge Structural Database (CSD, 3.34(18) Å).¹²³

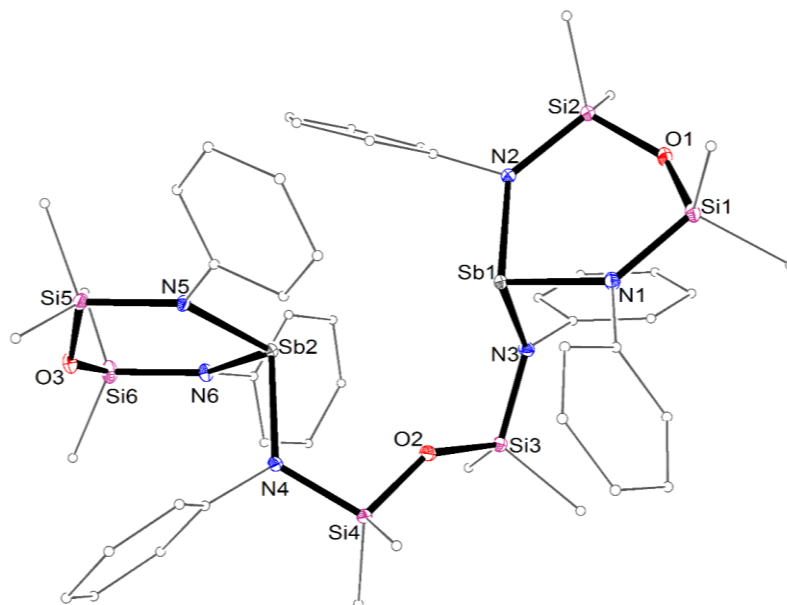


Figure 4.6. Molecular structures of **4.16b** (thermal ellipsoids displayed at 30% probability level). Hydrogen atoms are omitted and carbon atoms are displayed in wireframe format for clarity. Selected bond lengths (Å) and angles (°): Sb1-N1 2.055(2), Sb1-N2 2.037(3), Sb1-N3 2.056(2), Sb2-N4 2.055(2), Sb2-N5 2.063(2), Sb2-N6 2.057(2); N1-Sb1-N2 98.69(9), N1-Sb1-N3 97.16(9), N2-Sb1-N3 100.69(9), N5-Sb2-N6 99.15(8), N4-Sb2-N5 98.03(8), N4-Sb2-N6 99.13(8).

The solid-state structures of **4.17c** and **4.17d** were determined using X-ray crystallography confirming formation of the antimony(III) hydride species, Sb(NON^R)H (Figure 4.7). **4.17d**

crystallises with two essentially identical but crystallographically distinct molecules in the asymmetric unit (denoted **4.17d-1** and **4.17d-2**). In both cases, a (NON^R)-ligand chelates the antimony centre with standard bite angles (**4.17c**, 98.28(9)°; **4.17d-1**, 98.54(7)°; **4.17d-2**, 98.96(7)°) and standard Sb-N bond distances (range 2.043(3) – 2.054(2) Å). A hydride ligand completes the coordination spheres to give a three-coordinate pyramidal antimony (Sb-H: **4.17c**, 1.75(4) Å; **4.17d-1**, 1.66(3) Å; **4.17d-2**, 1.67(2) Å). These values are within the very broad range reported for Sb-H distances determined using X-ray diffraction, where the hydride atoms have been located in the electron difference map (1.58(7) – 1.79(9) Å).^{71a, 122, 124}

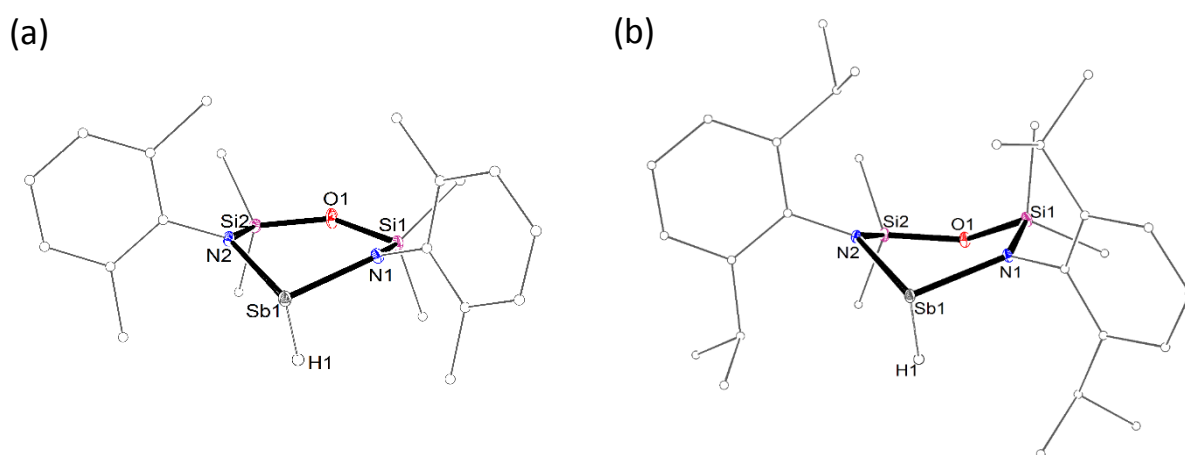


Figure 4.7. Molecular structures of **4.17c** (a) and **4.17d-1** (b) determined using X-ray diffraction (thermal ellipsoids displayed at 30% probability level). Selected hydrogen atoms, the second independent molecule of **4.17d-2** and hexane solvent molecule in **4.17d** are omitted. Carbon atoms are displayed in wireframe format for clarity. Selected bond lengths (Å) and angles (°): **4.17c**, Sb1-N1 2.043(3), Sb-N2 2.049(2), Sb-H1 1.75(4), Sb1...O1 3.398(2); N1-Sb-N2 98.28(9), N1-Sb-H1 91(1), N2-Sb-H1 95(1). **4.17d**, Sb1-N1 2.049(2), Sb1-N2 2.048(2), Sb2-N3 2.043(2), Sb2-N4 2.054(2), Sb1-H1 1.66(3), Sb2-H2 1.67(2), Sb1...O1 3.300(1), Sb2...O2 3.367(2); N1-Sb1-N2 98.54(7), N3-Sb2-N4 98.96(7), N1-Sb1-H1 94(1), N2-Sb1-H1 92(1), N1-Sb-H1 96(1), N2-Sb-H1 95(1).

X-ray diffraction measurements concerning hydrogen atoms are generally very inaccurate due to the poor X-ray scattering factor of hydrogen.¹²⁵ This becomes increasingly difficult for

hydrogen atoms adjacent to strongly diffracting heavy elements, and can lead to large disparities in the observed parameters. The only definitive method for measuring the atomic position of hydrogen atoms is through the use of neutron diffraction. In collaboration with Dr Alison Edwards, the Australian Nuclear Science and Technology Organisation (ANSTO) and the Australian Institute of Nuclear Science and Engineering (AINSE), neutron diffraction was used to analyse a single crystal sample of **4.17c**, providing the first accurate measurements of a Sb(III)-H bond.[†]

The neutron diffraction data was collected at 120 K, using the KOALA instrument at the Australian Nuclear Science and Technology Organisation (ANSTO), and the data reduction was performed using the LaueG suite of programs.¹²⁶ Data collection was performed on several relatively small single crystals (approximately 0.4 mm³), using the Laue method and a polychromatic neutron beam (wavelength = 0.8 – 1.6 Å) (see Appendix 7.3 for further details).

A valid model for the crystal structure of **4.17c** was determined using the neutron diffraction data. Most of the atoms were modelled anisotropically and all of the hydrogen atoms were evident in the nuclear density map. The hydrogen atoms of one of the methyl groups is significantly disordered, with the largest localised component identified in the difference map and the remainder of the nuclear density modelled as an isotropic annulus of hydrogen nuclear density about 1.08 Å from the methyl carbon.

Most of the atomic positions remain unchanged, with the only major differences in the positions of the hydrogen atoms. The neutron data confirms coordination of the hydrogen atom to a pyramidal antimony(III) centre ($\Sigma(\angle\text{Sb}): 287.54^\circ$). The Sb-H distance (1.72(2) Å) is consistent with the sum of covalent radii for Sb and H (1.73 Å) and, while comparable to the distance assigned in the X-ray crystal structure (1.75(4) Å), is significantly more reliable. The SbH hydrogen atom sits in a hydrophobic pocket, surrounded by methyl groups with C-H units oriented towards the Sb-H hydrogen atom (Figure 4.8). However, all of the H...H distances are

[†] There has been a report of a neutron study of an antimony(II) hydride species.^{60a}

longer than the standard sum of van der Waals radii (2.40 Å), suggesting that no short H...H contacts are present.³¹

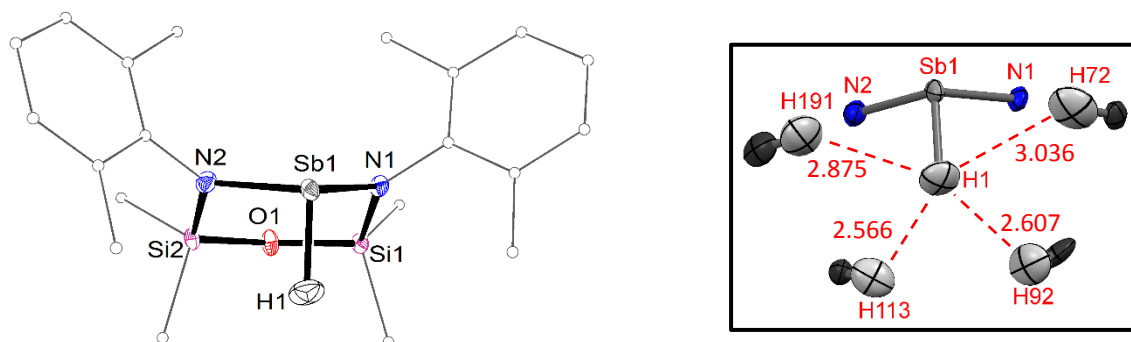


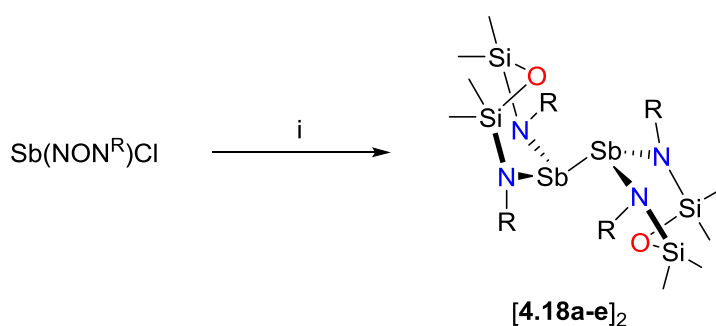
Figure 4.8. Molecular structure of **4.17c** determined using neutron diffraction and local environment of H1 (thermal ellipsoids displayed at 30% probability level). Selected hydrogen atoms are omitted. Carbon atoms are displayed in wireframe format for clarity. Selected bond lengths (Å) and angles (°): Sb-N1 2.03(1), Sb-N2 2.04(1), Sb-H1 1.72(2), Sb...O 3.40(1); N1-Sb-N2 98.3(5), N1-Sb-H1 95.6(9), N2-Sb-H1 93.6(9).

4.3.2.2. Reduction of Antimony(III) Chlorides using Magnesium(I) Reagents

Attempts to reduce the antimony(III) chloride species $\text{Sb}(\text{NON}^{\text{R}})\text{Cl}$ using magnesium metal were unsuccessful, with no reaction occurring even after stirring for extended periods of time (>7 days) at room temperature. The reduction potential of magnesium (Mg/Mg^{2+}) suggests spontaneous reduction is possible and magnesium metal has previously been used in the synthesis of reduced antimony species.¹²⁷ The lack of an observed reaction may be due to the heterogeneous nature of the reaction. Magnesium(I) reagents have previously been demonstrated to be useful reducing agents in the synthesis of low-valent metal species that are soluble in organic solvents.^{17b}

The reaction of $\text{Sb}(\text{NON}^{\text{R}})\text{Cl}$ (**4.15a-c**) with 0.5 equivalents of the magnesium(I) reducing agents $[\text{Mg}(\text{BDI}^{\text{Ar}^{\text{S}}})_2]$ ($\text{Ar}^{\text{S}} = \text{mes}$ (**1.1**) or Ar (**1.2**)), proceeds with a colour change from colourless to yellow (**4.15a** and **4.15b**) or red (**4.15c**), giving the corresponding reduced antimony species $[\text{Sb}(\text{NON}^{\text{R}})]_2$ ($\text{R} = t\text{Bu}$ (**4.18a**), Ph (**4.18b**), Ar' (**4.18c**)) in almost quantitative yields by ^1H

NMR spectroscopy (Scheme 4.3). Separation of the reduced antimony species from the other reaction product, “Mg(BDI^{Ar^s})Cl”, was achieved through either extraction into hexane and filtration (Ar^s = mes) or fractional recrystallization from hexane (Ar^s = Ar). In the latter case, significantly lower isolated yields were obtained (20 – 30 % lower). ¹H NMR spectroscopy revealed resonances in the normal region for a diamagnetic species in all cases, suggesting formation of a distibane. Two high field resonances corresponding to the SiMe₂ protons (δ_{H} [4.18a]₂, 0.40 and 0.51; [4.18b]₂, 0.13 and 0.24; [4.18c]₂, 0.26 and 0.30) are consistent with a pyramidal antimony centre chelated by a (NON^R)-ligand. Other key resonances for the *t*Bu and *o*-Me resonances of [4.18b]₂ and [4.18c]₂ are found at δ_{H} 1.43 and δ_{H} 2.21 and 2.40, respectively. In the ¹H NMR spectrum of [4.18c]₂, several of the resonances are broad, including the SiMe₂ resonance at δ_{H} 0.30 and the *o*-Me resonance at δ_{H} 2.21, suggesting a fluxional process in solution. When the solution is warmed to 60 °C, the SiMe₂ and *o*-Me resonances coalesce into sharp singlets at δ_{H} 0.23 and 2.31, respectively, consistent with an averaged C_{2h}-symmetric species. The Gibbs free energy (ΔG^\ddagger) for the fluxional process was estimated from the coalescence temperature (T_{c} = 49 °C) and maximum peak separation ($\Delta\delta$ = 30 Hz) to be ΔG^\ddagger = 67.8 kJmol⁻¹.



Scheme 4.3. Synthesis of distibanes [Sb(NON^R)]₂ (R = *t*Bu ([4.18a]₂), Ph ([4.18b]₂), Ar' ([4.18c]₂)). i) 0.5 equiv. **1.1** or **1.2**, -Mg(BDI^{Ar^s})Cl.

The difference in colour for [4.18b]₂ and [4.18c]₂ is unexpected, as both systems are expected to have similar electronic properties. The red colour observed for [4.18c]₂ corresponds to three transitions in the visible region at λ_{max} 386 nm (ϵ = 1421 mol⁻¹dm³cm⁻¹), 420 nm (ϵ =

1683 mol⁻¹dm³cm⁻¹) and 537 nm (ϵ = 364 mol⁻¹dm³cm⁻¹) (Figure 4.9). Heating the solution to 60 °C did not result in an observable change in the UV-visible spectrum, contrasting the results by NMR spectroscopy. The only transition observed in the visible spectrum of [4.18b]₂ is at λ_{max} 397 nm (ϵ = 730 mol⁻¹dm³cm⁻¹), consistent with the observed yellow colour. The transitions at 420 nm and 537 nm in the electronic absorption spectrum of [4.18c]₂ are similar to those observed in the bismuth radical species 2.17d• (417 nm and 482 nm) and 2.17e• (441 nm and 490 nm), and indicate that a similar radical species may be present in solution (i.e. 4.18c•).

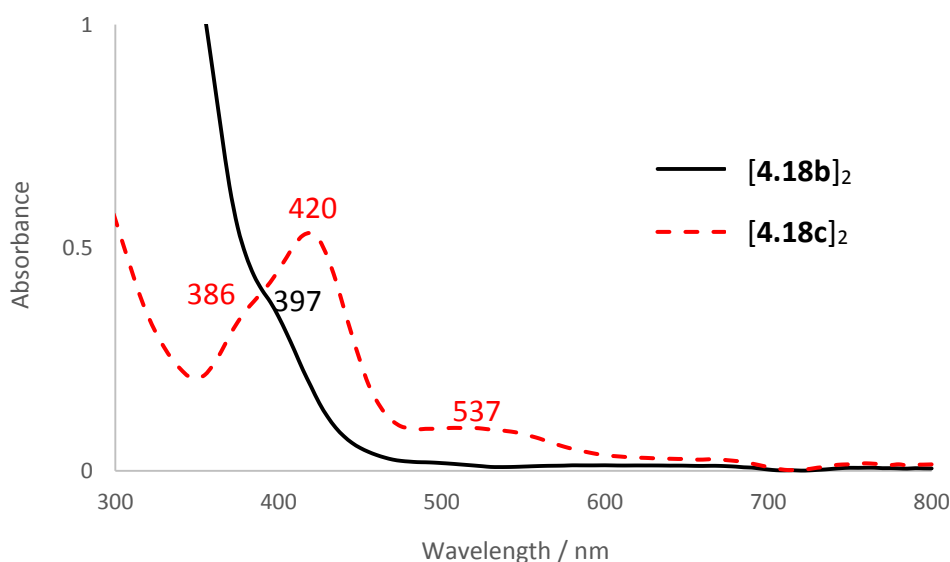


Figure 4.9. Electronic absorption spectrum of [4.18b]₂ (black, solid) and [4.18c]₂ (red, dotted). λ_{max} / nm (ϵ / mol⁻¹dm³cm⁻¹): [4.18b]₂, 397 (730); [4.18c]₂, 386 (1421), 420 (1683) and 537 (364).

The solid-state structures of the reduced antimony species [4.18a-c]₂ were determined using X-ray crystallography (Figure 4.10), confirming formation of the Sb-Sb bonded species [Sb(NON^R)]₂. While the asymmetric unit of [4.18a]₂ contains a single molecule of the distibane, [4.18b]₂ and [4.18c]₂ both crystallise with two independent half-molecules in the asymmetric unit. The half molecules are grown through either an inversion centre ([4.18b]₂) or a two-fold rotation axis ([4.18c]₂) to give Sb-Sb bonds to their symmetry equivalents. In all cases, the

(NON^R)-ligand chelates the antimony centre with a κ_2 -*N,N'*-bidentate bonding mode with Sb-N bond distances ([**4.18a**]₂, 2.067(2) – 2.082(2) Å; [**4.18b**]₂, 2.054(3) – 2.069(4) Å; [**4.18c**]₂, 2.069(5) – 2.077(3) Å) significantly longer than those of **4.15a-c** (2.011(2) – 2.036(2) Å), consistent with the formation of a reduced antimony centre. The metallacycles of [**4.18a**]₂ and [**4.18b**]₂ adopt boat conformations, which coincide with Sb...O contacts ([**4.18a**]₂, 3.334(2) and 3.375(2) Å; [**4.18b**]₂, 3.586(2) and 3.556(3) Å) between the antimony atoms and siloxane oxygen atom of the opposing (NON^R)-ligand, analogous to those seen in the dibismuthine [**2.17a**]₂. In contrast, despite the metallacycles of [**4.18c**]₂ also adopting boat conformations, the shortest Sb...O distance (5.887(3) Å) is much larger than the sum of van der Waals radii for Sb and O (3.58 Å).

The Sb-Sb bond distances vary significantly with the R-substituent. The smaller *t*Bu and Ph derivatives feature Sb-Sb bond distances ([**4.18a**]₂, 2.9015(5) Å; [**4.18b**]₂, 2.8909(4) Å and 2.8589(7) Å), within the typical range for R₂Sb-SbR₂ (2.835(1) – 2.9194(6) Å).⁶¹ However, the bulkier Ar' derivative has an elongated Sb-Sb bond (3.0351(7) Å and 3.0975(7) Å), significantly longer than the labile Sb-Sb bond in [**4.12**]₂ (3.0297(4) Å) which was described as two loosely associated units of the corresponding antimony(II) radical species, •Sb(C{(SiMe₃)₂CH₂})₂ (**4.12•**). The relative arrangement of the (NON^R)-ligand about the Sb-Sb bond also differs considerably between the compounds. While [**4.18a**]₂ and [**4.18b**]₂ adopt the expected *anti*-conformations with the (NON^R)-ligands staggered about the Sb-Sb bond (Ct_{SbN2}-Sb-Sb-Ct_{SbN2} torsion angle: [**4.18a**]₂, 173.3°; [**4.18b**]₂, 180.0°), the (NON^{Ar'})-ligands of [**4.18c**]₂ adopt an unexpected conformation, where two nitrogen atoms are eclipsed, and the ligands are rotated 112.4° and 121.5° about the Sb-Sb bond (Figure 4.11). Investigations into the nature of the bonding interaction using DFT are ongoing.

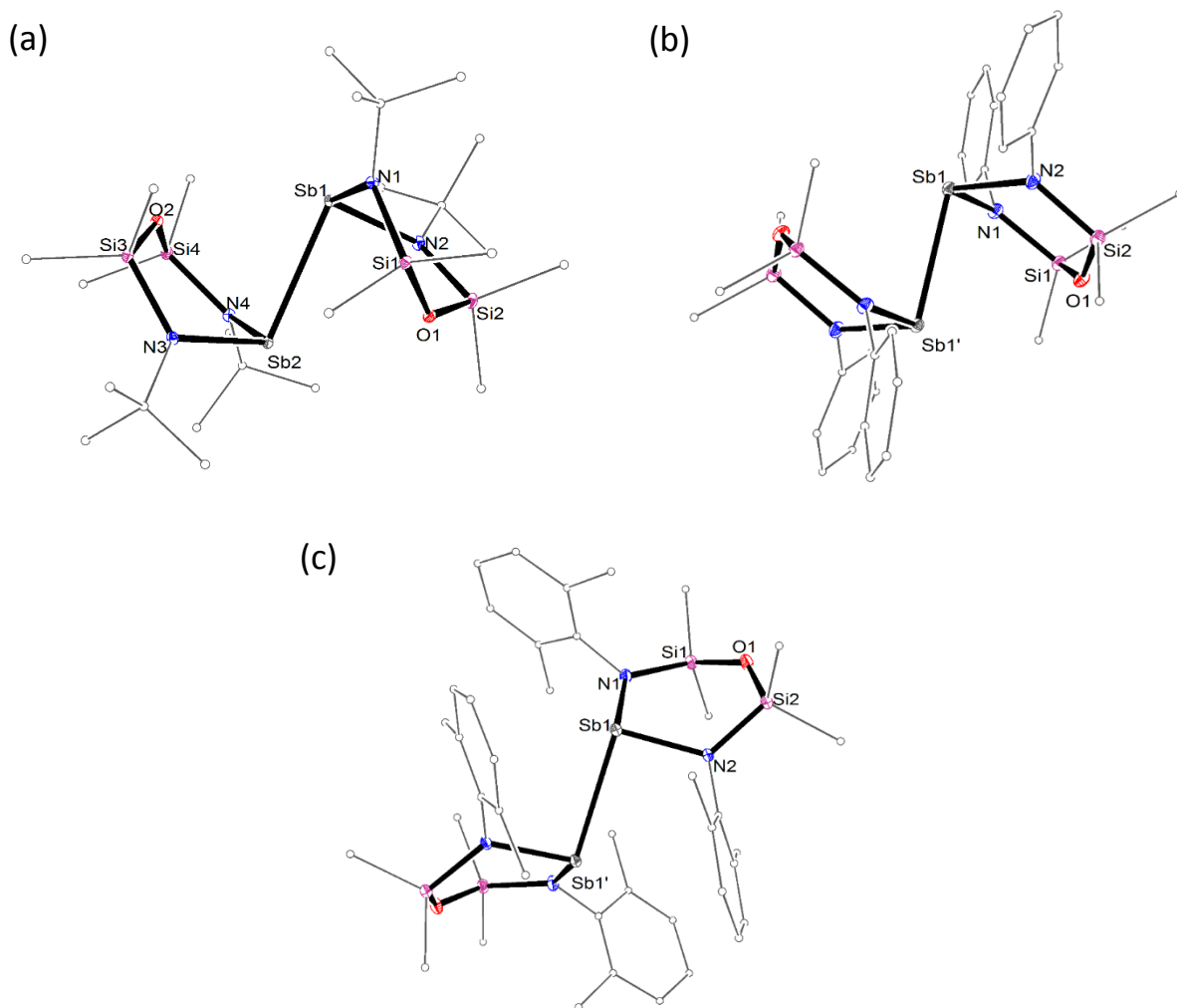


Figure 4.10. Molecular structures of **[4.18a]₂** (a), **[4.18b]₂** (b) and **[4.18c]₂** (c) (thermal ellipsoids displayed at 30% probability level, symmetry relationship (') = 2-x, 1-y, 1-z (**[4.18b]₂**) and -x, y, -z (**[4.18c]₂**)). Hydrogen atoms and the second molecules of 4.18b and 4.18c are omitted and carbon atoms are displayed in wireframe format for clarity. Selected bond lengths (Å) and angles (°): **[4.18a]₂**, Sb1-Sb2 2.9015(5), Sb1-N1 2.067(2), Sb1-N2 2.075(2), Sb2-N3 2.072(2), Sb2-N4 2.082(2), Sb1...O2 3.334(2), Sb2...O1 3.375(2); N1-Sb1-N2 98.69(8), N3-Sb2-N4 99.70(8). **[4.18b]₂**, Sb1-Sb1' 2.8909(3), Sb2-Sb2' 2.8589(5), Sb1-N1 2.054(3), Sb1-N2 2.057(4), Sb2-N3 2.069(4), Sb2-N4 2.057(3), Sb1...O1' 3.586(2), Sb2...O2' 3.556(3); N1-Sb1-N2 97.1(1), N3-Sb2-N4 99.2(1). **[4.18c]₂**, Sb1-Sb1' 3.0351(5), Sb2-Sb2' 3.0975(5), Sb1-N1 2.069(5), Sb1-N2 2.077(3), Sb2-N3 2.075(3), Sb2-N4 2.077(5); N1-Sb1-N2 95.7(1), N3-Sb2-N4 95.4 (1).

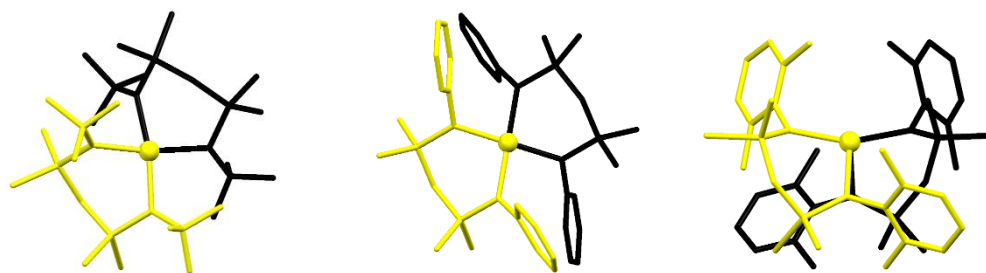
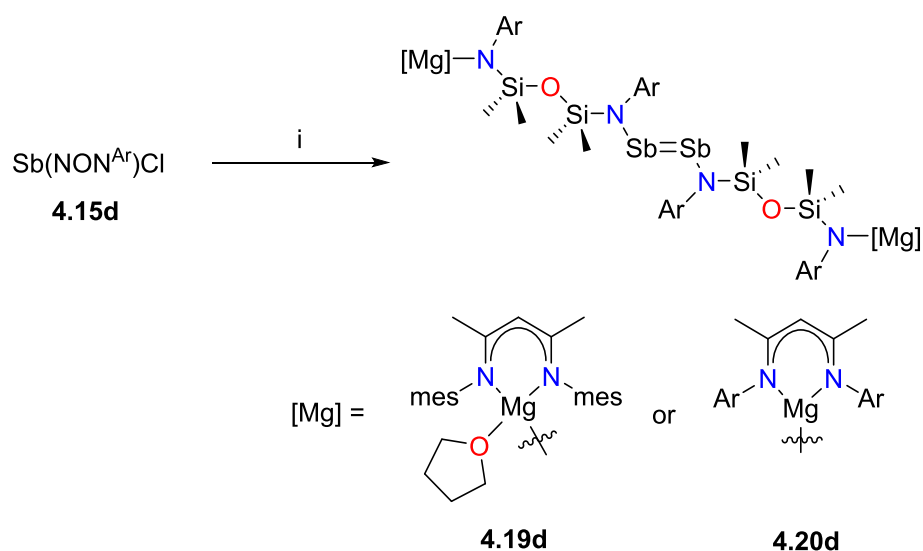


Figure 4.11. View along the Sb-Sb bond in X-ray crystal structure of **[4.18a]₂** (left), **[4.18b]₂** (middle), **[4.18c]₂** (right).

In contrast to the reactions of **4.15a-c** with the magnesium(I) species, the reaction of **4.15d** with 0.5 equiv. $[\text{Mg}(\text{BDI}^{\text{mes}})]_2$ (**1.1**) in toluene results in an immediate colour change from colourless to pink/red. Leaving the solution for 30 minutes results in formation of a pink solid, which was isolated by filtration. Attempts to crystallise the pink solid using hydrocarbon solvents were unsuccessful due to the poor solubility of the solid and the constant formation of an amorphous powder. However, when a few drops of THF was added, pink crystals were obtained from the reaction mixture, which were identified as the distibene $[(\text{BDI}^{\text{mes}})\text{Mg}(\text{THF})(\text{NON}^{\text{Ar}})\text{Sb}]_2$ (Scheme 4.4, **4.19d**) using X-ray crystallography and NMR spectroscopy. When $[\text{Mg}(\text{BDI}^{\text{Ar}})]_2$ (**1.2**) was used as the reducing agent, heating was required in order to see formation of pink/red solution, consistent with previous reports of reduced reactivity for the more encumbered magnesium centres. Pink crystals were isolated from the reaction mixture, and were identified as the THF-free analogue of **4.19d**, $[(\text{BDI}^{\text{Ar}})\text{Mg}(\text{NON}^{\text{Ar}})\text{Sb}]_2$ (**4.20d**). Improved yields were obtained when the reaction was performed using a 1 : 1 mixture of **4.15d** and **1.1** or **1.2**. In contrast, the addition the magnesium(I) species to **4.15e** did not result in an observable reaction by ^1H NMR spectroscopy, even when the mixture was heated to 70 °C for 48 hours. Both **4.19d** and **4.20d** are stable as solids or in solution for months at room temperature and can survive heating to 100 °C without visible decomposition.



Scheme 4.4. Synthesis of **4.19d** and **4.20d**. i) 1 equiv. $[\text{Mg}(\text{BDI}^{\text{Ar}^{\text{S}}})_2]$ ($\text{Ar}^{\text{S}} = \text{mes}$ (**1.1**), Ar (**1.2**), toluene.

The ^1H NMR spectra of **4.19d** and **4.20d** indicate the formation of a diamagnetic species, with similar spectral features to those reported for the analogous dibismuthene **2.26d** (Section 2.3.3). Each spectrum displays two high field singlets, consistent with asymmetric SiMe_2 groups (δ_{H} **4.19d**, 0.15 and 0.18; **4.20d**, -0.12 and -0.15). In both cases, a sharp resonance corresponding to the BDI-methine proton (δ_{H} 4.98 and 4.80, respectively) is observed, with integrals consistent with a 1 : 1 ratio of $(\text{NON}^{\text{Ar}}) : (\text{BDI}^{\text{Ar}^{\text{S}}})$.

The UV-visible spectra of **4.19d** and **4.20d** show that the observed pink colour derives from absorptions at 512 nm and 515 nm, respectively (Figure 4.12). Strong absorptions are also observed in the UV-region at 287 nm (shoulder) and 313 nm or 281 nm, 340 nm and 351 nm, respectively. The absorption bands at 512 and 515 nm are assigned to symmetry allowed $\pi \rightarrow \pi^*$ transitions, similar to the related amide supported distibene **4.7** (Figure 4.2), which displays a strong $\pi \rightarrow \pi^*$ absorption at 510 nm.^{38b, 40}

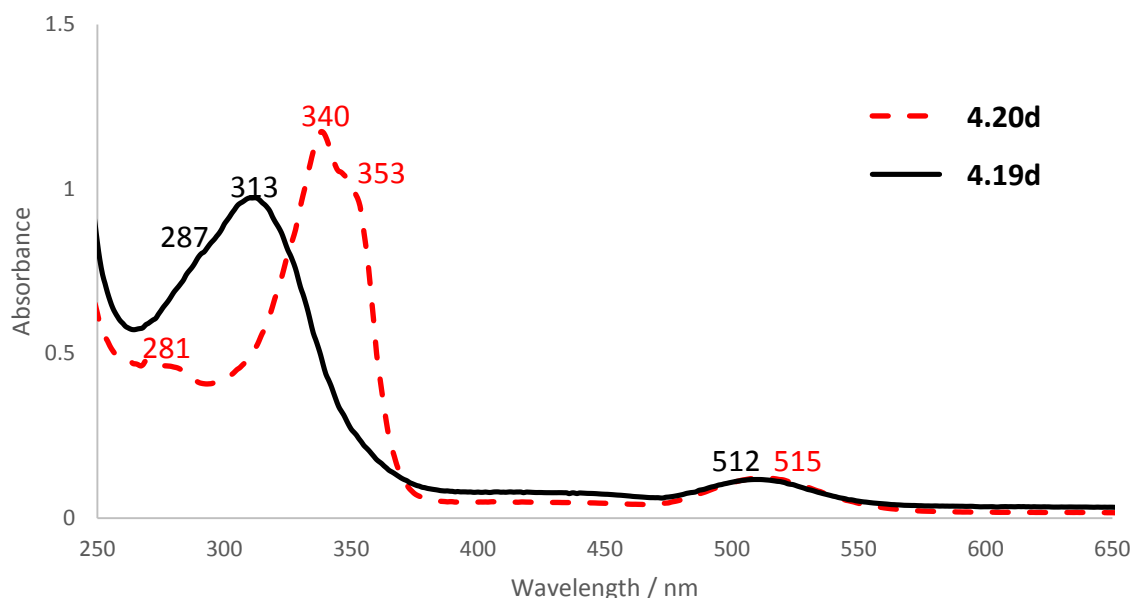


Figure 4.12. Electronic absorption spectrum of **4.19d** (black, solid) and **4.20d** (red, dotted). λ_{max} / nm (ϵ / mol⁻¹dm³cm⁻¹): **4.19d**, 287 (2958), 313 (3611), 512 (461); **4.20d**, 281 (1652), 340 (4456), 353 (3764), 515 (422).

The solid-state structures of **4.19d** and **4.20d** were determined using X-ray diffraction (Figure 4.13). The crystal structures are similar, with each asymmetric unit containing half a molecule of the distibene with a 'Mg(BDI^{ArS})' unit linked to an antimony atom through a bridging (NON^{Ar})-ligand. In both cases, growing the asymmetric unit (via an inversion) reveals the molecular unit of the distibine, containing a Sb=Sb bond (2.6648(7) Å and 2.6621(4) Å, respectively), which is significantly shorter than the single bonding interactions in **4.18a-c** but within the range reported for other structurally characterised distibenes (2.642(1) – 2.710(1) Å).^{38a-b, 39, 40, 112, 113} The Sb-N1 distances (**4.19d**, 2.072(2) Å; **4.20d**, 2.077(3) Å) are significantly longer than the distances observed in **4.15d** (2.0251(13) – 2.395(12) Å), consistent with coordination to a reduced antimony species. The bridging (NON^{Ar})-ligands are *trans* across the Sb=Sb bond, with Sb-Sb-N angles (94.31(6)° and 94.50(6)°, respectively) indicative of a bent geometry. In both cases, the Ar substituent of N1 eclipses the symmetry related Sb' (Ct_{C1-C6}-N1-Sb-Sb' torsion angle: 0.08° and 3.14°, respectively), leading to short Sb...aryl interactions

(Sb...Ct_{C1'-C6'} 3.430(2) Å and 3.444(2) Å, respectively) between Sb' and the Ar substituent. The only major difference between the two structures are at the magnesium centre. The magnesium in **4.19d** contains a coordinated THF molecule (Mg-O2, 2.089(2) Å) to give a four-coordinate magnesium with a tetrahedral geometry. In contrast, the magnesium in **4.20d** is three coordinate with a trigonal planar geometry. As a result, the Mg-N bond distances are significantly longer for the magnesium atom in **4.19d** (**4.19d**, 2.027(2)*, 2.116(2) and 2.080(2) Å; **4.20d**, 1.975(2)*, 2.030(2) and 2.053(3) Å; *corresponds to the (NON^{Ar})-ligand).

In an attempt to achieve similar reactivity with the other antimony(III) chlorides, excess magnesium(I) reagent was added to samples of **4.15a-c** and the reaction mixtures monitored using ¹H NMR spectroscopy. However, unlike the reaction with **4.15d**, the reaction stopped after formation of the Sb(II) species. Heating the solutions to 70 °C resulted in the gradual formation (*ca.* 20 % over 3 days) of a new species in the ¹H NMR spectra featuring a single SiMe₂ resonance (**4.15a**, -0.09; **4.15b**, -0.31; **4.15c**, -0.01) and a γ-CH resonance (**4.15a**, 4.90; **4.15b**, 4.94; **4.15c**, 4.84). The integrals suggest a relative ratio of 1 : 2 for the (NON^R) : (BDI^{ArS}), and we therefore postulated loss of the ligand from the antimony and formation of '[Mg(BDI^{ArS})]₂(NON^R)'. The presence of this species in the reaction mixture was confirmed for the phenyl derivative, with crystals isolated from the reaction mixture of **4.15b** and **1.1** identified as a 1 : 1 co-crystalline mixture of {Mg(BDI^{mes})}₂(μ₂-NON^{Ph}) (Scheme 4.5, **4.21b**) and the Sb₈-cluster [Mg(BDI^{mes})]₄Sb₈ (**4.22**) recently reported by Schulz and co-workers.¹²⁸ The isolation of these species accounts for both components of the starting materials and may proceed through an unstable intermediate distibene species.

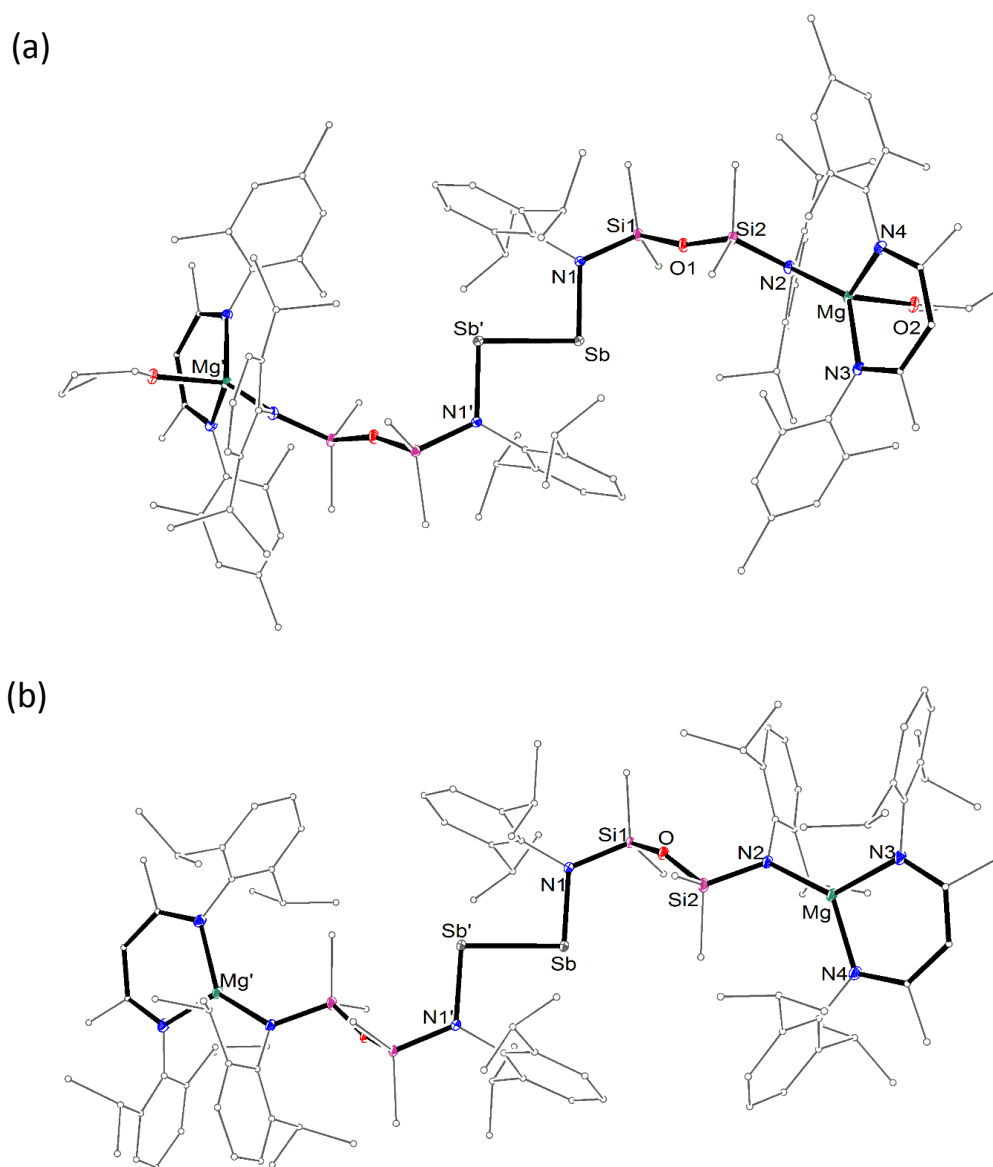
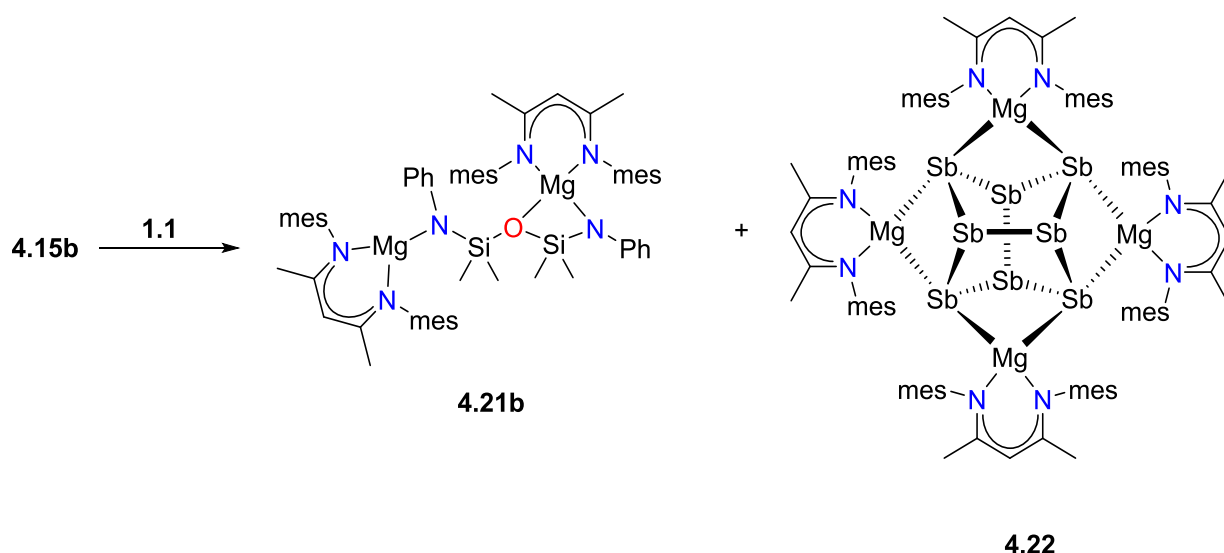


Figure 4.13. Molecular structures of **4.19d** (a) and **4.20d** (b) (thermal ellipsoids displayed at 30% probability level, symmetry relationship (') = 0.5-x, 0.5-y, 1-z (**4.19d**) and 1-x, 2-y, 1-z (**4.20d**)). Hydrogen atoms and solvent molecules omitted and carbon atoms are displayed in wireframe format for clarity. Selected bond lengths (Å) and angles (°): **4.19d**, Sb-Sb' 2.6648(7), Sb-N1 2.072(2), Mg-N2 2.027(2), Mg-N3 2.116(2), Mg-N4 2.080(2), Mg-O2 2.089(2), Sb...Ct_{C1-C6} 3.430(2); N1-Sb-Sb' 94.31(6), N3-Mg-N4 91.12(8), Ct_{C1-C6}-N1-Sb-Sb' 0.08. **4.20d**, Sb-Sb' 2.6621(4), Sb-N1 2.077(2), Mg-N2 1.975(2), Mg-N3 2.030(2), Mg-N4 2.053(3), Sb...Ct_{C1-C6} 3.444(2); N1-Sb-Sb' 94.50(6), N3-Mg-N4 96.9(1), Ct_{C1-C6}-N1-Sb-Sb' 3.14.



Scheme 4.5. Reactivity of **4.15b** with 1 equiv. **1.1**.

The solid-state structure of the co-crystalline mixture of **4.21b** and **4.22** was determined using X-ray crystallography (Figure 4.14 and S4.1). After assignment of the atoms corresponding to these two components, residual electron density peaks remained, likely corresponding to poorly resolved solvent residues, which were treated as a diffuse contribution to the overall scattering without specific atom positions by SQUEEZE/PLATON.⁶³ The bonding parameters of the Sb₈ cluster are almost identical to those described by Schulz and co-workers, with similar Sb-Sb bonds (range 2.8019(6) – 2.8545(6) Å) and Sb-Mg distances (range 2.837(1) – 2.883(1) Å). The other component of the crystal, {Mg(BDI^{mes})}₂(μ₂-NON^{Ph}), involves two ‘Mg(BDI^{mes})’ units bridged by a (NON^{Ph})-ligand. The (NON^{Ph})-ligand is bound differently to each Mg centre, with a κ₂-N,O-coordination mode to Mg5 and coordination to Mg6 through a single N-atom (Figure 1.6, F). Despite these large differences in coordination, the Mg-N distances (1.990(3) and 1.970(3) Å) involving the (NON^{Ph})-ligand are essentially identical. The Mg-O distance (2.091(2) Å) is standard for a Mg-O dative interaction, similar to the Mg-O bond in the related compound Mg(BDI^{Ar})(NiPr₂)(THF) (2.092(2) Å). The (BDI^{mes})-ligands chelate the Mg centres with standard Mg-N distances (range 2.004(3) – 2.022(2) Å) and bite angles (94.0(1)° and 95.3(1)°), despite the different coordination environments of the magnesium atoms.

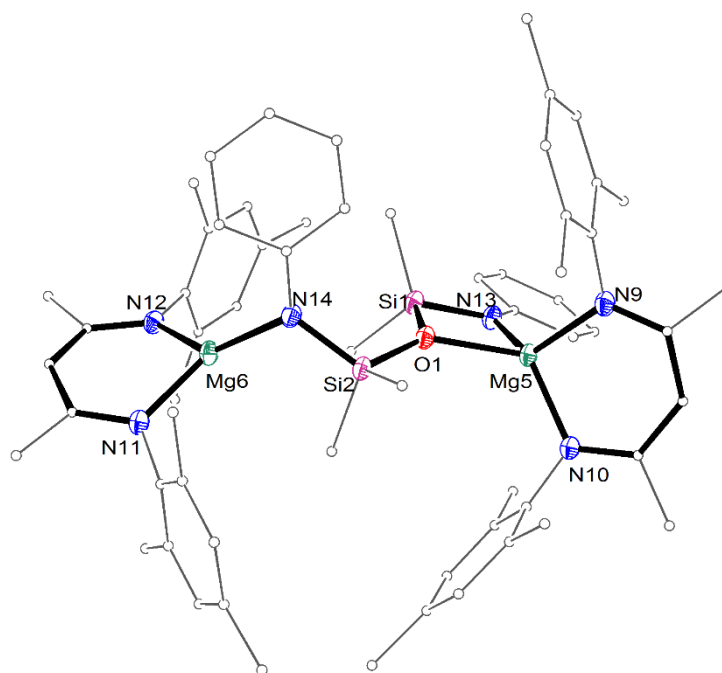


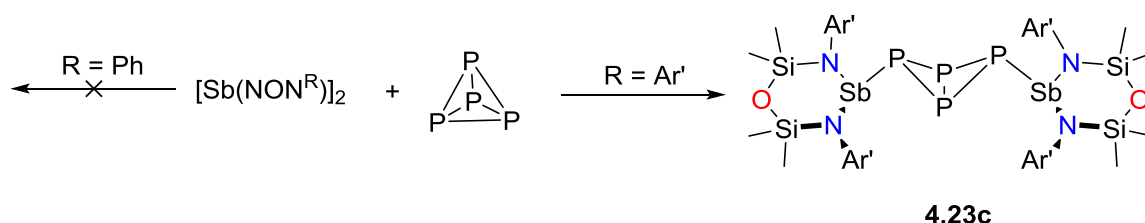
Figure 4.14. Molecular structure of **4.21b** (thermal ellipsoids displayed at 30% probability level). Hydrogen atoms, solvent molecules and molecule of **4.22** omitted and carbon atoms are displayed in wireframe format for clarity. Selected bond lengths (Å) and angles (°): Mg5-N9 2.022(3), Mg5-N10 2.013(2), Mg5-N13 1.999(3), Mg5-O1 2.091(2), Mg6-N11 2.044(3), Mg6-N12 2.018(3), Mg6-N14 1.970(3); N9-Mg5-N10 94.0(1), N13-Mg5-O1 76.5(1), N11-Mg6-N12 95.3(1).

4.3.3. Reactivity of Reduced Antimony Species with White Phosphorus (P₄)

We previously discussed the reaction of the bismuth(II) species with P₄, which was selective to the monometallic bismuth radical species **2.17d•**, with no reaction observed for the dibismuthine [**2.17a**]₂ (Section 3.3.4). In order to investigate whether the observed differences in the Sb-Sb interaction of distibines [**4.18b**]₂ and [**4.18c**]₂ would affect the reactivity, we sought to investigate their reaction with P₄.

The reaction of [**4.18c**]₂ with 1 equiv. P₄ performed on an NMR scale in C₆D₆ proceeds spontaneously at room temperature with a slight colour change from red to orange. The ¹H NMR spectrum of the crude reaction mixture is consistent with almost quantitative (>95%)

formation of a new species. Two sharp high-field singlets for the SiMe_2 protons (δ_{H} 0.14 and 0.42), in addition to two singlets corresponding to the *o*-Me protons (δ_{H} 2.38 and 2.62) are consistent with a pyramidal antimony centre chelated by a $(\text{NON}^{\text{Ar}'})$ -ligand. The ^{31}P NMR spectrum (Figure 4.15) shows two triplets at δ_{P} -110.1 and -349.6 ($J_{\text{PP}} = 152$ Hz), similar to those observed for the P_4 -bridged bis(bismuthanyl) complex **3.25d** (2 x triplets, δ_{P} -107.2 and -350.3, $J_{\text{PP}} = 164$ Hz). This likely reflects a similar arrangement of atoms, suggesting that the species formed is the tetraphosphabicyclo[1.1.0]butane-bridged bis(stibanyl) compound $\{\text{Sb}(\text{NON}^{\text{Ar}'})\}_2[\text{P}_4]$ (**4.23c**), formed through cleavage of one of the P-P bonds of the P_4 tetrahedron (Scheme 4.6). Unfortunately, attempts to crystallise the product were unsuccessful, precluding characterisation using X-ray diffraction. In contrast, attempts to perform the analogous reaction using $[\text{4.18b}]_2$ does not result in the formation of a new species, even in the presence of excess P_4 and heating the solution. Assuming the activation of P_4 occurs by reaction with an antimony radical species, as was observed for the bismuth system discussed in Section 3.3.4, this difference in reactivity suggests greater radical character in $[\text{4.18c}]_2$.



Scheme 4.6. Reactivity of $[\text{4.18b}]_2$ and $[\text{4.18c}]_2$ with P_4 .

This result is the first example of an antimony species activating P_4 and joins only a handful of heavy main group compounds that have been shown to activate this species. Unlike the bismuth system reported in section 3.3.4, no evidence of reversibility was observed upon heating the NMR sample to 70 °C, which may reflect a difference in stability of the M-P (M = Sb, Bi) bond.

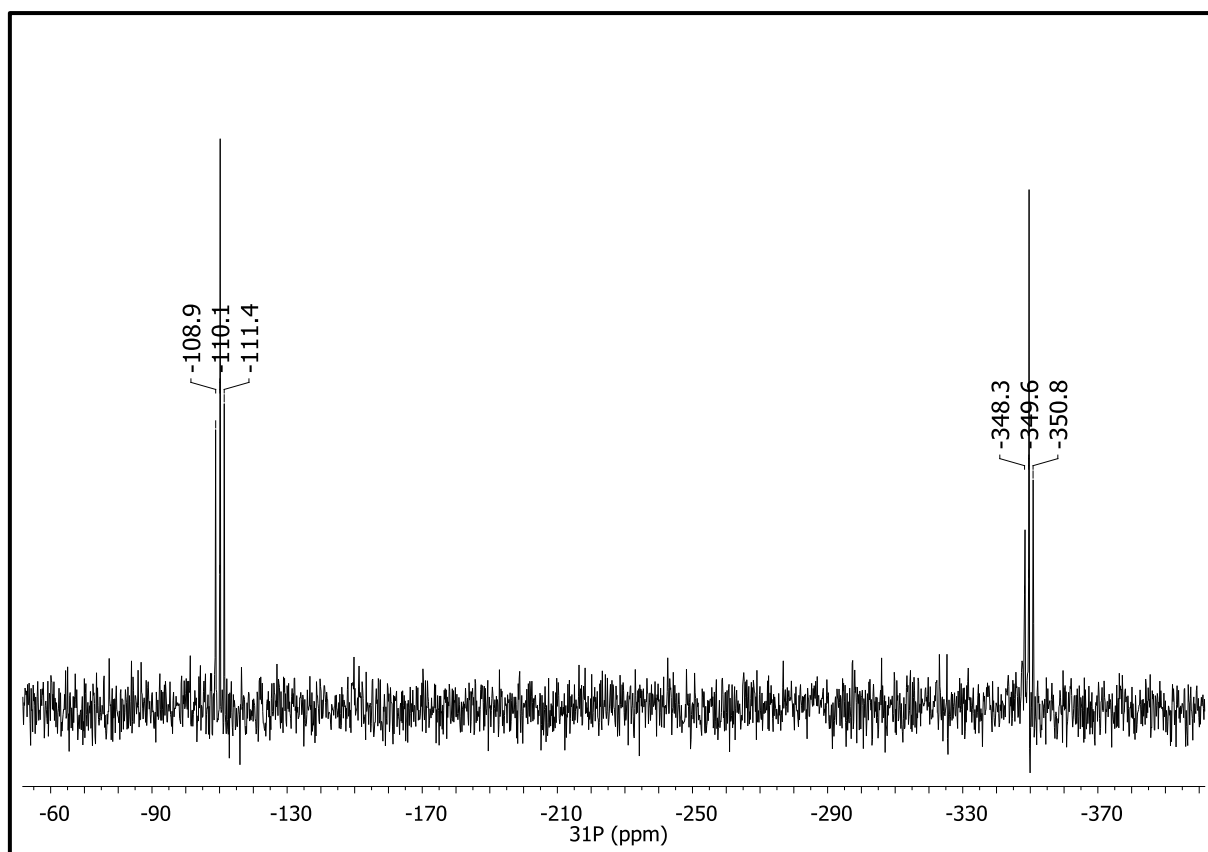


Figure 4.15. ^{31}P NMR spectrum of **4.23c**.

4.4. Conclusion

This chapter describes the isolation of a number of distibanes $[\text{Sb}(\text{NON}^{\text{R}})]_2$ ($\text{R} = t\text{Bu}, \text{Ph}, \text{Ar}'$), synthesised from their corresponding antimony(III) chloride species. Initial attempts to synthesise the distibanes using LiHBEt_3 were unsuccessful, giving either an ill-defined mixture of products, the (NON^{Ph}) -bridged species $\{\text{Sb}(\text{NON}^{\text{Ph}})\}_2(\mu\text{-NON}^{\text{Ph}})$ (**4.16b**), or the antimony(III) hydride species $\text{Sb}(\text{NON}^{\text{R}})\text{H}$ ($\text{R} = \text{Ar}'$ (**4.17c**) or Ar (**4.17d**)). The use of magnesium(I) compounds **1.1** and **1.2** as reducing agents allowed the isolation of the distibanes. While the $t\text{Bu}$ and Ph derivatives showed standard Sb-Sb bonding, the bulkier Ar' derivative had a significantly weaker Sb-Sb bond. This was exploited in a reaction with P_4 , while the Ph derivative was unreactive under the same conditions. Attempts to reduce the more encumbered antimony(III) chloride, $\text{Sb}(\text{NON}^{\text{Ar}})\text{Cl}$, using **1.1** or **1.2** resulted in formation of the distibene $[(\text{BDI}^{\text{Ar}^{\text{S}}})\text{Mg}(\text{THF})_n(\text{NON}^{\text{Ar}})\text{Sb}]_2$ ($\text{Ar}^{\text{S}} = \text{mes}$ ($n = 1$), Ar ($n = 0$)), containing rare examples of $\text{Sb}=\text{Sb}$

bonds. In contrast, no reaction was observed between $\text{Sb}(\text{NON}^{\text{Ar}\ddagger})\text{Cl}$ and **1.1** or **1.2**, presumably due to the greater steric encumbrment of the antimony centre.

4.5. Experimental

4.5.1. Synthesis of Antimony(III) Chloride Species

*General Procedure for $\text{Sb}(\text{NON}^{\text{R}})\text{Cl}$ (used in the preparation of **4.15a-d**)*

A solution of $n\text{BuLi}$ in hexane (1.6M) was added drop wise to a stirring solution of $(\text{NON}^{\text{R}})\text{H}_2$ in hexane (7 mL) at $-30\text{ }^\circ\text{C}$. The resulting suspension was allowed to warm to room temperature and stirred for 4 hours. The suspension was added drop wise to a stirring solution of freshly sublimed SbCl_3 in hexane (10 mL), giving a grey suspension, which was stirred for a further 5 hours at room temperature. The precipitates were removed by filtration through celite to give a clear colourless solution. Colourless crystals were obtained upon concentration of the solution and storage at $-30\text{ }^\circ\text{C}$ for 24 hours.

*Synthesis of $\text{Sb}(\text{NON}^{\text{tBu}})\text{Cl}$ (**4.15a**)*

Synthesised according to the general procedure using 2.38 mL of a 1.6M solution of $n\text{BuLi}$ in hexane (3.80 mmol), 0.5 g of $(\text{NON}^{\text{tBu}})\text{H}_2$ (1.81 mmol) and 0.410 g of SbCl_3 (1.81 mmol). Isolated as colourless needles. Yield 0.591 g, 76 %. ^1H NMR (C_6D_6 , 600 MHz): δ 1.24 (s, 18H, CMe_3) 0.53, 0.29 (s, 6H, SiMe_2). $^{13}\text{C}\{^1\text{H}\}$ NMR (C_6D_6 , 150 MHz): δ 54.3 (CMe_3), 35.5 (CMe_3), 6.9, 6.2 (SiMe_2).

*Synthesis of $\text{Sb}(\text{NON}^{\text{Ph}})\text{Cl}$ (**4.15b**)*

Synthesised according to the general procedure using 1.60 mL of a 1.6M solution of $n\text{BuLi}$ in hexane (2.67 mmol), 0.40 g of $(\text{NON}^{\text{Ph}})\text{H}_2$ (1.27 mmol) and 0.29 g of SbCl_3 (1.27 mmol). Yield 0.386 g, 65 %. ^1H NMR (C_6D_6 , 300 MHz): δ 7.10 (d, 4H, $J = 6.8$, $m\text{-C}_6\text{H}_5$), 7.04 (t, 4H, $J = 6.8$, $o\text{-C}_6\text{H}_5$), 6.92 (t, 2H, $J = 6.8$, $p\text{-C}_6\text{H}_5$), 0.46, 0.26 (s, 6H, SiMe_2). $^{13}\text{C}\{^1\text{H}\}$ NMR (C_6D_6 , 75 MHz): δ 145.6, 130.0, 128.06, 124.9 (C_6H_5), 2.4, 2.3 (SiMe_2).

Synthesis of $Sb(NON^{Ar'})Cl$ (**4.15c**)

Synthesised according to the general procedure using 2.47 mL of a 1.6M solution of *n*BuLi in hexane (3.95 mmol), 0.70 g of $(NON^{Ar})H_2$ (1.88 mmol) and 0.43 g of $SbCl_3$ (1.88 mmol). Yield 0.812 g, 82 %. 1H NMR (C_6D_6 , 600 MHz): δ 7.00, * 6.96* (d, 2H, $J = 7.5$, *m*- C_6H_3), 6.89 (t, 2H, $J = 7.5$, *p*- C_6H_3), 2.61, 2.34 (s, 6H, *o*-Me), 0.53, 0.10 (s, 6H, SiMe₂). $^{13}C\{^1H\}$ NMR (C_6D_6 , 75 MHz): δ 141.9, 139.1, 137.1, 129.9, 128.9, 125.7 (C_6H_3), 21.3, 21.1 (*o*-Me), 3.6, 1.5 (SiMe₂). *two resonances overlap

Synthesis of $Sb(NON^{Ar})Cl$ (**4.15d**)

Synthesised according to the general procedure using 1.70 mL of a 1.6M solution of *n*BuLi in hexane (2.73 mmol), 0.60 g of $(NON^{Ar})H_2$ (1.24 mmol) and 0.28 g of $SbCl_3$ (1.24 mmol). Yield 0.410 g, 52 %. Melting point: 166-169 °C. Anal. Calcd. for $C_{28}H_{46}SbClN_2OSi_2$ (640.07): C, 52.54; H, 7.24; N, 4.38 %. Found: C, 52.43; H, 7.17; N, 4.33 %. 1H NMR (C_6D_6 , 300 MHz): δ 7.16–7.02 (m, 6H, *m*-/*p*- C_6H_3), 4.17, 3.70 (sept, $J = 6.9$, 2H, CHMe₂), 1.38 (d, $J = 6.9$, 6H, CHMe₂), 1.27 (d, $J = 6.9$, 12H, CHMe₂), 1.08 (d, $J = 6.9$, 6H, CHMe₂), 0.53, 0.17 (s, 6H, SiMe₂). $^{13}C\{^1H\}$ NMR (C_6D_6 , 75 MHz): δ 150.4, 147.8, 137.6, 126.8, 125.4, 124.6 (C_6H_3), 28.6, 28.2, 28.1, 27.9, 24.5, 24.2 (CHMe₂ and CHMe₂), 3.7, 2.1 (SiMe₂). ^{29}Si NMR (C_6D_6 , 100 MHz): δ -4.7.

Synthesis of $Sb(NON^{Ar\ddagger})Cl$ (**4.15e**)

A solution of *n*BuLi in hexane (1.3 mL of a 1.6M solution, 2.05 mmol) was added drop wise to a stirring solution of $(NON^{Ar\ddagger})H_2$ (1.10 g, 1.01 mmol) in toluene (7 mL) at -30 °C. The resulting orange suspension was allowed to warm to room temperature and stirred for 24 hours. The suspension was added drop wise to a stirring solution of freshly sublimed $SbCl_3$ (0.231 g, 1.01 mmol) in toluene (10 mL) resulting in formation of a red solution and black precipitate, which was stirred for a further 24 hours. Removal of the volatiles in vacuo gave a thick oil which was extracted with hexane and filtered through celite to give a clear red solution. Concentration of the reaction mixture to 3 mL and storage at room temperature resulted in the slow formation of colourless crystals of **4.15e** after 24 hours. Yield 0.285 g, 23 %. 1H NMR (C_6D_6 ,

300 MHz): δ 7.16–7.02 (m, 46H, CHPh_2 , C_6H_2 and C_6H_5), 6.45 (s, 2H, CHPh_2), 1.03 (s, 18H, CMe_3), 0.07, 0.03 (s, 6H, SiMe_2). $^{13}\text{C}\{^1\text{H}\}$ NMR (C_6D_6 , 75 MHz): δ 147.5, 147.3, 146.4, 144.9, 144.8, 144.0, 141.5, 140.1, 131.1, 131.0, 130.8, 130.6, 130.2, 128.6, 128.35, 127.0, 126.9, 126.7, 126.2 (C_6H_5 and C_6H_2), 51.8, 51.2 (CHPh_2), 34.5 (CMe_3) and, 31.0 (CMe_3), 4.2, 4.0 (SiMe_2).

4.5.2. Reactivity of $\text{Sb}(\text{NON}^{\text{R}})\text{Cl}$ with LiHBEt_3

*Synthesis of $\{\text{Sb}(\text{NON}^{\text{Ph}})\}_2(\text{NON}^{\text{Ph}})$ (**4.16b**)*

A solution of LiHBEt_3 in THF (0.20 mL of a 1.0 M solution, 0.20 mmol) was diluted further with Et_2O (10 mL), cooled to $-30\text{ }^\circ\text{C}$ and added dropwise to a stirring solution of **4.15b** (0.10 g, 0.21 mmol) in Et_2O (10 mL) resulting in the formation of a fine white precipitate. The resulting suspension was allowed to warm to room temperature, resulting in formation of a large amount of black solid and a colourless solution. Removal of the solid by filtration through celite followed by concentration to *ca.* 1 mL and storage at $-30\text{ }^\circ\text{C}$ for 24 hours yielded colourless blocks of **4.16b**. Yield 0.035 g, 44 % (based on **4.15b**). ^1H NMR (C_6D_6 , 300 MHz): δ 7.35 – 6.90 (m, 30H, C_6H_5), 0.19, 0.15, 0.14 (s, 12H, SiMe_2). $^{13}\text{C}\{^1\text{H}\}$ NMR (C_6D_6 , 75 MHz): δ 147.3, 146.9, 131.0, 129.7, 129.1, 128.7, 124.1, 123.9 (C_6H_5), 2.6, 2.4, 2.1 (SiMe_2).

*Synthesis of $\text{Sb}(\text{NON}^{\text{Ar'}})\text{H}$ (**4.17e**) or $\text{Sb}(\text{NON}^{\text{Ar}})\text{H}$ (**4.17d**)*

A solution of LiHBEt_3 in THF (0.40 mL of a 1.0 M solution, 0.40 mmol) was diluted further with Et_2O (10 mL), cooled to $-30\text{ }^\circ\text{C}$ and added dropwise to a stirring solution of **4.15c** (0.222 g, 0.42 mmol) or **4.15d** (0.269 g, 0.42 mmol) in Et_2O (10 mL) resulting in the formation of a fine white precipitate. The resulting suspension was allowed to warm to room temperature, resulting in formation of a small amount of a fine black solid. Removal of the solid by filtration through celite followed by concentration to *ca.* 1 mL and storage at $-30\text{ }^\circ\text{C}$ for 24 hours yielded colourless blocks of **4.17c** or **4.17d**. Yield 0.156 g, 79 % (**4.17c**) and 0.197 g, 81 % (**4.17d**). **4.17c**: ^1H NMR (C_6D_6 , 300 MHz): δ 10.90 (s, 1H, SbH), 7.04, 6.98 (d, 2H, $J = 7.5$, $m\text{-C}_6\text{H}_3$), 6.90 (t, 2H, $J = 7.5$, $p\text{-C}_6\text{H}_3$), 2.51, 2.25 (s, 6H, $o\text{-Me}$), 0.35, 0.19 (s, 6H, SiMe_2). $^{13}\text{C}\{^1\text{H}\}$ NMR (C_6D_6 , 75 MHz): δ 145.4, 137.7, 137.5, 129.1, 128.9, 124.6 (C_6H_3), 20.8, 20.5 ($o\text{-Me}$), 1.5, 1.0 (SiMe_2). **4.17d**: ^1H

NMR (C_6D_6 , 300 MHz): δ 11.34 (s, 1H, SbH), 7.12-7.00 (m, 6H, C_6H_3), 4.07, 3.71 (sept, J = 6.9, 2H, $CHMe_2$), 1.35 (d, J = 6.9, 6H, $CHMe_2$), 1.25 (m, 12H, $CHMe_2$), 1.19 (d, J = 6.9, 6H, $CHMe_2$), 0.39, 0.31 (s, 6H, $SiMe_2$). $^{13}C\{^1H\}$ NMR (C_6D_6 , 75 MHz): δ 149.3, 148.2, 140.8, 128.4, 126.0, 124.6 (C_6H_3), 28.2, 28.0, 27.8, 26.6, 24.2, 24.0 ($CHMe_2$ and $CHMe_2$), 1.6, 0.7 ($SiMe_2$).

4.5.3 Synthesis of Reduced Antimony Species

*General Procedure for $[Sb(NON^R)]_2$ ($R = tBu$ ([**4.18a**]₂), Ph ([**4.18b**]₂) or Ar' ([**4.18c**]₂))*

Method 1: Using $[Mg(BDI^{mes})]_2$ (**1.1**)

A solution of $[Mg(BDI^{mes})]_2$ (**1.1**) in toluene (5 mL) was added dropwise to a solution of $Sb(NON^R)Cl$ in toluene (5 mL), resulting in the immediate formation of a colourless precipitate and yellow ([**4.18a**]₂ and [**4.18b**]₂) or red ([**4.18c**]₂) solution. Stirring the suspension for a further 2h followed by removal of the volatiles *in vacuo*, extraction into hot hexane and hot filtration through celite gave a clear yellow or red solution. Concentration of the solution to ca. 2 mL and storage at -30 °C gave yellow crystals of $[Sb(NON^R)]_2$ after 24 hours.

Method 2: Using $[Mg(BDI^{Ar})]_2$ (**1.2**)

A solution of $[Mg(BDI^{Ar})]_2$ (**1.2**) in toluene (5 mL) was added dropwise to a solution of $Sb(NON^R)Cl$ in toluene (5 mL). Heating the resulting reaction mixture to 50 °C resulted in formation of a colourless precipitate and yellow or red solution. Stirring the suspension for a further 24h followed by removal of the volatiles *in vacuo* and extraction into hot hexane. The solids were removed by hot filtration through celite to give a clear yellow or red solution which was concentrated to ca. 2 mL. Storage of the solution at -30 °C yielded a mixture of colourless crystals of $Mg(BDI^{Ar})Cl$ and yellow or red crystals of $[Sb(NON^R)]_2$. Fractional recrystallisation from hexane at -30 °C of the mixture gave samples enriched in $Mg(BDI^{Ar})Cl$ (crop 1) and $[Sb(NON^R)]_2$ (crop 2). An additional clean crop of $[Sb(NON^R)]_2$ was obtained upon further concentration of the mother liquor.

Synthesis of [Sb(NON^{tbu})]₂ ([4.18a]₂)

Synthesised according to the general procedures using 0.086 g of **1.1** (0.12 mmol) and 0.10 g of **4.15a** (0.23 mmol, method 1) or 0.102 g of **1.2** (0.12 mmol) and 0.10 g of **4.15a** (0.23 mmol, method 2). Yield 0.061 g, 68 % (method 1) or 0.032 g, 35 % (method 2). ¹H NMR (C₆D₆, 600 MHz): δ 1.44 (s, 18H, CMe₃) 0.52, 0.40 (s, 6H, SiMe₂). ¹³C{¹H} NMR (C₆D₆, 150 MHz): δ 54.1 (CMe₃), 35.4 (CMe₃), 8.2, 7.5 (SiMe₂).

Synthesis of [Sb(NON^{ph})]₂ ([4.18b]₂)

Synthesised according to the general procedures using 0.114 g of **1.1** (0.16 mmol) and 0.151 g of **4.15b** (0.32 mmol, method 1) or 0.142 g of **1.2** (0.16 mmol) and 0.150 g of **4.15b** (0.32 mmol, method 2). Yield 0.078 g, 56 % (method 1) or 0.042 g, 31 % (method 2). ¹H NMR (C₆D₆, 300 MHz): δ 7.25 (d, 4H, *J* = 6.8, *m*-C₆H₅), 7.17 (t, 4H, *J* = 6.8, *o*-C₆H₅), 6.93 (t, 2H, *J* = 6.8, *p*-C₆H₅), 0.24, 0.13 (s, 6H, SiMe₂). ¹³C{¹H} NMR (C₆D₆, 75 MHz): δ 150.4, 129.7, 126.7, 123.0 (C₆H₅), 5.4, 1.0 (SiMe₂).

Synthesis of [Sb(NON^{Ar})]₂ ([4.18c]₂)

Synthesised according to the general procedures using 0.143 g of **1.1** (0.20 mmol) and 0.212 g of **4.15c** (0.40 mmol, method 1) or 0.100 g of **1.2** (0.12 mmol) and 0.120 g of **4.15b** (0.23 mmol, method 2). Yield 0.083 g, 42 % (method 1) or 0.011 g, 31 % (method 2). ¹H NMR (C₆D₆, 300 MHz): δ 7.02 (d, 2H, *J* = 7.2, C₆H₃), 6.83 (m, 6H, C₆H₃), 2.39 (s, 6H, *o*-Me), 2.21 (br, 6H, *o*-Me), 0.29, 0.19 (s, 6H, SiMe₂). ¹³C{¹H} NMR (C₆D₆, 75 MHz): δ 138.6, 137.2, 129.8, 128.9, 124.7 (C₆H₃), 30.1, 21.1 (*o*-Me), 2.4 (br, SiMe₂).

Synthesis of [(BDI^{mes})Mg(NON^{Ar})Sb]₂ (4.19d)

A solution of **1.1** (0.28 g, 0.39 mmol) in toluene (5 mL) was added dropwise to a solution of Sb(NON^{Ar})Cl (0.25 g, 0.39 mmol) in toluene (5 mL), resulting in the immediate formation of a colourless precipitate and a pink/red solution. Stirring the suspension for a further 2h followed by hot filtration through celite gave a clear pink/red solution. Concentration of the solution to ca. 2 mL, addition of a few drops of THF and storage at -30 °C gave pink crystals of **4.19d** after

24 hours. Yield 0.189 g, 47 %. ^1H NMR (C_6D_6 , 300 MHz): δ 7.26 (d, 4H, $J = 7.5$, C_6H_3), 7.15–6.90 (m, 8H, C_6H_3), 6.92 (s, 8H, C_6H_2), 6.82 (s, 4H, C_6H_3), 4.98 (s, 2H, $\gamma\text{-CH}$), 3.66 (sept, 4H, $J = 7.5$, CHMe_2), 3.50 (br, 4H, CHMe_2), 3.27 (br, 12H, THF-CH_2), 2.29 (s, 12H, $p\text{-Me}$), 2.21 (br, 24H, $o\text{-Me}$), 1.57 (s, 12H, CMe), 1.45, 1.27 (d, 12H, $J = 7.5$, CHMe_2), 1.15 (br, 24H, CHMe_2), 0.18, 0.05 (s, 6H, SiMe_2). $^{13}\text{C}\{^1\text{H}\}$ NMR (C_6D_6 , 150 MHz): δ 168.6 ($\gamma\text{-C}$), 161.5, 158.4, 146.9, 144.7, 142.2, 137.9, 133.6, 125.7, 123.6 (C_6H_3), 96.3 (CMe), 28.0, 27.9, 26.4, 26.2, 25.0, 24.0, 23.1, 19.7 (CHMe_2 , CHMe_2 and CMe), 5.4, 1.9 (br, SiMe_2).

*Synthesis of $[(\text{BDI}^{\text{mes}})\text{Mg}(\text{NON}^{\text{Ar}})\text{Sb}]_2$ (**4.20d**)*

A solution of **1.2** (0.183 g, 0.21 mmol) in toluene (5 mL) was added dropwise to a solution of $\text{Sb}(\text{NON}^{\text{Ar}})\text{Cl}$ (0.132 g, 0.21 mmol) in toluene (5 mL). Heating the resulting yellow solution to 50 °C for 20 mins results in formation of a red/pink solution and a colourless precipitate. Hot filtration of the suspension through celite and storage at -30 °C for 24 hours gave pink crystals of **4.20d**. Yield 0.075 g, 34 %. ^1H NMR (C_6D_6 , 600 MHz): δ 7.16 – 7.00 (m, 22H, C_6H_3), 7.01 (d, 4H, $J = 7.5$, C_6H_3), 6.88 (t, 2H, $J = 7.5$, C_6H_3), 4.80 (s, 2H, $\gamma\text{-CH}$), 3.75, 3.52, 3.14 (sept, 4H, $J = 7.5$, CHMe_2), 3.04 (br, 4H, CHMe_2), 1.47 (s, 12H, CMe), 1.32 (d, 12H, $J = 7.5$, CHMe_2), 1.16 (d, 24H, $J = 7.5$, CHMe_2), 1.16 (br, 12H, CHMe_2), -0.12, -0.15 (s, 6H, SiMe_2). $^{13}\text{C}\{^1\text{H}\}$ NMR (C_6D_6 , 150 MHz):* δ 171.6 ($\gamma\text{-C}$), 142.1, 126.4, 126.1 (C_6H_3), 29.3, 27.7, 26.2, 25.4, 24.4, 23.1 (CHMe_2 , CHMe_2 and CMe), 5.4, 1.6 (SiMe_2). *Due to poor solubility, some peaks are missing from the ^{13}C NMR spectrum.

*NMR reaction of **4.15a-c** with excess **1.1** or **1.2***

A J. Young's NMR tube was charged with **1.1** or **1.2** (0.2 mmol) and $\text{Sb}(\text{NON}^{\text{R}})\text{Cl}$ (0.05 mmol, R = $t\text{Bu}$ (**4.15a**) Ph (**4.15b**) or (**4.15c**)) in C_6D_6 (0.5 mL) and heated to 70 °C and monitored using ^1H NMR spectroscopy at regular intervals over 78 h.

4.5.3. Reactivity of Sb(II) Compounds with White Phosphorus (P_4)

A J. Young's NMR tube was charged with $[\text{Sb}(\text{NON}^{\text{R}})]_2$ (0.025 mmol, R = Ph (**4.18b**, 0.020 g) or (**4.18c**, 0.025)) and P_4 (0.003 g, 0.025 mmol) in C_6D_6 (0.5 mL) and was heated to 70 °C and

monitored using ^1H NMR spectroscopy at regular intervals over 78 h. Data for **4.23c**: ^1H NMR (C_6D_6 , 600 MHz): δ 7.11 (d, 2H, $J = 7.2$, C_6H_3), 6.97 (m, 6H, C_6H_3), 2.62, 2.38 (s, 6H, *o*-Me), 0.42, 0.14 (s, 6H, SiMe_2). $^{13}\text{C}\{^1\text{H}\}$ NMR (C_6D_6 , 150 MHz): δ 143.8, 138.3, 137.0, 129.6, 129.5, 125.2 (C_6H_3), 30.1, 21.1 (*o*-Me), 3.8, 1.9 (SiMe_2). $^{31}\text{P}\{^1\text{H}\}$ NMR (C_6D_6 , 121 MHz): δ -110.1, -349.6 (t, $J_{\text{PP}} = 152$).

Chapter 5. Synthesis of Low Oxidation State Indium Species

5.1. Introduction

5.1.1. Low Oxidation State Indium Compounds

With an electron configuration of $[\text{Kr}]4d^{10}5s^25p^1$, indium is most commonly found in the +3 and +1 oxidation states which are formed through loss of the 5s/p and 5p electrons, respectively. While the chemistry of the lighter elements in group 13 (B, Al and Ga) is dominated by complexes in the +3 oxidation state, the 5s electrons of indium are sufficiently inert that the +1 oxidation state is readily accessible.¹²⁹ As such, simple salts of both In(I) and In(III) are commercially available. In contrast, monohalide salts of aluminium and gallium are metastable, and while they have been demonstrated to behave as M(I) species, are believed to have complex mixed-valent polymetallic structures.¹³⁰

Indium dichloride, ' InCl_2 ', in which a formal oxidation state of +2 is suggested, is also commercially available. However, analogous to gallium dichloride, this species exists as a mixed-valent species containing In(I) and In(III) and is better described as $\text{In}[\text{InCl}_4]$, highlighting the relative stability of the +1/+3 oxidation states compared to the +2 oxidation state.¹³¹ The addition of a Lewis base (e.g. THF, $\text{P}(\text{nBu})_3$, tmeda, NHC's) allows the isolation and structural authentication of indium dihalide species of the form $[\text{InX}_2(\text{L})_n]_2$ (where L = Lewis base, $n = 1$ or 2, X = halogen), which contains an In-In single bond with both indium centres formally in the +2 oxidation state (Figure 5.1, **5.1**).¹³² Base free indium(II) species $\{\text{R}_2\text{In}\}_2$ have also been isolated, with structurally characterised examples stabilised by sterically demanding monodentate alkyl,¹³³ aryl¹³⁴ or silyl¹³⁵ ligands (**5.2 – 5.7**). Diindanes supported by dianionic di(amido) frameworks have also been reported (**5.8 – 5.10**).¹³⁶ Despite the bulk imposed by the nitrogen substituents in these compounds, the nitrogen atoms do not adopt a staggered

conformation about the In-In bond in the solid-state, instead crystallising with eclipsed conformations.

The only monometallic In(II) species with no covalent metal-metal bonding interactions is the bis(boryl) stabilised In(II) radical $\bullet\text{In}(\text{B}\{\text{N}(\text{Ar})\text{C}(\text{H})\}_2)$ (**5.11**).¹³⁷ EPR and computational analysis revealed a predominantly metal-centred radical with ~73 % of the spin density located on the indium. The stability of the radical is due to a combination of electronic stabilisation (i.e. spin delocalisation onto the ligands) and the steric protection provided by the bulky Ar substituents.

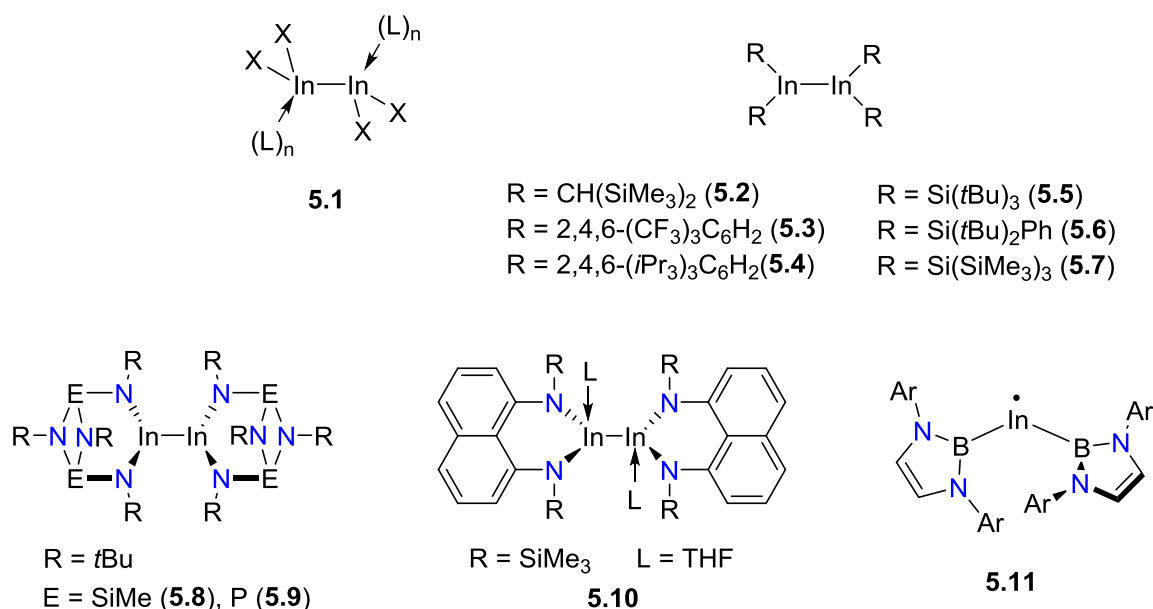


Figure 5.1. Examples of structurally characterised In(II) species.

Homonuclear $\text{M}=\text{M}$ bonding in the heavier group 13 elements is currently unknown, with most structurally characterised In(I) species existing as either monomeric units or loosely associated dimers with long In-In bonds. In contrast, boron and aluminium can form homonuclear multiple bonds, often stabilised by neutral σ -donor ligands ($\text{L} = \text{phosphine, NHC}$).¹³⁸ Bimetallic complexes of the general form $\text{M}'_2(\text{ArMMAr})$ (where $\text{M}' = \text{alkali metal}$, $\text{M} = \text{Al, Ga}$ and $\text{Ar} = \text{bulky aryl group}$) have also been reported, alleged to have triple bonded $\text{M}\equiv\text{M}$ cores.¹³⁹ This may be rationalised by the relatively low singlet-triplet energy separation in the lighter

elements, allowing ‘alkene-like’ double bond formation via the interaction of triplet states. As the group is descended, the singlet-triplet energy separation becomes significantly larger (Section 1.1.3) and the valence lone pair of electrons become predominantly s-character resulting in a lack of electron density that can be used in bond formation.¹⁸ Dimeric In(I) species therefore often exist as loosely associated dimers, with calculations showing that the attraction is predominantly caused by a closed shell interactions (dispersion forces).¹⁴⁰ For example, the ter-phenyl supported In(I) species $[\text{In}(\text{2,6-Ar}_2\text{C}_6\text{H}_3)]_2$ (Figure 5.2, **[5.12]**₂) exists as a dimer in the solid-state, with a trans-bent structure and an In-In distance (2.9786(5) Å) longer than typical single bonding interactions (2.6464(3) – 2.9382(4) Å).¹⁴¹ When dissolved in solution, this species dissociates into monomeric $\text{In}(\text{2,6-Ar}_2\text{C}_6\text{H}_3)$ (**5.12**), consistent with calculations which show a small energy barrier to dissociation/dimerization.

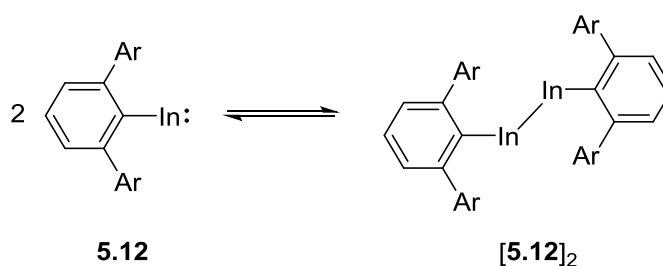


Figure 5.2. Reversible dimerization of **5.12**.

5.1.2. N-heterocyclic Group 13 Compounds

5.1.2.1. Boron, Aluminium and Gallium

N-heterocyclic carbenes have emerged as some of the most versatile and widely used stabilising ligands in coordination chemistry.¹⁴² The stabilisation of these singlet carbenes derives from the ability to form multiple resonance structures and often involve steric protection. These species feature relatively large singlet-triplet energy gaps, with a lone pair of electrons in a p-type orbital on the carbene carbon centre. The stabilising properties offered by these ligands has prompted the investigation of isovalent group 13 species, in which a lone pair of electrons is present in a p-type orbital on the group 13 element.¹⁴³

The most developed systems in this compound class are anionic N-heterocyclic gallium(I) compounds, featuring 5-membered metallacycles balanced by group 1 metals as either non-contact or contact ion-pairs.¹⁴⁴ In all cases, these species are stabilised by sterically demanding di(amido) ligands featuring organic backbones (Figure 5.3, **5.13** – **5.22**). Calculations performed on model systems show that these complexes possess a singlet lone pair of electrons localised in a sp-type orbital on the gallium centre with significant directionality, suggesting these species will behave as good σ -donors.¹⁴⁵ This has been demonstrated for $[\text{:Ga}\{\text{N}(\text{Ar})\text{C}(\text{H})\}_2]^-$ (**5.13**), which has been used to form an array of compounds containing metal-gallium bonds, many of which were unprecedented.¹⁴³

The first structurally characterised anionic N-heterocyclic boryl(I) $[\text{:B}\{\text{N}(\text{Ar})\text{C}(\text{H})\}_2]^-$ (**5.23**) was reported in 2006 by Yamashita, Nozaki and co-workers, formed by reduction of the corresponding B(III) bromide species using Li in dimethoxyethane and a catalytic amount of naphthalene.¹⁴⁶ This species was identified as a dimer in the solid-state, with B-Li bonds 8.5 % longer than the sum of covalent radii and calculations showing a highly polarised bond with significant anionic character on the boron. Since this landmark discovery, several related N-heterocyclic boron(I) compounds have been reported, all involving formation of a 5-membered heterocycle and a long B-Li bond (**5.24**).¹⁴⁷ These species have been demonstrated to behave as a source of nucleophilic boron, mirroring the behaviour of **5.13**. In contrast, there are no examples of anionic N-heterocyclic aluminium(I) species, with attempts to synthesise the aluminium analogue of **5.13** and **5.23** instead resulting in the deposition of aluminium metal.^{144d} However, calculations performed on the model species $[\text{:Al}\{\text{N}(\text{H})\text{C}(\text{H})\}_2]^-$ suggest that these species should be more stable than their boryl analogues.¹⁴⁸

Neutral N-heterocyclic M(I) complexes have been reported for Al and Ga, featuring resonance stabilised *N,N'*-chelating guanidinate or β -diketiiminate ligands to give 4- and 6-membered heterocycles, respectively (Figure 5.4, **5.25** – **5.28**).¹⁴⁹ In all cases, the HOMO involves a singlet pair of electrons localised on the metal centre in an sp-mixed orbital, with an empty p-orbital also present as either the LUMO (**5.25**) or LUMO+1 (**5.26** – **5.28**). In contrast, no examples of

neutral N-heterocyclic boryl complexes have been reported in the literature, with all attempts to synthesise these types of species either resulting in no reaction or intractable product mixtures.¹⁵⁰

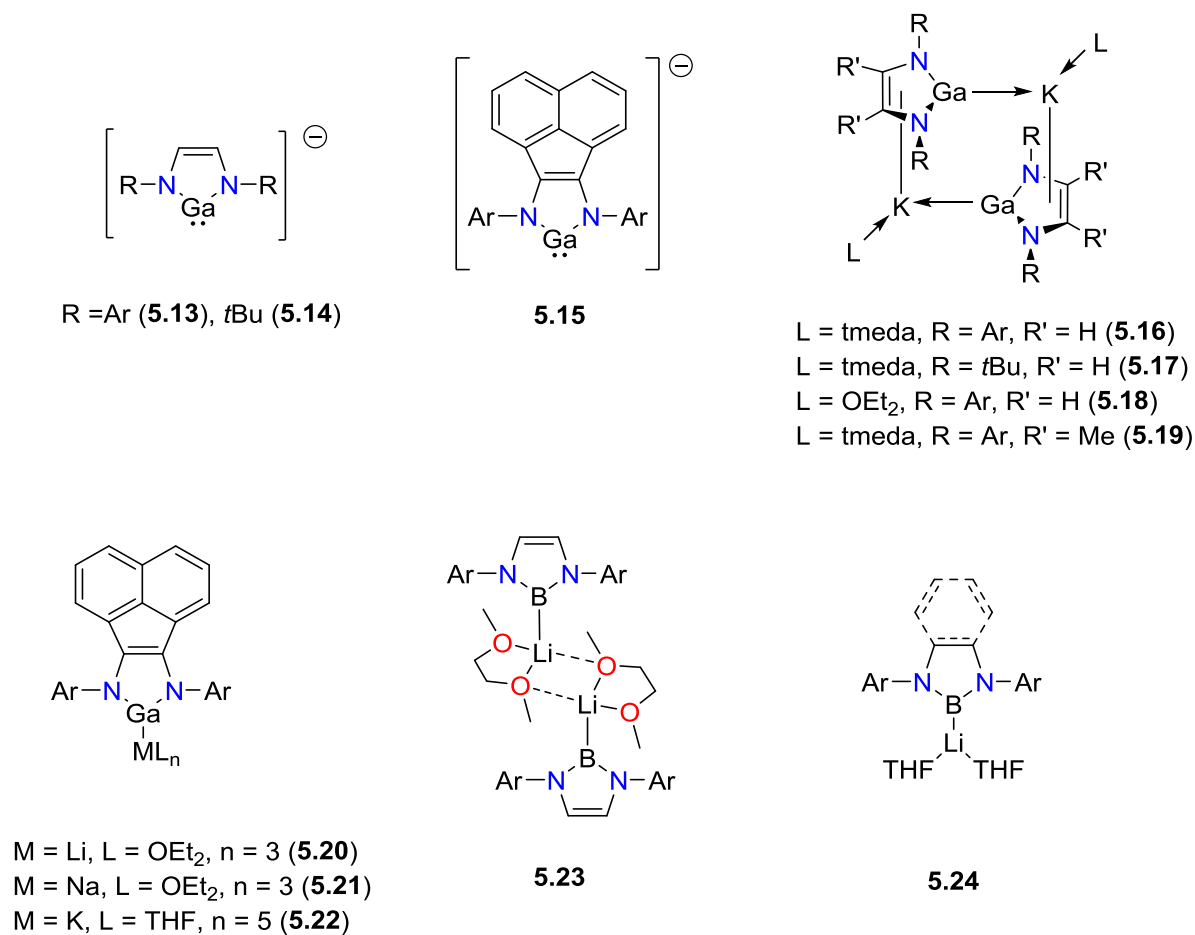


Figure 5.3. Examples of anionic 5-membered N-heterocyclic gallyl and boryl compounds.

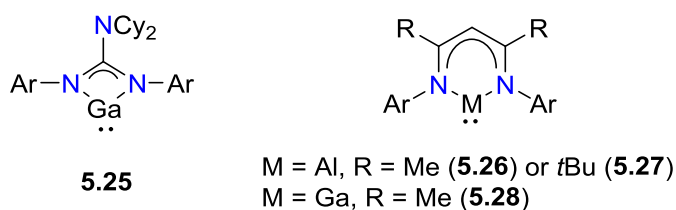
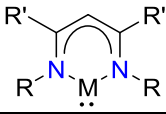
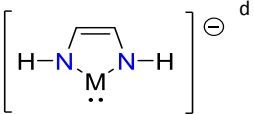


Figure 5.4. Examples of Neutral 4- and 6-membered N-heterocyclic gallyl and aluminyll compounds.

Calculations performed on model systems for N-heterocyclic M(I) species (e.g. $[\text{M}\{\text{N}(\text{H})\text{C}(\text{H})\}_2]^-$, $\text{M} = \text{B} - \text{In}$) reveal a general trend in singlet-triplet energy separation (Table 5.1).¹⁵¹ N-heterocyclic boron(I) compounds have relatively small singlet-triplet energy separation ($-4.3 - 22.2 \text{ kcalmol}^{-1}$, negative value corresponds to $E_{\text{triplet}} < E_{\text{singlet}}$) likely explaining the low stability and difficulty in isolation of the neutral N-heterocyclic B(I) species. The singlet-triplet energy separation in N-heterocyclic Al(I) and Ga(I) compounds are significantly larger ($35.4 - 54.5 \text{ kcalmol}^{-1}$).¹⁵²

Table 5.1. Singlet-triplet energy separation in N-heterocyclic compounds.^a

M				
	R = R' = H ^b	R = Me, R' = H ^b	R = Ph, R' = Me ^c	
B	-4.3	-1.2	3.5	22.2
Al	35.4	39.2	45.7	50.5
Ga	54.3	53.5	54.5	47.9
In	61.4	67.4	55.1	38.8

^aunits = kcalmol^{-1} , negative values indicate $E_{\text{triplet}} < E_{\text{singlet}}$. ^bcalculated at B3LYP level of theory.^{151b} ^ccalculated at B3LYP/LANL2DZ level of theory.^{151a} ^dcalculated at B3LYP/6-31++g(d,p) level of theory.¹⁵²

5.1.2.2. Indium

Despite the enhanced stability of In(I) and the fact that indium(I) halide salts are commercially available, the first N-heterocyclic In(I) compounds were not reported until 2004.¹⁵³ To date, these species are limited to neutral In(I) species featuring resonance stabilised guanidinate or β -diketiiminate ligands (Figure 5.5, **5.29 – 5.34**).^{149d, 154} In the latter case, when $\text{R} = \text{Ar}$ the species exists as a monomeric In(I) species in the solid-state, while loosely associated dimers were observed when $\text{R} = \text{mesityl}$ or 2,6-dimethylphenyl (Ar') ($\text{In} \cdots \text{In}$ distance 3.1967 and 3.3400(5) Å). Calculations show that the lone pair of electrons is localised in hybridised sp-type orbitals on the indium centre with significant directionality, suggesting that these species

will behave as σ -donor ligands. This was confirmed for **5.29**, which has been demonstrated to behave as ligands at Pt and Ru metal centres.¹⁵⁵

No anionic N-heterocyclic In(I) species have been reported in the literature. However, calculations performed on $[\text{In}\{\text{N}(\text{H})\text{C}(\text{H})\}_2]^-$ (Table 5.1) reveal a smaller singlet-triplet energy separation ($38.8 \text{ kcal mol}^{-1}$) than its aluminium and gallium analogues, but significantly larger than its boron analogue.¹⁵² The lone pair is centred on the indium in a molecular orbital with significant p-character and, despite being more diffuse than those of the lighter elements, exhibits significant directionality and was predicted to be a good nucleophile. Attempts to isolate the indium analogue of **5.13**, $[\text{In}\{\text{N}(\text{Ar})\text{C}(\text{H})\}_2]^-$, were reported to be unsuccessful, instead forming the In(II) species $[\text{In}(\text{Cl})\{\text{N}(\text{Ar})\text{C}(\text{H})\}_2]_2$ which contains an In-In bond and a chloride atom on each indium centre.^{132c}

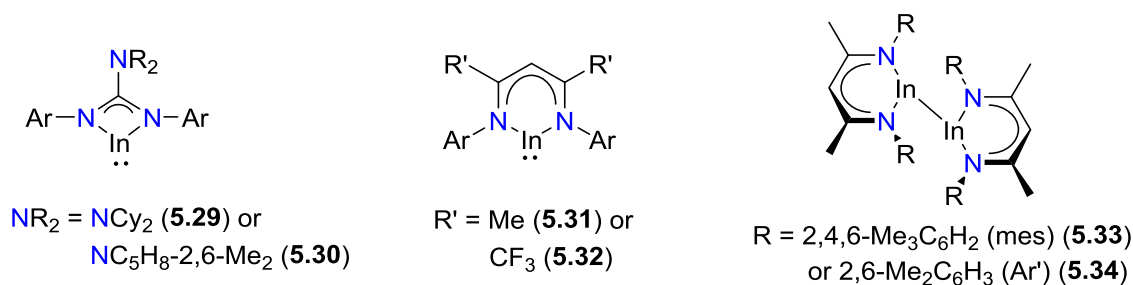


Figure 5.5. Isolated examples of N-heterocyclic Indium compounds.

5.1.3. Indium Hydrides

The chemistry of group 13 metal hydrides is dominated by B, Al and Ga, which play key roles in synthetic chemistry and are widely used as reducing agents. In contrast, indium hydrides are relatively uncommon, owing in part to the reduced stability of M-H bonds for the heavier p-block elements (Section 1.1.2).

Indium trihydride exists predominantly in the polymeric form $[\text{InH}_3]_x$ as a thermally unstable white solid.^{15b} Prior to 1996, neutral indium hydrides were limited to investigation at low temperature using IR spectroscopy and matrix-isolation techniques.¹⁵⁶ Over the last 20 years, several examples of stable indium hydrides have been reported in the literature. These are

typically stabilised by sterically demanding ligands or multidentate ligands containing neutral donor atoms. Jones and co-workers reported the synthesis of a series of indium trihydride species stabilised by phosphine σ -donor ligands, $[\text{InH}_3(\text{PR}_3)_n]$ (Figure 5.6, **5.35**; $\text{R} = \text{Cy}, \text{Cy}^{\text{P}}, \text{Ph}$; $\text{Cy}^{\text{P}} = \text{cyclopentane}$; $n = 1$ or 2), displaying a significant increase in the thermal stability of the InH_3 moiety (stable up to 50°C).¹⁵⁷ The solid-state structures of these species show no bridging hydride motifs, demonstrating the effectiveness of using a Lewis base to break the polymeric nature of indium trihydride. Changing the σ -donor to the Arduengo-type carbene 1,3-bis(2,4,6-trimethylphenyl)imidazol-2-ylidene improved the thermal stability of the InH_3 moiety (decomp. 115°C) (**5.36**).¹⁵⁸ This species also had a monomeric structure with no close contacts observed in the solid-state.

Indane derivatives containing only one In-H moiety have also been investigated. The neutral species $\text{In}(2-(\text{Me}_2\text{NCH}_2)\text{C}_6\text{H}_4)_2\text{H}$ (**5.37**) features a five-coordinate metal centre with a single In-H bond.¹⁵⁹ The amine groups stabilise the indium centre through dative interactions, acting to encapsulate the metal centre. More recently, the amidinate species $\text{In}(\text{CH}\{\text{NAr}\}_2)_2\text{H}$ (**5.38**, $\text{Ar} = 2,6\text{-iPr}_2\text{C}_6\text{H}_3$) was isolated; this species was observed to be stable up to 160°C .¹⁶⁰

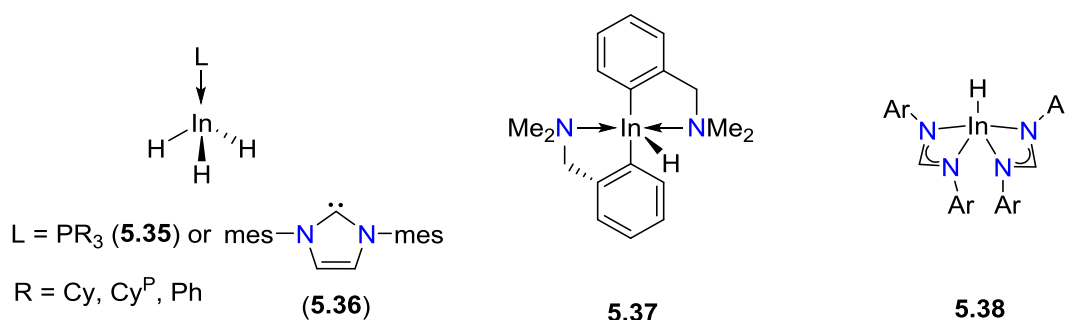


Figure 5.6. Reported examples of stable indium hydride species.

5.2. Chapter Outline

The work described in this chapter aims to synthesise low oxidation state indium compounds (i.e. In(I) and In(II)) supported by the (NON^{Ar}) -ligand. It is anticipated that this ligand will provide sufficient steric bulk to protect the metal centre and disfavour disproportionation

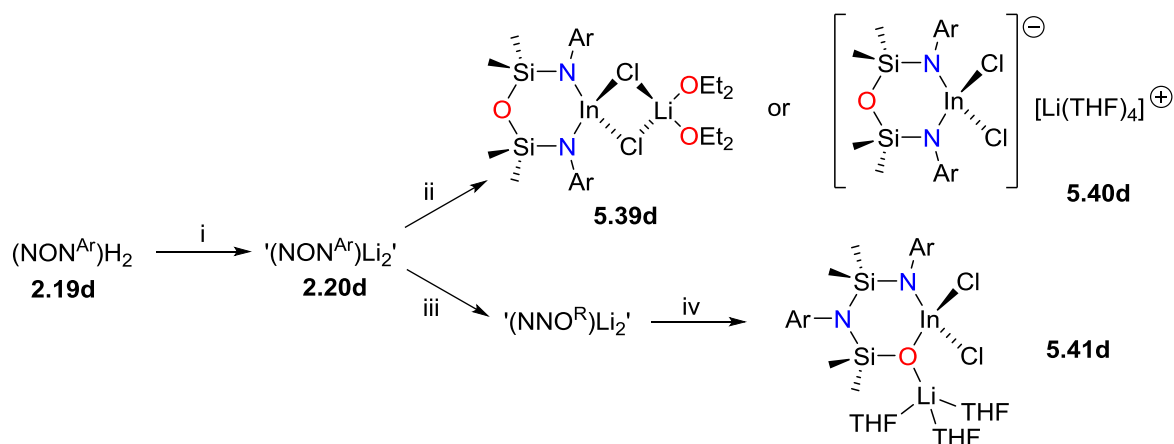
reactions. Of particular interest is the synthesis of an unprecedented anionic N-heterocyclic In(I) species. Analogous to the previously discussed synthesis of low oxidation state Bi and Sb compounds (chapter 2 and 4, respectively), access to the In(I) and In(II) species will be attempted through In-H bond homolysis and reduction of In(III) halide precursors using a group 1 metal reducing agent. However, the stability of compounds featuring In-H bonds supported by bulky ligands suggests that the former may not be an appropriate route to low oxidation-state indium compounds. While commercially available In(I) and In(II) halide salts may be used to access these types of compounds, reactions involving these materials are expensive, uncontrolled and often low yielding.

5.3. Results and Discussion

5.3.1. Synthesis of Indium(III) Halide Species

The reaction of $(\text{NON}^{\text{Ar}})\text{Li}_2'$ (**2.20d**) (generated *in-situ* from **2.19d** and 2 equiv. *n*BuLi) with InCl_3 in Et_2O or THF proceeds with formation of a colourless solution and white powder. Removal of the solvent *in vacuo*, extraction into Et_2O and filtration through celite gave a colourless solution, from which colourless crystals of $\text{In}(\text{NON}^{\text{Ar}})(\mu\text{-Cl})_2\text{Li}(\text{Et}_2\text{O})_2$ (**5.39d**) or $[\text{Li}(\text{THF})_4][\text{In}(\text{NON}^{\text{Ar}})\text{Cl}_2]$ (**5.40d**) were isolated (Scheme 5.1). In contrast, when **2.20d** was stirred in THF for 24 hours prior to the addition to a suspension of InCl_3 in THF, the mixed amide-alkoxide species $\text{In}(\text{NNO}^{\text{Ar}}.\text{Li}(\text{THF})_3)\text{Cl}_2$ (**5.41d**) was obtained as colourless crystals. This presumably proceeds according to the THF-promoted retro-Brook rearrangement proposed by Leznoff and co-workers (see Section 1.4.3), resulting in the *in-situ* formation of $(\text{NNO})\text{Li}_2'$. Attempts to synthesise and isolate the neutral species $\text{In}(\text{NON}^{\text{Ar}})\text{Cl}$ or $\text{In}(\text{NNO}^{\text{Ar}})\text{Cl}$ using a 'non-coordinating' solvent (e.g. toluene) were unsuccessful, instead forming an intractable white solid from which no clean products could be isolated. The ^1H NMR spectra of **5.39d** and **5.40d** show a single set of resonances for the SiMe_2 (δ_{H} 0.43 and 0.58, respectively) and CHMe_2 protons (δ_{H} 4.19 and 4.35, respectively). In contrast, the ^1H NMR spectrum of **5.41d** shows

two sets of resonances for the SiMe_2 (δ_{H} 0.23 and 0.35) and CHMe_2 protons (δ_{H} 4.00 and 4.31), reflecting the magnetically inequivalent SiMe_2 and NAr groups.



Scheme 5.1. Synthesis of indium(III) halide species **5.39-41d**. i) 2 $n\text{BuLi}$, Et_2O . ii) InCl_3 , Et_2O (**5.39d**) or THF (**5.40d**), 12 h. iii) THF, 24 h, RT. iv) InCl_3 , THF, 12 h.

Single crystal X-ray diffraction was used to investigate the solid-state structures of **5.39-5.41d** (Figure 5.7 and Figure 5.8). **5.39d** was identified as the bis(chloride)-bridged lithium indate species $\text{In}(\text{NON}^{\text{Ar}})(\mu\text{-Cl})_2\text{Li}(\text{Et}_2\text{O})_2$, while **5.40d** exists as the charge separated ion pair consisting of discrete $[\text{In}(\text{NON}^{\text{Ar}})\text{Cl}_2]^-$ anions balanced by $[\text{Li}(\text{THF})_4]^+$ cations. In both cases, the (NON^{Ar}) -ligand chelates a 4-coordinate indium metal centre with a $\kappa_2\text{-N,N'}$ -bidentate bonding mode, with two chloride ligands occupying the other coordination sites. The chloride ligands in **5.39d** bridge the indium centre and a lithium atom solvated by 2 x Et_2O molecules, while the chloride ligands in **5.40d** are terminal. The planar InCl_2Li metallacycle in **5.39d** sits almost perpendicular to the N_2In and LiO_2 least squares planes (88.5° and 81.9° , respectively). As expected, the bridging In-Cl distances in **5.39d** (2.4288(9) and 2.4194(8) Å) are significantly longer than the terminal In-Cl bonds of **5.40d** (2.3866(13) and 2.3769(14) Å). Both of these distances are significantly longer than In-Cl bond distances observed in the $[\text{InCl}_4]^-$ anion (range 2.328(3) – 2.364(4) Å).¹⁶¹ The lithium-chloride distances in **5.39d** (2.432(4) and 2.428(4) Å) are also long ($\Sigma_{\text{cov}}(\text{Li-Cl}) = 2.30$ Å). The In-N distances of **5.39d** (2.078(1) and 2.070(2) Å) are shorter than those of **5.40d** (2.092(3) and 2.094(4) Å). As a result, the bite angle of the ligand (NON^{Ar}) -ligand in **5.39d** ($109.33(7)^\circ$) is significantly larger than that of **5.40d** ($105.0(1)^\circ$), and

coincides with a concomitant decrease in the Cl-In-Cl angle ($93.15(2)^\circ$ and $100.96(5)^\circ$, respectively).

The solid-state structure of **5.41d** confirms the formation of a contact ion-pair and confirms the rearrangement of the (NON^{Ar})-ligand to form the (NNO^{Ar})-ligand, which chelates the indium centre in a κ_2 -*N,O*-bidentate fashion to form a 6-membered metallacycle with a boat conformation. The In-N and In-O bond distances ($2.072(1)$ and $2.061(1)$ Å, respectively) are consistent with single bonding interactions and are similar to the In-N distances in **5.39d**, while the bite angle for the (NNO^{Ar})-ligand ($104.45(5)^\circ$) is similar to that observed for the (NON^{Ar})-ligand in **5.40d**. In addition, the In \cdots N2 distance ($3.316(1)$ Å) is significantly longer than the sum of covalent radii (2.13 Å), and is similar to the In \cdots O1 distance in **5.39d** and **5.40d** ($3.313(2)$ and $3.413(2)$ Å, respectively), confirming bidentate coordination with no significant bonding contributions from N2. Two terminal chloride atoms complete the coordination sphere of the indium to give a 4-coordinate tetrahedral metal centre. The In-Cl bond distances ($2.3628(6)$ and $2.3768(6)$ Å) and Cl-In-Cl angle ($103.48(2)^\circ$) are similar to those in **5.40d**, reflecting the terminal nature of the chloride atoms. The siloxane oxygen atom (O1) bridges the indium centre and the lithium counter-ion which is also coordinated by three THF molecules ([Li(THF)₃]⁺).

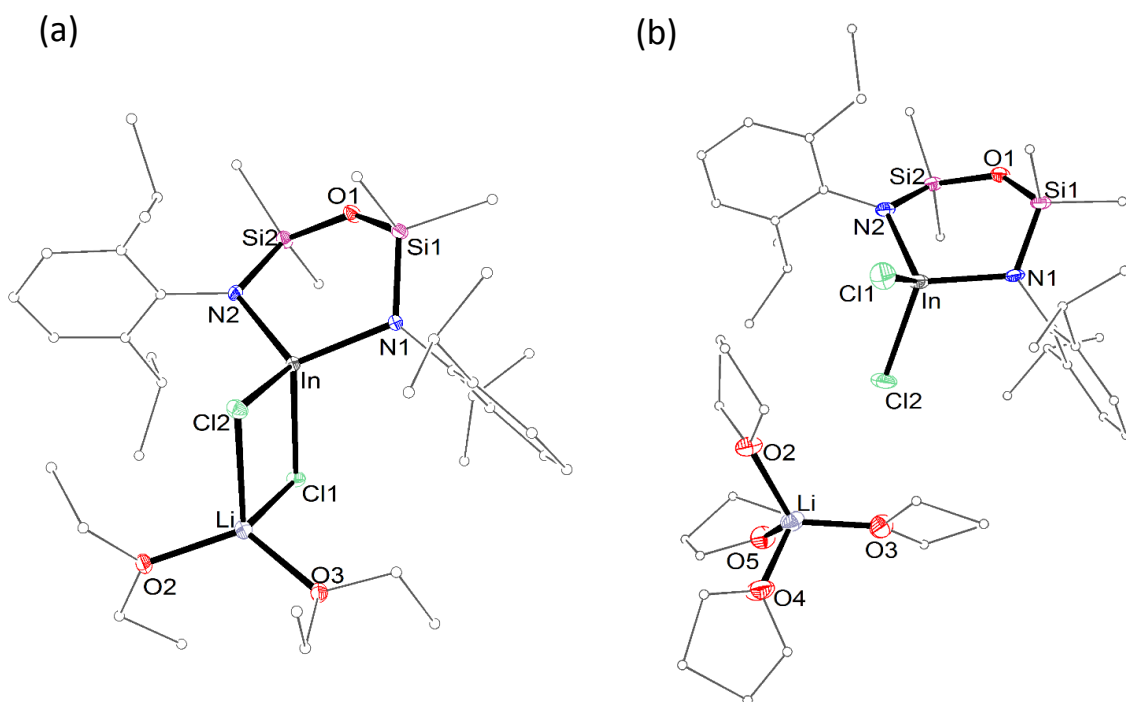


Figure 5.7. Molecular structures of **5.39d** and **5.40d** (thermal ellipsoids displayed at 30% probability level). Carbon atoms are displayed in wireframe format and hydrogen atoms are omitted for clarity. Selected bond lengths (Å) and angles (°): **5.39d**, In-Cl1 2.4288(9), In-Cl2 2.4194(8), In-N1 2.078(1), In-N2 2.070(2), Li-Cl1 2.428(4), Li-Cl2 2.432(4), Li-O2 1.923(3), Li-O3 1.910(4), In...O1 3.313(2); N1-In-N2 109.33(7), Cl1-In-Cl2 93.15(2), Cl1-Li-Cl2 92.8(1), In-Cl1-Li 86.94(9), In-Cl2-Li 87.05(9), O2-Li-O3 119.4(2). **5.40d**, In-Cl1 2.387(1), In-Cl2 2.377(1), In-N1 2.094(4), In-N2 2.092(3), Li-O2 1.928(9), Li-O3 1.888(9), Li-O4 1.922(8), Li-O5 1.943(8), In...O1 3.414(2); N1-In-N2 105.0(1), Cl1-In-Cl2 100.96(5).

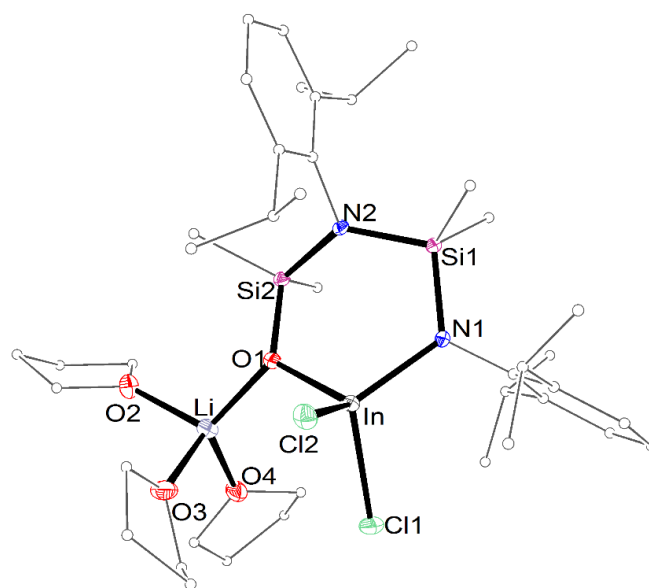


Figure 5.8. Molecular structure of **5.41d** (thermal ellipsoids displayed at 30% probability level). Carbon atoms are displayed in wireframe format for clarity. Hydrogen atoms and the minor component of disorder (THF methylene) are omitted. Selected bond lengths (Å) and angles (°): In-Cl1 2.3628(6), In-Cl2 2.3768(6), In-N1 2.072(1), In-O1 2.061(1), Li-O1 1.948(4), Li-O2 1.990(4), Li-O3 1.955(4), Li-O4 1.959(4), In...N2 3.316(1); N1-In-N2 104.45(5), Cl1-In-Cl2 103.43(2), In-O1-Li 115.7(1).

5.3.2. Synthesis of Indium(III) Hydride Species

The reaction of **5.39d** or **5.41d** with 1 equiv. LiHBEt₃ in a mixture of Et₂O/THF (approx. 9:1 mixture) at -30 °C results in the immediate formation of a grey precipitate. Stirring the reaction mixtures for 2 hours followed by filtration yielded colourless solutions which slowly deposit a black precipitate over 24 hours at room temperature. However, immediate concentration of the solution and storage at -30 °C gave colourless crystals of [Li(THF)₄][In(NON^{Ar})H₂] (**5.42d**) and [Li(THF)₃][In(NNO^{Ar})H₂] (**5.43d**), respectively (Figure 5.9). Both crystalline samples were stable for weeks at room temperature, but decompose to metallic indium and (NON^{Ar})H₂ (**2.19d**) over 24 hours at room temperature when in a hydrocarbon solution. The crystalline samples decompose when heated above 125 °C (**5.42d**) and 90 °C (**5.43d**), while heating a hydrocarbon solution to 50 °C results in the rapid deposition of metallic indium over several

minutes in both cases. These results suggest that In-H bond homolysis is a poor route to low oxidation-state indium compounds.

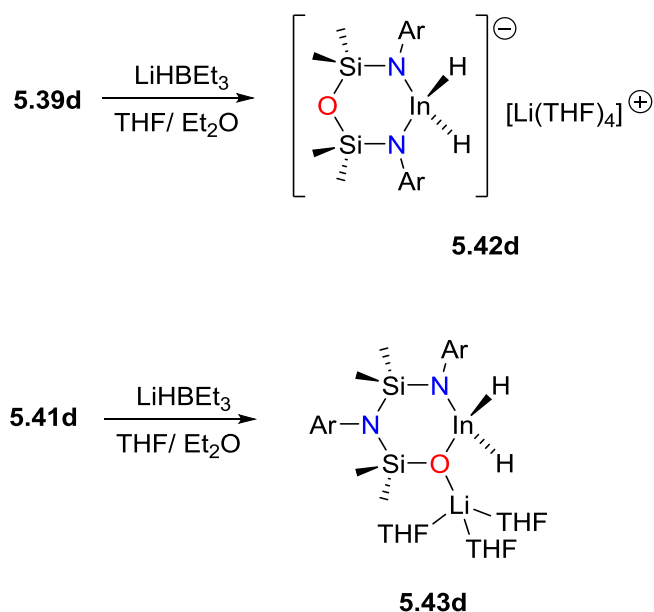


Figure 5.9. Synthesis of **5.42d** (top) and **5.43d** (bottom).

The ^1H NMR spectrum of **5.42d** shows a single set of resonances corresponding to the SiMe_2 and CHMe_2 protons (δ_{H} 0.59 and 4.51, respectively), while the ^1H NMR spectrum of **5.43d** shows two singlets (δ_{H} 0.31 and 0.35) and two septets (δ_{H} 4.36 and 4.51) for the SiMe_2 and CHMe_2 protons, respectively, consistent with a single (NNO^{Ar}) -ligand environment. A broad resonance at δ_{H} 5.98 was observed in the ^1H NMR spectrum of **5.42d**, corresponding to the hydride ligands attached to the quadrupolar indium ($I = 9/2$) metal centre, and is slightly downfield from the broad range reported for InH resonances (δ_{H} 2.93 – 5.61).^{157-160, 162} The integration of this resonance indicates a 2 : 1 ratio of $\text{InH} : (\text{NON}^{\text{Ar}})$, consistent with two hydride ligands on the indium centre. In contrast, no InH resonance was observed in the ^1H NMR spectrum of **5.43d**, presumably due to quadrupolar broadening of the resonance. The lack of an observable InH resonance was also reported for the neutral 5-coordinate indium hydride **5.38** (Figure 5.6). However, the IR spectra of **5.42d** and **5.43d** both show two strong absorptions in the region typical for In-H containing species (**5.42d**, 1656 and 1701 cm^{-1} ; **5.43d**, 1678 and 1709 cm^{-1}), consistent with an asymmetric and symmetric In-H stretching mode.

These are comparable to stretching frequencies observed for other In-H bonds (range 1640 – 1880 cm⁻¹).^{157-160, 162}

The solid-state structures of **5.42d** and **5.43d** were determined using X-ray crystallography (Figure 5.10). The X-ray crystal structure of **5.42d** confirms formation of a non-contact ion-pair, analogous to **5.40d**. The anionic component consists of a tetrahedral indium centre chelated by a (NON^{Ar})-ligand in a κ_2 -*N,N'*-bidentate fashion and is balanced by a lithium cation solvated by four THF molecules. In contrast, **5.43d** exists as a contact ion-pair, featuring a 4-coordinate indate dihydride. The (NNO^{Ar})-ligand retains κ_2 -*N,O*-coordination, with the indate containing a negative charge balanced by a lithium counter-ion coordinated by the siloxane oxygen atom (Li-O1, 1.901(6) Å). The In-N and In-O bond distances (In-N: **5.42d**, 2.142(2) and 2.154(2) Å; **5.43d**, 2.129(2) Å; In-O: **5.43d**, 2.119(1) Å) are significantly longer than those in their indium(III) chloride pre-cursors and coincide with smaller ligand bite angles (**5.42d**, 100.28(7)°; **5.43d**, 99.85(7)°). In both cases, two hydrogen atoms were located in the electron difference map within the coordination sphere of the indium (approximately 1.68 Å away).

Due to the inherent limitations of the characterisation of heavy metal hydrides by X-ray diffraction, these data cannot be used as conclusive evidence for the presence of an In-H bond. Neutron diffraction was performed on single crystals of **5.42d** and **5.43d**, allowing the atomic positions of the hydrogen atoms to be accurately determined. In the latter case, crystal cracking under the cold-stream hindered data collection at low temperature (120 K), and thus, neutron diffraction data was collected at 200 K. The data collection was performed using the KOALA instrument at the Australian Nuclear Science and Technology Organisation (ANSTO), and the data reduction was performed using the LaueG suite of programs.¹²⁶

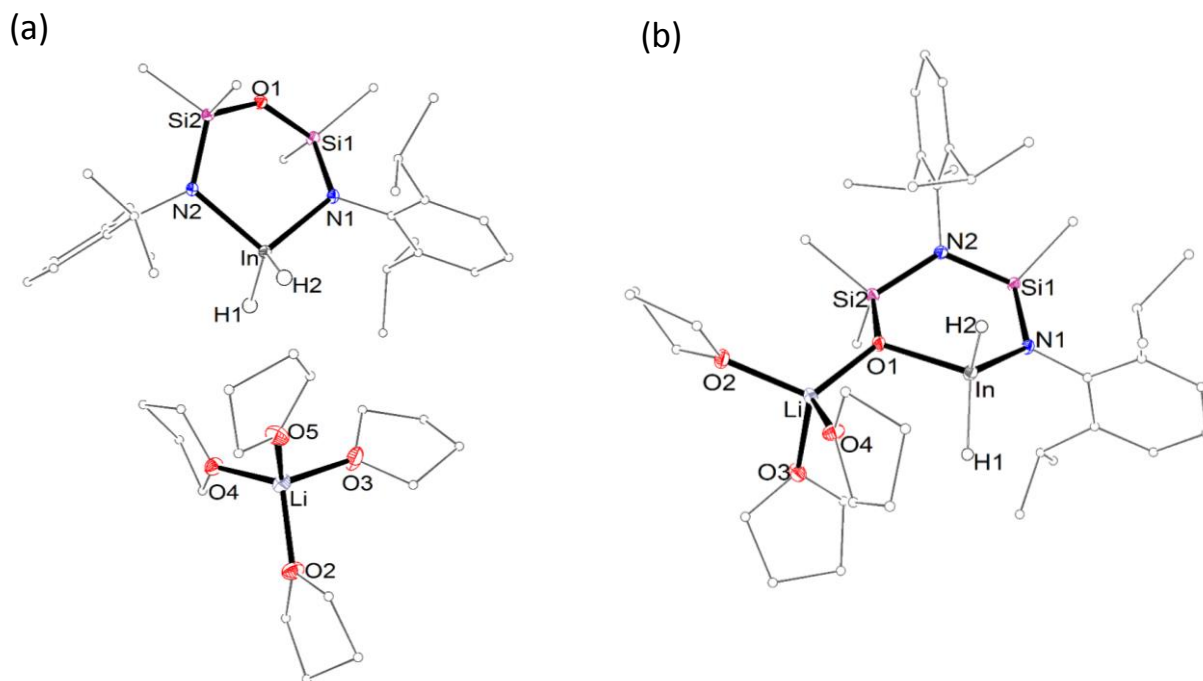


Figure 5.10. Molecular structures of **5.42d** and **5.43d** determined using X-ray crystallography (thermal ellipsoids displayed at 30% probability level). Carbon atoms are displayed in wireframe format and selected hydrogen atoms are omitted for clarity. Selected bond lengths (Å) and angles (°): **5.42d**, In-H1 1.69(3), In-H2 1.67(3), In-N1 2.142(2), In-N2 2.154(2), Li-O2 1.914(4), Li-O3 1.900(4), Li-O4 1.918(5), Li-O5 1.919(5), In...O1 3.535(1); H1-In-H2 113(1), N1-In-N2 100.28(7). **5.43d**, In-H1 1.67(4), In-H2 1.67(3), In-N1 2.129(2), In-O1 2.119(1), Li-O1 1.901(6), Li-O2 1.963(4), Li-O3 1.943(5), Li-O4 1.980(4), In...N2 3.472(2); H1-In-H2 120(2), N1-In-N2 99.85(7), In-O1-Li 110.0(2).

All atoms (including hydrogen atoms) in the crystal structure of **5.42d** determined using neutron diffraction data were modelled anisotropically (Figure 5.11). In contrast to the X-ray crystal structure measured at 120K, the crystal structure measured at 200K features methylene (CH₂) disorder in several THF molecules of the [Li(THF)₄]⁺ fragment. This disorder was not modelled due to the complexity, resulting in expansion of the displacement ellipsoids and preventing discussion of the bond lengths and angles in the cationic component. However, a valid model for the anion was obtained, with sensible bond lengths and angles.

The neutron crystal structure of **5.43d**, measured at 120K, was modelled with most of the atoms refined anisotropically and all hydrogen atoms were evident in the nuclear density map. The hydrogen atoms of one methyl group are significantly disordered, with the largest localised component identified in the difference map and the remainder of the nuclear density modelled as an isotropic ring of hydrogen nuclear density about 1.08 Å from the methyl carbon atom.

These structures are the first examples determined using neutron diffraction data taken from indium hydride species (Figure 5.11). In both cases, the hydride atoms were located in the difference maps, confirming the terminal nature of the indium hydride and providing the first accurate metric parameters for an In-H bond. The In-H bond distances (**5.42d**, 1.741(13) and 1.716(13) Å; **5.43d**, 1.737(17) and 1.743(18) Å) are essentially identical and are consistent with the sum of covalent radii for In and H ($\Sigma_{\text{cov}}(\text{In-H}) = 1.73 \text{ Å}$).¹⁰¹ The In-H bond distances trend towards being longer than those assigned in the X-ray crystal structure, reflecting the difference in the positioning of the nuclear density (determined via neutron diffraction) compared to the electron density (determined via X-ray diffraction) of the hydrogen atom, with much of the electron density located in the In-H bond. Surprisingly, the H1-In1-H2 angles are significantly different (**5.42d**, 113.5(7)°; **5.43d**, 119.5(6)°), despite similar ligand bite angles, and may correspond to different local environments of the hydride ligands.

Based on the relative electronegativity of H and In (2.20 and 1.78, respectively), an $\text{In}^{\delta+}\text{-H}^{\delta-}$ dipole is expected. In both cases, the hydride ligands sit in a hydrophobic pocket, surrounded by C-H units (Figure 5.11). In each case, several of the interatomic H...H distances involving the hydride ligands are within the sum of van der Waals radii for each atom (2.4 Å). The hydride ligands in **5.42d** each form a short contact to a hydrogen atom in the *iso*-propyl methyl substituents (H1...H282 2.33 Å, H2...H82 2.42(2) Å), while the hydride ligand H2 in **5.43d** forms short contacts with two *iso*-propyl methyl hydrogen atoms (H2...H121 2.42(2) Å, H2...H263' 2.33(3) Å) and one THF hydrogen atom (H2...H402 2.32(3) Å) (Figure 5.11b).

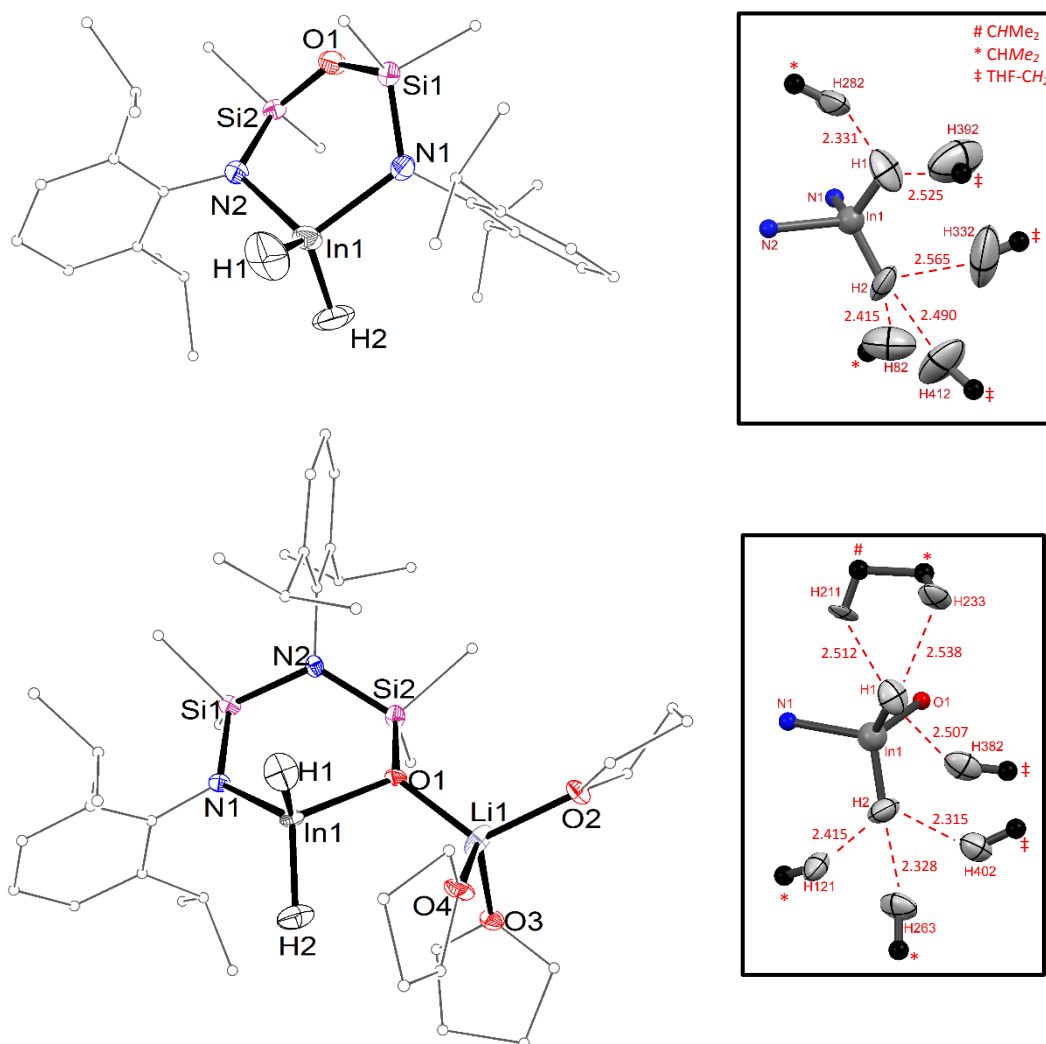
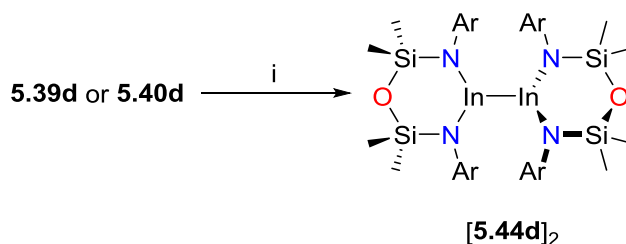


Figure 5.11. Neutron crystal structure of **5.42d** (top) and **5.43d** (bottom) with local environments of H1 and H2 (thermal ellipsoids displayed at 30% probability level). Carbon atoms are displayed in wireframe format and selected hydrogen atoms are omitted for clarity. [Li(THF)₄]⁺ cation omitted for **5.42d**. Selected bond lengths (Å) and angles (°): **5.42d**, In1-H1 1.741(13), In1-H2 1.716(13); H1-In1-H2 113.5(7). **5.43d**, In1-H1 1.737(17), In1-H2 1.743(18); H1-In1-H2 119.5(6).

5.3.3. Reduction of $[\text{In}(\text{NON}^{\text{Ar}})\text{Cl}_2]^-$ with Group 1 Metals

5.3.3.1. Synthesis of $[(\text{NON}^{\text{Ar}})\text{In}]_2$

The reaction of **5.39d** or **5.40d** with Na metal proceeds slowly, giving a yellow solution with concomitant formation of black solid. Removal of the solvents, extraction into hexane and hot filtration through celite gave a yellow solution from which yellow crystals of $[\text{In}(\text{NON}^{\text{Ar}})]_2$ (**[5.44d]₂**) were obtained after work-up (Scheme 5.2).



Scheme 5.2. Synthesis of **[5.44d]₂**. i) Na, THF, 48h, -NaCl, -LiCl

The ^1H NMR spectrum of **[5.44d]₂** in C_6D_6 shows a diamagnetic species with broadened resonances for the SiMe_2 (δ_{H} -0.03 and 0.47) and CHMe_2 protons (δ_{H} 3.74) at room temperature. In addition, a sharp low field singlet (δ_{H} 6.98) accounts for all aryl protons. Upon heating the NMR sample to 65 °C, the SiMe_2 and CHMe_2 resonances coalesce into a sharp singlet and septet at δ_{H} 0.14 and 3.71, respectively, while the CHMe_2 and aryl protons remain unchanged (Figure 5.12). This behaviour is consistent with a fluxional process involving the metallacycle and may correspond to a restricted ring flip at room temperature, which becomes energetically accessible at elevated temperatures.

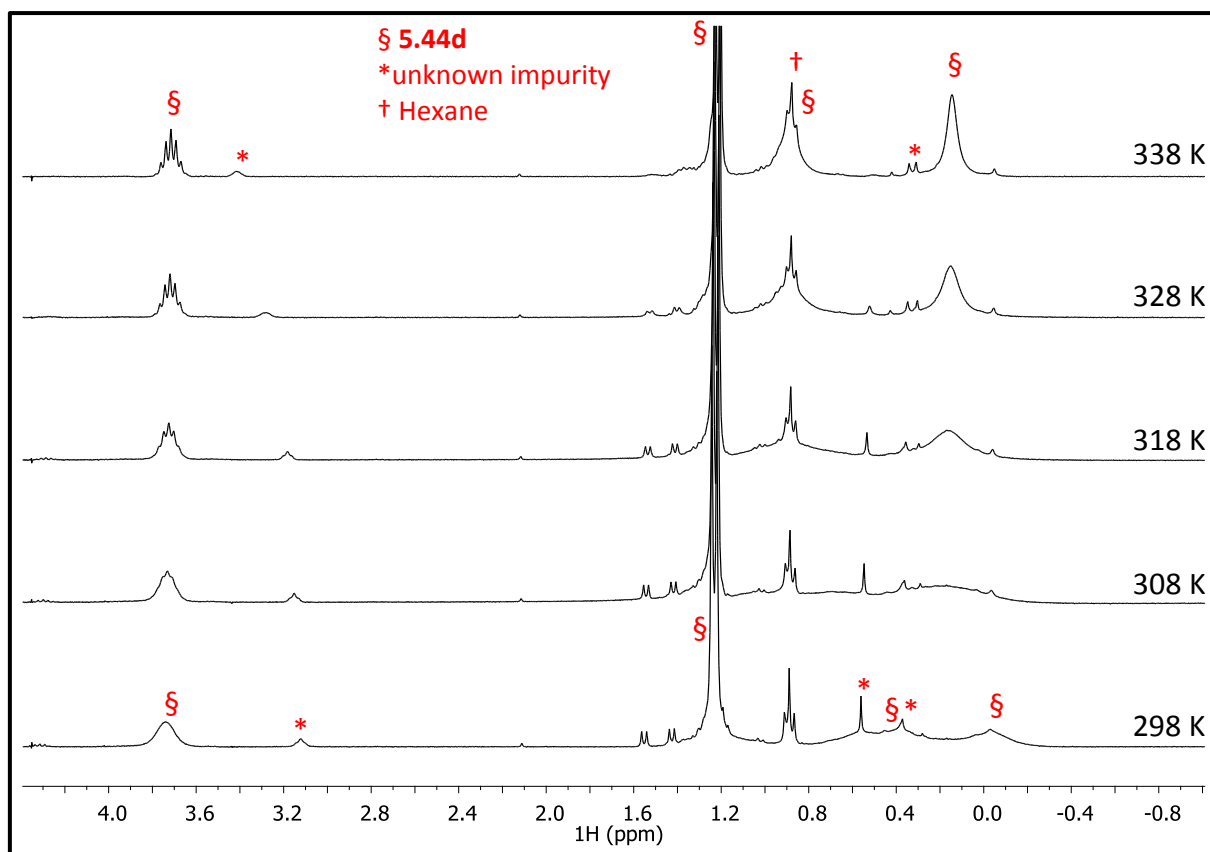


Figure 5.12. Variable temperature (VT) NMR spectra of **[5.44d]₂**.

The solid-state structure of **[5.44d]₂** was determined using X-ray crystallography (Figure 5.13), confirming the formation of the diindane $[\text{In}(\text{NON}^{\text{Ar}})]_2$ with a standard In-In bond (2.7986(4) Å). Both indium centres are planar ($\Sigma(\angle \text{In})$: 359.7° and 359.6°), and are chelated by (NON^{Ar})-ligands to form metallacycles with boat conformations. The (NON^{Ar})-ligands are staggered about the In-In bond and sit almost perpendicular to each other (InN₂ : InN₂ interplanar angle = 80.41°), a reflection of the extremely encumbered metal centres. Despite the supposed formation of a reduced indium centre, the In-N distances (In1: 2.077(2), 2.091(2) Å; In2: 2.092(2), 2.064(2) Å) are similar to those seen in **5.39d**, but are, on average, longer than standard In-N bonds in neutral indium(III) species $\text{In}(\text{NR}_2)_3$ (R = alkyl/aryl, range 2.019(2) – 2.080(2) Å).¹⁶³ These results are consistent with both indium centres being in the +2 oxidation state as opposed to a mixed In(I)/In(III) ion pair.

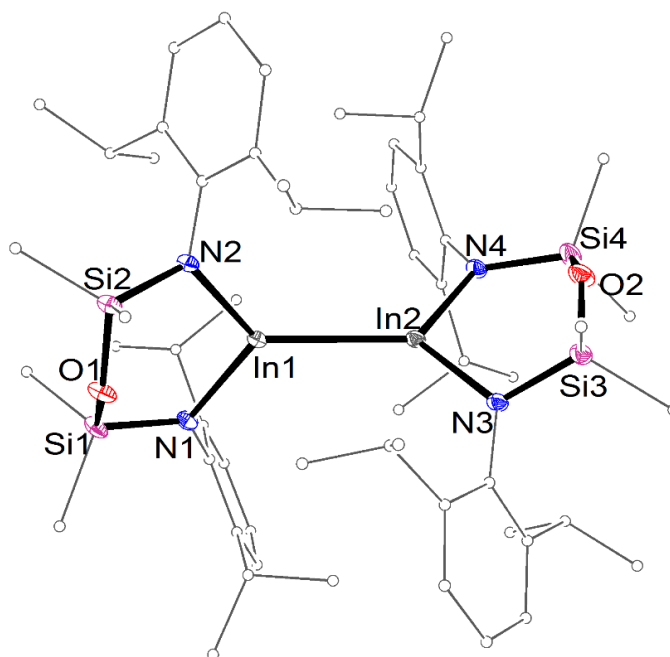
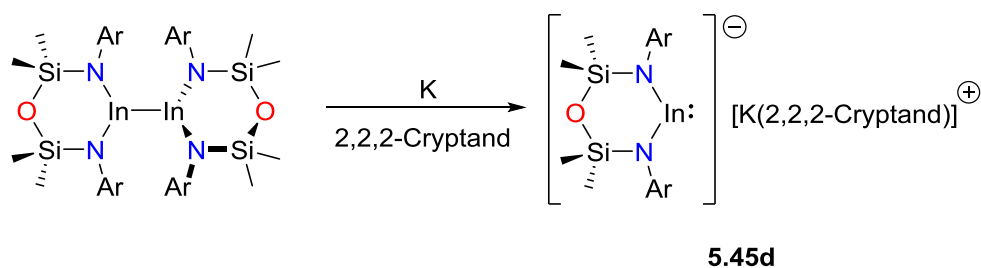


Figure 5.13. Molecular structure of **[5.44d]₂** (thermal ellipsoids displayed at 30% probability level). Carbon atoms are displayed in wireframe format and selected hydrogen atoms are omitted for clarity. Selected bond lengths (Å) and angles (°): In1-In2 2.7986(4), In1-N1 2.077(2), In1-N2 2.091(2), In2-N3 2.092(2), In2-N4 2.064(2), In1...O1 3.106(2), In2...O2 3.178(2); N1-In1-N2 108.06(8), N1-In1-In2 126.64(6), N2-In1-In2 124.99(6), N3-In2-N4 105.62(8), N3-In2-In1 127.67(6), N4-In2-In1 126.32(6).

5.3.3.2. Synthesis of [K(2,2,2-cryptand)][In(NON^{Ar})]

The reaction of **[5.44d]₂** with 2 equivalents of K in the presence of 2,2,2-cryptand in THF results in the formation of [K(2,2,2-cryptand)][In(NON^{Ar})] (**5.45d**), isolated as bright yellow crystals after work-up (Scheme 5.3). Alternatively, access to **5.45d** can be achieved through a one-pot synthesis from **5.39d**, using 2 equivalents of K and 2,2,2-cryptand. Crystalline samples of **5.45d** are stable indefinitely under an inert atmosphere and can be stored for months at room temperature in an ethereal solvent. While the crystals were insoluble in non-polar solvents, NMR spectra were obtained using d₈-THF. The ¹H NMR spectrum of **5.45d** shows a single set of resonances for the SiMe₂, CHMe₂ and CHMe₂ protons (δ_H 0.04, 1.22 and 4.23) with relative integrals of 12 : 24 : 4, consistent with a symmetric (NON^{Ar})-ligand. Two multiplets (δ_H 2.51

and 3.53) and a sharp singlet (δ_{H} 3.62) are consistent with an equivalent of 2,2,2-cryptand in the crystals.



Scheme 5.3. Synthesis of **5.45d**.

X-ray diffraction was used to elucidate the solid-state structure of **5.45d**, confirming formation of a non-contact ion pair (Figure 5.14). The anionic component consists of a two-coordinate indium centre chelated by a (NON^{Ar})-ligand, and is balanced by a potassium cation encapsulated by the 2,2,2-cryptand ligand. The In-N distances (2.246(4) and 2.243(3) Å) are significantly longer than those in **5.39-5.41d** and **5.44d**, and is concomitant with a smaller ligand bite angle (95.5°), as is expected for an In(I) centre.

The development of group 1 boryl and gallyl species as pre-ligands has led to their use in the stabilisation of a plethora of unprecedented metal species. **5.45d** is the first example of an anionic N-heterocyclic In(I) compound, and may lead to the development of indyl species as ligands. Investigations in this area are on-going within our group.

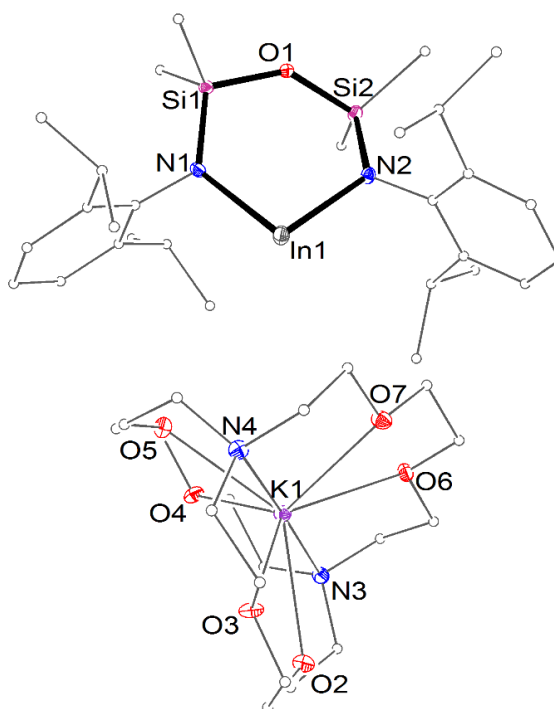


Figure 5.14. Molecular structure of **5.45d** (thermal ellipsoids displayed at 30% probability level). Carbon atoms are displayed in wireframe format and hydrogen atoms are omitted for clarity. Selected bond lengths (Å) and angles (°): In-N1 2.243(3), In-N2 2.246(4), In...O1 3.628(3); N1-In-N2 95.5(1).

5.4. Conclusion

This chapter describes the synthesis and characterisation of a number of rare indium species supported by the sterically demanding (NON^{Ar})-ligand or its retro-Brook rearranged (NNO^{Ar})-ligand isomer. Indium(III) chloride species supported by these ligands were synthesised by the reaction of the dilithiated ligand with InCl₃ (**5.39-5.41d**). In contrast to previously discussed bismuth(III) and antimony(III) chloride species, an equivalent of LiCl was retained in the structure to form a dichloroindate species [In(NON^{Ar})Cl₂]⁻ or [In(NNO^{Ar})Cl₂]⁻ balanced by a lithium cation. Attempts to synthesise salt-free indium(III) chlorides were unsuccessful and **5.39-5.41d** were used for further derivatisation reactions. The reaction of **5.39-5.41d** with the hydride source LiHBET₃ in THF gives the corresponding hydride species **5.42d** or **5.43d**, which were investigated using X-ray and neutron diffraction, providing the first accurate metric

parameters for an In-H bond. The sequential reduction of **5.39d** or **5.40d** was achieved using a group 1 metal reductant (Na or K) to give the In(II) species **[5.44d]₂**, which exists as the dimeric diindane, and the first example of an anionic N-heterocyclic indene species **5.45d**. The latter compound is predicted to be a good σ -donor, with the potential to be used as a source of nucleophilic indium.

5.5. Experimental

5.5.1. Synthesis of Indium(III) Halides

*Synthesis of $\text{In}(\text{NON}^{\text{Ar}})(\mu\text{-Cl})_2\text{Li}(\text{Et}_2\text{O})_2$ (**5.39d**)*

A solution of *n*BuLi in hexane (1.80 mL of a 1.6 M solution, 2.90 mmol) was added dropwise to a stirring solution of $(\text{NON}^{\text{Ar}})\text{H}_2$ (0.70 g, 1.45 mmol) in Et_2O (7 mL) at $-30\text{ }^\circ\text{C}$. The resulting suspension was allowed to warm to room temperature and stirred for 2h. The suspension was added dropwise to a stirring suspension InCl_3 (0.32 g, 1.45 mmol) in Et_2O (10 mL), followed by stirring for 3h. Filtration through celite gave a colourless solution, which was concentrated *in vacuo* and stored at $-30\text{ }^\circ\text{C}$, yielding colourless crystals of **5.39d** after 24 hours. Yield 0.83 g, 69 %. ^1H NMR (C_6D_6 , 300 MHz): δ 7.13 – 6.98 (m, 6H, C_6H_3), 4.25 (sept, 4H, $J = 6.7$, CHMe_2), 2.88 (q, 8H, $J = 7.1$, OCH_2CH_3), 1.52, 1.40 (d, 12H, $J = 6.7$, CHMe_2), 0.64 (t, 12H, $J = 7.1$, OCH_2CH_3), 0.52 (s, 12H, SiMe_2). $^{13}\text{C}\{^1\text{H}\}$ NMR (C_6D_6 , 75 MHz): δ 147.1, 144.8, 123.8, 123.2 (C_6H_3), 66.5 (OCH_2CH_3), 27.8, 26.3, 25.5 (CHMe_2 and CHMe_2), 14.3 (OCH_2CH_3), 3.1 (SiMe_2).

*Synthesis of $[\text{Li}(\text{THF})_4][\text{In}(\text{NON}^{\text{Ar}})\text{Cl}_2]$ (**5.40d**)*

A solution of *n*BuLi in hexane (1.30 mL of a 1.6 M solution, 2.08 mmol) was added dropwise to a stirring solution of $(\text{NON}^{\text{Ar}})\text{H}_2$ (0.50 g, 1.03 mmol) in Et_2O (10 mL) and allowed to stir for 4 h. The colourless solution was then added dropwise to a stirring solution of InCl_3 (0.23 g, 1.05 mmol) in THF (8 mL). The resulting pale yellow solution was stirred for 12 hours at RT followed by removal of the volatiles *in vacuo* to give a white solid, which was extracted into Et_2O and filtered through celite. Concentration of the solvent *in vacuo* and storage of the solution at $-30\text{ }^\circ\text{C}$ for 24 hours yielded colourless crystals of **5.40d**. Yield 0.65 g, 65 %. ^1H NMR (C_6D_6 , 300

MHz): δ 7.18 – 6.99 (m, 6H, C₆H₃), 4.35 (sept, 4H, J = 6.8, CHMe₂), 3.32 (m, 16H, THF), 1.58, 1.45 (d, 12H, J = 6.8, CHMe₂), 1.31 (m, 16H, THF-CH₂), 0.58 (s, 12H, SiMe₂). ¹³C{¹H} NMR (C₆D₆, 75 MHz): δ 146.7, 144.4, 123.4, 122.8 (C₆H₃), 65.2 (THF-CH₂), 27.4, 25.9, 25.1 (THF-CH₂), (CHMe₂ and CHMe₂), 2.66 (SiMe₂).

Synthesis of In(NNO^{Ar}.Li(THF)₃)Cl₂ (5.41d)

A solution of *n*BuLi in hexane (1.8 mL of a 1.6 M solution, 2.90 mmol) was added dropwise to a stirring solution of (NON^{Ar})H₂ (0.70 g, 1.45 mmol) in THF (7 mL) at -30 °C. The resulting suspension was allowed to warm to room temperature and stirred for 24h, followed by dropwise addition to a stirring suspension InCl₃ (0.32 g, 1.45 mmol) in THF (10 mL), followed by stirring for 12h at room temperature. Removal of the volatiles *in vacuo* followed by extraction into Et₂O and filtration through celite gave a colourless solution, which was concentrated *in vacuo* and stored at -30 °C, yielding colourless crystals of **5.41d** after 24 hours. Yield 0.92 g, 70 %. ¹H NMR (C₆D₆, 300 MHz): δ 7.25 – 7.10 (m, 6H, C₆H₃), 4.31, 4.00 (sept, 2H, J = 6.8, CHMe₂), 3.54 (m, 16H, THF), 1.56, 1.49 (d, 6H, J = 6.8, CHMe₂), 1.45 (d, 12H, J = 6.8, CHMe₂), 1.38 (m, 16H, THF-CH₂), 0.36, 0.23 (s, 12H, SiMe₂). ¹³C{¹H} NMR (C₆D₆, 75 MHz): δ 147.5, 147.4, 143.2, 142.6, 125.5, 124.7, 124.3, 124.2 (C₆H₃), 68.4 (THF-CH₂), 28.7, 27.9, 27.7, 26.0, 25.7, 25.5, 25.4, 24.2 (THF-CH₂, CHMe₂ and CHMe₂), 3.5, 3.1 (SiMe₂).

5.5.2. Synthesis of Indium(III) Hydrides

Synthesis of [Li(THF)₄][In(NON^{Ar})H₂] (5.42d)

A solution of LiHBET₃ in THF (0.48 mL of a 1.0 M solution, 0.48 mmol) was diluted in 10 mL of Et₂O and cooled to -30 °C. The mixture was then added dropwise to a stirring solution of **5.39d** (0.20 g, 0.24 mmol) in Et₂O (10 mL) at -30 °C, resulting in the immediate formation of a white precipitate. Upon allowing the suspension to warm to room temperature, a black precipitate formed, giving a grey suspension, which was stirred for a further 2 hours and filtered through celite to give a colourless solution. Immediate concentration of the solution to *ca.* 2 mL and storage at -30 °C yielded colourless blocks of **5.42d**. Yield 0.163 g, 76 %. ¹H NMR (C₆D₆, 300

MHz): δ 7.17 (d, 4H, $J = 7.5$, $m\text{-C}_6\text{H}_3$), 6.97 (t, 2H, $J = 7.5$, C_6H_3), 5.98 (br, 2H, InH), 4.52 (sept, 4H, $J = 6.7$, CHMe_2), 3.22 (m, 16H, THF-CH_2), 1.52, 1.42 (d, 12H, $J = 6.7$, CHMe_2), 1.29 (m, 16H, THF-CH_2), 0.60 (s, 12H, SiMe_2). $^{13}\text{C}\{^1\text{H}\}$ NMR (C_6D_6 , 75 MHz): δ 150.0, 146.9, 123.4, 120.6 (C_6H_3), 68.2 (THF-CH_2), 27.4, 26.4, 25.5 (CHMe_2 and CHMe_2), 14.3 (OCH_2CH_3), 3.1 (SiMe_2).

*Synthesis of $[\text{Li}(\text{THF})_3][\text{In}(\text{NNO}^{\text{Ar}})\text{H}_2]$ (**5.43d**)*

A solution of LiHBEt_3 in THF (0.68 mL of a 1.0 M solution, 0.68 mmol) was diluted in 10 mL of Et_2O and cooled to $-30\text{ }^\circ\text{C}$. The mixture was then added dropwise to a stirring solution of **5.39d** (0.30 g, 0.34 mmol) in Et_2O (10 mL) at $-30\text{ }^\circ\text{C}$, resulting in the immediate formation of a white precipitate. Upon allowing the suspension to warm to room temperature, a black precipitate formed, giving a grey suspension, which was stirred for a further 2 hours and filtered through celite to give a colourless solution. Immediate concentration of the solution to ca. 2 mL and storage at $-30\text{ }^\circ\text{C}$ yielded colourless blocks of **5.43d**. Yield 0.220 g, 80 %. ^1H NMR (C_6D_6 , 300 MHz): δ 7.25 – 7.16 (m, 6H, C_6H_3), 4.51, 4.34 (sept, 2H, $J = 6.8$, CHMe_2), 3.43 (m, 16H, THF), 1.58, 1.52, 1.51, 1.47 (d, 6H, $J = 6.8$, CHMe_2), 1.38 (m, 16H, THF-CH_2), 0.35, 0.31 (s, 12H, SiMe_2). $^{13}\text{C}\{^1\text{H}\}$ NMR (C_6D_6 , 75 MHz): δ 148.6, 147.6, 147.1, 145.0, 124.7, 124.4, 123.9, 123.5 (C_6H_3), 68.3 (THF-CH_2), 28.1, 27.9, 27.4, 25.8, 25.5, 24.2 (THF-CH_2 , CHMe_2 and CHMe_2), 4.2, 3.6 (SiMe_2).

5.5.3. Synthesis of Reduced Indium Species

*Synthesis of $[\text{In}(\text{NON}^{\text{Ar}})]_2$ (**[5.44d]₂**)*

A solution of **5.39d** (0.40 g, 0.48 mmol) or **5.40d** (0.30 g, 0.31 mmol) in THF (10 mL) was added to mirrored Na (0.011 g (0.48 mmol) or 0.007 g (0.31 mmol), respectively) and stirred for 48 hours resulting in formation of a black precipitate and the consumption of metallic Na. Removal of the volatiles in vacuo followed by extraction into boiling hexane (10 mL) and hot filtration through celite gives a clear yellow solution. Allowing the solution to cool to room temperature followed by storage at $-30\text{ }^\circ\text{C}$ gave yellow blocks of **[5.44d]₂**. Yield: 0.10 g, 35 % (from **5.39d**) or 0.080 g, 43 % (from **5.40d**). ^1H NMR (C_6D_6 , 300 MHz, 298 K): δ 6.98 (s, 6H,

C_6H_3), 3.74 (br, 4H, $CHMe_2$), 1.23 (d, 24H, $J = 6.7$, $CHMe_2$), 0.47, -0.03 (br, 12H, $SiMe_2$). 1H NMR (C_6D_6 , 300 MHz, 338 K): δ 6.98 (s, 6H, C_6H_3), 4.52 (sept, 4H, $J = 6.7$, $CHMe_2$), 1.22 (d, 18H, $J = 6.7$, $CHMe_2$), 0.88 (br, 6H, $CHMe_2$), 0.15 (br s, 12H, $SiMe_2$).

*Synthesis of $[K(2,2,2\text{-cryptand})][In(NON^{Ar})]$ (**5.45d**)*

Method 1:

A solution of [**5.44d**]₂ (0.10 g, 0.084 mmol) and 2,2,2-cryptand (0.063 g, 0.168 mmol) in THF (10 mL) was added to mirrored K (0.007 g, 0.168 mmol) and stirred for 24 hours resulting in formation of a small amount of black precipitate. Filtration through celite gave a pale yellow solution, which was concentrated to ca. 5 mL and stored at -30 °C for 24 hours, yielding bright yellow crystals of **5.45d**. Yield 0.102 g, 60 %.

Method 2:

A solution of **5.39d** (0.20 g, 0.24 mmol) and 2,2,2-cryptand (0.182 g, 0.48 mmol) in THF (10 mL) was added to mirrored K (0.019 g, 0.48 mmol) and stirred for 24 hours resulting in formation of a small amount of black precipitate. Filtration through celite gave a pale yellow solution, which was concentrated to ca. 5 mL and stored at -30 °C for 24 hours, yielding bright yellow crystals of **5.45d**. Yield 0.85 g, 35 %. 1H NMR (THF- d_8 , 600 MHz): δ 6.83 (d, 4H, $J = 7.5$, $o\text{-}C_6H_3$), 6.48 (t, 2H, $J = 7.5$, $p\text{-}C_6H_3$), 4.15 (sept, 4H, $J = 7.0$, $CHMe_2$), 3.54 (s, 12H, Crypt- CH_2), 3.51 – 3.38 (t, 12H, Crypt), 2.57 – 2.44 (m, 6H, Crypt), 1.15, 1.13 (d, 12H, $J = 7.0$, $CHMe_2$), -0.04 (s, 6H, $SiMe_2$). $^{13}C\{^1H\}$ NMR (THF- d_8 , 150 MHz) δ 152.0, 145.8, 122.4, 118.0 (C_6H_3), 71.5, 68.6, 67.6, 55.0 (2,2,2-Crypt), 27.7, 27.6, 26.0, 25.8, 25.0 ($CHMe_2$ and $CHMe_2$), 4.2 ($SiMe_2$).

Chapter 6. Summary and Outlook

In recent years, the area of main group chemistry has seen a surge of interest, with advances in the low oxidation state chemistry of these elements a significant driving force for this interest. Initially investigated due to a fundamental interest in heavy analogues of the commonly employed lighter p-block elements, recent advances have demonstrated that the heavier p-block elements display significantly different chemistry to their lighter congeners, which stems from differences in the size and energy of the frontier orbitals. The work presented in this thesis expands on the low oxidation state chemistry of the heavy p-block elements. This contribution is also an extension of previous work performed in our group focussing on the use of sterically demanding di(amido) ligands to kinetically stabilise reactive bismuth species. Much of the work involved in this thesis utilises ligands derived from the di(amido)siloxane framework $[O\{SiMe_2N(R)\}_2]^{2-}$ ($[(NON^R)]^{2-}$) featuring sterically demanding alkyl and aryl substituents bound to the nitrogen atoms (R). In closely related work to that presented here, we have previously reported the synthesis and characterisation of the low oxidation state bismuth(II) radical species $\bullet Bi(NON^{Ar})$ (**2.17d**•, Ar = 2,6-*i*Pr₂C₆H₃).⁴⁸

Chapter 2 describes the synthesis and characterisation of a number of rare and unprecedented low oxidation state bismuth species. A series of bismuth(III) chlorides $Bi(NON^R)Cl$ (R = *t*Bu (**2.16a**), Ph (**2.16b**), 2,6-Me₂C₆H₃ (Ar', **2.16c**), Ar (**2.16d**), 2,6-(CHPh₂)₂-4-*t*BuC₆H₂ (Ar⁺, **2.16e**)) supported by five different (NON^R)-ligands featuring R-substituents with varying steric and electronic properties. The steric properties of these ligands have been investigated and show that these different ligands provide significantly different degrees of steric bulk, which likely dictates the observed reactivity of the bismuth species. These species were reduced using either LiHBEt₃ or Mg, affording the corresponding bismuth(II) species in several cases. These compounds showed surprisingly different structures depending on the R-substituent. When R = *t*Bu, a dibismuthane $[Bi(NON^{tBu})]_2$ (**2.17a**)₂ is formed, featuring a standard Bi-Bi bond, while the R = Ar⁺ derivative exists as a rare bismuth radical species

•Bi(NON^{Ar†}) (**2.17e•**), and is only the second example of a bismuth radical observed in the solid-state. Bismuth(I) species were also targeted, with a number of Bi-Bi bonded compounds featuring core bismuth units of [Bi_n]ⁿ⁺ (n = 2, 3 or 4) isolated and structurally characterised using X-ray crystallography. Bi₄(NON^{Ar})₂ (**2.24d**) and [K(2,2,2-cryptand)][Bi₃(NON^{tBu})₂] (**2.27b**) feature [Bi₄]⁴⁺ and [Bi₃]³⁺ cores, respectively, with arrangements of metal atoms which are unprecedented in bismuth chemistry. In addition, the dibismuthene [(BDI^{Ar})Mg(NON^{Ar})Bi]₂ (**2.26d**) was isolated and structurally authenticated, featuring a standard Bi=Bi bond, and is the only example that is stabilised solely by amide ligands. A common theme in the formation of these novel compounds involves breaking of a Bi-N bond, illustrating the importance of the di(amido) ligand.

Chapter 3 presents an investigation into the reactivity of the bismuth(II) species [**2.17a**]₂, **2.17d•** and **2.17e•** with a series of reagents. A primary focus of this chapter is the potential differences in reactivity for the different nature of the bismuth atoms (i.e. Bi-Bi bond vs. Bi radical). Initial experiments investigated the reactivity of these species with *N*-bromosuccinimide or iodine followed by oxidative addition reactions with sulfur, selenium and tellurium. Of particular note is the reaction of the reduced bismuth species with elemental sulfur, which gave compounds of the general form [Bi(NON^R)]₂(μ-S_n). For R = *t*Bu, the mono- and tri-sulfide compounds were observed, while the Ar derivative gave an inseparable mixture of the mono-, tri- and penta-sulfide compounds. In contrast, the reaction of **2.17e•** with elemental sulfur gave [Bi(NON^{Ar†})(S₄)]₂ (**3.21e**)₂ as the major product, which contains an S₈ polysulfide chain between two metal centres. However, the bonding in the sulfur chain is not consistent with typical polysulfide bonding with DFT calculations suggesting that this species can be considered as a dimer of the first metal complex of an S₄ radical anion. Further reactivity studies revealed that the bismuth(II) species can react with the stable nitroxyl radical TEMPO. In contrast, the activation of white phosphorus (P₄) using reduced bismuth species is limited to **2.17d•**, which was demonstrated to undergo reversible P-P cleavage under standard conditions. The reaction of the reduced bismuth species with terminal aromatic alkynes was

also limited to **2.17d•** and demonstrated to be reversible. This chapter discusses the first investigation into the reactivity of an isolated bismuth radical species and show a surprising dependence of the reactivity on both the nature of the reduced bismuth species and the steric encumbrance of the bismuth centre.

Chapter 4 describes efforts towards the synthesis and characterisation of a number of low oxidation state antimony compounds supported by the (NON^R)-ligand. A series of antimony(III) chloride species Sb(NON^{Ar})Cl (R = *t*Bu (**4.15a**), Ph (**4.15b**), Ar' (**4.15c**), Ar (**4.15d**), Ar[‡] (**4.15e**)) were synthesised in an analogous manner to that used for the corresponding bismuth(III) chlorides. Initial attempts to form reduced compounds using a similar method to that reported for the bismuth systems and reacting **4.15a-e** with a hydride source LiHBEt₃ were unsuccessful, instead forming either decomposition products (R = *t*Bu and Ph) or antimony(III) hydrides Sb(NON^R)H (R = Ar' (**4.17c**) and Ar (**4.17d**)). The latter compounds are likely a reflection of the increased stability of Sb-H bonds compared to Bi-H bonds and were isolated and analysed using X-ray and neutron diffraction (for **4.17c**). Attempts to reduce **4.15a-e** using other traditional reducing agents (e.g. Mg, K) were also unsuccessful. However, the use of magnesium(I) reagents as reducing agents afforded either the distibanes [Sb(NON^R)]₂ (R = *t*Bu ([**4.18a**]₂), Ph ([**4.18b**]₂), Ar' ([**4.18c**]₂)) or the distibene species [(BDI^{mes})Mg(THF)(NON^{Ar})Sb]₂ (**4.19d**) and [(BDI^{Ar})Mg(NON^{Ar})Sb]₂ (**4.20d**). The latter two species feature a standard Sb=Sb bond and were limited to the R = Ar derivative, with smaller ligand systems instead resulting in the slow decomposition and transmetallation of the ligand upon the addition of further equivalents magnesium(I) reagent.

Chapter 5 focusses on the synthesis and characterisation of low oxidation state indium compounds supported by the sterically demanding (NON^{Ar})-ligand. Attempts to isolate the indium(III) chloride species 'In(NON^{Ar})Cl' in an analogous manner to those reported for antimony and bismuth were unsuccessful, instead forming -ate complexes In(NON^{Ar})(μ-Cl)₂Li(Et₂O) (**5.39d**) and [Li(THF)₄][In(NON^{Ar})Cl₂] (**5.40d**), with an equivalent of lithium chloride incorporated into the structure. In addition, we highlighted the potential for a retro-Brook

rearrangement of the (NON^R)-ligand to give a mixed amide/siloxide ligand system [(NNO^{Ar})]²⁻, which was coordinated to the indium centre. Initial attempts to synthesise reduced indium species involved the addition of a hydride source (LiHBEt₃) to the indium chloride pre-cursors. However, the stable indium hydride species [Li(THF)₄][In(NON^{Ar})H₂] (**5.42d**) and [Li(THF)₃][In(NNO^{Ar})H₂] (**5.43d**) were instead isolated. These species were analysed using neutron diffraction, providing the first accurate parameters for an In-H bond. The reduction of **5.39d** with Na resulted in formation of the indium(II) species [In(NON^{Ar})]₂ (**5.44d**). The addition of two equivalents of K and 2,2,2-cryptand to this species afforded the indium(I) species [K(2,2,2-cryptand)][In(NON^{Ar})] (**5.45d**). This species is the first example of the long sought after anionic *N*-heterocyclic indene and may be a source of nucleophilic indium. The versatility of the (NON^{Ar})-ligand is also demonstrated, as this is the first example of a ligand system that has been used to stabilise indium in the +1, +2 and +3 oxidation states.

The work presented in this thesis contributes to an expanding field of research and provides examples of many novel and unprecedented compounds. In addition, several aspects of this work provide a platform for further investigations. Chapter 2 highlights the potential for the (NON^R)-framework to provide tight control over the coordination environment of metal centres through simple modifications. Surprisingly, this ligand system has seen limited applications in metal chemistry. One area where I think this ligand system would excel is in lanthanide chemistry, which is dominated by the +3 oxidation state and often requires considerable steric protection to achieve low coordinate compounds. Chapter 3 highlights the importance of developing reactivity profiles for low oxidation state metal complexes. An important development from this research is the potential to exploit simple bond making/breaking reactions to form catalytic systems. As demonstrated by the dehydrocoupling of TEMPO and phenylsilane, the labile nature of the Bi-H bond opens up possibilities for further investigations into dehydrocoupling using other substrates. For example, the dehydrosilylation of P₄ and terminal aromatic alkynes should be explored. Chapter 4 highlights the key differences and similarities in the chemistries of bismuth and

antimony. An area that warrants further investigation is the divergent reactivity observed for the different distibanes **[4.18b]₂** and **[4.18c]₂**, where the radical-like behaviour of **[4.18c]₂** may result in a surprisingly different reactivity profile. Chapter 5 describes the synthesis of the first anionic *N*-heterocyclic indene **5.45d**. This species is of interest as a source of nucleophilic indium and may have applications as a ligand system and in small molecule activation.

Over the past 40 years, conventional views that compounds of the main group elements lack interesting reactivity and properties have changed significantly.¹ A major driving force for this change is the development of main group complexes which show transition metal-like behaviour and reactivity. The ability to readily interchange between different oxidation states has played a fundamental role in development of transition metal catalysts, with most catalytic cycles involving two key steps: oxidative addition and reductive elimination. In contrast, most of the main group metal catalytic systems involve concerted mechanisms with no change in the oxidation state of the metal. The development of main group element systems capable of exploiting multiple oxidation states for catalysis (i.e. oxidative addition and reductive elimination reactivity) will allow access to a range of previously inaccessible chemical transformations, and may allow the development of highly active and cost-effective catalysts for reactions which are typically limited to expensive transition metal catalysts. However, research in this area is still in its infancy. While there are numerous reports of oxidative addition to low oxidation state metal centres, examples of reductive elimination occurring at a main group metal centre are rare and are the largest hurdle towards catalytic pathways incorporating these two steps.¹⁶⁴ Current efforts in this field seek to exploit weak bonding interactions and favourable singlet-triplet energy separation in order to achieve reductive bond cleavage. Tight control over the steric/geometric and electronic properties of the metal centre is believed to allow control of the singlet-triplet energy separation in these compounds. In this context, the work presented in this thesis demonstrates that bismuth can undergo both oxidative addition and reductive elimination pathways (e.g. Bi-H homolysis) to generate two stable oxidation states. In addition, the reversible activation of white

phosphorus and alkynes by **2.17d**• described in this thesis demonstrate a remarkable situation in which oxidative addition and reductive elimination are occurring in tandem. These results suggest that the bismuth(II) systems reported here may be good model systems for further investigations into redox active main group metal catalysis.

Chapter 7. Appendix

7.1 General Experimental

7.2 Supplementary Figures

Figure S2.1. Molecular structure of Bi(NON^{Ph})Cl (**2.16b**).

Figure S2.2. Molecular structure of Bi(NON^{Ar})Cl (**2.16d'**).

Figure S2.3. Graphical representation of the G parameter for Bi(NON^R)Cl.

Figure S2.4. Molecular Structure of Mg(NON^{Ph})(THF)₃ (**2.23b**).

Figure S2.5. Molecular Structure of [Li(THF)₄][Li(NNO^{Ar}).BEt₃] (**2.26b**).

Figure S2.6. ¹H NMR spectrum and Solution-State Magnetic Susceptibility Measurements for **2.17e•**.

Figure S3.1. Molecular Structure of Bi(NON^{Ar})(N{C(O)CH₂}₂) (**3.15d'**).

Figure S3.2. Molecular Structure of K₂(NON^{Ar}).(Et₂O)₂ (**3.16d**).

Figure S3.3. Molecular Structure of [Bi(NON^{Ar})]₂(μ-S₃) (**3.19d**) and Bi(NON^{Ar})Cl (**2.16d**).

Figure S3.4. VT NMR of Bi(NON^{Ar})(OTEMP) (**3.24d**) and possible solution-state behaviour.

Figure S3.5. ¹H NMR spectra and plot of dehydrosilylation catalysis initiated by •Bi(NON^{Ar}) (**2.17d•**) (10mol%) at 70 °C in C₆D₆.

Figure S3.6. ¹H NMR spectra and plot of dehydrosilylation catalysis initiated by [Bi(NON^{tBu})]₂ (**2.17a**) (10mol%) at 70 °C in C₆D₆.

Figure S3.7. ¹H NMR spectra and plot of dehydrosilylation catalysis initiated by •Bi(NON^{Ar}) (**2.17e•**) (10mol%) at 70 °C in C₆D₆.

Figure S3.8. VT ¹H NMR spectra for [Bi(NON^{Ar})]₂(P₄) (**3.25d**).

Figure S3.9. VT ³¹P NMR spectra for [Bi(NON^{Ar})]₂(P₄) (**3.25d**).

Figure S3.10. UV-visible spectrum of [Bi(NON^{Ar})]₂(P₄) (**3.25d**) at 273K, 243K and 233K in Et₂O.

Figure S3.11. ¹H NMR spectrum of [Bi(NON^{Ar})]₂(P₄)(NHC^{mes}) (**3.27d**).

Figure S3.12. ²⁹Si-¹H HMBC spectrum of [Bi(NON^{Ar})]₂(P₄)(NHC^{mes}) (**3.27d**).

Figure S3.13. Van't Hoff plot for [Bi(NON^{Ar})]₂(HC=C(4-*t*BuC₆H₄)) (**3.28d**).

Figure S4.1. Molecular Structure of [(BDI^{Ar})Mg]₄[Sb₈] (**4.22**).

7.3 Crystallographic Details

General

Summary tables of crystallographic details

Neutron crystallography details

7.1 General Experimental Details

All manipulations were performed under dry nitrogen using standard Schlenk-line techniques, or in a conventional nitrogen-filled glovebox. Solvents were dried over appropriate drying agents and degassed before use. NMR spectra were recorded using a Bruker Avance DPX 300 MHz spectrometer at 300.1 (^1H), 75.1 (^{13}C) and 121.1 (^{31}P) MHz, a Varian VNMRS 500 MHz spectrometer at 99.3 (^{29}Si) MHz or a Varian DirectDrive 600MHz spectrometer at 600.1 (^1H) and 150.9 (^{13}C) MHz. Proton and carbon chemical shifts were referenced internally to residual solvent resonances and all coupling constants are reported in Hz. UV-visible spectra were recorded in Et_2O on a Varian Cary 50 instrument in a sealed (J. Young's tap) quartz cuvette under a N_2 atmosphere. Mass spectra were collected on an Agilent 6530 Accurate Mass QTOF LC / MS High Resolution Mass Spectrometer (HRMS). Melting points were measured in sealed glass capillaries under a N_2 atmosphere using a Gallenkamp Melting Point Apparatus and are uncorrected. Cyclic voltammetry was performed by A. Kilpatrick at the University of Sussex. Computational analyses were performed by M. Lein at Victoria University of Wellington. Elemental analyses were performed by S. Boyer at London Metropolitan University. BiCl_3 and SbCl_3 were purchased from Sigma-Aldrich and sublimed immediately prior to use. $(\text{NON}^{\text{R}})\text{H}_2$ (**2.19**, $\text{R} = t\text{Bu}$ (**a**), Ph (**b**), Ar (**d**)),^{24e, 50} $\text{Bi}(\text{NON}^{\text{Ar}})\text{Cl}$ (**2.16d**),⁴⁸ $\text{Ar}^{\ddagger}\text{NH}_2$ ³² and $[\text{Mg}(\text{BDI}^{\text{Ar}^{\text{S}}})]_2$ ($\text{Ar}^{\text{S}} = \text{mes}$ (**1.1**), Ar (**1.2**))^{17a} were prepared according to literature procedures. All other chemicals were purchased from Sigma-Aldrich and used without further purification.

7.2 Supplementary Figures

Figure S2.1. Molecular Structure of Bi(NON^{Ph})Cl (**2.16b**). (a) Two independent molecular units in the asymmetric units (disorder in the Bi and Cl atoms omitted). (b) Extended solid-state structure of **2.16b**. Thermal ellipsoids displayed at 30% probability level and hydrogen atoms not shown.

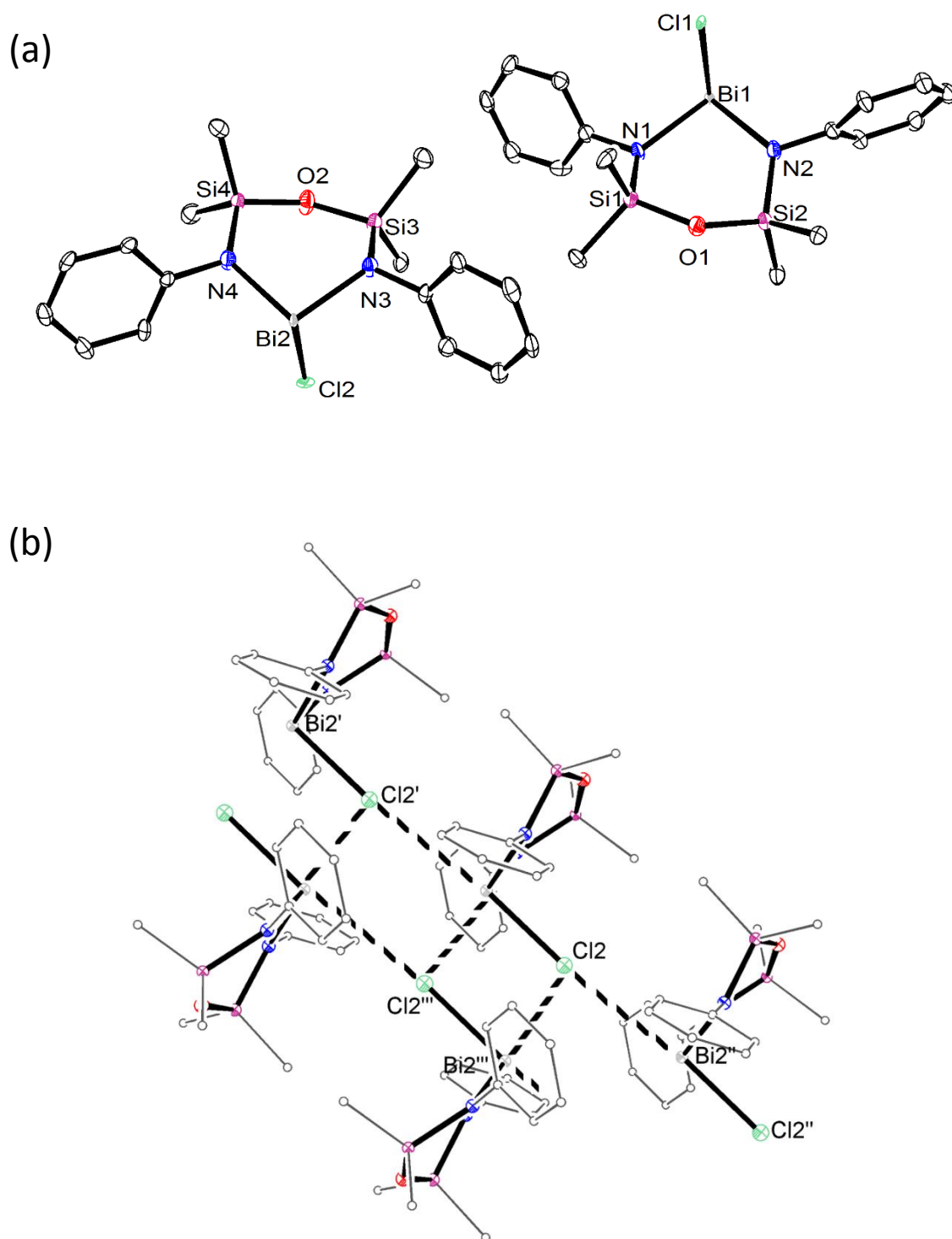
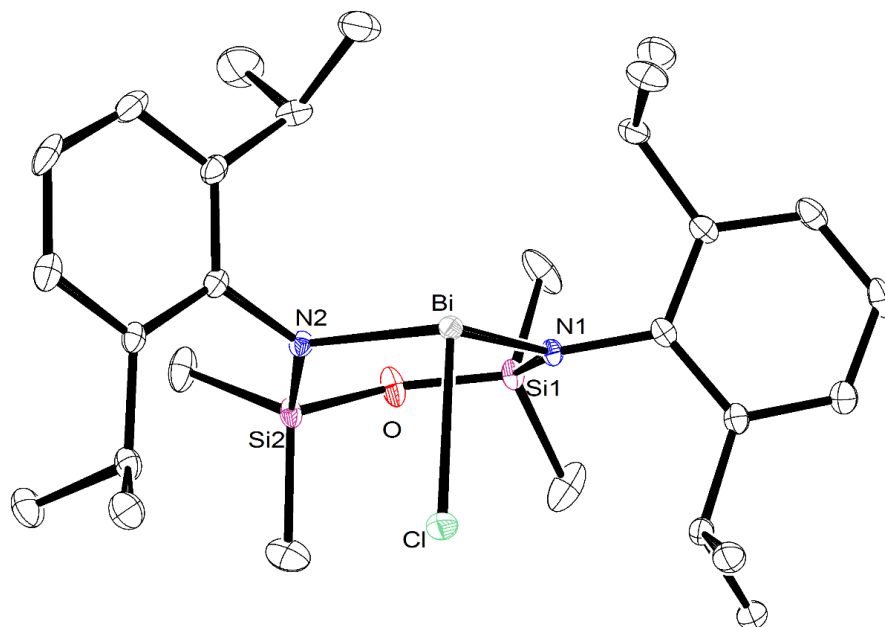


Figure S2.2. Molecular Structure of Bi(NON^{Ar})Cl (**2.16d'**). (a) Asymmetric unit of **2.16d'**. (b) Extended solid-state structure of **2.16d'**. Thermal ellipsoids displayed at 30% probability level and hydrogen atoms not shown.

(a)



(b)

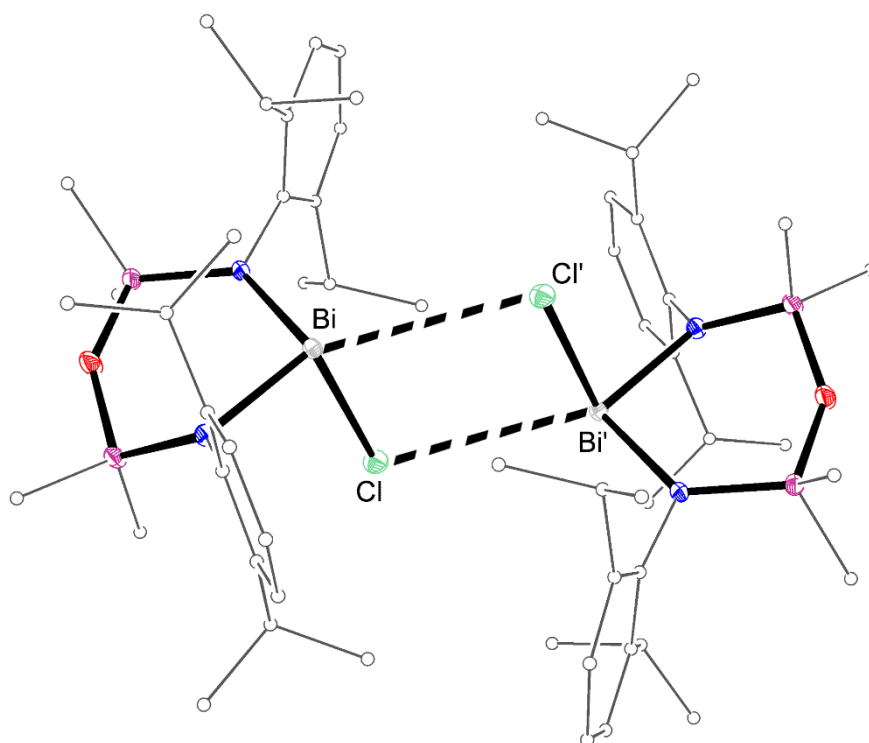
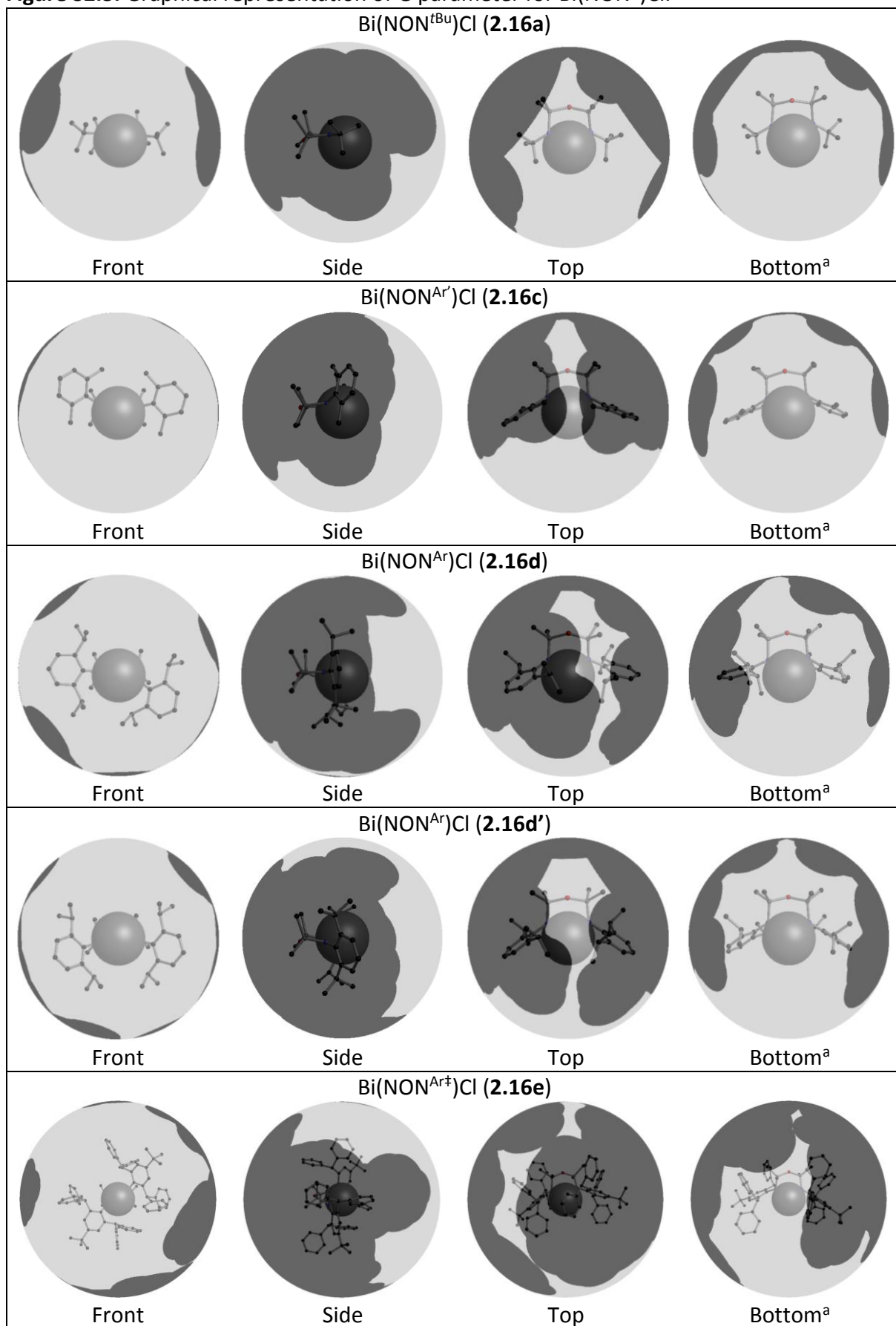


Figure S2.3. Graphical representation of G parameter for Bi(NON^R)Cl.



^a Corresponds to the chloride side of the bismuth atom.

Figure S2.4. Molecular Structure of $\text{Mg}(\text{NON}^{\text{Ph}})(\text{THF})_3$ (**2.23b**). Thermal ellipsoids displayed at 30% probability level and hydrogen atoms not shown.

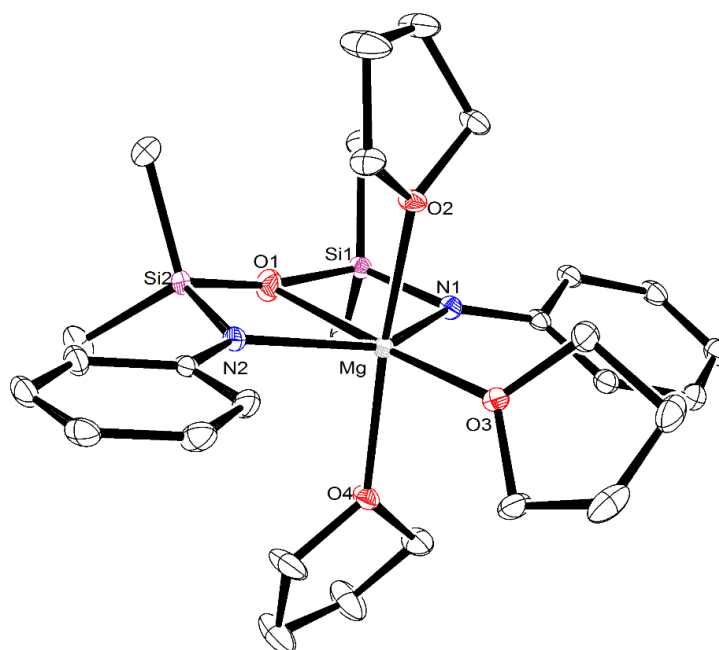


Figure S2.5. Molecular Structure of $[\text{Li}(\text{THF})_4][\text{Li}(\text{NNO}^{\text{Ar}}).\text{BET}_3]$ (**2.26b**). Thermal ellipsoids displayed at 30% probability level and hydrogen atoms not shown.

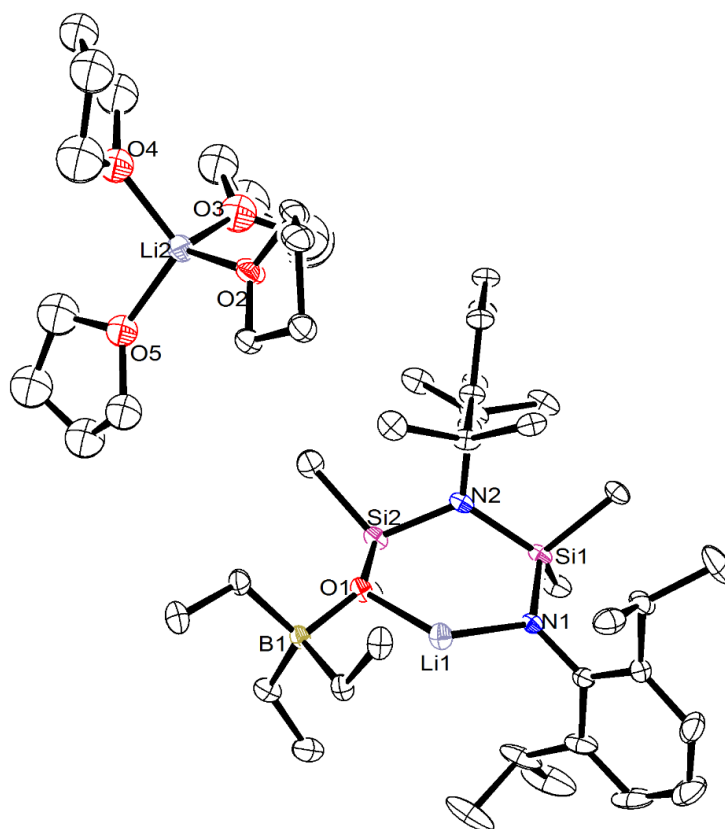
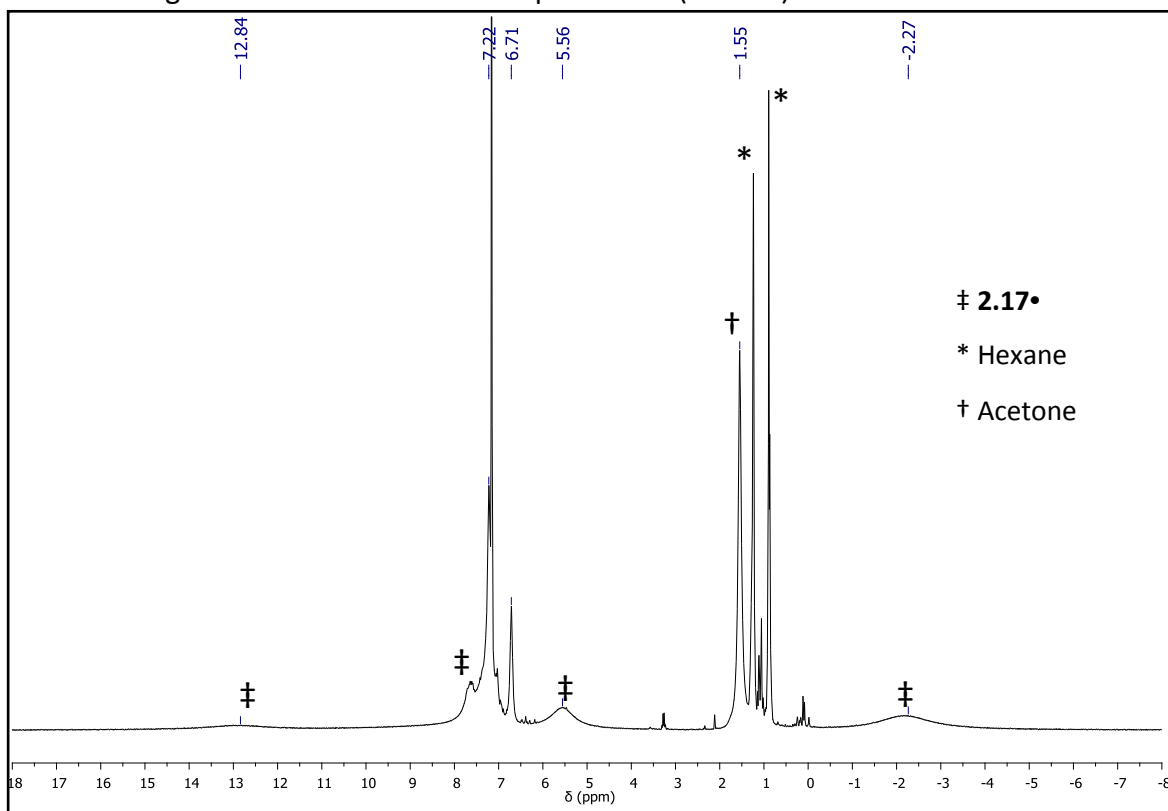


Figure S2.6. ^1H NMR spectrum and Solution-State Magnetic Susceptibility Measurements for **2.17e**. Diamagnetic measurements correspond to $\text{Pb}(\text{NON}^{\text{Ar}\ddagger})$.



Equation 1:
$$\chi_M^p = \frac{1}{v_0 S_f} \left[\frac{\delta v^p M^p}{m^p} - \frac{\delta v^{dia} M^{dia}}{m^{dia}} \right]$$

Equation 2:
$$\mu_{eff} = 2.828 \sqrt{\frac{T}{v_0 S_f} \left[\frac{\delta v^p M^p}{m^p} - \frac{\delta v^{dia} M^{dia}}{m^{dia}} \right]}$$

v_0 = operating frequency of the NMR spectrometer = 600,000 Hz

S_f = shape factor = $4\pi/3$ (cylinder)

δv^p = change in chemical shift (paramagnetic) = -0.14 ppm = 84 Hz

M^p = molecular mass (paramagnetic) = $1300.62 \text{ g mol}^{-1}$

m^p = mass of sample (paramagnetic) = 32.1 mg

δv^{dia} = change in chemical shift (diamagnetic) = $+0.04$ ppm = -24 Hz

M^{dia} = molecular mass (diamagnetic) = $1298.84 \text{ g mol}^{-1}$

m^{dia} = mass of sample (diamagnetic) = 33.2 mg

$$\chi_M^p = 1.73 \times 10^{-3}$$

$$\mu_{eff} = 2.005 \mu_B$$

Figure S3.1. Molecular Structure of $\text{Bi}(\text{NON}^{\text{Ar}})(\text{N}\{\text{C}(\text{O})\text{CH}_2\}_2)$ (**3.15d'**). Thermal ellipsoids displayed at 30% probability level and hydrogen atoms not shown.

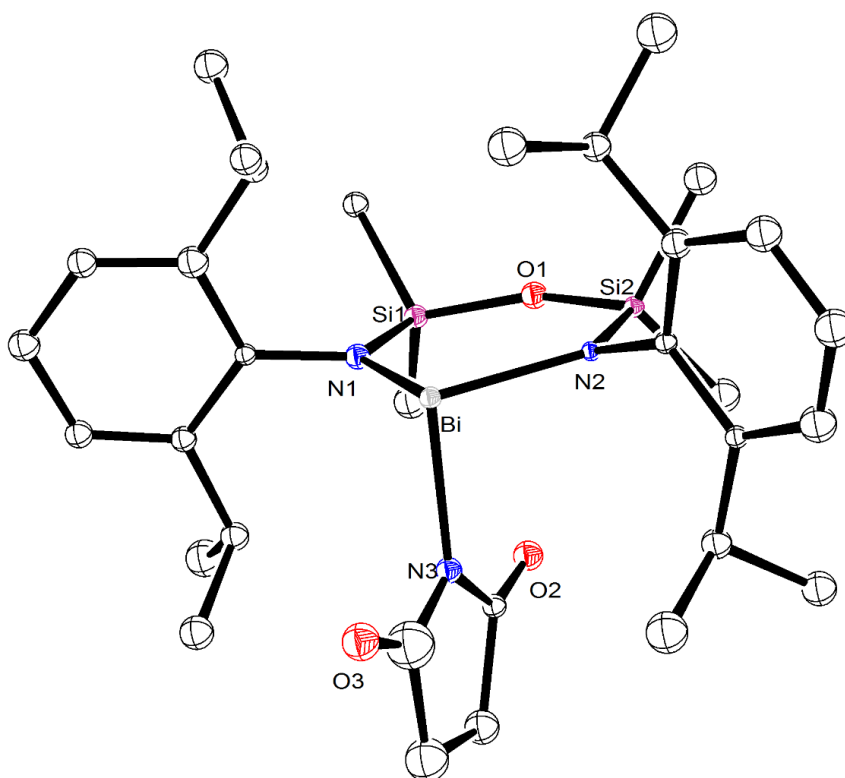


Figure S3.2. Molecular Structure of $\text{K}_2(\text{NON}^{\text{Ar}})(\text{Et}_2\text{O})_2$ (**3.16d**). Thermal ellipsoids displayed at 30% probability level and hydrogen atoms not shown.

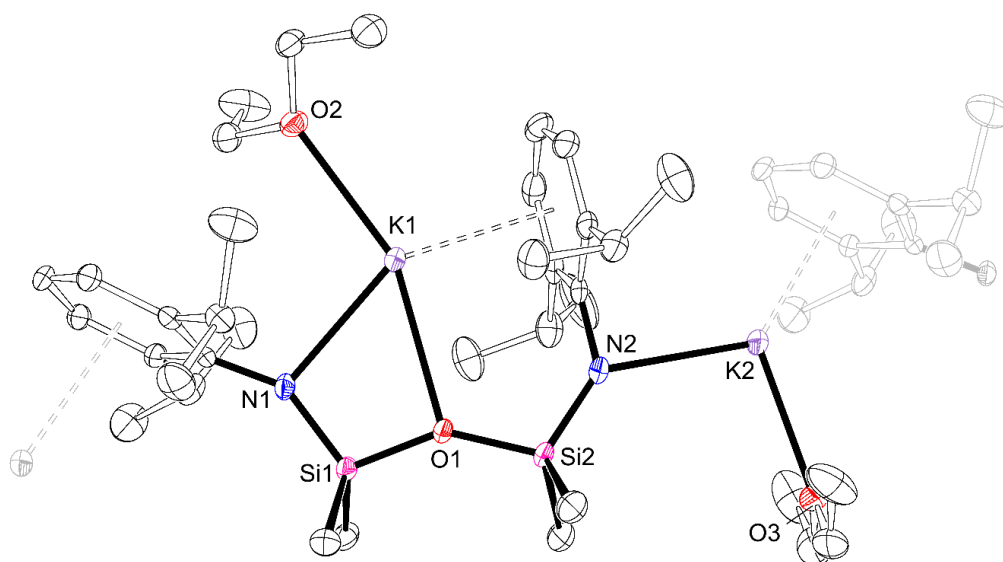


Figure S3.3. Molecular Structure of $[\text{Bi}(\text{NON}^{\text{Ar}})]_2(\mu\text{-S}_3)$ (**3.19d**) and $\text{Bi}(\text{NON}^{\text{Ar}})\text{Cl}$ (**2.16d**). Thermal ellipsoids displayed at 30% probability level and hydrogen atoms not shown.

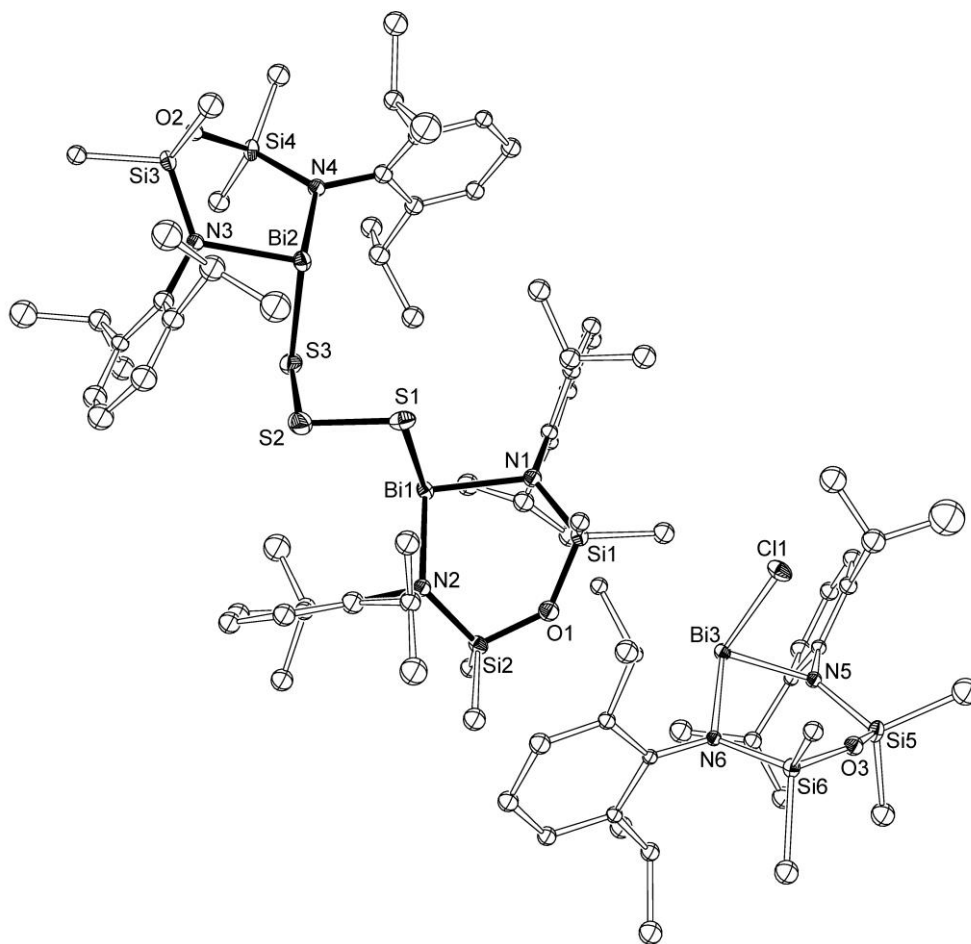
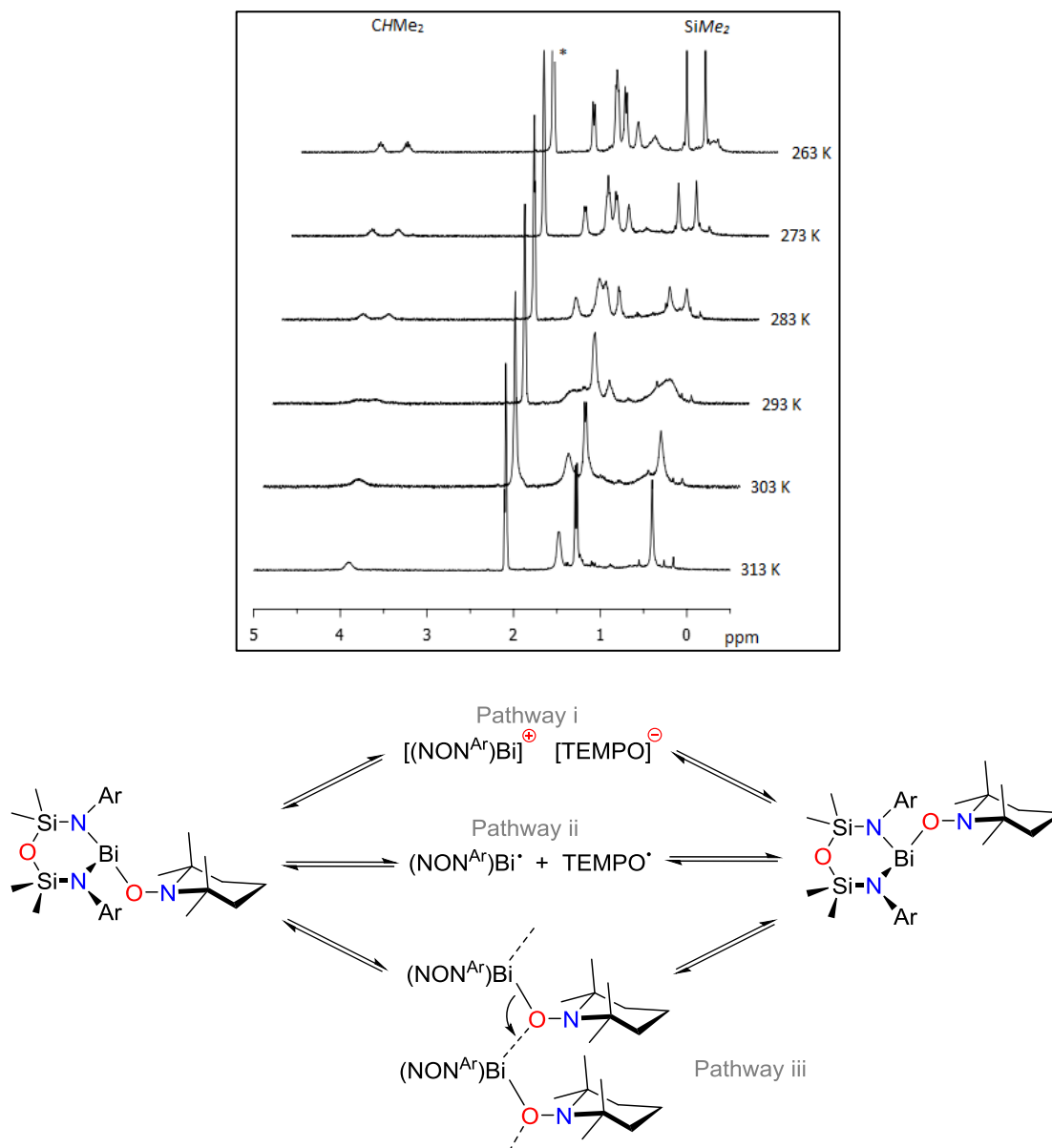


Figure S3.4. VT NMR spectrum of Bi(NON^{Ar})(OTEMP) (**3.24d**) in C₇D₈ and possible solution-state behaviour.



Calculation of the Gibbs Free Energy (ΔG^\ddagger) in D₈-toluene

The coalescence temperature (T_c) was found to be 26 °C (299 K). The lowest exchange limit is found at −40 °C with the two proton resonances for the CHMe₂ separated by $\Delta\delta$ 67.4 Hz.

$$k_c = \frac{\pi(67.4)}{\sqrt{2}} = 149.72 \text{ s}^{-1}$$

The free energy of activation (ΔG^\ddagger) was calculated using eq. 2:

$$\Delta G^\ddagger = (1.914 \times 10^{-2})(299)[10.319 + \log_{10} \left(\frac{299}{149.72} \right)] = 60.8 \text{ kJ mol}^{-1}$$

Figure S3.5. ^1H NMR spectra and plot of dehydrosilylation catalysis initiated by $\bullet\text{Bi}(\text{NON}^{\text{Ar}})$ (**2.17d**) (10mol%) at 70 °C in C_6D_6 .

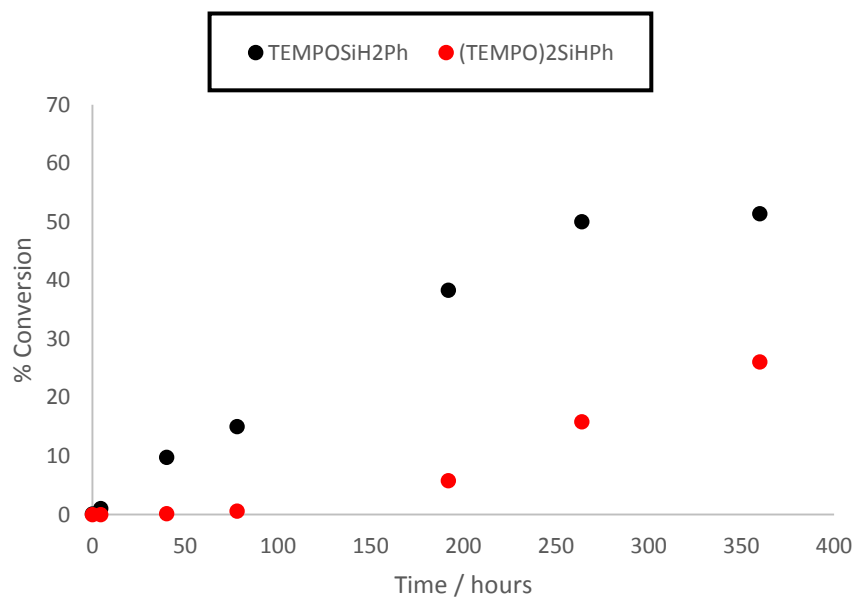
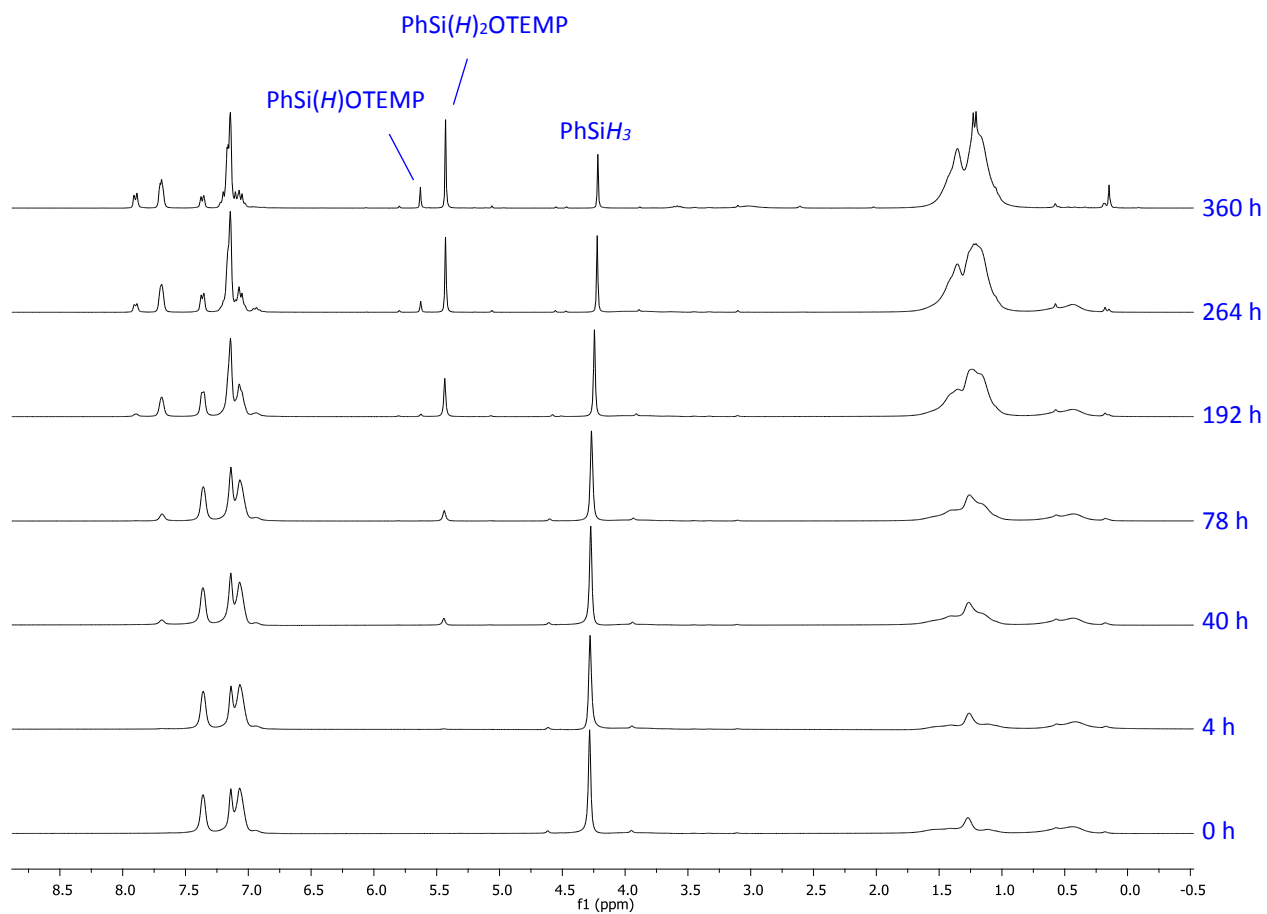


Figure S3.6. ^1H NMR spectra and plot of dehydrosilylation catalysis initiated by $[\text{Bi}(\text{NON}^{\text{tBu}})]_2$ (**[2.17a]**) (10mol%) at 70 °C in C_6D_6 .

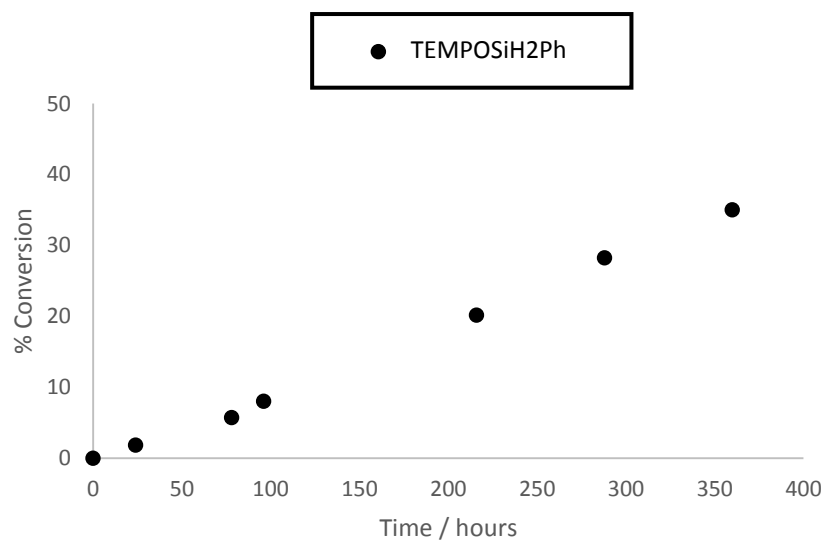
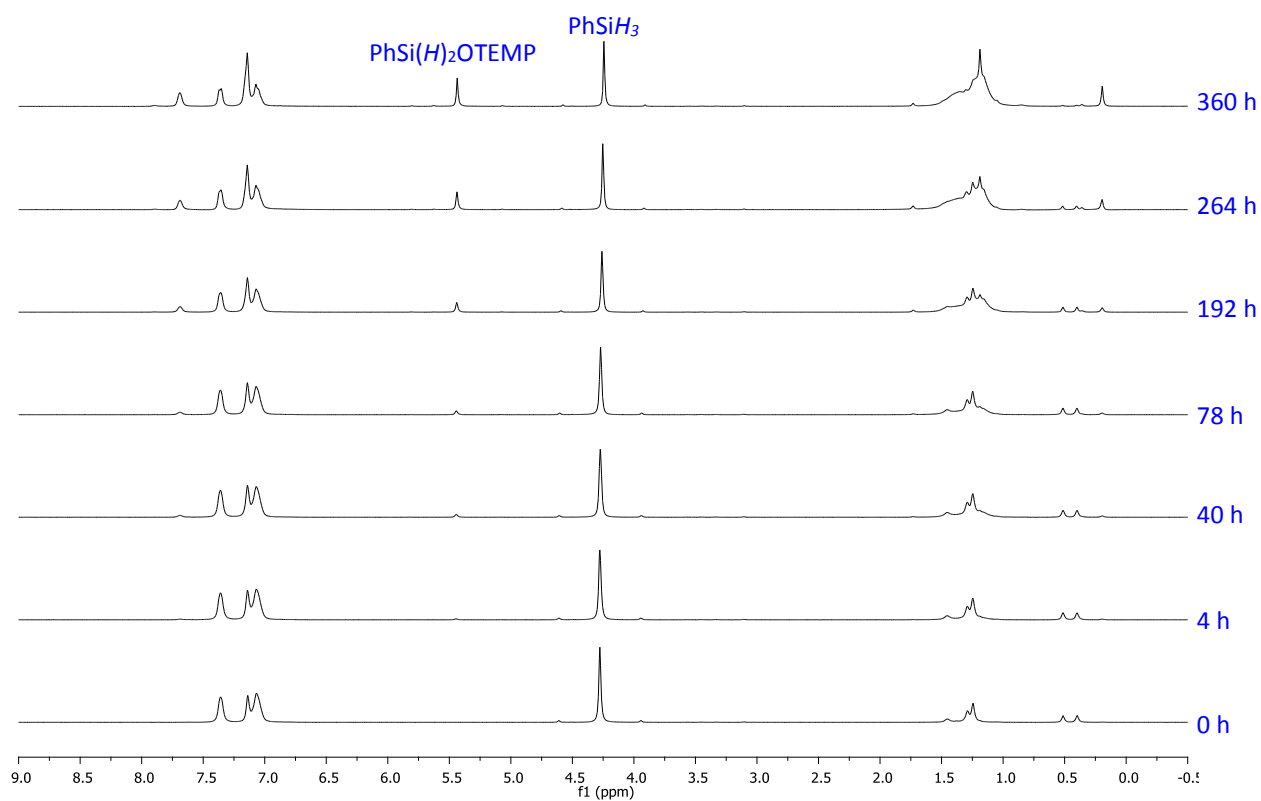


Figure S3.7. ^1H NMR spectra and plot of dehydrosilylation catalysis initiated by $\bullet\text{Bi}(\text{NON}^{\text{Ar}})$ (**2.17e•**) (10mol%) at 70 °C in C_6D_6 .

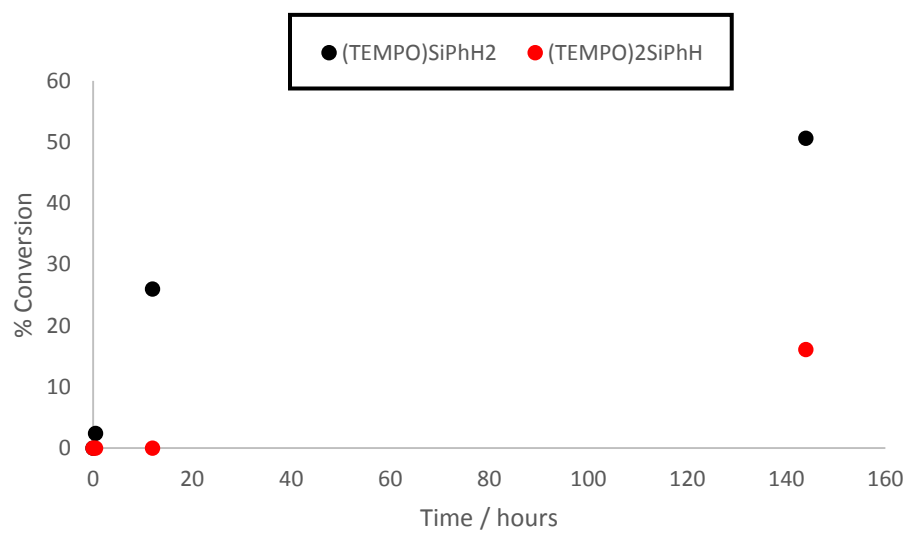
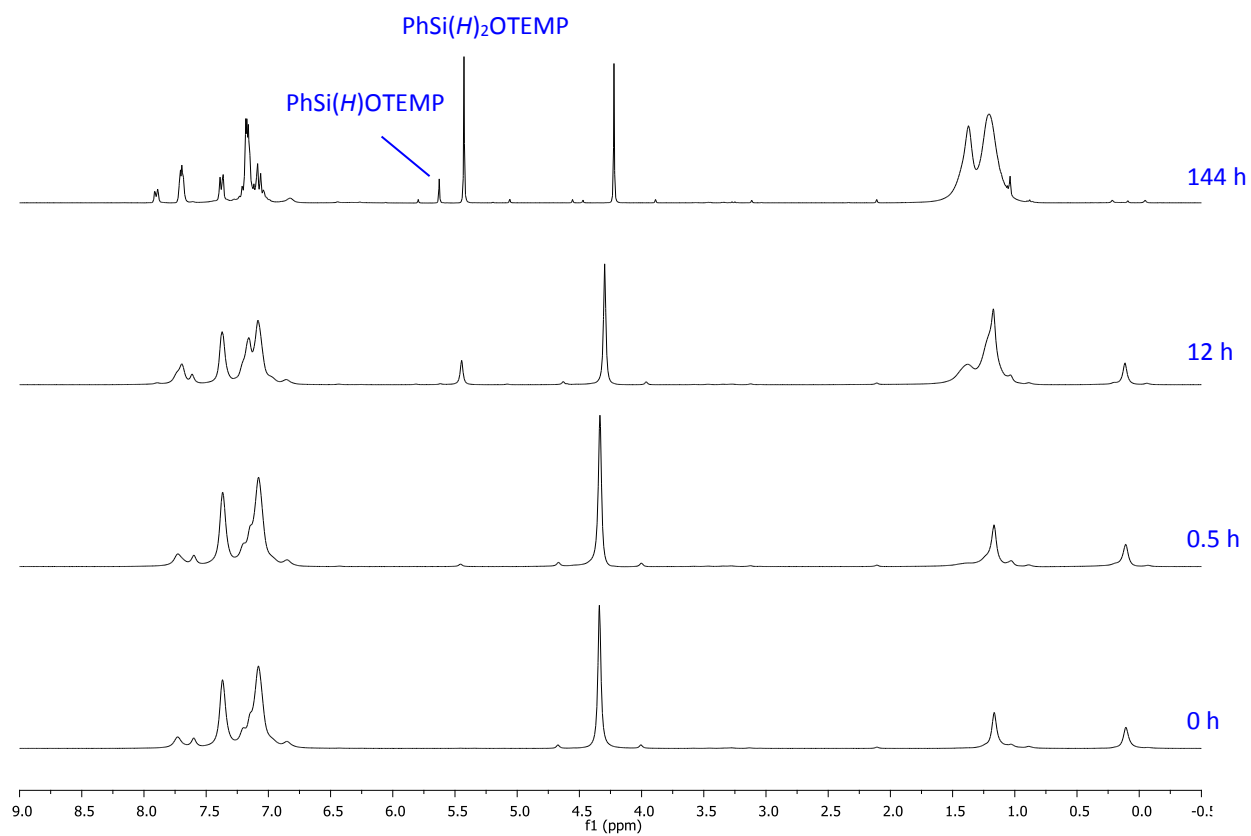


Figure S3.8. VT ^1H NMR spectra for $[\text{Bi}(\text{NON}^{\text{Ar}})]_2(\text{P}_4)$ (**3.25d**).

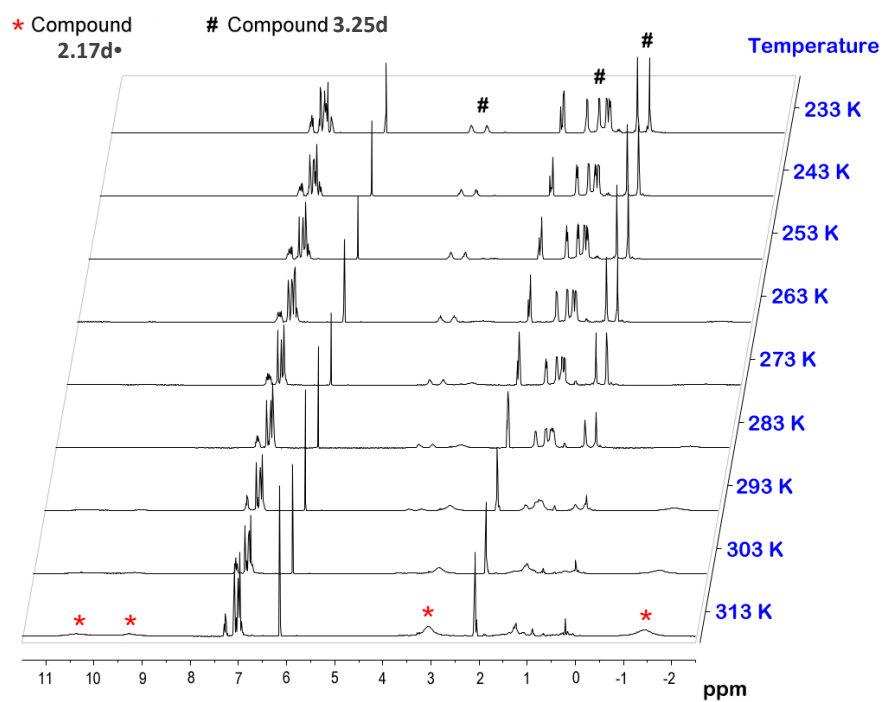


Figure S3.9. VT ^{31}P NMR spectra for $[\text{Bi}(\text{NON}^{\text{Ar}})]_2(\text{P}_4)$ (**3.25d**).

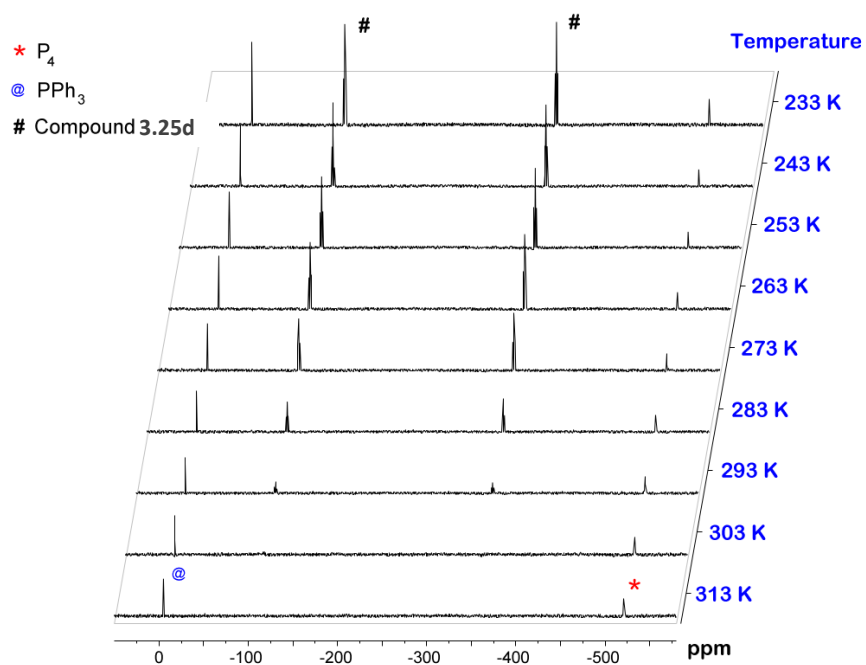


Figure S3.10. UV-visible spectrum of $[\text{Bi}(\text{NON}^{\text{Ar}})]_2(\text{P}_4)$ (**3.25d**) at 273K, 243K and 233K in Et_2O .

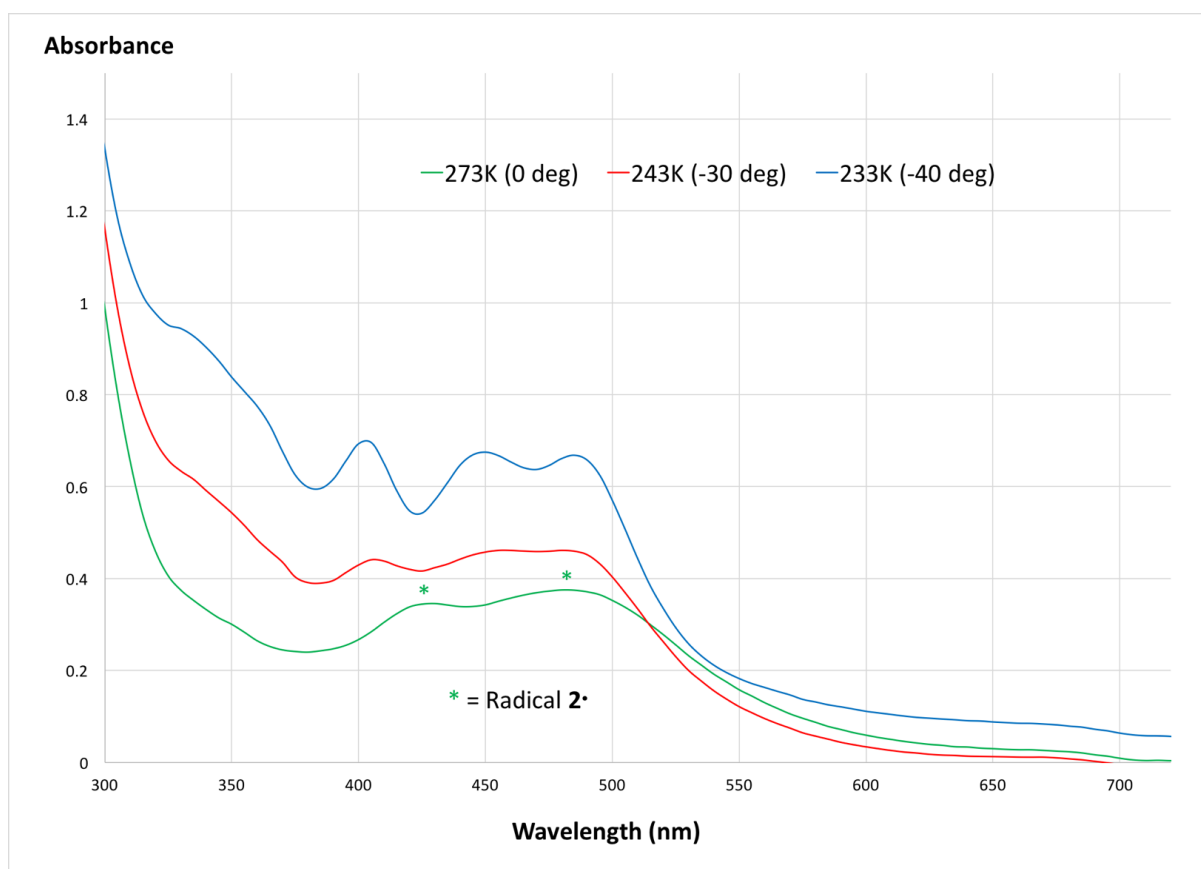


Figure S3.11. ^1H NMR spectrum of $[\text{Bi}(\text{NON}^{\text{Ar}})]_2(\text{P}_4)(\text{NHC}^{\text{mes}})$ (**3.27d**).

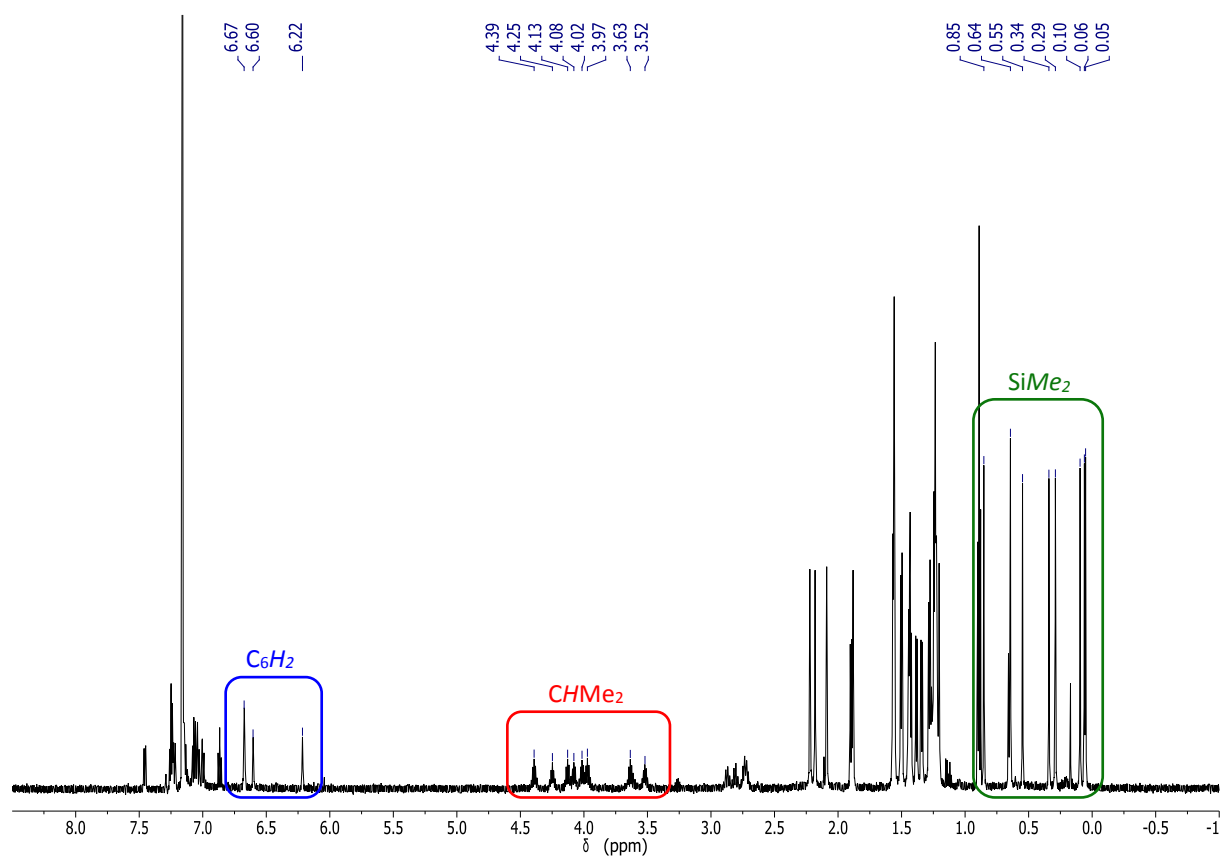


Figure S3.12. ^{29}Si - ^1H HMBC spectrum of $[\text{Bi}(\text{NON}^{\text{Ar}})]_2(\text{P}_4)(\text{NHC}^{\text{mes}})$ (**3.27d**).

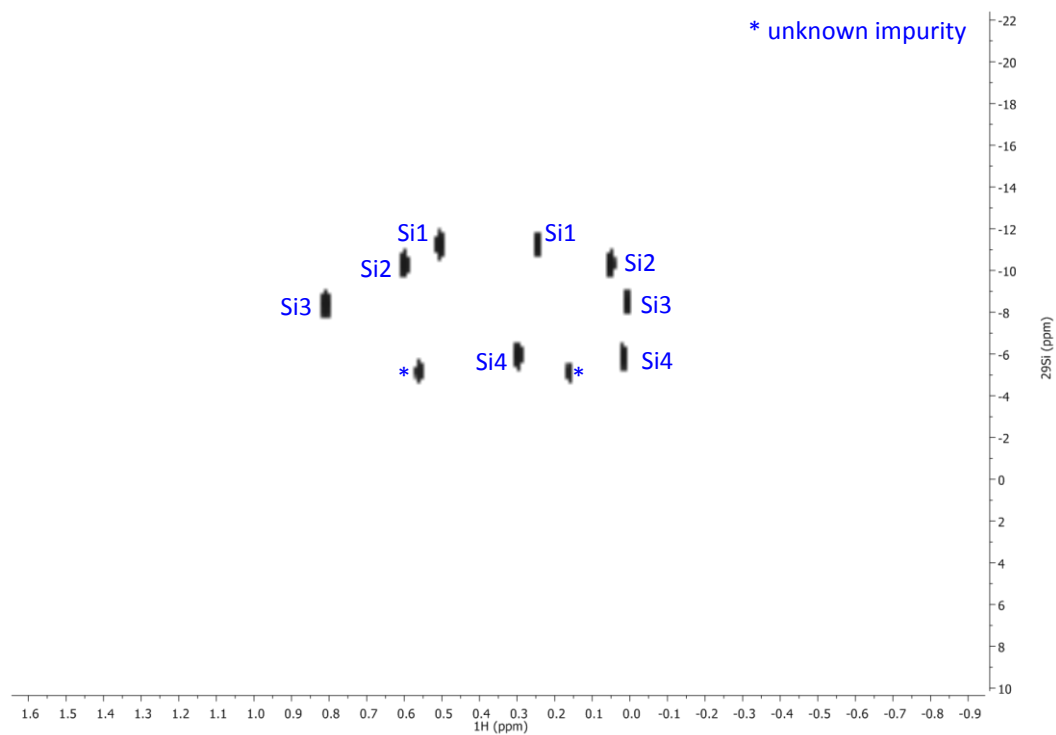


Figure S3.13. Van't Hoff plot for $[\text{Bi}(\text{NON}^{\text{Ar}})]_2(\text{HC}=\text{C}(4\text{-tBuC}_6\text{H}_4))$ (**3.28d**).

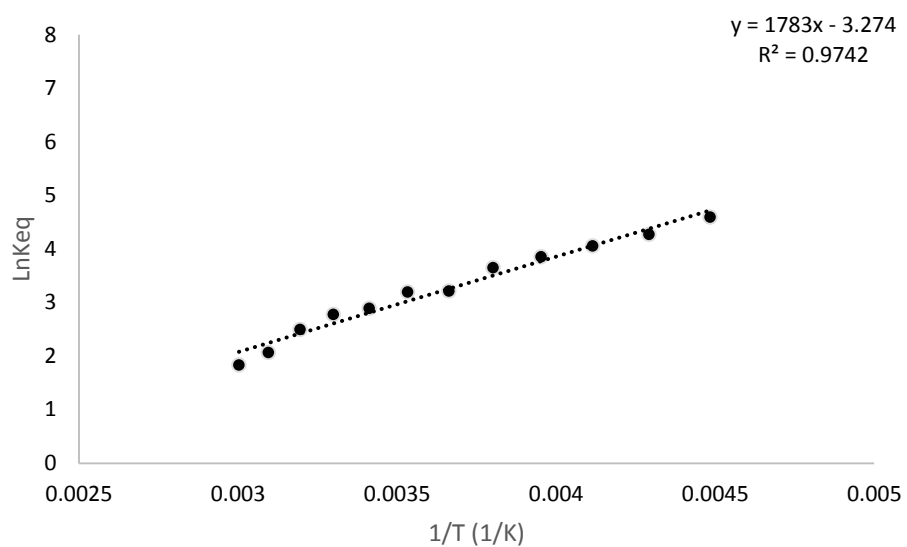
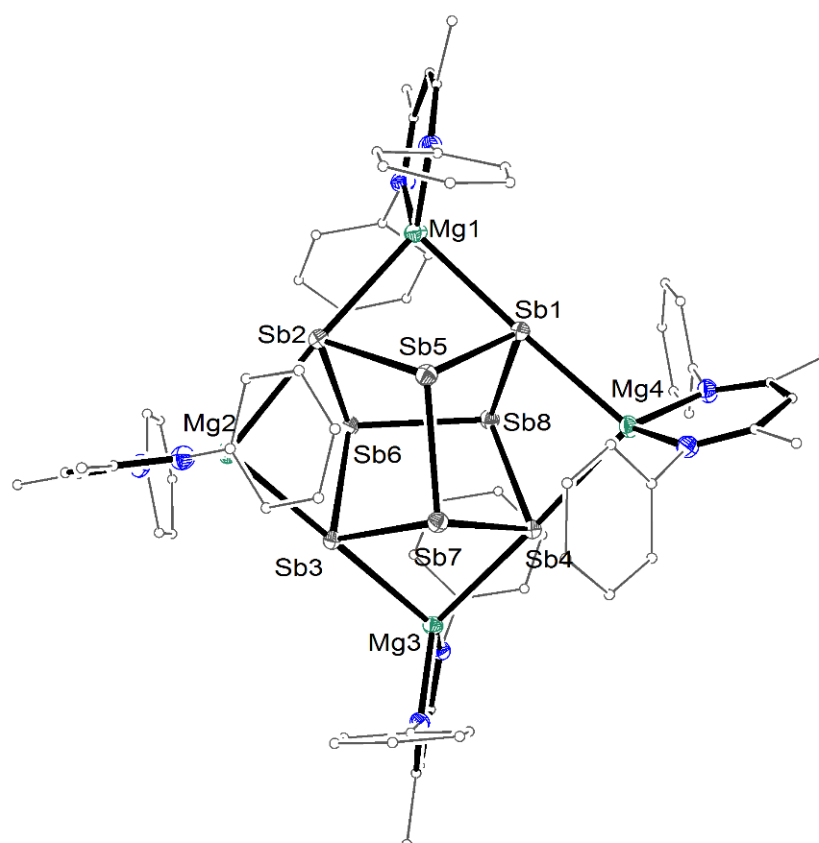


Figure S4.1. Molecular Structure of $[(\text{BDI}^{\text{Ar}})\text{Mg}]_4[\text{Sb}_8]$ (**4.22**).



7.3 Crystallographic Details

General

Crystals were covered in inert oil and suitable single crystals were selected under a microscope and mounted on an Agilent SuperNova diffractometer fitted with an Atlas or EOS S2 detector. Data were collected at the temperature indicated using focused microsource Mo K α radiation at 0.71073 Å or Cu K α radiation at 1.54184 Å. Intensities were corrected for Lorentz and polarisation effects and for absorption using multi-scan methods. Space groups were determined from systematic absences and checked for higher symmetry. All structures were solved using direct methods with SHELXS, refined on F^2 using all data by full matrix least-squares procedures with SHELXL-97, within OLEX2.3, or WinGX. Non-hydrogen atoms were refined with anisotropic displacement parameters, unless stated otherwise. Hydrogen atoms were placed in calculated positions or manually assigned from residual electron density where appropriate. Crystals were mounted by either Dr Chris Fitchett, Assoc. Prof. Martyn Coles or Ryan Schwamm, and final report preparation was performed by either Dr Chris Fitchett or Assoc. Prof. Martyn Coles. See attached electronic data for full crystallographic details (.cif files).

Neutron Crystallography Details

Neutron diffraction data were collected on the KOALA instrument at the Australian Nuclear Science and Technology Organisation (ANSTO). The KOALA instrument is a Laue neutron diffractometer that uses a large cylindrical detector and polychromatic neutron beam (wavelengths 0.8 – 1.6 Å). Crystal systems which are triclinic or monoclinic, required collection of multiple orientations in order to ensure collection of a hemisphere of data. Crystals were mounted by Ryan Schwamm and solved by Ryan Schwamm and Dr Alison Edwards.

Sb(NON^{Ar})H (4.17c):

Data collection were performed at 120 K on three different single crystal samples. The crystals were transported to the facility under an inert atmosphere and covered in an inert oil. A single crystal of **4.17c** (0.30 x 0.40 x 0.50 mm) was selected and mounted on an aluminium mount

and placed in a N₂ cryostream set to 120 K. Neutron diffraction data were collected at this temperature with an exposure time of 6000 seconds. Due to the moisture sensitivity of **4.17c**, the build-up of ice on the surface of the frozen oil resulted in cracking of the single crystal after 6-9 images. Therefore, data was collected for three crystals of similar volume. A total of 20 images were collected, with the crystal rotated at 17° increments after each increment. The orientation of the crystals differed by between 45 and 60°, allowing collection of a complete data set. The data reduction was performed using the LaueG suite of programs. The diffraction pattern was indexed to the unit cell obtained from the X-ray crystal structure and the intensities of the peaks measured for peaks with a d-spacing > 1.0. The data were normalised and merged to give a final merging R factor of 7.9 % (wR₂ = 10.0 %) for 1922 reflections. The neutron data was modelled using the Crystals suite of programs. The hydrogen atoms were located in the nuclear density map and most of the atoms were refined anisotropically. One of the methyl groups had significant hydrogen disorder, and was modelled with the largest nuclear density peaks located and an annulus of hydrogen nuclear density about 1.08 Å from the carbon centre to give a total occupancy of 3.

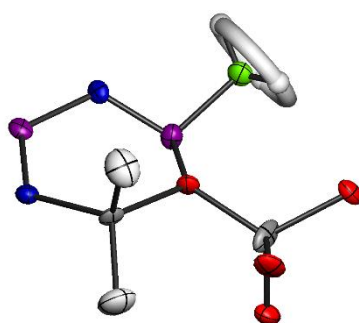
[Li(THF)₄][In(NON^{Ar})H₂] (5.42d)

Data collection was performed in an analogous manner to **4.17c**, using a large single crystal of **5.42d** (1.0 x 0.5 x 0.4 mm), with the cryostream set to 200 K and the exposure time set to 6000 seconds. A total of 19 images were collected at 17° increments, with the data collected over two distinct crystal orientations with a >45° rotation. The data reduction was also performed in an analogous manner to **4.17c**, for data with a d-spacing > 1.10. The data was normalised and merged to give a final merging R factor of 6.8 % (wR₂ = 9.3 %) for 6952 reflections. The neutron data was modelled using the Crystals suite of programs. The hydrogen atoms were located in the nuclear density map and all of the atoms were refined anisotropically. Complex disorder in the several methylene carbons of the [Li(THF)₄] cations was observed at 200 K, which was left unmodelled, resulting in enlarged displacement ellipsoids for this component

and inaccurate bond distances and angles. However, the anionic component of interest was left largely unaffected, with sensible bond lengths and angles for the atoms of this component.



Data collection was performed in an analogous manner to **4.17c**, using a large single crystal of **5.43d** (1.0 x 0.8 x 0.6 mm), with the cryostream set to 120 K and the exposure time set to 8000 seconds. A total of 38 images were collected at 17° increments, with the data collected over two distinct crystal orientations with a >45° rotation. The data reduction was also performed in an analogous manner to **4.17c**, for data with a d-spacing > 0.90. The data was normalised and merged to give a final merging R factor of 6.8 % (wR2 = 9.3 %) for 7346 reflections. The neutron data was modelled using the Crystals suite of programs. The hydrogen atoms were located in the nuclear density map and most of the atoms were refined anisotropically. One of the methyl groups had significant hydrogen disorder, and was modelled with the largest nuclear density peaks located and an annulus of hydrogen nuclear density about 1.08 Å from the carbon centre to give a total occupancy of 3.



Picture of the annulus used to model the disordered methyl group

Summary of Crystallographic Details for Compounds in Chapter 2

	2.16a	2.16d'	2.16e	[2.17a]₂	2.17e•-C2/c
Empirical formula	C ₁₂ H ₃₀ BiClN ₂ OSi ₂	C ₂₈ H ₄₆ BiClN ₂ OSi ₂	C ₁₀₄ H ₁₁₀ BiClN ₂ OSi ₂	C ₁₂ H ₃₀ BiN ₂ OSi ₂	C ₇₆ H ₇₈ BiN ₂ OSi ₂
<i>M_r</i>	518.99	727.28	1704.54	483.54	1300.56
Radiation	MoK α	MoK α	MoK α	MoK α	MoK α
<i>T</i> [K]	120.0(1)	120.0(1)	120.0(1)	120.0(1)	120.0(1)
Crystal size [mm]	0.32 × 0.15 × 0.11	0.25 × 0.23 × 0.16	0.15 × 0.08 × 0.06	0.19 × 0.13 × 0.12	0.24 × 0.16 × 0.13
Crystal system	orthorhombic	monoclinic	orthorhombic	monoclinic	monoclinic
Space group	<i>P</i> 212121	<i>C</i> 2/ <i>c</i>	<i>P</i> 2 ₁ 2 ₁ 2 ₁	<i>P</i> 2 ₁ / <i>c</i>	<i>C</i> 2/ <i>c</i>
<i>a</i> [Å]	6.29576(8)	27.7465(7)	18.0673(3)	15.5677(3)	24.5463(6)
<i>b</i> [Å]	14.56103(13)	11.8086(3)	19.7078(3)	13.1162(2)	11.1899(3)
<i>c</i> [Å]	20.8380(2)	19.6800(4)	24.4460(4)	18.8025(4)	23.9777(7)
α [°]	90	90	90	90	90
β [°]	90	95.992(2)	90	105.888(2)	101.928(3)
γ [°]	90	90	90	90	90
<i>V</i> [Å ³]	1910.28(4)	6412.8(3)	8704.4(3)	3692.60(13)	6443.8(3)
<i>Z</i>	4	8	4	8	4
<i>D</i> _{calc.} [mg m ⁻³]	1.805	1.507	1.301	1.74	1.341
μ [mm ⁻¹]	9.491	5.657	2.134	9.641	2.805
2 θ range for data col. [°]	5.596 to 59.998	6.6236 to 58.7348	6.734 to 59.0194	6.6388 to 58.8996	6.7702 to 59.1232
Reflections collected	38954	14683	33252	19828	17591
Independent Reflections	5564	7406	17160	8674	7600
Data/restraints/parameters	5564/0/182	7406/0/328	17160/0/1014	8674/0/345	7600/0/376
Final <i>R</i> indices [<i>I</i> > 2 σ (<i>I</i>)]	<i>R</i> ₁ = 0.017, w <i>R</i> ₂ = 0.040	<i>R</i> ₁ = 0.032, w <i>R</i> ₂ = 0.059	<i>R</i> ₁ = 0.026, w <i>R</i> ₂ = 0.053	<i>R</i> ₁ = 0.027, w <i>R</i> ₂ = 0.051	<i>R</i> ₁ = 0.027, w <i>R</i> ₂ = 0.053
Final <i>R</i> indices (all data)	<i>R</i> ₁ = 0.017, w <i>R</i> ₂ = 0.040	<i>R</i> ₁ = 0.046, w <i>R</i> ₂ = 0.063	<i>R</i> ₁ = 0.031, w <i>R</i> ₂ = 0.055	<i>R</i> ₁ = 0.037, w <i>R</i> ₂ = 0.054	<i>R</i> ₁ = 0.033, w <i>R</i> ₂ = 0.055
GOOF on <i>F</i> ²	1.054	1.027	1.036	1.021	1.059
Large diff. peak/hole[e.Å ⁻³]	1.52/-0.88	1.47/-0.85	0.85/-0.66	1.30/-1.27	0.57/-0.62
	2.17e•-P2₁/n	2.19e	2.20e	2.21e	2.22d
Empirical formula	C ₈₄ H ₉₈ BiN ₂ O ₃ Si ₂	C ₈₄ H ₉₆ N ₂ O ₃ Si ₂	C ₄₈ H ₅₉ LiNO ₃ Si	C ₁₀₀ H ₁₂₂ Li ₄ N ₂ O ₆ Si ₂	C ₅₅ H ₇₄ Bi ₂ N ₆ O ₃ Si ₆
<i>M_r</i>	1448.8	1237.80	732.99	1531.93	1453.7
Radiation	CuK α	MoK α	CuK α	CuK α	MoK α
<i>T</i> [K]	120.0(1)	120.0(1)	170.0(1)	278.87(10)	120.0(1)
Crystal size [mm]	0.28 × 0.26 × 0.18	0.23 × 0.22 × 0.11	0.51 × 0.48 × 0.45	0.45 × 0.37 × 0.3	0.24 × 0.15 × 0.11
Crystal system	monoclinic	monoclinic	monoclinic	monoclinic	orthorhombic
Space group	<i>P</i> 2 ₁ / <i>n</i>	<i>P</i> 2 ₁ / <i>n</i>	<i>C</i> 2/ <i>c</i>	<i>P</i> 2 ₁ / <i>c</i>	<i>P</i> b <i>c</i> n
<i>a</i> [Å]	12.7552(5)	15.7886(3)	23.9315(5)	21.7416(3)	16.1256(3)
<i>b</i> [Å]	24.9034(7)	12.3313(2)	19.5340(4)	17.1216(2)	15.2321(3)
<i>c</i> [Å]	24.5987(7)	18.8823(3)	18.5814(3)	24.3333(3)	24.8726(5)
α [°]	90	90	90	90	90
β [°]	103.143(4)	106.214(2)	93.4128(18)	106.3470(10)	90
γ [°]	90	90	90	90	90
<i>V</i> [Å ³]	7609.1(4)	3530.05(10)	8671.0(3)	8691.92(19)	6109.4(2)
<i>Z</i>	4	2	8	4	4
<i>D</i> _{calc.} [mg m ⁻³]	1.265	1.165	1.123	1.171	1.58
μ [mm ⁻¹]	5.2	0.839	0.776	0.792	5.892
2 θ range for data col. [°]	4.004 to 74.577	3.5670 to 76.4780	2.922 to 67.684	3.201 to 67.684	6.763 to 58.9242
Reflections collected	35974	19728	17355	71813	24092
<i>R</i> _{int}	15518	7360	8574	18102	7305
Data/restraints/parameters	15518/0/749	7360/0/420	8574/60/ 494	18102/0/ 1107	7305/0/352
Final <i>R</i> indices [<i>I</i> > 2 σ (<i>I</i>)]	<i>R</i> ₁ = 0.07, w <i>R</i> ₂ = 0.1732	<i>R</i> ₁ = 0.0467, w <i>R</i> ₂ = 0.1143	<i>R</i> ₁ = 0.0641, w <i>R</i> ₂ = 0.1753	<i>R</i> ₁ = 0.0427, w <i>R</i> ₂ = 0.1091	<i>R</i> ₁ = 0.020, w <i>R</i> ₂ = 0.036
Final <i>R</i> indices (all data)	<i>R</i> ₁ = 0.0757, w <i>R</i> ₂ = 0.1769	<i>R</i> ₁ = 0.0516, w <i>R</i> ₂ = 0.1185	<i>R</i> ₁ = 0.0738, w <i>R</i> ₂ = 0.1858	<i>R</i> ₁ = 0.0491, w <i>R</i> ₂ = 0.1159	<i>R</i> ₁ = 0.033, w <i>R</i> ₂ = 0.041
GOOF on <i>F</i> ²	1.044	1.056	1.035	1.023	1.024
Large diff. peak/hole[e.Å ⁻³]	5.872/-3.712	0.410/-0.406	0.801/-0.612	0.550/-0.364	0.48/-0.68

	2.22c	2.24d	2.26d	2.27a	2.28e
Empirical formula	C ₆₀ H ₉₀ Bi ₂ N ₆ O ₃ Si ₆	C ₅₆ H ₉₂ Bi ₄ N ₄ O ₂ Si ₄	C ₇₂ H ₁₁₈ BiMgN ₄ O ₄ Si ₂	C ₄₂ H ₉₆ Bi ₃ KN ₆ O ₈ Si ₄	C ₉₄ H ₁₁₂ BiKN ₄ O ₇
M_r	1529.87	1801.61	1393.18	1591.64	1657.95
Radiation	CuK α	CuK α	MoK α	MoK α	CuK α
T [K]	120.0(1)	120.0(1)	120.0(1)	120.0(1)	120.0(1)
Crystal size [mm]	0.21 \times 0.17 \times 0.06	0.15 \times 0.12 \times 0.05	0.22 \times 0.11 \times 0.07	0.23 \times 0.16 \times 0.07	0.21 \times 0.17 \times 0.10
Crystal system	triclinic	orthorhombic	monoclinic	orthorhombic	monoclinic
Space group	$P\bar{1}$	$Pbca$	$P2_1/n$	$Pbcn$	$P2_1/n$
a [Å]	11.7744(3)	15.7233(1)	11.9926(3)	20.3709(4)	18.80982(10)
b [Å]	15.3339(4)	15.3035(1)	28.4477(7)	16.0105(4)	20.49993(13)
c [Å]	19.9763(5)	55.6974(4)	21.4995(4)	18.8989(3)	22.99017(14)
α [°]	102.811(2)	90	90	90	90
β [°]	90.9255(19)	90	92.1502(18)	90	106.1008(6)
γ [°]	107.564(2)	90	90	90	90
V [Å ³]	3339.52	13402.0(2)	7329.7(3)	6163.9(2)	8517.28(9)
Z	2	8	4	4	4
D_{calc} [mg m ⁻³]	1.52	1.786	1.258	1.715	1.293
μ [mm ⁻¹]	11.608	21.225	2.493	8.742	4.929
2θ range for data col. [°]	3.11 to 69.99	8.5856 to 143.2262	3.461 to 27.772	6.77 to 52.7412	9.2164 to 143.679
Reflections collected	38204	51718	47951	18259	67434
R_{int}	12659	12960	14952	6288	16564
Data/restraints/parameters	12659/0/718	12960/50/621	14952/0/ 775	6288/0/300	16564/54/998
Final R indices [$I > 2\sigma(I)$]	$R_1 = 0.031$, $wR_2 = 0.080$	$R_1 = 0.062$, $wR_2 = 0.15$	$R_1 = 0.0332$, $wR_2 = 0.063$	$R_1 = 0.039$, $wR_2 = 0.073$	$R_1 = 0.025$, $wR_2 = 0.060$
Final R indices (all data)	$R_1 = 0.031$, $wR_2 = 0.081$	$R_1 = 0.069$, $wR_2 = 0.15$	$R_1 = 0.053$, $wR_2 = 0.069$	$R_1 = 0.050$, $wR_2 = 0.076$	$R_1 = 0.027$, $wR_2 = 0.062$
GOOF on F^2	1.103	1.180	1.05	1.504	1.060
Large diff. peak/hole [e.Å ⁻³]	1.39/-2.52	4.35/-2.68	1.188/-0.655	1.17/-1.22	0.84/-1.09

Summary of Crystallographic Details for Compounds in Chapter 3

	3.15a	3.15d	3.15e	3.17a	3.17d
Empirical formula	C ₁₂ H ₃₀ BiBrN ₂ OSi ₂	C ₂₈ H ₄₆ BiBrN ₂ OSi ₂	C ₇₉ H ₈₅ BiBrN ₂ OSi ₂	C ₁₂ H ₃₀ BiIn ₂ OSi ₂	C ₂₈ H ₄₆ BiIn ₂ OSi ₂
<i>M_r</i>	563.45	771.74	1423.56	610.44	818.73
Radiation	MoK α	MoK α	CuK α	MoK α	MoK α
<i>T</i> [K]	120.0(1)	120.0(1)	120.0(1)	120.0(1)	120.0(1)
Crystal size [mm]	0.19 × 0.06 × 0.06	0.24 0.21 × 0.13	0.18 × 0.15 × 0.10	0.13 × 0.10 × 0.07	0.18 × 0.13 × 0.06
Crystal system	orthorhombic	monoclinic	triclinic	triclinic	triclinic
Space group	<i>P</i> 2 ₁ 2 ₁ 2 ₁	<i>C</i> 2/ <i>c</i>	<i>P</i> $\bar{1}$	<i>P</i> $\bar{1}$	<i>P</i> $\bar{1}$
<i>a</i> [Å]	6.3429(3)	27.6952(8)	12.3272(3)	6.4476(4)	9.7255(5)
<i>b</i> [Å]	14.5353(6)	11.7204(4)	15.3897(3)	11.0141(8)	10.5069(5)
<i>c</i> [Å]	20.8596(7)	19.9202(5)	19.0972(3)	15.258(1)	16.7509(8)
α [°]	90	90	79.6704(14)	69.287(6)	98.696(4)
β [°]	90	96.826(3)	73.9307(19)	86.678(5)	95.593(4)
γ [°]	90	90	89.3765(17)	76.206(5)	108.843(4)
<i>V</i> [Å ³]	1923.17(13)	6420.2(3)	3422.09(12)	983.83(11)	1581.63(14)
<i>Z</i>	4	8	2	2	2
<i>D</i> _{calc.} [mg m ⁻³]	1.946	1.597	1.382	2.061	1.719
μ [mm ⁻¹]	11.318	6.79	6.414	10.648	6.648
2 θ range for data col. [°]	7.009 to 58.6506	6.8044 to 59.3742	4.14 to 73.006	6.8238 to 58.6344	6.9588 to 58.8598
Reflections collected	6249	16923	24109	6594	13284
<i>R</i> _{int}	3946	7597	12119	4435	7365
Data/restraints/parameters	3946/24/182	7597/0/328	12119/0/770	4435/0/182	7365/0/328
Final <i>R</i> indices [<i>I</i> > 2 σ (<i>I</i>)]	<i>R</i> ₁ = 0.026, w <i>R</i> ₂ = 0.049	<i>R</i> ₁ = 0.026, w <i>R</i> ₂ = 0.045	<i>R</i> ₁ = 0.0389, w <i>R</i> ₂ = 0.1058	<i>R</i> ₁ = 0.030, w <i>R</i> ₂ = 0.05	<i>R</i> ₁ = 0.046, w <i>R</i> ₂ = 0.111
Final <i>R</i> indices (all data)	<i>R</i> ₁ = 0.030, w <i>R</i> ₂ = 0.050	<i>R</i> ₁ = 0.034, w <i>R</i> ₂ = 0.048	<i>R</i> ₁ = 0.0402, w <i>R</i> ₂ = 0.1069	<i>R</i> ₁ = 0.036, w <i>R</i> ₂ = 0.055	<i>R</i> ₁ = 0.049, w <i>R</i> ₂ = 0.112
GOOF on <i>F</i> ²	0.981	1.034	1.064	1.005	1.291
Large diff. peak/hole [e.Å ⁻³]	0.80/-0.69	0.58/-0.69	2.953/-3.077	0.93/-0.82	3.41/-1.84
	3.17e	3.18a	3.18d	3.19a	3.20d
Empirical formula	C ₇₆ H ₇₈ BiIn ₂ OSi ₂	C ₂₄ H ₆₀ Bi ₂ N ₄ O ₂ SSi ₄	C ₆₂ H ₁₀₆ Bi ₂ N ₄ O ₂ SSi ₄	C ₂₄ H ₆₀ Bi ₂ N ₄ O ₂ S ₃ Si ₄	C ₅₆ H ₉₂ Bi ₂ N ₄ O ₂ S ₅ Si ₄
<i>M_r</i>	848.07	999.14	1501.88	1063.26	1630.12
Radiation	CuK α	MoK α	MoK α	MoK α	CuK α
<i>T</i> [K]	120.0(1)	120.0(1)	120.0(1)	120.0(1)	120.0(1)
Crystal size [mm]	0.15 × 0.10 × 0.05	0.40 × 0.17 × 0.10	0.26 × 0.17 × 0.11	0.25 × 0.21 × 0.07	0.05 × 0.05 × 0.11
Crystal system	monoclinic	triclinic	monoclinic	monoclinic	triclinic
Space group	<i>P</i> 2 ₁ / <i>n</i>	<i>P</i> $\bar{1}$	<i>P</i> 2 ₁ / <i>n</i>	<i>I</i> 2/ <i>a</i>	<i>P</i> $\bar{1}$
<i>a</i> [Å]	12.79606(18)	8.2256(3)	18.2632(3)	13.4362(5)	12.2335(2)
<i>b</i> [Å]	24.4641(4)	13.5394(5)	17.7081(3)	10.8026(4)	16.5506(2)
<i>c</i> [Å]	24.7234(4)	18.0192(6)	21.6183(3)	28.5609(8)	18.8461(2)
α [°]	90	101.127(3)	90	90	91.8495(11)
β [°]	102.6729(14)	91.135(3)	100.0674(13)	92.026(3)	90.7584(13)
γ [°]	90	101.759(3)	90	90	105.5564(15)
<i>V</i> [Å ³]	7550.98(19)	1924.09(12)	6883.84(18)	4142.9(2)	3673.15(10)
<i>Z</i>	4	2	4	4	2
<i>D</i> _{calc.} [mg m ⁻³]	1.369	1.725	1.449	1.705	1.474
μ [mm ⁻¹]	8.436	9.342	5.247	8.752	11.551
2 θ range for data col. [°]	3.5403 to 68.1328	6.8692 to 58.7866	6.6646 to 58.8722	6.7976 to 58.6614	3.5665 to 74.3338
Reflections collected	60991	17494	26845	23515	75938
<i>R</i> _{int}	13827	8902	15680	5085	14792
Data/restraints/parameters	13827 / 0 / 816	8902/0/354	15680/0/711	5085/0/187	14792/2/782
Final <i>R</i> indices [<i>I</i> > 2 σ (<i>I</i>)]	<i>R</i> ₁ = 0.0474, w <i>R</i> ₂ = 0.1166	<i>R</i> ₁ = 0.033, w <i>R</i> ₂ = 0.060	<i>R</i> ₁ = 0.029, w <i>R</i> ₂ = 0.056	<i>R</i> ₁ = 0.050, w <i>R</i> ₂ = 0.120	<i>R</i> ₁ = 0.0455, w <i>R</i> ₂ = 0.1299
Final <i>R</i> indices (all data)	<i>R</i> ₁ = 0.0533, w <i>R</i> ₂ = 0.1204	<i>R</i> ₁ = 0.045, w <i>R</i> ₂ = 0.065	<i>R</i> ₁ = 0.047, w <i>R</i> ₂ = 0.063	<i>R</i> ₁ = 0.064, w <i>R</i> ₂ = 0.128	<i>R</i> ₁ = 0.047, w <i>R</i> ₂ = 0.1308
GOOF on <i>F</i> ²	1.189	1.007	1.039	1.081	1.344
Large diff. peak/hole [e.Å ⁻³]	1.892/-1.33	1.80/-1.14	1.17/-0.93	3.97/-1.75	3.584/-1.449

	3.21e	3.22a	3.22d	3.23a	3.23d
Empirical formula	C ₇₆ H ₇₈ BiN ₂ O ₈ S ₄ Si ₂	C ₂₄ H ₆₀ Bi ₂ N ₄ O ₂ Se Si ₄	C ₆₂ H ₁₀₆ Bi ₂ N ₄ O ₂ SeSi ₄	C ₂₄ H ₆₀ Bi ₂ N ₄ O ₂ Si ₄ Te	C ₅₆ H ₉₂ Bi ₂ N ₄ O ₂ Si ₄ Te
<i>M_r</i>	1613.07	1046.04	1548.78	1094.68	1511.25
Radiation	CuKα	MoKα	MoKα	MoKα	MoKα
<i>T</i> [K]	120.0(1)	120.0(1)	120.0(1)	120.0(1)	120.0(1)
Crystal size [mm]	0.18 × 0.08 × 0.04	0.25 × 0.12 × 0.11	0.36 × 0.12 × 0.06	0.22 × 0.07 × 0.06	0.22 × 0.17 × 0.15
Crystal system	orthorhombic	triclinic	triclinic	triclinic	monoclinic
Space group	<i>Pbca</i>	<i>P</i> $\bar{1}$	<i>P</i> $\bar{1}$	<i>P</i> $\bar{1}$	<i>C2/c</i>
<i>a</i> [Å]	19.0380(2)	8.21745(18)	13.4622(5)	8.19472(19)	53.6498(5)
<i>b</i> [Å]	27.4178(3)	13.5504(3)	14.0782(4)	13.7332(4)	12.22283(15)
<i>c</i> [Å]	29.8069(3)	18.1613(3)	19.2071(7)	18.5469(4)	19.3321(2)
α [°]	90	101.3902(17)	78.589(3)	102.871(2)	90
β [°]	90	91.3691(17)	77.999(3)	90.4530(18)	93.0151(9)
γ [°]	90	101.8810(19)	81.147(3)	103.556(2)	90
<i>V</i> [Å ³]	15558.6(3)	1935.56(7)	3466.0(2)	1974.16(8)	12659.5(2)
<i>Z</i>	8	2	2	2	8
<i>D</i> _{calc.} [mg m ⁻³]	1.377	1.795	1.484	1.842	1.586
μ [mm ⁻¹]	6.106	10.168	5.664	9.772	6.1
2 θ range for data col. [°]	4.076 to 71.547	6.9248 to 52.7428	6.6856 to 58.9528	6.652 to 58.7804	6.714 to 58.8038
Reflections collected	25997	42862	31835	44304	26453
<i>R</i> _{int}	15038	9583	16064	9812	14419
Data/restraints/parameters	15038/30/ 932	9583/0/354	16064/6/695	9812/48/385	14419/0/646
Final <i>R</i> indices [<i>I</i> > 2 σ (<i>I</i>)	<i>R</i> ₁ = 0.0481, w <i>R</i> ₂ = 0.1428	<i>R</i> ₁ = 0.028, w <i>R</i> ₂ = 0.053	<i>R</i> ₁ = 0.029, w <i>R</i> ₂ = 0.058	<i>R</i> ₁ = 0.024, w <i>R</i> ₂ = 0.041	<i>R</i> ₁ = 0.029, w <i>R</i> ₂ = 0.054
Final <i>R</i> indices (all data)	<i>R</i> ₁ = 0.0567, w <i>R</i> ₂ = 0.1428	<i>R</i> ₁ = 0.034, w <i>R</i> ₂ = 0.056	<i>R</i> ₁ = 0.041, w <i>R</i> ₂ = 0.062	<i>R</i> ₁ = 0.032, w <i>R</i> ₂ = 0.043	<i>R</i> ₁ = 0.040, w <i>R</i> ₂ = 0.057
GOOF on <i>F</i> ²	1.125	1.105	1.012	1.055	1.069
Large diff. peak/hole[e.Å ⁻³]	2.515/-2.007	1.49/-1.29	1.66/-0.81	1.00/-1.05	1.16/-1.04
	3.24a	3.24d	3.24e	3.25d	3.27d
Empirical formula	C ₃₇ H ₆₄ BiN ₃ O ₂ Si ₂	C ₂₁ H ₄₈ BiN ₃ O ₂ Si ₂	C ₂₀₀ H ₂₆₂ N ₆ O ₄ Si ₄ Bi ₂	C ₅₆ H ₉₂ Bi ₂ N ₄ O ₂ P ₄ Si ₄	C ₈₆ H ₁₃₉ Bi ₂ N ₆ O ₂ P ₄ Si ₄
<i>M_r</i>	848.07	639.78	1672.23	1507.53	1943.22
Radiation	MoKα	MoKα	triclinic	MoKα	CuKα
<i>T</i> [K]	120.0(1)	120.0(1)	173.15	120.0(1)	120.0(1)
Crystal size [mm]	0.20 × 0.09 × 0.06	0.47 × 0.29 × 0.22	0.24 × 0.10 × 0.08	0.29 × 0.20 × 0.12	0.11 × 0.10 × 0.04
Crystal system	triclinic	orthorhombic	triclinic	monoclinic	triclinic
Space group	<i>P</i> $\bar{1}$	<i>Pnma</i>	<i>P</i> $\bar{1}$	<i>C2/c</i>	<i>P</i> $\bar{1}$
<i>a</i> [Å]	9.8235(5)	11.8697(3)	11.3593(3)	30.6287(10)	13.3429(2)
<i>b</i> [Å]	11.3232(4)	17.1607(4)	15.2315(2)	10.6676(3)	16.0361(3)
<i>c</i> [Å]	19.8873(11)	13.7508(3)	26.2935(6)	24.4557(8)	23.5433(4)
α [°]	96.254(3)	90	93.8553(17)	90	95.9333(15)
β [°]	91.689(4)	90	102.413(2)	104.611(3)	94.1662(14)
γ [°]	115.381(4)	90	96.4187(17)	90	111.3662(18)
<i>V</i> [Å ³]	1979.57(18)	2800.94(11)	4395.53(17)	7732.1(4)	4632.95(15)
<i>Z</i>	2	4	1	4	2
<i>D</i> _{calc.} [mg m ⁻³]	1.423	1.517	1.263	1.295	1.393
μ [mm ⁻¹]	4.547	6.4	2.083	4.721	8.869
2 θ range for data col. [°]	6.9248 to 52.7428	7.1236 to 58.6874	6.6152 to 59.1148	6.7408 to 58.52	8.3256 to 143.6068
Reflections collected	12880	8659	41878	31439	27859
<i>R</i> _{int}	7996	3412	20420	9355	17409
Data/restraints/parameters	7996/0/410	3412/0/139	20420/5/980	9355/37/363	17409/19/922
Final <i>R</i> indices [<i>I</i> > 2 σ (<i>I</i>)	<i>R</i> ₁ = 0.038, w <i>R</i> ₂ = 0.083	<i>R</i> ₁ = 0.024, w <i>R</i> ₂ = 0.050	<i>R</i> ₁ = 0.036, w <i>R</i> ₂ = 0.076	<i>R</i> ₁ = 0.037, w <i>R</i> ₂ = 0.092	<i>R</i> ₁ = 0.035, w <i>R</i> ₂ = 0.083
Final <i>R</i> indices (all data)	<i>R</i> ₁ = 0.045, w <i>R</i> ₂ = 0.087	<i>R</i> ₁ = 0.031, w <i>R</i> ₂ = 0.052	<i>R</i> ₁ = 0.045, w <i>R</i> ₂ = 0.079	<i>R</i> ₁ = 0.054, w <i>R</i> ₂ = 0.097	<i>R</i> ₁ = 0.042, w <i>R</i> ₂ = 0.087
GOOF on <i>F</i> ²	1.027	1.036	1.069	1.074	1.034
Large diff. peak/hole[e.Å ⁻³]	5.02/-1.50	0.75/-1.20	4.66/-1.91	2.64/-0.72	1.58/-1.13

Summary of Crystallographic Details for Compounds in Chapter 4

	4.15a	4.15b	4.15c	4.15d	4.15e
Empirical formula	C ₁₂ H ₃₀ ClN ₂ OSbSi ₂	C ₁₆ H ₂₂ ClN ₂ OSbSi ₂	C ₂₀ H ₃₀ N ₂ OSi ₂ ClSb	C ₈₄ H ₁₃₈ Cl ₃ N ₆ O ₃ Sb ₃ Si ₆	C ₁₀₄ H ₁₁₀ ClN ₂ OSbSi ₂
M_r	431.76	471.73	527.84	1920.14	1617.31
Radiation	MoK α	MoK α	MoK α	CuK α	MoK α
T [K]	120.0(1)	120.0(1)	120.0(1)	286.0(1)	120.0(1)
Crystal size [mm]	0.20 × 0.11 × 0.08	0.29 × 0.10 × 0.06	0.35 × 0.18 × 0.06	0.51 × 0.37 × 0.1	0.25 × 0.20 × 0.15
Crystal system	monoclinic	monoclinic	triclinic	triclinic	orthorhombic
Space group	$P2_1/c$	$P\bar{1}$	$P\bar{1}$	$P\bar{1}$	$P2_12_12_1$
a [Å]	6.55519(9)	6.3495(2)	9.8816(2)	9.43069(12)	18.0602(5)
b [Å]	34.6568(5)	11.8075(4)	10.5121(3)	22.2904(3)	19.6327(4)
c [Å]	16.9839(2)	13.7568(5)	12.2372(3)	23.4692(3)	24.5576(5)
α [°]	90	97.039(3)	85.493(2)	102.9174(10)	90
β [°]	93.4335(12)	100.943(3)	77.295(2)	99.8049(10)	90
γ [°]	90	100.943(3)	68.969(3)	96.0590(10)	90
V [Å ³]	3851.51(9)	959.71(6)	1157.43(6)	4685.17(10)	8707.4(3)
Z	8	2	2	2	4
D_{calc} [mg m ⁻³]	1.489	1.632	1.515	1.361	1.234
μ [mm ⁻¹]	1.691	1.703	1.424	1.068	0.425
2θ range for data col. [°]	6.6438 to 58.9866	7.0924 to 58.158	6.8266 to 58.754	3.1240 to 37.5920	3.929 to 28.962
Reflections collected	18571	7833	10065	124963	28438
Independent Reflections	8953	4401	5341	41232	19347
Data/restraints/parameters	8953/0/363	4401/0/222	5341/0/252	41232/0/982	19347/0/ 1014
Final R indices [$I > 2\sigma(I)$]	$R_1 = 0.028$, $wR_2 = 0.050$	$R_1 = 0.0373$, $wR_2 = 0.0711$	$R_1 = 0.036$, $wR_2 = 0.076$	$R_1 = 0.0328$, $wR_2 = 0.0692$	$R_1 = 0.0368$, $wR_2 = 0.0801$
Final R indices (all data)	$R_1 = 0.032$, $wR_2 = 0.052$	$R_1 = 0.0432$, $wR_2 = 0.0735$	$R_1 = 0.042$, $wR_2 = 0.081$	$R_1 = 0.0478$, $wR_2 = 0.0758$	$R_1 = 0.0443$, $wR_2 = 0.0842$
GOOF on F^2	1.064	1.140	1.001	1.080	1.023
Large diff. peak/hole[e.Å ⁻³]	0.56/-0.34	0.75/-0.71	1.49/-0.51	1.236/-0.614	0.94/-0.38
	4.16b	4.17c	4.17d	[4.18a] ₂	[4.18b] ₂
Empirical formula	C ₄₈ H ₆₆ N ₆ O ₃ Sb ₂ Si ₆	C ₂₀ H ₃₁ N ₂ OSbSi ₂	C ₆₂ H ₁₀₈ N ₄ O ₂ Sb ₂ Si ₄	C ₂₄ H ₆₀ N ₄ O ₂ Sb ₂ Si ₄	C ₃₂ H ₄₄ N ₄ O ₂ Sb ₂ Si ₄
M_r	1187.1	493.4	1297.40	792.62	872.57
Radiation	MoK α	MoK α	MoK α	MoK α	CuK α
T [K]	120.0(1)	120.0(1)	120.0(1)	120.0(1)	120.0(1)
Crystal size [mm]	0.34 × 0.19 × 0.14	0.17 × 0.11 × 0.07	0.31 × 0.24 × 0.15	0.28 × 0.21 × 0.19	0.12 × 0.07 × 0.05
Crystal system	triclinic	triclinic	triclinic	monoclinic	triclinic
Space group	$P\bar{1}$	$P\bar{1}$	$P\bar{1}$	$P2_1/c$	$P\bar{1}$
a [Å]	12.0844(4)	7.6028(5)	12.3588(2)	15.6347(2)	10.84620(17)
b [Å]	13.4532(5)	11.5896(8)	16.8810(4)	12.97374(19)	11.5145(2)
c [Å]	19.2551(5)	13.8020(7)	17.0204(4)	18.6746(3)	17.8148(3)
α [°]	97.860(3)	99.459(5)	73.916(2)	90	71.7105(17)
β [°]	103.002(3)	100.012(5)	84.8280(16)	105.9186(18)	80.6803(15)
γ [°]	109.830(3)	107.557(6)	85.4219(16)	90	62.9088(18)
V [Å ³]	2790.65(16)	1110.98(12)	3392.47(13)	3642.72(10)	1880.22(6)
Z	2	2	2	4	2
D_{calc} [mg m ⁻³]	1.413	1.475	1.27	1.445	1.541
μ [mm ⁻¹]	1.138	1.358	0.908	1.64	12.879
2θ range for data col. [°]	3.73 to 28.884	3.794 to 28.961	6.908 to 59.0536	6.5994 to 58.6428	8.9678 to 143.4618
Reflections collected	24480	8554	17238	18203	12656
R_{int}	12870	4543	15797	8470	7346
Data/restraints/parameters	12870/0/598	4543/0/ 247	15797/0/709	8470/0/345	7346/0/405
Final R indices [$I > 2\sigma(I)$]	$R_1 = 0.0304$, $wR_2 = 0.059$	$R_1 = 0.0308$, $wR_2 = 0.0652$	$R_1 = 0.030$, $wR_2 = 0.065$	$R_1 = 0.028$, $wR_2 = 0.050$	$R_1 = 0.027$, $wR_2 = 0.078$
Final R indices (all data)	$R_1 = 0.0388$, $wR_2 = 0.0638$	$R_1 = 0.0344$, $wR_2 = 0.0673$	$R_1 = 0.038$, $wR_2 = 0.069$	$R_1 = 0.035$, $wR_2 = 0.054$	$R_1 = 0.030$, $wR_2 = 0.079$
GOOF on F^2	0.996	1.027	1.050	1.036	1.190
Large diff. peak/hole[e.Å ⁻³]	0.501/-0.431	0.925/-0.459	1.28/-0.53	0.49/-0.46	0.72/-0.88

	[4.18c]₂	4.19d	4.20d	4.21b/4.22
Empirical formula	C ₂₀ H ₃₀ N ₂ OSbSi ₂	C ₁₂₂ H ₁₉₄ Mg ₂ N ₈ O ₄ Sb ₂ Si ₄	C ₁₂₁ H ₁₈₂ Mg ₂ N ₈ O ₂ Sb ₂ Si ₄	C ₁₇₂ H ₂₃₈ Mg ₆ N ₁₄ OSb ₈ Si ₂
<i>M_r</i>	492.39	2241.35	2185.22	3693.79
Radiation	CuKα	MoKα	CuKα	CuKα
<i>T</i> [K]	120.0(1)	120.0(1)	120.0(1)	120.0(1)
Crystal size [mm]	0.26 × 0.13 × 0.07	0.22 × 0.12 × 0.06	0.13 × 0.10 × 0.04	0.26 × 0.16 × 0.12
Crystal system	monoclinic	monoclinic	triclinic	triclinic
Space group	<i>C</i> 2	<i>C</i> 2/ <i>c</i>	<i>P</i> $\bar{1}$	<i>P</i> $\bar{1}$
<i>a</i> [Å]	17.2186(3)	19.1840(3)	12.76522(17)	18.14752(12)
<i>b</i> [Å]	16.3859(4)	27.3003(4)	13.0273(2)	21.82636(18)
<i>c</i> [Å]	16.2779(3)	24.1575(3)	21.6796(3)	23.25415(19)
α [°]	90	90	87.0847(12)	98.1505(7)
β [°]	90.9117(16)	95.8642(13)	73.7449(12)	96.8711(6)
γ [°]	90	90	63.8343(15)	94.4582(6)
<i>V</i> [Å ³]	4592.09(16)	12585.8(3)	3095.39(8)	9010.20(12)
<i>Z</i>	8	4	1	2
<i>D</i> _{calc.} [mg m ⁻³]	1.424	1.183	1.172	1.361
μ [mm ⁻¹]	10.583	0.529	4.3	10.078
2 θ range for data col. [°]	7.448 to 149.5546	6.6264 to 58.6294	9.0136 to 143.5096	4.32 to 71.733
Reflections collected	18170	25771	39994	130877
<i>R</i> _{int}	9174	14383	12024	35050
Data/restraints/parameters	9174/1/485	14383/6/639	12024/4/650	35050/13/1719
Final <i>R</i> indices [<i>I</i> > 2 σ (<i>I</i>)]	<i>R</i> ₁ = 0.025, w <i>R</i> ₂ = 0.064	<i>R</i> ₁ = 0.041, w <i>R</i> ₂ = 0.097	<i>R</i> ₁ = 0.034, w <i>R</i> ₂ = 0.097	<i>R</i> ₁ = 0.029, w <i>R</i> ₂ = 0.0827
Final <i>R</i> indices (all data)	<i>R</i> ₁ = 0.025, w <i>R</i> ₂ = 0.065	<i>R</i> ₁ = 0.063, w <i>R</i> ₂ = 0.106	<i>R</i> ₁ = 0.037, w <i>R</i> ₂ = 0.099	<i>R</i> ₁ = 0.033, w <i>R</i> ₂ = 0.0875
GOOF on <i>F</i> ²	1.022	1.020	0.929	0.652
Large diff. peak/hole[e.Å ⁻³]	2.04/-0.60	.85/-0.65	0.83/-0.74	0.86/-0.735

Summary of Crystallographic Details for Compounds in Chapter 5

	5.39d	5.40d	5.41d	5.42d	5.43d
Empirical formula	C ₃₆ H ₆₆ Cl ₂ InLiN ₂ O ₅ S _{i2}	C ₄₄ H ₇₇ Cl ₂ InLiN ₂ O ₅ Si ₂	C ₄₀ H ₇₀ Cl ₂ InLiN ₂ O ₄ Si ₂	C ₄₄ H ₈₀ InLiN ₂ O ₅ Si ₂	C ₄₀ H ₇₂ InLiN ₂ O ₄ Si ₂
M_r	823.74	962.91	891.82	895.04	822.93
Radiation	MoK α	MoK α	MoK α	MoK α	MoK α
T [K]	120.0(1)	278.9(1)	120.0(1)	120.0(1)	120.0(1)
Crystal size [mm]	0.23 × 0.22 × 0.09	0.18 × 0.11 × 0.04	0.26 × 0.19 × 0.11	0.31 × 0.23 × 0.09	0.22 × 0.19 × 0.09
Crystal system	monoclinic	triclinic	triclinic	triclinic	triclinic
Space group	$P2_1/c$	$P\bar{1}$	$P\bar{1}$	$P\bar{1}$	$P\bar{1}$
a [Å]	12.5274(2)	12.6940(4)	9.9876(3)	12.1902(3)	11.5379(5)
b [Å]	32.6584(4)	13.0718(6)	11.8469(3)	12.7309(5)	11.7768(5)
c [Å]	11.9206(2)	15.4325(6)	19.9935(5)	16.0896(7)	17.7223(9)
α [°]	90	87.465(3)	83.757(2)	85.297(3)	82.961(4)
β [°]	117.404(2)	82.137(3)	79.476(2)	85.720(3)	73.327(4)
γ [°]	90	80.711(3)	87.976(2)	82.296(3)	71.646(4)
V [Å ³]	4329.73(12)	2502.78(17)	2311.78(11)	2461.00(15)	2188.13(17)
Z	4	2	2	2	2
D_{calc} [mg m ⁻³]	1.264	1.278	1.281	1.208	1.249
μ [mm ⁻¹]	0.758	0.668	0.716	0.57	0.63
2θ range for data col. [°]	6.6408 to 54.204	3.0850 to 32.3270	6.8236 to 58.8776	6.7598 to 58.9138	6.8186 to 58.7712
Reflections collected	36962	12155	50700	23946	15479
R_{int}	9466	9815	11313	11409	9922
Data/restraints/parameters	9466/0/424	9815/0/526	11313/0/488	11409/0/504	9922/0/459
Final R indices [$I > 2\sigma(I)$]	$R_1 = 0.029$, $wR_2 = 0.061$	$R_1 = 0.0597$, $wR_2 = 0.1443$	$R_1 = 0.031$, $wR_2 = 0.02$	$R_1 = 0.039$, $wR_2 = 0.083$	$R_1 = 0.038$, $wR_2 = 0.084$
Final R indices (all data)	$R_1 = 0.035$, $wR_2 = 0.063$	$R_1 = 0.0789$, $wR_2 = 0.1629$	$R_1 = 0.036$, $wR_2 = 0.074$	$R_1 = 0.048$, $wR_2 = 0.088$	$R_1 = 0.047$, $wR_2 = 0.089$
GOOF on F^2	1.061	1.075	1.073	1.036	1.038
Large diff. peak/hole[e.Å ⁻³]	0.46/-0.35	1.569/-1.075	0.60/-0.39	1.20/-1.00	0.94/-0.51
	5.44d	5.45d			
Empirical formula	C ₆₂ H ₁₀₆ In ₂ N ₄ O ₂ Si ₄	C ₄₆ H ₈₂ InKN ₄ O ₇ Si ₂			
M_r	1281.5	1013.25			
Radiation	MoK α	MoK α			
T [K]	120.0(1)	120.0(1)			
Crystal size [mm]	0.28 × 0.27 × 0.20	0.23 × 0.19 × 0.14			
Crystal system	triclinic	triclinic			
Space group	$P\bar{1}$	$P\bar{1}$			
a [Å]	13.0804(4)	12.3840(7)			
b [Å]	13.8505(5)	12.5381(7)			
c [Å]	19.3873(6)	19.0572(10)			
α [°]	76.777(3)	106.499(5)			
β [°]	81.518(3)	104.121(5)			
γ [°]	81.309(3)	99.436(4)			
V [Å ³]	3356.6(2)	2663.5(3)			
Z	2	2			
D_{calc} [mg m ⁻³]	1.268	1.263			
μ [mm ⁻¹]	0.798	0.615			
2θ range for data col. [°]	6.589 to 58.686	3.9870 to 29.0590			
Reflections collected	30017	19489			
R_{int}	15338	19489			
Data/restraints/parameters	15338/3/723	19489/0/564			
Final R indices [$I > 2\sigma(I)$]	$R_1 = 0.0346$, $wR_2 = 0.0747$	$R_1 = 0.0431$, $wR_2 = 0.0995$			
Final R indices (all data)	$R_1 = 0.0453$, $wR_2 = 0.0812$	$R_1 = 0.0587$, $wR_2 = 0.1029$			
GOOF on F^2	1.022	0.993			
Large diff. peak/hole[e.Å ⁻³]	1.01/-0.72	0.831/-0.714			

References

1. Power, P. P., *Nature* 2010, 463, 171.
2. Yadav, S.; Saha, S.; Sen, S. S., *ChemCatChem* 2016, 8, 486-501.
3. Liddle, S. T., *Molecular Metal-Metal Bonds: Compounds, Synthesis, Properties*. Wiley: 2015.
4. Fischer, R. C.; Power, P. P., *Chem. Rev.* 2010, 110, 3877-3923.
5. Clementi, E.; Raimondi, D. L.; Reinhardt, W. P., *J. Chem. Phys.* 1967, 47, 1300-1307.
6. Kutzelnigg, W., *Angew. Chem. Int. Ed.* 1984, 23, 272-295.
7. Schwerdtfeger, P.; Heath, G. A.; Dolg, M.; Bennett, M. A., *J. Am. Chem. Soc.* 1992, 114, 7518-7527.
8. Pyykko, P., *Chem. Rev.* 1988, 88, 563-594.
9. (a) Mudring, A.-V., Stereochemical Activity of Lone Pairs in Heavier Main-group Element Compounds. In *Inorganic Chemistry in Focus III*, Wiley-VCH Verlag GmbH & Co. KGaA: 2006; pp 15-28; (b) Walsh, A.; Payne, D. J.; Egdell, R. G.; Watson, G. W., *Chem. Soc. Rev.* 2011, 40, 4455-4463.
10. Dunitz, J. D.; Orgel, L. E., Stereochemistry of Ionic Solids. In *Advances in Inorganic Chemistry and Radiochemistry*, Emeleus, H. J.; Sharpe, A. G., Eds. Academic Press: 1960; Vol. 2, pp 1-60.
11. Macdonald, C. L. B.; Bandyopadhyay, R.; Cooper, B. F. T.; Friedl, W. W.; Rossini, A. J.; Schurko, R. W.; Eichhorn, S. H.; Herber, R. H., *J. Am. Chem. Soc.* 2012, 134, 4332-4345.
12. Mudring, A.-V.; Rieger, F., *Inorg. Chem.* 2005, 44, 6240-6243.
13. Aldridge, S.; Downs, A. J., *Chem. Rev.* 2001, 101, 3305-3366.
14. Kurth, F. A.; Eberlein, R. A.; Schnockel, H.; Downs, A. J.; Pulham, C. R., *J. Chem. Soc., Chem. Commun.* 1993, 1302-1304.
15. (a) Pulham, C. R.; Downs, A. J.; Goode, M. J.; Rankin, D. W. H.; Robertson, H. E., *J. Am. Chem. Soc.* 1991, 113, 5149-5162; (b) Andrews, L.; Wang, X., *Angew. Chem.* 2004, 116, 1738-1741.
16. Labinger, J. A.; Bercaw, J. E., *Organometallics* 1988, 7, 926-928.

17. (a) Green, S. P.; Jones, C.; Stasch, A., *Science* 2007; (b) Jones, C., *Nat. Rev. Chem.* 2017, 1, 0059.
18. Power, P. P., *Chem. Rev.* 1999, 99, 3463-3504.
19. (a) Jones, C., *Coord. Chem. Rev.* 2010, 254, 1273-1289; (b) Rauchfuss, T. B., Complexes of Bulky β -Diketiminato Ligands. In *Inorganic Syntheses*, John Wiley & Sons, Inc.: 2010; pp 1-55; (c) Kissounko, D. A.; Zabalov, M. V.; Brusova, G. P.; Dmitrii, A. L., *Russ. Chem. Rev.* 2006, 75, 351.
20. Lappert, M.; Protchenko, A.; Power, P.; Seeber, A., *Metal Amide Chemistry*. Wiley: 2008.
21. (a) Coles, M. P., *Coord. Chem. Rev.* 2015, 297-298, 2-23; (b) Coles, M. P., *Coord. Chem. Rev.* 2015, 297-298, 24-39.
22. Kays, D. L., *Chem. Soc. Rev.* 2016, 45, 1004-1018.
23. (a) Schwamm, R. J.; Coles, M. P.; Fitchett, C. M., *Organometallics* 2015, 34, 2500-2507; (b) Schwamm, R. J.; Day, B. M.; Coles, M. P.; Fitchett, C. M., *Inorg. Chem.* 2014, 53, 3778-3787; (c) Day, B. M.; Coles, M. P., *Organometallics* 2013, 32, 4270-4278.
24. (a) Das, A. K.; Moatazedi, Z.; Mund, G.; Bennet, A. J.; Batchelor, R. J.; Leznoff, D. B., *Inorg. Chem.* 2007, 46, 366-368; (b) Hayes, C. E.; Leznoff, D. B., *Organometallics* 2010, 29, 767-774; (c) Jantunen, K. C.; Batchelor, R. J.; Leznoff, D. B., *Organometallics* 2004, 23, 2186-2193; (d) Jantunen, K. C.; Haftbaradaran, F.; Katz, M. J.; Batchelor, R. J.; Schatte, G.; Leznoff, D. B., *Dalton Trans.* 2005, 3083-3091; (e) Leznoff, D. B.; Mund, G.; Jantunen, K. C.; Bhatia, P. H.; Gabert, A. J.; Batchelor, R. J., *J. Nucl. Sci. Tech.* 2002, 39, 406-409; (f) Moatazedi, Z.; Katz, M. J.; Leznoff, D. B., *Dalton Trans.* 2010, 39, 9889-9896; (g) Mund, G.; Batchelor, R. J.; Sharma, R. D.; Jones, C. H. W.; Leznoff, D. B., *J. Chem. Soc., Dalton Trans.* 2002, 136-137; (h) Mund, G.; Vidovic, D.; Batchelor, R. J.; Britten, J. F.; Sharma, R. D.; Jones, C. H. W.; Leznoff, D. B., *Chem. Eur. J.* 2003, 9, 4757-4763; (i) Wong, E. W. Y.; Das, A. K.; Katz, M. J.; Nishimura, Y.; Batchelor, R. J.; Onishi, M.; Leznoff, D. B., *Inorg. Chim. Acta* 2006, 359, 2826-2834.
25. Groom, C. R.; Bruno, I. J.; Lightfoot, M. P.; Ward, S. C., *Acta Crystallogr., Sect. B* 2016, 72, 171-179.
26. (a) Haftbaradaran, F.; Kuchison, A. M.; Katz, M. J.; Schatte, G.; Leznoff, D. B., *Inorg. Chem.* 2008, 47, 812-822; (b) Haftbaradaran, F.; Mund, G.; Batchelor, R. J.; Britten, J. F.; Leznoff, D. B., *Dalton Trans.* 2005, 2343-2345; (c) Hayes, C. E.; Gill, D. E.; Brown, M. L.; Leznoff, D. B., *Eur. J. Inorg. Chem.* 2014, 2014, 3690-3700.
27. Gomez-Suarez, A.; Nelson, D. J.; Nolan, S. P., *Chem. Commun.* 2017, 53, 2650-2660.

28. Tolman, C. A., *Chem. Rev.* 1977, 77, 313-348.
29. Falivene, L.; Credendino, R.; Poater, A.; Petta, A.; Serra, L.; Oliva, R.; Scarano, V.; Cavallo, L., *Organometallics* 2016, 35, 2286-2293.
30. Guzei, I. A.; Wendt, M., *Dalton Trans.* 2006, 3991-3999.
31. Bondi, A., *J. Phys. Chem.* 1964, 68, 441-451.
32. Maity, A. K.; Fortier, S.; Griego, L.; Metta-Magaña, A. J., *Inorg. Chem.* 2014, 53, 8155-8164.
33. Paneth, F. A.; Loleit, H., *J. Chem. Soc.* 1935, 366-371.
34. (a) Ashe, A. J.; Ludwig, E. G., *Organometallics* 1982, 1, 1408-1408; (b) Breunig, H. J.; Müller, D., *Angew. Chem. Int. Ed.* 1982, 21, 439-440.
35. Calderazzo, F.; Morvillo, A.; Pelizzi, G.; Poli, R., *J. Chem. Soc., Chem. Commun.* 1983, 507-508.
36. (a) He, G.; Shynkaruk, O.; Lui, M. W.; Rivard, E., *Chem. Rev.* 2014, 114, 7815-7880; (b) Breunig, H. J., *Z. Anorg. Allg. Chem.* 2005, 631, 621-631.
37. Tokitoh, N.; Arai, Y.; Okazaki, R.; Nagase, S., *Science* 1997, 277, 78-80.
38. (a) Takahiro, S.; Yoshimitsu, A.; Nobuhiro, T.; Renji, O.; Yukio, F.; Masahiro, K.; Shigeru, N.; Norihiro, T., *Bull. Chem. Soc. Jpn.* 2002, 75, 661-675; (b) Twamley, B.; Sofield, C. D.; Olmstead, M. M.; Power, P. P., *J. Am. Chem. Soc.* 1999, 121, 3357-3367; (c) Wolf, R.; Fischer, J.; Fischer, R. C.; Fettingner, J. C.; Power, P. P., *Eur. J. Inorg. Chem.* 2008, 2008, 2515-2521.
39. Sakagami, M.; Sasamori, T.; Sakai, H.; Furukawa, Y.; Tokitoh, N., *Chem. Asian J.* 2013, 8, 690-693.
40. Dange, D.; Davey, A.; Abdalla, J. A. B.; Aldridge, S.; Jones, C., *Chem. Commun.* 2015, 51, 7128-7131.
41. von Hänisch, C.; Nikolova, D., *Eur. J. Inorg. Chem.* 2006, 2006, 4770-4773.
42. Prabusankar, G.; Gemel, C.; Parameswaran, P.; Flener, C.; Frenking, G.; Fischer, R. A., *Angew. Chem. Int. Ed.* 2009, 48, 5526-5529.
43. (a) Benda, C. B.; Fässler, T. F., *Z. Anorg. Allg. Chem.* 2014, 640, 40-45; (b) Hanauer, T.; Korber, N., *Z. Anorg. Allg. Chem.* 2004, 630, 2532-2534.

44. (a) Cho, H.-G.; Andrews, L., *J. Phys. Chem. A* 2012, *116*, 8500-8506; (b) Wang, X.; Souter, P. F.; Andrews, L., *J. Phys. Chem. A* 2003, *107*, 4244-4249.
45. Šimon, P.; de Proft, F.; Jambor, R.; Růžička, A.; Dostál, L., *Angew. Chem. Int. Ed.* 2010, *49*, 5468-5471.
46. Vránová, I.; Alonso, M.; Lo, R.; Sedlák, R.; Jambor, R.; Růžička, A.; Proft, F. D.; Hobza, P.; Dostál, L., *Chem. Eur. J.* 2015, *21*, 16917-16928.
47. Ishida, S.; Hirakawa, F.; Furukawa, K.; Yoza, K.; Iwamoto, T., *Angew. Chem. Int. Ed.* 2014, *53*, 11172-11176.
48. Schwamm, R. J.; Harmer, J. R.; Lein, M.; Fitchett, C. M.; Granville, S.; Coles, M. P., *Angew. Chem. Int. Ed.* 2015, *54*, 10630-10633.
49. Ganesamoorthy, C.; Helling, C.; Wölper, C.; Frank, W.; Bill, E.; Cutsail, G. E.; Schulz, S., *Nat. Commun.* 2018, *9*, 87.
50. (a) A. H. Male, N.; Thornton-Pett, M.; Bochmann, M., *J. Chem. Soc., Dalton Trans.* 1997, 2487-2494; (b) Perry, R. J., *Organometallics* 1989, *8*, 906-910.
51. Jeffrey, G. A., *An Introduction to Hydrogen Bonding*. Oxford University Press: 1997.
52. Veith, M.; Wieczorek, S.; Fries, K.; Huch, V., *Z. Anorg. Allg. Chem.* 2000, *626*, 1237-1245.
53. Hayes, C. E.; Platel, R. H.; Schafer, L. L.; Leznoff, D. B., *Organometallics* 2012, *31*, 6732-6740.
54. (a) Brooks, J. J.; Stucky, G. D., *J. Am. Chem. Soc.* 1972, *94*, 7333-7338; (b) Bartlett, R. A.; Dias, H. V. R.; Power, P. P., *J. Organomet. Chem.* 1988, *341*, 1-9.
55. (a) Chen, X.; Xue, X.; Zhang, L.; Sun, W.-H., *Inorg. Chem. Commun.* 2011, *14*, 235-237; (b) Wang, M.; Xu, G.; Wang, D.; Zou, Y.; Frey, W.; Buchmeiser, M. R., *Polym. Chem.* 2015, *6*, 3290-3304.
56. (a) Chivers, T.; Fedorchuk, C.; Parvez, M., *Inorg. Chem.* 2004, *43*, 2643-2653; (b) Mommertz, A.; Leo, R.; Massa, W.; Harms, K.; Dehnicke, K., *Z. Anorg. Allg. Chem.* 1998, *624*, 1647-1652; (c) Daniele, S.; Drost, C.; Gehrhus, B.; Hawkins, S. M.; Hitchcock, P. B.; Lappert, M. F.; Merle, P. G.; Bott, S. G., *J. Chem. Soc., Dalton Trans.* 2001, 3179-3188; (d) M. Boesveld, W.; F. Lappert, M., *Chem. Commun.* 1997, 2091-2092; (e) Cole, M. L.; Davies, A. J.; Jones, C.; Junk, P. C., *J. Organomet. Chem.* 2004, *689*, 3093-3107.

57. (a) Clegg, W.; Compton, N. A.; Errington, R. J.; Fisher, G. A.; Green, M. E.; Hockless, D. C. R.; Norman, N. C., *Inorg. Chem.* 1991, 30, 4680-4682; (b) Clegg, W.; Compton, N. A.; Errington, R. J.; Norman, N. C.; Wishart, N., *Polyhedron* 1989, 8, 1579-1580; (c) Vehkamäki, M.; Hatanpää, T.; Ritala, M.; Leskela, M., *J. Mater. Chem.* 2004, 14, 3191-3197.
58. Schwamm, R. J.; Coles, M. P.; Fitchett, C. M., *Dalton Trans.* 2017, 46, 4066-4074.
59. Hardman, N. J.; Twamley, B.; Power, P. P., *Angew. Chem. Int. Ed.* 2000, 39, 2771-2773.
60. (a) Balázs, G.; Balázs, L.; Breunig, H. J.; Lork, E., *Organometallics* 2003, 22, 2919-2924; (b) Balázs, G.; Breunig, H. J.; Lork, E., *Organometallics* 2002, 21, 2584-2586.
61. Jones, J. S.; Pan, B.; Gabbai, F. P., Group 15 Metal–Metal Bonds. In *Molecular Metal-Metal Bonds*, Wiley-VCH Verlag GmbH & Co. KGaA: 2015; pp 519-558.
62. (a) Frank, W.; Schneider, J.; Müller-Becker, S., *J. Chem. Soc., Chem. Commun.* 1993, 799-800; (b) Müller-Becker, S.; Frank, W.; Schneider, J., *Z. Anorg. Allg. Chem.* 1993, 619, 1073-1082; (c) Schier, A.; Wallis, J. M.; Müller, G.; Schmidbaur, H., *Angew. Chem. Int. Ed.* 1986, 25, 757-759; (d) Schmidbaur, H.; Nowak, R.; Schier, A.; Wallis, J. M.; Huber, B.; Müller, G., *Chem. Ber.* 1987, 120, 1829-1835.
63. Spek, A., *Acta Crystallogr., Sect. C* 2015, 71, 9-18.
64. Luqman, A.; Blair, V. L.; Bond, A. M.; Andrews, P. C., *Angew. Chem. Int. Ed.* 2013, 52, 7247-7251.
65. (a) Monakhov, K. Y.; Gourlaouen, C.; Zessin, T.; Linti, G., *Inorg. Chem.* 2013, 52, 6782-6784; (b) Whitmire, K. H.; Churchill, M. R.; Fettinger, J. C., *J. Am. Chem. Soc.* 1985, 107, 1056-1057; (c) Xu, L.; Sevov, S. C., *Inorg. Chem.* 2000, 39, 5383-5389; (d) Perla, L. G.; Oliver, A. G.; Sevov, S. C., *Inorg. Chem.* 2015, 54, 872-875.
66. Masuda, J. D.; Schoeller, W. W.; Donnadieu, B.; Bertrand, G., *Angew. Chem. Int. Ed.* 2007, 46, 7052-7055.
67. Hey, E.; Lappert, M. F.; Atwood, J. L.; Bott, S. G., *J. Chem. Soc., Chem. Commun.* 1987, 597-598.
68. Bresien, J.; Hering, C.; Schulz, A.; Villinger, A., *Chem. Eur. J.* 2014, 20, 12607-12615.
69. Tan, R. P.; Comerlato, N. M.; Powell, D. R.; West, R., *Angew. Chem. Int. Ed.* 1992, 31, 1217-1218.

70. Ganesamoorthy, C.; Krüger, J.; Wölper, C.; Nizovtsev, A. S.; Schulz, S., *Chem. Eur. J.* 2017, 23, 2461-2468.
71. (a) Breunig, H. J.; Ghesner, M. E.; Lork, E., *Z. Anorg. Allg. Chem.* 2005, 631, 851-856; (b) Althaus, H.; Breunig, H. J.; Probst, J.; Rösler, R.; Lork, E., *J. Organomet. Chem.* 1999, 585, 285-289; (c) Breunig, H. J.; Ghesner, M. E.; Lork, E., *J. Organomet. Chem.* 2002, 660, 167-172; (d) Bartlett, R. A.; Rasika Dias, H. V.; Hope, H.; Murray, B. D.; Olmstead, M. M.; Power, P. P., *J. Am. Chem. Soc.* 1986, 108, 6921-6926; (e) Grubba, R.; Chojnacki, J.; Pikies, J., *Acta Crystallogr., Sect. E* 2010, 66, m1403; (f) Kovacs, I.; Krautscheid, H.; Matern, E.; Sattler, E.; Fritz, G.; Hönle, W.; Borrmann, H.; Von Schnering, H. G., *Z. Anorg. Allg. Chem.* 1996, 622, 1564-1572.
72. Balázs, L.; Breunig, H. J., *Coord. Chem. Rev.* 2004, 248, 603-621.
73. Ashe, A. J.; Ludwig, E. G., *J. Organomet. Chem.* 1986, 303, 197-204.
74. Ashe, A. J.; Ludwig, E. G.; Oleksyszyn, J., *Organometallics* 1983, 2, 1859-1866.
75. Breunig Hans, J.; Müller, D., *Z. Naturforsch B* 1986, 41, 1129.
76. Balazs, L.; Breunig, H. J.; Lork, E.; Soran, A.; Silvestru, C., *Inorg. Chem.* 2006, 45, 2341-2346.
77. Heimann, S.; Bläser, D.; Wölper, C.; Schulz, S., *Organometallics* 2014, 33, 2295-2300.
78. (a) Wieber, M.; Sauer, I., *Z. Naturforsch B* 1987, 42, 695; (b) Ashe, A. J.; Ludwig, E. G., *J. Organomet. Chem.* 1986, 308, 289-296; (c) Heimann, S.; Kuczkowski, A.; Bläser, D.; Wölper, C.; Haack, R.; Jansen, G.; Schulz, S., *Eur. J. Inorg. Chem.* 2014, 2014, 4858-4864.
79. (a) Takahiro, S.; Eiko, M.; Norihiro, T., *Bull. Chem. Soc. Jpn.* 2007, 80, 2425-2435; (b) Sasamori, T.; Mieda, E.; Takeda, N.; Tokitoh, N., *Angew. Chem. Int. Ed.* 2005, 44, 3717-3720.
80. (a) Greszta, D.; Matyjaszewski, K., *Macromolecules* 1996, 29, 7661-7670; (b) Pfaendner, R., *C. R. Chim* 2006, 9, 1338-1344.
81. Forbes, G. C.; Kennedy, A. R.; Mulvey, R. E.; Rodger, P. J. A., *Chem. Commun.* 2001, 1400-1401.

82. (a) Spikes, G. H.; Peng, Y.; Fetting, J. C.; Steiner, J.; Power, P. P., *Chem. Commun.* 2005, 6041-6043; (b) Leung, W.-P.; Kan, K.-W.; So, C.-W.; Mak, T. C. W., *Organometallics* 2007, 26, 3802-3806; (c) Iwamoto, T.; Masuda, H.; Ishida, S.; Kabuto, C.; Kira, M., *J. Am. Chem. Soc.* 2003, 125, 9300-9301; (d) Naka, A.; Hill, N. J.; West, R., *Organometallics* 2004, 23, 6330-6332.
83. (a) Jones, C.; Rose, R. P., *New J. Chem.* 2007, 31, 1484-1487; (b) Liptrot, D. J.; Hill, P. M. S.; Mahon, M. F., *Angew. Chem. Int. Ed.* 2014, 53, 6224-6227.
84. (a) Balázs, L.; Breunig, H. J.; Lork, E., *Z. Anorg. Allg. Chem.* 2004, 630, 1937-1940; (b) Breunig, H. J.; Balázs, L.; Philipp, N.; Soran, A.; Silvestru, C., *Phosphorus, Sulfur Silicon Relat. Elem.* 2004, 179, 853-857.
85. Kuczkowski, A.; Schulz, S.; Nieger, M., *Angew. Chem. Int. Ed.* 2001, 40, 4222-4225.
86. Ganesamoorthy, C.; Bläser, D.; Wölper, C.; Schulz, S., *Angew. Chem. Int. Ed.* 2014, 53, 11587-11591.
87. (a) Lehmann, M.; Schulz, A.; Villinger, A., *Angew. Chem. Int. Ed.* 2012, 51, 8087-8091; (b) Ebert, K. H.; Schulz, R. E.; Breunig, H. J.; Silvestru, C.; Haiduc, I., *J. Organomet. Chem.* 1994, 470, 93-98; (c) Breunig, H. J.; Haddad, N.; Lork, E.; Mehring, M.; Mügge, C.; Nolde, C.; Raț, C. I.; Schürmann, M., *Organometallics* 2009, 28, 1202-1211.
88. (a) Chovancová, M.; Jambor, R.; Růžička, A.; Jirásko, R.; Císařová, I.; Dostál, L., *Organometallics* 2009, 28, 1934-1941; (b) Breunig, H. J.; Ghesner, I.; Lork, E., *J. Organomet. Chem.* 2002, 664, 130-135; (c) Breunig, H. J.; Königsmann, L.; Lork, E.; Nema, M.; Philipp, N.; Silvestru, C.; Soran, A.; Varga, R. A.; Wagner, R., *Dalton Trans.* 2008, 1831-1842.
89. Knop, O.; Boyd, R. J.; Choi, S. C., *J. Am. Chem. Soc.* 1988, 110, 7299-7301.
90. Dostál, L.; Jambor, R.; Erben, M.; Růžička, A., *Z. Anorg. Allg. Chem.* 2012, 638, 614-616.
91. (a) Müller, A.; Römer, M.; Bögge, H.; Krickemeyer, E.; Baumann, F.-W.; Schmitz, K., *Inorg. Chim. Acta* 1984, 89, L7-L8; (b) Müller, A.; Baumann, F.-W.; Bögge, H.; Römer, M.; Krickemeyer, E.; Schmitz, K., *Angew. Chem. Int. Ed.* 1984, 23, 632-633.
92. (a) Beneberu, H. Z.; Tian, Y.-H.; Kertesz, M., *Phys. Chem. Chem. Phys.* 2012, 14, 10713-10725; (b) Preuss, K. E., *Polyhedron* 2014, 79, 1-15; (c) Gleiter, R.; Haberhauer, G., *Coord. Chem. Rev.* 2017, 344, 263-298.
93. Fairhurst, S. A.; Johnson, K. M.; Sutcliffe, L. H.; Preston, K. F.; Banister, A. J.; Hauptman, Z. V.; Passmore, J., *J. Chem. Soc., Dalton Trans.* 1986, 1465-1472.

94. Yao, S.; Milsmann, C.; Bill, E.; Wieghardt, K.; Driess, M., *J. Am. Chem. Soc.* 2008, **130**, 13536-13537.
95. Breunig Hans, J.; Ebert, K. H.; Schulz, R. E., *Z. Naturforsch B* 1995, **50**, 735.
96. Scheer, M.; Balázs, G.; Seitz, A., *Chem. Rev.* 2010, **110**, 4236-4256.
97. Bresien, J.; Faust, K.; Hering-Junghans, C.; Rothe, J.; Schulz, A.; Villinger, A., *Dalton Trans.* 2016, **45**, 1998-2007.
98. Bezombes, J.-P.; Hitchcock, P. B.; Lappert, M. F.; Nycz, J. E., *Dalton Trans.* 2004, 499-501.
99. (a) Heinl, S.; Scheer, M., *Chem. Sci.* 2014, **5**, 3221-3225; (b) Pelties, S.; Herrmann, D.; de Bruin, B.; Hartl, F.; Wolf, R., *Chem. Commun.* 2014, **50**, 7014-7016; (c) Scherer, O. J.; Hilt, T.; Wolmershäuser, G., *Organometallics* 1998, **17**, 4110-4112; (d) Agnew, D. W.; Moore, C. E.; Rheingold, A. L.; Figueroa, J. S., *Angew. Chem. Int. Ed.* 2015, **54**, 12673-12677.
100. Khan, S.; Michel, R.; Dieterich, J. M.; Mata, R. A.; Roesky, H. W.; Demers, J.-P.; Lange, A.; Stalke, D., *J. Am. Chem. Soc.* 2011, **133**, 17889-17894.
101. Cordero, B.; Gomez, V.; Platero-Prats, A. E.; Reves, M.; Echeverria, J.; Cremades, E.; Barragan, F.; Alvarez, S., *Dalton Trans.* 2008, 2832-2838.
102. (a) Hinz, A.; Schulz, A.; Villinger, A., *Inorg. Chem.* 2016, **55**, 3692-3699; (b) Traut, S.; Hahnel, A. P.; von Hanisch, C., *Dalton Trans.* 2011, **40**, 1365-1371; (c) von Hänisch, C.; Stahl, S., *Z. Anorg. Allg. Chem.* 2009, **635**, 2230-2235.
103. Dube, J. W.; Graham, C. M. E.; Macdonald, C. L. B.; Brown, Z. D.; Power, P. P.; Ragnogna, P. J., *Chem. Eur. J.* 2014, **20**, 6739-6744.
104. (a) Back, O.; Kuchenbeiser, G.; Donnadieu, B.; Bertrand, G., *Angew. Chem. Int. Ed.* 2009, **48**, 5530-5533; (b) Masuda, J. D.; Schoeller, W. W.; Donnadieu, B.; Bertrand, G., *J. Am. Chem. Soc.* 2007, **129**, 14180-14181.
105. (a) Del Rio, N.; Lopez-Reyes, M.; Baceiredo, A.; Saffon-Merceron, N.; Lutters, D.; Müller, T.; Kato, T., *Angew. Chem. Int. Ed.* 2017, **56**, 1365-1370; (b) Asami, S.-s.; Okamoto, M.; Suzuki, K.; Yamashita, M., *Angew. Chem. Int. Ed.* 2016, **55**, 12827-12831.
106. Ohshita, J.; Tsuchida, T.; Murakami, K.; Ooyama, Y.; Nakanishi, T.; Hasegawa, Y.; Kobayashi, N.; Higashimura, H., *Z. Naturforsch B* 2014, **69**, 1181.

107. (a) Peng, Y.; Ellis, B. D.; Wang, X.; Fetting, J. C.; Power, P. P., *Science* 2009, 325, 1668-1670; (b) Fedushkin, I. L.; Nikipelov, A. S.; Lyssenko, K. A., *J. Am. Chem. Soc.* 2010, 132, 7874-7875; (c) Fedushkin, I. L.; Moskalev, M. V.; Lukoyanov, A. N.; Tishkina, A. N.; Baranov, E. V.; Abakumov, G. A., *Chem. Eur. J.* 2012, 18, 11264-11276.
108. Sakakura, T.; Choi, J.-C.; Yasuda, H., *Chem. Rev.* 2007, 107, 2365-2387.
109. Kou, X.; Wang, X.; Mendoza-Espinosa, D.; Zakharov, L. N.; Rheingold, A. L.; Watson, W. H.; Brien, K. A.; Jayarathna, L. K.; Hanna, T. A., *Inorg. Chem.* 2009, 48, 11002-11016.
110. Kaupp, M., Chemical Bonding of Main-Group Elements. In *The Chemical Bond*, Wiley-VCH Verlag GmbH & Co. KGaA: 2014; pp 1-24.
111. (a) Balázs, G.; Breunig, H. J.; Lork, E., *Z. Anorg. Allg. Chem.* 2003, 629, 1937-1942; (b) Balázs, G.; Breunig, H. J.; Lork, E.; Mason, S., *Organometallics* 2003, 22, 576-585.
112. Breunig, H. J.; Ebert, K. H.; Gülec, S.; Probst, J., *Chem. Ber.* 1995, 128, 599-603.
113. Tokitoh, N.; Arai, Y.; Sasamori, T.; Okazaki, R.; Nagase, S.; Uekusa, H.; Ohashi, Y., *J. Am. Chem. Soc.* 1998, 120, 433-434.
114. Tuscher, L.; Ganesamoorthy, C.; Bläser, D.; Wölper, C.; Schulz, S., *Angew. Chem. Int. Ed.* 2015, 54, 10657-10661.
115. Dostál, L., *Coord. Chem. Rev.* 2017, 353, 142-158.
116. von Seyerl, J.; Huttner, G., *Angew. Chem. Int. Ed.* 1978, 17, 843-844.
117. Cook, W. T.; Vincent, J. S., *J. Chem. Phys.* 1977, 67, 5766-5769.
118. (a) Kretschmer, R.; Ruiz, D. A.; Moore, C. E.; Rheingold, A. L.; Bertrand, G., *Angew. Chem. Int. Ed.* 2014, 53, 8176-8179; (b) Dorsey, C. L.; Mushinski, R. M.; Hudnall, T. W., *Chem. Eur. J.* 2014, 20, 8914-8917.
119. Martin, C. D.; Soleilhavoup, M.; Bertrand, G., *Chem. Sci.* 2013, 4, 3020-3030.
120. (a) Hering, C.; Rothe, J.; Schulz, A.; Villinger, A., *Inorg. Chem.* 2013, 52, 7781-7790; (b) Ma, X.; Ding, Y.; Roesky, H. W.; Sun, S.; Yang, Z., *Z. Anorg. Allg. Chem.* 2013, 639, 49-52.
121. (a) Breunig, H. J.; Ghesner, I.; Ghesner, M. E.; Lork, E., *J. Organomet. Chem.* 2003, 677, 15-20; (b) Dostál, L.; Jambor, R.; Růžička, A.; Šimon, P., *Eur. J. Inorg. Chem.* 2011, 2011, 2380-2386.

122. (a) Balázs, G.; Breunig, H. J.; Lork, E.; Offermann, W., *Organometallics* 2001, 20, 2666-2668; (b) Breunig, H. J.; Lork, E.; Moldovan, O.; Raț, C. I., *J. Organomet. Chem.* 2008, 693, 2527-2534; (c) Baker, R. J.; Brym, M.; Jones, C.; Waugh, M., *J. Organomet. Chem.* 2004, 689, 781-790.
123. Cangelosi, V. M.; Pitt, M. A.; Vickaryous, W. J.; Allen, C. A.; Zakharov, L. N.; Johnson, D. W., *Cryst. Growth Des.* 2010, 10, 3531-3536.
124. Twamley, B.; Hwang, C.-S.; Hardman, N. J.; Power, P. P., *J. Organomet. Chem.* 2000, 609, 152-160.
125. Benesch, R.; Malli, G., *Int. J. Quantum Chem* 1968, 2, 371-389.
126. Piltz, R., *Acta Crystallogr., Sect. A* 2011, 67, C155.
127. Haynes, W. M., *CRC Handbook of Chemistry and Physics: A Ready-reference Book of Chemical and Physical Data*. CRC Press: 2016.
128. Ganesamoorthy, C.; Wölper, C.; Nizovtsev, A. S.; Schulz, S., *Angew. Chem. Int. Ed.* 2016, 55, 4204-4209.
129. Pardoe, J. A. J.; Downs, A. J., *Chem. Rev.* 2007, 107, 2-45.
130. (a) Tacke, M.; Schnoeckel, H., *Inorg. Chem.* 1989, 28, 2895-2896; (b) Widdifield, C. M.; Jurca, T.; Richeson, D. S.; Bryce, D. L., *Polyhedron* 2012, 35, 96-100.
131. Meyer, G.; Blachnik, R., *Z. Anorg. Allg. Chem.* 1983, 503, 126-132.
132. (a) Hirayama, L. C.; Haddad, T. D.; Oliver, A. G.; Singaram, B., *J. Org. Chem.* 2012, 77, 4342-4353; (b) M. Godfrey, S.; J. Kelly, K.; Kramkowski, P.; A. McAuliffe, C.; G. Pritchard, R., *Chem. Commun.* 1997, 1001-1002; (c) Baker, R. J.; Farley, R. D.; Jones, C.; Kloth, M.; Murphy, D. M., *Chem. Commun.* 2002, 1196-1197; (d) Green, S. P.; Jones, C.; Stasch, A., *Angew. Chem. Int. Ed.* 2007, 46, 8618-8621; (e) Gabbai, F. P.; Schier, A.; Riede, J.; Schmidbaur, H., *Inorg. Chem.* 1995, 34, 3855-3856.
133. Uhl, W.; Layh, M.; Hiller, W., *J. Organomet. Chem.* 1989, 368, 139-154.
134. (a) Schluter, R. D.; Cowley, A. H.; Atwood, D. A.; Jones, R. A.; Bond, M. R.; Carrano, C. J., *J. Am. Chem. Soc.* 1993, 115, 2070-2071; (b) Brothers, P. J.; Hübler, K.; Hübler, U.; Noll, B. C.; Olmstead, M. M.; Power, P. P., *Angew. Chem. Int. Ed.* 1996, 35, 2355-2357.
135. (a) Wiberg, N.; Blank, T.; Amelunxen, K.; Nöth, H.; Schnöckel, H.; Baum, E.; Purath, A.; Fenske, D., *Eur. J. Inorg. Chem.* 2002, 2002, 341-350; (b) Wochele, R.; Schwarz, W.; Klinkhammer, K. W.; Locke, K.; Weidlein, J., *Z. Anorg. Allg. Chem.* 2000, 626, 1963-1973.

136. (a) Veith, M.; Goffing, F.; Becker, S.; Huch, V., *J. Organomet. Chem.* 1991, 406, 105-118; (b) Hellmann, K. W.; Galka, C. H.; Rüdenauer, I.; Gade, L. H.; Scowen, I. J.; McPartlin, M., *Angew. Chem. Int. Ed.* 1998, 37, 1948-1952; (c) Grocholl, L.; Schranz, I.; Stahl, L.; Staples, R. J., *Inorg. Chem.* 1998, 37, 2496-2499.
137. Protchenko, A. V.; Dange, D.; Harmer, J. R.; Tang, C. Y.; Schwarz, A. D.; Kelly, M. J.; Phillips, N.; Tirfoin, R.; Birjkumar, K. H.; Jones, C.; Kaltsoyannis, N.; Mountford, P.; Aldridge, S., *Nat. Chem.* 2014, 6, 315.
138. (a) Braunschweig, H.; Dewhurst, R. D., *Organometallics* 2014, 33, 6271-6277; (b) Bag, P.; Porzelt, A.; Altmann, P. J.; Inoue, S., *J. Am. Chem. Soc.* 2017, 139, 14384-14387.
139. (a) Wright, R. J.; Brynda, M.; Power, P. P., *Angew. Chem. Int. Ed.* 2006, 45, 5953-5956; (b) Hardman, N. J.; Wright, R. J.; Phillips, A. D.; Power, P. P., *Angew. Chem. Int. Ed.* 2002, 41, 2842-2844; (c) Xie, Y.; Grev, R. S.; Gu, J.; Schaefer, H. F.; Schleyer, P. v. R.; Su, J.; Li, X.-W.; Robinson, G. H., *J. Am. Chem. Soc.* 1998, 120, 3773-3780; (d) Su, J.; Li, X.-W.; Crittendon, R. C.; Robinson, G. H., *J. Am. Chem. Soc.* 1997, 119, 5471-5472.
140. Moilanen, J.; Power, P. P.; Tuononen, H. M., *Inorg. Chem.* 2010, 49, 10992-11000.
141. (a) Abdalla, J. A. B.; Aldridge, S., Group 13 Metal–Metal Bonds. In *Molecular Metal-Metal Bonds*, Wiley-VCH Verlag GmbH & Co. KGaA: 2015; pp 455-484; (b) Wright, R. J.; Phillips, A. D.; Hardman, N. J.; Power, P. P., *J. Am. Chem. Soc.* 2002, 124, 8538-8539.
142. Hopkinson, M. N.; Richter, C.; Schedler, M.; Glorius, F., *Nature* 2014, 510, 485.
143. Asay, M.; Jones, C.; Driess, M., *Chem. Rev.* 2011, 111, 354-396.
144. (a) Schmidt, E. S.; Schier, A.; Schmidbaur, H., *J. Chem. Soc., Dalton Trans.* 2001, 505-507; (b) Fedushkin, I. L.; Lukoyanov, A. N.; Fukin, G. K.; Ketkov, S. Y.; Hummert, M.; Schumann, H., *Chem. Eur. J.* 2008, 14, 8465-8468; (c) Fedushkin, I. L.; Lukoyanov, A. N.; Tishkina, A. N.; Fukin, G. K.; Lyssenko, K. A.; Hummert, M., *Chem. Eur. J.* 2010, 16, 7563-7571; (d) Baker, R. J.; Farley, R. D.; Jones, C.; Kloth, M.; Murphy, D. M., *J. Chem. Soc., Dalton Trans.* 2002, 3844-3850; (e) Baker, R. J.; Jones, C.; Mills, D. P.; Pierce, G. A.; Waugh, M., *Inorg. Chim. Acta* 2008, 361, 427-435.
145. Tuononen, H. M.; Roesler, R.; Dutton, J. L.; Ragogna, P. J., *Inorg. Chem.* 2007, 46, 10693-10706.
146. Segawa, Y.; Yamashita, M.; Nozaki, K., *Science* 2006, 314, 113-115.

147. (a) Makoto, Y.; Yuta, S.; Yasutomo, S.; Kyoko, N., *Chem. Lett.* 2008, 37, 802-803; (b) Segawa, Y.; Suzuki, Y.; Yamashita, M.; Nozaki, K., *J. Am. Chem. Soc.* 2008, 130, 16069-16079; (c) Segawa, Y.; Yamashita, M.; Nozaki, K., *Angew. Chem. Int. Ed.* 2007, 46, 6710-6713.
148. Metzler-Nolte, N., *New J. Chem.* 1998, 22, 793-795.
149. (a) Cui, C.; Roesky, H. W.; Schmidt, H.-G.; Noltemeyer, M.; Hao, H.; Cimpoesu, F., *Angew. Chem. Int. Ed.* 2000, 39, 4274-4276; (b) Hardman, N. J.; Eichler, B. E.; Power, P. P., *Chem. Commun.* 2000, 1991-1992; (c) Li, X.; Cheng, X.; Song, H.; Cui, C., *Organometallics* 2007, 26, 1039-1043; (d) Jones, C.; Junk, P. C.; Platts, J. A.; Stasch, A., *J. Am. Chem. Soc.* 2006, 128, 2206-2207.
150. Findlater, M.; Hill, N. J.; Cowley, A. H., *Dalton Trans.* 2008, 4419-4423.
151. (a) Chen, C.-H.; Tsai, M.-L.; Su, M.-D., *Organometallics* 2006, 25, 2766-2773; (b) Reiher, M.; Sundermann, A., *Eur. J. Inorg. Chem.* 2002, 2002, 1854-1863.
152. Sundermann, A.; Reiher, M.; Schoeller, W. W., *Eur. J. Inorg. Chem.* 1998, 1998, 305-310.
153. Hill, M. S.; Hitchcock, P. B., *Chem. Commun.* 2004, 1818-1819.
154. (a) Jin, G.; Jones, C.; Junk, P. C.; Stasch, A.; Woodul, W. D., *New J. Chem.* 2008, 32, 835-842; (b) Hill, M. S.; Hitchcock, P. B.; Pongtavornpinyo, R., *Dalton Trans.* 2005, 273-277; (c) Hill, M. S.; Hitchcock, P. B.; Pongtavornpinyo, R., *Dalton Trans.* 2007, 731-733; (d) Hill, M. S.; Hitchcock, P. B.; Pongtavornpinyo, R., *Angew. Chem. Int. Ed.* 2005, 44, 4231-4235.
155. (a) Moxey, G. J.; Jones, C.; Stasch, A.; Junk, P. C.; Deacon, G. B.; Woodul, W. D.; Drago, P. R., *Dalton Trans.* 2009, 2630-2636; (b) Green, S. P.; Jones, C.; Stasch, A., *Inorg. Chem.* 2007, 46, 11-13; (c) Jones, C.; Stasch, A.; Moxey, G. J.; Junk, P. C.; Deacon, G. B., *Eur. J. Inorg. Chem.* 2009, 2009, 3593-3599.
156. (a) Pullumbi, P.; Bouteiller, Y.; Manceron, L.; Mijoule, C., *Chem. Phys.* 1994, 185, 25-37; (b) Downs, A. J.; Pulham, C. R., *Chem. Soc. Rev.* 1994, 23, 175-184.
157. E. Hibbs, D.; Jones, C.; A. Smithies, N., *Chem. Commun.* 1999, 185-186.
158. Abernethy, C. D.; Cole, M. L.; Jones, C., *Organometallics* 2000, 19, 4852-4857.
159. Kümmel, C.; Meller, A.; Noltemeyer, M., *Z. Naturforsch B* 1996, 51, 209.
160. Baker, R. J.; Jones, C.; Junk, P. C.; Kloth, M., *Angew. Chem. Int. Ed.* 2004, 43, 3852-3855.

161. (a) Khan, M. A.; Tuck, D. G., *Acta Crystallogr., Sect. B* 1982, 38, 803-806; (b) Trotter, J.; Einstein, F. W. B.; Tuck, D. G., *Acta Crystallogr., Sect. B* 1969, 25, 603-604; (c) Scaife, D., *Aust. J. Chem.* 1970, 23, 2205-2216.
162. Baker, R. J.; Jones, C.; Kloth, M.; Platts, J. A., *Angew. Chem. Int. Ed.* 2003, 42, 2660-2663.
163. (a) Silverman, J. S.; Carmalt, C. J.; Cowley, A. H.; Culp, R. D.; Jones, R. A.; McBurnett, B. G., *Inorg. Chem.* 1999, 38, 296-300; (b) Luo, B.; Cramer, C. J.; Gladfelter, W. L., *Inorg. Chem.* 2003, 42, 3431-3437; (c) Frey, R.; Gupta, V. D.; Linti, G., *Z. Anorg. Allg. Chem.* 1996, 622, 1060-1064.
164. Chu, T.; Nikonov, G. I., *Chem. Rev.* 2018, 118, 3608-3680.

Publications in Support of this Thesis

1. Schwamm, R. J.; Lein, M.; Coles, M. P.*; Fitchett, C. M., "Bi–P Bond Homolysis as a Route to Reduced Bismuth Compounds and Reversible Activation of P₄" *Angew. Chem. Int. Ed.* **2016**, 14798 – 14801.
2. Schwamm R. J.; Fulton, J. R.; Coles, M. P.; Fitchett, C. M., "Hydrophosphination-Type Reactivity Promoted by Bismuth Phosphanides: Scope and Limitations" *Dalton Trans.* **2017**, 2068 – 2071.
3. Schwamm, R. J.; Coles, M. P.*; Fitchett, C. M., "Neutral and Cationic Bismuth Compounds Supported by Bis(amidodimethyl)disiloxane Ligands" *Dalton Trans.* **2017**, 4066 – 4074.
4. Schwamm, R. J.; Lein, M.; Coles, M. P.*; Fitchett, C. M., "Bismuth(III) Complex of the [S₄]^{•–} Radical Anion: Dimer Formation via Pancake Bonds" *J. Am. Chem. Soc.* **2017**, 16490 – 16493.
5. Schwamm, R. J.; Lein, M.; Coles, M. P.*; Fitchett, C. M., Catalytic Oxidative Coupling Promoted by Bismuth TEMPO_x Complexes" *Chem. Commun.* **2018**, 916 – 919.
6. Schwamm, R. J.; Anker, M.; Lein, M.; Coles, M. P.*; Fitchett, C. M., "Indyllithium and the Indyl Anion [InL][–]. Heavy Analogues of N-Heterocyclic Carbenes" *Angew. Chem. Int. Ed.* **2018**, *in press*. DOI: 10.1002/anie.201802444.